Flue Gas Injection for Methane Recovery from Gas Hydrate Reservoirs and Geological Storage of CO_2

Anthony Okwananke

Thesis submitted for the degree of Doctor of Philosophy in

Petroleum Engineering

Heriot-Watt University

Institute of Petroleum Engineering

School of Energy, Geoscience, Infrastructure, and Society

March 2017.

ABSTRACT

The global energy system has been gradually de-carbonised over the years, from wood to coal, coal to oil, and then natural gas. Natural gas hydrates with their abundance in nature, therefore represent a potentially significant new clean energy source for the future. A few field trials have been conducted to recover natural gas (methane) from gas hydrate reservoirs. While the outcomes of these trials offer a glimmer of hope on the possibility of methane production from gas hydrate resources, there remains the nagging question of production sustainability as most field trials are short-lived due to high energy penalty, sand management issues, excessive water production, and potential environmental risks.

This thesis reports the development of a novel technique for methane recovery from natural gas hydrate reservoirs by flue gas injection. Compared to the existing methods, the principal concept of the technique is to break the thermodynamic equilibrium of methane hydrate by flue gas injected, causing a shift in the equilibrium phase boundary to accommodate the presence of flue gas while releasing methane from hydrate dissociation. A series of experiments were conducted at different simulated hydrate reservoir conditions to demonstrate the feasibility of the technique vis-à-vis understanding how methane hydrate decomposes in the presence of flue gas, the impact of flue gas on the depressurisation process, and the possibility of the CO_2 component in the flue gas being sequestered as CO_2 or CO_2-mixed hydrates. Furthermore, the impact of the excess aqueous phase, salinity, and sediment mineralogy on methane recovery were also investigated. Finally, peculiarities of gas flow in hydrate-bearing sediments were also investigated and modelled with existing permeability models.

Results indicated significant dissociation of methane hydrate by a shift in the methane hydrate equilibrium phase boundary leading to a rise in methane concentration in the vapour phase. Enhanced methane recovery by depressurisation in the presence of flue gas generated a methane-rich vapour phase of up to 80 mol% methane at experimental conditions within the methane hydrate stability zone (HSZ). CO_2 hydrate, N_2-CO_2-CH_4 hydrate, and CO_2-CH_4 were formed simultaneously alongside methane recovery after flue gas injection. Up to 70% of CO_2 in the vapour phase was captured and retained in the hydrate phase. Increased aqueous phase salinity enhanced methane recovery and increased CO_2 capture and storage in excess water environments.

Extension of the concept to air and nitrogen injection showed enhance depressurisation compared to flue gas injection with up to 90 mol% methane in the vapour phase at conditions still within the methane HSZ. It is also flexible, with the possibility of stepwise depressurisation with continuous and incremental methane recovery.

Potentially these techniques are economically feasible as they save on costs in terms of thermal energy supply and chemical additives. On the operational front, it is not subject to injectivity constraints due to secondary hydrate formation. It also has the capacity to maintain reservoir energy, limit water production, and deliver better sand management. Additionally, direct capture and storage of CO_2 from flue gas could provide huge savings in carbon capture and storage processes.

PREFACE

This thesis is submitted to the Institute of Petroleum Engineering, School of Energy, Geoscience, Infrastructure and Society (EGIS), Heriot-Watt University in partial fulfilment of the requirements for the award of the degree of doctor of philosophy (PhD). It is a documentation of work done in the laboratories of the Centre for Hydrate Research, Institute of Petroleum Engineering, Heriot-Watt University. Parts of the materials in this thesis has been presented or published elsewhere as contained in the "LIST OF PUBLICATIONS BY THE CANDIDATE''

Anthony Okwananke

March 2017.

DEDICATION

To the Okwanankes, nuclear, extended, and the yet to come.

ACKNOWLEDGMENTS

I am thankful to the government of Nigeria through the Petroleum Technology Development Fund (PTDF) for granting the PhD scholarship to carry out this research. I am eternally grateful to my supervisor, Dr Jinhai Yang for his meticulous supervision which is unequalled and unparalleled. I appreciate his day-to-day guidance in the laboratory and the many critical discussions we had. I attribute the success of this research to him. I also learned from the best, I learned from Professor Bahman Tohidi. I thank him for giving me the privilege to work in his group, thereby working in the same laboratory as great minds such as Professor Ali Danesh and Professor Adrian Todd. I appreciate his fatherly love and expert guidance.

Many thanks to other members of the Hydrate, PVT and Flow Assurance Research Group. I thank Dr Rod Burgass for his clever solutions to leakage problems in my experimental rig. Special thanks to Dr Antonin Chapoy for his help with the GC. I commend Alastair Reid, the Laboratory Safety Officer, for ensuring that I stay alive and in one piece throughout the duration of the study. My appreciation goes to Evgeny Chuvillin, Boris Bukhanov, Alexei Cheremisin and Kirill Maerle for their contributions during the collaborative research with their Centre for Hydrocarbon Recovery, Skolkovo Institute of Science and Technology, Moscow Russia.

I shared office space with wonderful people: Luis Pereira, Alfonso Gonzalez, Foroogh Tohidi, Houra Mozaffar, and Edris Joonaki. They made the office a home away from home. My appreciation also goes to other colleagues in the group; Mohammadreza Amerimahabadian, Ramin Mousavi, Mohsen Hoopanah and Aliakbar Hassanpouryouzband for their warmth and friendship. You all will always be remembered.

Finally, to my *personal persons* - the Okwanankes, for their love, encouragement and prayers made me *iron like the lion in Zion*. I am eternally indebted to you all.

DECLARATION STATEMENT

TABLE OF CONTENTS

ABSTRACT……**ii**

PREFACE……**iv**

DEDICATION……**v**

ACKNOWLEDGMENTS ..... **vi**

TABLE OF CONTENTS..... **viii**

LIST OF TABLES……**xii**

LIST OF FIGURES……..**xiv**

LIST OF PUBLICATIONS BY THE CANDITATE..... **xix**

NOMENCLATURE……..…..**xx**

CHAPTER 1 INTRODUCTION..... **1**

1.1 World Energy Demand..... 1

1.2 Gas Hydrates 1

1.2.1 Gas hydrates in history..... 2

1.2.2 Structure of hydrates 3

1.2.3 Hydrate phase diagram..... 5

1.3 Gas Hydrates in the Earth..... 6

1.4 Hydrate - Geohazard Nexus 11

1.5 Classification of Gas Hydrate Accumulations 12

1.6 Hydrate Resource Assessment 14

1.7 Techniques for Methane Recovery from Hydrate Reservoirs..... 16

1.8 Field production Tests 21

1.9 Gas Hydrate Application in Carbon dioxide Capture and Storage (CCS) 24

1.10 Aims and Outline of Thesis..... 25

CHAPTER 2 THEORETICAL BACKGROUND **27**

2.1 Phase Diagrams of Hydrate Systems..... 27

2.2 Hydrate Thermodynamic Model 33

2.2.1 Multi-phase equilibrium..... 34

2.2.2 Vapour and liquid phases 35

2.2.3 Solid (hydrate) phase 36
2.3 Hydrate Formation 39
2.3.1 Hydrate nucleation 39
2.3.2 Hydrate growth 41
2.4 Hydrate Dissociation 43
2.5 Summary 43
CHAPTER 3 FLUE GAS INJECTION FOR METHANE RECOVERY FROM METHANE HYDRATE RESERVOIRS 44
3.1 Introduction 44
3.2 Experimental Apparatus 45
3.3 Materials 47
3.4 Experimental Procedure 49
3.4.1 Test conditions 49
3.4.2 Sample preparations 50
3.4.3 Methane hydrate synthesis 51
3.4.4 Flue gas injection 52
3.4.5 Methane recovery 53
3.4.6 GC analysis 53
3.5 Results and Discussions 56
3.5.1 Decomposition kinetics 56
3.5.2 CO_2 sequestration 67
3.6 Summary 70
CHAPTER 4 INFLUENCE OF WATER SALINITY ON METHANE RECOVERY BY FLUE GAS INJECTION 72
4.1 Introduction 72
4.2 Experimental Section 73
4.2.1 Experimental apparatus 73
4.2.2 Experimental materials 75
4.2.3 Experimental procedure 75
4.3 Results and Discussions 76
4.3.1 Formation behaviour of methane hydrate in water and NaCl solutions 77
4.3.2 Decomposition kinetics 80
4.3.3 Influence of water salinity on methane recovery by depressurisation 82
4.3.4 Influence of water salinity on CO_2 sequestration 84

4.4 Summary 89
CHAPTER 5 INFLUENCE OF SEDIMENT MINERALOGY ON METHANE RECOVERY BY FLUE GAS INJECTION 91
5.1 Introduction 91
5.2 Experimental Section 93
5.2.1 Experimental apparatus and materials 93
5.2.2 Experimental procedure 95
5.3 Results and Discussions 95
5.3.1 Effect of sediment mineralogy on hydrate formation 96
5.3.2 Effect of sediment mineralogy on methane hydrate decomposition in the presence of flue gas 100
5.3.3 Effect on sediment mineralogy on methane recovery by depressurisation in the presence of flue gas 102
5.3.4 Effect of sediment mineralogy on CO_2 sequestration 104
5.4 Summary 107
CHAPTER 6 ENHANCED DEPRESSURISATION FOR METHANE RECOVERY BY COMPRESSED AIR INJECTION 110
6.1 Introduction 110
6.2 Experimental Section 111
6.2.1 Experimental apparatus and materials 111
6.2.2 Experimental procedure 111
6.3 Results and Discussions 113
6.3.1 Multi-stage depressurisation 114
6.3.2 Methane recovery ratios 116
6.3.3 Kinetics of methane recovery in the presence of air 120
6.3.4 Depressurisation for enhanced recovery 124
6.4 Summary 126
CHAPTER 7 EXPERIMENTAL STUDY OF GAS PERMEATION THROUGH GAS HYDRATE-BEARING SEDIMENTS 128
7.1 Introduction 128
7.2 Experimental Section 130
7.2.1 Materials 130
7.2.2 Experimental apparatus and set-up 131
7.2.3 Experimental procedure 133

7.3 Gas Permeability Calculation 135
7.4 Experimental Results and Discussions 136
7.4.1 Permeability-pressure relationship 137
7.4.2 Permeability in the presence of hydrate 138
7.4.3 Permeability measurement in solid sandstone core 141
7.5 Permeability Reduction Models 143
7.5.1 Parallel capillary model 144
7.5.2 Kozeny grain model 144
7.6 Prediction Performance of Permeability Reduction Models 145
7.7 Summary 147
CHAPTER 8 CONCLUSIONS AND RECOMMENDATIONS 149
8.1 Introduction 149
8.2 Conclusions 149
8.3 Recommendations 155
REFERENCES 158

LIST OF TABLES

Table 3.1 *Mineralogical composition of Fife sand* *47*

Table 3.2 *Particle size distribution for the silica (Fife, Scotland) sand used in the experiments* *48*

Table 3.3*. Summary of experimental conditions* *50*

Table 3.4. *Properties and initial parameters of the hydrate bearing sediment samples* *56*

Table 3.5*. Initial and maximum vapour phase methane concentration in stages 1 and 2 of the kinetic recovery phase, experimental conditions, and elapsed time* *58*

Table 3.6*. Rates of methane recovery, amount recovered, and percentage recovery for at the end of the kinetic phase* *62*

Table 3.7*. Methane released, % methane recovery with time, and elapsed time for Experiment 1* *63*

Table 3.8*. Methane released, % methane recovery with time, and elapsed time for Experiment 2* *63*

Table 3.9*. Methane released, % methane recovery with time, and elapsed time for Experiment 3* *63*

Table 3.10*. Methane released, % methane recovery with time, and elapsed time for Experiment 4* *64*

Table 3.11. *Depressurisation pressure range, initial and final vapour phase methane concentration during the depressurisation phase.* *66*

Table 3.12. *Amount of CO_2 in the vapour phase captured and stored as hydrates.* *70*

Table 4.1 *Summary of experimental conditions* *75*

Table 4.2 *Properties and initial parameters of the hydrate bearing sediment samples* *77*

Table 4.3. *Vapour phase methane concentration, methane release rates, and CO_2 ratio during methane recovery (Stages 1 and 2).* *82*

Table 4.4*. Kinetics of CO_2 hydrate formation and the amount of CO_2 captured in the hydrate phase during Stages 1 and 2.* *88*

Table 5.1 *Mineralogical composition of the IODP sediment* *94*

Table 5.2 *Particle size distribution for the IODP sediment used in the experiments* *94*

Table 5.3 *Properties and initial parameters of the hydrate bearing sediment samples* *96*

Table 5.4. *Vapour phase methane concentration, methane release rates, and CO_2 ratio during methane recovery (Stages 1 and 2).* *102*

Table 5.5*. Kinetics of CO_2 hydrate formation and the amount of CO_2 captured in the hydrate phase during Stages 1 and 2.* *107*

Table 6.1 *Properties and initial parameters of the hydrate bearing sediment samples* *114*

Table 6.2 *Initial pressure, target pressure, equilibrium pressure, and vapour phase methane concentration* *117*

Table 6.3 *Summary of recovery experiments during the multi-stage depressurisation phase showing rate of methane recovery, amount of methane released from methane hydrate and percentage methane recovery* *122*

Table 7.1 *Particle size distribution of the montmorillonite used in the experiments 130*

Table 7.2 *Properties and initial parameters of the unconsolidated core samples used..... 137*

Table 7.3 *Properties and initial parameters of the solid sandstone core samples used..... 141*

LIST OF FIGURES

Figure 1.1 *Gas hydrate structure [24].* *4*

Figure 1.2 *Phase boundary of methane hydrate.* *5*

Figure 1.3 *Methane hydrate stability envelope (region) for permafrost sediments [25].* *6*

Figure 1.4 *Methane hydrate stability envelope (region) for marine sediments [25]* *7*

Figure 1.5 *Classes of hydrates in sediments based on morphology [38]* *9*

Figure 1.6 *Seismic profile across the Blake Ridge during transect drilling at sites 994, 995, and 997 of the Ocean Drilling Program (ODP) Leg 164 [40].* *10*

Figure 1.7 *Class 1 hydrate accumulation showing the bottom of the hydrate interval coinciding with bottom of the hydrate stability zone and the underlying free gas and water zone.(Adapted from [60]).* ... *12*

Figure 1.8 *Class 2 hydrate accumulation showing the bottom of the hydrate interval not coinciding with bottom of the hydrate stability zone, and the underlying water zone. (Adapted from [60]).* *13*

Figure 1.9 *Class 3 hydrate accumulation showing the bottom of the hydrate interval not coinciding with bottom of the hydrate stability zone, with no underlying water and/or free gas zone. (Adapted from [60]).* *14*

Figure 1.10 *Map showing locations of known and inferred gas hydrate accumulations [63].* *15*

Figure 1.11 *Methane recovery from hydrate reservoir by depressurisation.* *17*

Figure 1.12 *Methane recovery from hydrate reservoir by thermal stimulation.* *18*

Figure 1.13 *Methane recovery from hydrate reservoir by inhibitor injection.* *19*

Figure 1.14 *Methane recovery from hydrate reservoir by gas injection.* *21*

Figure 2.1 *Schematic diagram of the phase behaviour of unary system of water in a P-T plane (adapted from [125])* *29*

Figure 2.2 *Schematic diagram of the phase behaviour of binary system of water and a hydrate forming component (▬) in a P-T plane. The phase diagram is representative of a gas with* $T_c<T_{tr,water}$ *eg. methane. The phase behaviour of the unary system of water (▬ ▬) included for reference purpose.(adapted from [125]).* *31*

Figure 2.3 *Schematic diagram of the phase behaviour of binary system of water and a hydrate forming component (▬) in a P-T plane. The phase diagram is representative of a gas with* $T_c>T_{tr,water}$ *eg. carbondioxide. The phase behaviour of the unary system of water (▬ ▬) included for reference purpose.(adapted from[127]).* *31*

Figure 2.4 *Schematic diagram of the phase behaviour of multicomponent natural gas and water system (a) natural gas systems with light and heavy components (b) natural gas systems with heavy liquid hydrocarbon mixture (adapted from [25]).* *32*

Figure 2.5 *Typical pressure profile with time for a hydrate formation experiment (adapted from [160]).* *40*

Figure 2.6 *Schematic representation of the two-film theory (adapted from [152]).* *42*

Figure 3.1 *Schematic diagram of experimental rig.* *46*

Figure 3.2 *Malvern Mastersizer particle size distribution analyser..... 48*

Figure 3.3 *Particle size distributions of the sand used in graphical form..... 49*

Figure 3.4 *Phase boundaries of methane-, nitrogen-, and CO_2-hydrates, phase boundaries of vapour phase compositions of 50:50 mol% flue gas + methane; 80:20 mol% flue gas + methane in equilibrium with methane hydrate, and the test conditions. 50*

Figure 3.5 *Methane hydrate equilibrium phase boundary and methane hydrate formation pressure profile. The circled part shows the abrupt change in slope of pressure profile indicating the onset of hydrate formation at approximately 281 K and 16 MPa..... 52*

Figure 3.6 *Methane hydrate formation temperature and pressure profile with time. Hydrate formation was completed at 140 hours after which the system pressure remains relatively constant..... 52*

Figure 3.7 *Chromatogram of a gas mixture containing nitrogen, methane, and carbon dioxide. 54*

Figure 3.8 *Calibration lines of (a) nitrogen, (b) methane, and (c) carbondioxide showing their moles as functions of their respective peak areas..... 55*

Figure 3.9 *Methane recovery stages after flue gas injection for Experiment 1 ..... 57*

Figure 3.10 *Shifting system phase boundaries for Experiment 1 from flue gas rich region (◆) 15.87 CH_4, 76.74 N_2, 7.39 CO_2 (mol%)) to methane rich region (●) 53.34 CH_4, 44.62 N_2, 2.02 CO_2 (mol%)). 58*

Figure 3.11 *Shifting system phase boundaries for Experiment 2 from flue gas rich region (◆) 18.52 CH_4, 70.05 N_2, 11.43 CO_2 (mol%)) to methane rich region (●) 49.52 CH_4, 47.46 N_2, 3.55 CO_2 (mol%)) 59*

Figure 3.12 *Shifting system phase boundaries for Experiment 3 from flue gas rich region (◆) 12.99 CH_4, 75.82 N_2, 11.19 CO_2 (mol%)) to methane rich region (●) 47.00 CH_4, 47.55 N_2, 5.45 CO_2 (mol%)). 59*

Figure 3.13 *Shifting system phase boundaries for Experiment 2 from flue gas rich region (◆) 24.79 CH_4, 67.43 N_2, 7.78 CO_2 (mol%)) to methane rich region (●) 46.79 CH_4, 47.45 N_2, 5.76 CO_2 (mol%)). 60*

Figure 3.14 *Evolution of the vapour phase methane concentration during the kinetic recovery phase 60*

Figure 3.15 *Amount of methane released from the hydrate phase into the vapour phase for Experiments 1 to 4. ..... 64*

Figure 3.16 *Percentage methane recovery for Experiments 1 to 4. ..... 64*

Figure 3.17 *Temperature profile of 0 to 5 hour for Experiments 1 and 3. ..... 65*

Figure 3.18 *Vapour phase methane concentration during depressurisation in the presence of flue gas. Dotted vertical lines represent decomposition pressure of methane hydrate at the experimental temperatures. Methane hydrate starts to decompose well inside the methane hydrate stability zone..... 66*

Figure 3.19 *Vapour phase concentrations of methane, nitrogen, and CO_2 after flue gas injection and during depressurisation. The ratio $CO_2/(CO_2+N_2)$ shows the absolute content of CO_2 in the flue gas component of the vapour phase at any instant. (a), (b), (c) and (d) represent Experiments 1, 2, 3 and 4 respectively..... 70*

Figure 4.1 *Schematic diagram of experimental rig for the excess gas method. The dashed red lines represent cables for electronic communications while the black solid lines represent conduits for fluid flow..... 74*

Figure 4.2 *Schematic diagram of experimental rig for the excess water method. The dashed red lines represent cables for electronic communications while the black solid lines represent conduits for fluid flow..... 74*

Figure 4.3 *Temperature and pressure profiles of methane hydrate formation during Experiments 5, 6, and 7 respectively. T1, T2, T3 and P1, P2, P3 represents temperature and pressure profiles for systems with 0, 3, and 10 mass% NaCl respectively.* *78*

Figure 4.4 *Hydrate formation rates for systems with 0, 3, and 10 mass% NaCl solution.* *79*

Figure 4.5 *Water injection rates for hydrate formation in excess water environment during Experiments8, 9, and 10 respectively.* *79*

Figure 4.6 *Methane conversion to hydrate for excess gas and excess water hydrate formation methods with varying degrees of water salinity.* *80*

Figure 4.7 *Evolution of the vapour phase methane concentration after flue gas injection. Thick lines represent experiments with excess gas hydrate formation method. Dashed lines represent experiments with excess water hydrate formation method.* *82*

Figure 4.8 *Vapour phase methane concentration during depressurisation in the presence of flue gas. (a) and (b) represents experiments with excess gas and excess water hydrate formation methods respectively. Dotted vertical lines (-----) (_ _ _) (_ . _ . _) represents decomposition pressure of methane hydrate for 0, 3, and 10 mass% NaCl systems at 273.2 K respectively. Methane hydrate starts to decompose well inside the methane hydrate stability zone. (+) and (×) represents model predictions (80 mol%) of vapour phase methane concentration by HydraFLASH given sufficient hydrate saturation.* *84*

Figure 4.9 *Vapour phase concentrations of methane, nitrogen, and CO_2 after flue gas injection and during depressurisation for experiments with excess gas hydrate formation method. The ratio $CO_2/(CO_2+N_2)$ shows the absolute content of CO_2 in the flue gas component of the vapour phase at any instant. (a), (b), and (c) represent experiments with 0, 3, and 10 mass% NaCl in the aqueous phase respectively.* *87*

Figure 4.10 *Vapour phase concentrations of methane, nitrogen, and CO_2 after flue gas injection and during depressurisation for experiments with excess water hydrate formation method. The ratio $CO_2/(CO_2+N_2)$ shows the absolute content of CO_2 in the flue gas component of the vapour phase at any instant. (a), (b), and (c) represent experiments with 0, 3, and 10 mass% NaCl in the aqueous phase respectively.* *88*

Figure 4.11 *CO_2 consumption after flue gas injection in the excess gas and excess water environments with varying degrees of water salinity.* *88*

Figure 5.1 *Particle size distributions of the IODP sediment used in graphical form.* *95*

Figure 5.2 *Temperature and pressure profiles of methane hydrate formation during Experiments 5 and 11 respectively using excess gas hydrate formation method. TS, TC, PS, and PC represent temperature and pressure profiles for systems silica sand and IODP sediment respectively.* *97*

Figure 5.3 *Methane consumption rate during hydrate formation for Experiments 5 and 11 respectively using excess gas method.* *97*

Figure 5.4 *Water injection rates for hydrate formation in excess water environment during Experiments8, 8, and 12 respectively.* *99*

Figure 5.5 *Methane conversion to hydrate for excess gas and excess water hydrate formation methods in silica sand and IODP sediment.* *100*

Figure 5.6 *Evolution of the vapour phase methane concentration after flue gas injection for experiments with Silica sand and IODP sediment as the porous media respectively. Thick lines represent experiments with excess gas hydrate formation method. Dashed lines represent experiments with excess water hydrate formation method.* *102*

Figure 5.7 *Vapour phase methane concentration during depressurisation in the presence of flue gas. (a) and (b) represents experiments with excess gas and excess water hydrate formation methods respectively. Dotted vertical lines represents dissociation pressure of pure methane hydrate at the experimental*

temperature of 273.2 K. Methane hydrate starts to decompose well inside the methane hydrate stability zone. *104*

Figure 5.8 *Vapour phase concentrations of methane, nitrogen, and CO_2 after flue gas injection and during depressurisation for experiments with excess gas hydrate formation method. The ratio $CO_2/(CO_2+N_2)$ shows the absolute content of CO_2 in the flue gas component of the vapour phase at any instant. (a) and (b) represent experiments with silica sand and IODP sediment respectively as the porous media.* *106*

Figure 5.9 *Vapour phase concentrations of methane, nitrogen, and CO_2 after flue gas injection and during depressurisation for experiments with excess water hydrate formation method. The ratio $CO_2/(CO_2+N_2)$ shows the absolute content of CO_2 in the flue gas component of the vapour phase at any instant. (a) and (b) represent experiments with silica sand and IODP sediment respectively as the porous media.* *106*

Figure 5.10 *CO_2 consumption after flue gas injection in the excess gas and excess water environments for silica sand and IODP sediments.* *107*

Figure 6.1 *Calibration lines of (a) nitrogen, (b) oxygen, and (c) methane showing their moles as functions of their respective peak areas.* *113*

Figure 6.2 *Methane recovery stages after air injection for experiment 6* *115*

Figure 6.3 *Vapour phase methane and air concentrations, $N_2/(N_2+O_2)$ at 273.2K (Experiment 13).* *115*

Figure 6.4 *Vapour phase methane and air concentrations, $N_2/(N_2+O_2)$ at 278K (Experiment 14).* *116*

Figure 6.5 *Vapour phase methane and air concentrations, $N_2/(N_2+O_2)$ at 283K (Experiment 15).* *116*

Figure 6.6 *Pressure profile during stage 1 of the kinetic recovery phase in Experiment 14 showing pressure reduction.* *118*

Figure 6.7 *Pressure profiles for stages 1-5 for Experiment 13(273.2K)* *118*

Figure 6.8 *Pressure profiles for Stages 1-5 for Experiment 14(278K)* *119*

Figure 6.9 *Pressure profiles for Stages 1-5 for Experiment 15(283K)* *119*

Figure 6.10 *Evolution of the vapour phase methane concentration during the multi-stage depressurisation phase for Experiments 13, 14, and 15.* *120*

Figure 6.11 *Amount of methane released from the hydrate phase into the vapour phase in each of the pressure stages for Experiment 13.* *121*

Figure 6.12 *Amount of methane released from the hydrate phase into the vapour phase in each of the pressure stages for Experiment 14.* *121*

Figure 6.13 *Amount of methane released from the hydrate phase into the vapour phase in each of the pressure stages for Experiment 15.* *121*

Figure 6.14 *Methane release in stage 1 of the kinetic recovery phase at 278K (Experiment 14).* *122*

Figure 6.15 *Percentage methane recovery for each of the stages during the multi-stage depressurisation recovery phase at 273.2 K (Experiment 13).* *123*

Figure 6.16 *Percentage methane recovery for each of the stages during the multi-stage depressurisation recovery phase at 278 K (Experiment 14).* *124*

Figure 6.17 *Percentage methane recovery for each of the stages during the multi-stage depressurisation recovery phase at 283K (Experiment 15).* *124*

Figure 6.18 *Vapour phase methane concentration during the entire depressurisation phases in the presence of compressed air. Dotted vertical lines (-------) (– – – –) (— . . — .) represents decomposition pressure of methane hydrate at 273.2 K, 278 K, and 283 K respectively. Methane hydrate starts to decompose well inside the methane hydrate stability zone. 126*

Figure 7.1 *Particle size distributions of the montmorillonite used in graphical form. 131*

Figure 7.2 *Schematic of Core Holder used for permeability measurement. 132*

Figure 7.3 *Schematic diagram of the experimental set-up for permeability measurement. The dashed red lines represent cables for electrical communications while the black solid lines represent conduits for fluid flow. 133*

Figure 7.4 *Permeability changes with pressure, (a) represents silica sand system, and (b) represents silica sand-montmorillonite system. 138*

Figure 7.5 *Gas Permeability at varying hydrate saturations. (a), (b), and (c) represents silica sand-montmorillonite sediments with 33, 36, and 48 vol% hydrate saturations respectively. 140*

Figure 7.6 *Comparison of gas permeabilities in the presence of varying hydrate saturations and in the absence of hydrate. 141*

Figure 7.7 *Permeability changes with pressure in solid sandstone core sample in the absence of hydrate. 142*

Figure 7.8 *Gas Permeability at varying hydrate saturations in solid sandstone core sample. (a) and (b) represents core samples with 15 and 44 vol% hydrate saturations respectively.* *143*

Figure 7.9 *Comparison of gas permeabilities in the presence of varying hydrate saturations and in the absence of hydrate for solid sandstone core. 143*

Figure 7.10 *Comparison of the measured permeability* $K_{\exp}$ *with Kozeny grain models for grain coating* K_c *and pore filling* K_f *. (a) represents unconsolidated silica sand-montmorillonite core samples and (b) represents solid sandstone core sample. 146*

Figure 7.11 *Comparison of the measured permeability* $K_{\exp}$ *with Parallel Capillary models for grain coating* K_c *and pore filling* K_f *. (a) represents unconsolidated silica sand-montmorillonite core samples and (b) represents solid sandstone core sample. 147*

LIST OF PUBLICATIONS BY THE CANDITATE

- **Okwananke, A.**, Yang, J., Tohidi, B., Chuvilin, E., Maerle, K., Istomin, V., Bukhanov, B., Cheremisin, A. Enhanced Depressurisation for Methane Recovery from Gas Hydrate Reservoirs by Flue Gas, Compressed Air and Nitrogen Injection. (in preparation).

- Yang, J., **Okwananke, A.**, Tohidi, B., Chuvilin, E., Maerle, K., Istomin, V., Bukhanov, B., Cheremisin, A. (2017). Flue gas injection into gas hydrate reservoirs for methane recovery and carbon dioxide sequestration, Energy Conversion and Management, Volume 136, PP 431-438.

- **Okwananke, A.**, Yang, J., Tohidi, B., Chuvilin, E., Maerle, K., Istomin, V., Bukhanov, B., Cheremisin, A. (2017). Compressed air injection for methane recovery from gas hydrate-bearing sediments, accepted for presentation at the 9th International Conference on Gas Hydrates, Denver, Colorado.

- **Okwananke, A.**, Yang, J., Tohidi, B., Chuvilin, E., Maerle, K., Istomin, V., Bukhanov, B., Cheremisin, A. (2017). Experimental study of gas permeation through gas hydrate-bearing sediments, accepted for presentation at the 9th International Conference on Gas Hydrates, Denver, Colorado.

- Hassanpouryouzband, A., **Okwananke, A.**, Yang, J., Tohidi, B., Chuvilin, E., Istomin, V., Bukhanov, B., Cheremisin, A. (2017) CO_2 capture and methane recovery by direct injection of flue gas into frozen gas hydrate-bearing sediments. Accepted for presentation at the 9th International Conference on Gas Hydrates, Denver, Colorado.

- **Okwananke, A.**, Yang, J., and Tohidi, B. (2014): 'Experimental studies of methane recovery from methane hydrates by a combination of flue gas injection and depressurisation' in proceedings of 8th International Conference on Gas Hydrates, Beijing, China.

- Tohidi, B., Yang, J., Chapoy, A., Burgess, R., Anderson, R., Salehabadi, A., **Okwananke, A**. Research on CCS in the Centre for Gas Hydrate Research. Presented at the Scottish Carbon Capture and Storage Society (SCCS) Group Meeting, ECCI, Edinburgh, 14th Nov., 2013.

NOMENCLATURE

Abbreviations / Chemical Formulae

BCM	Billion cubic meter
BGHS	Base of gas hydrate stability (zone)
BSR	Bottom simulating reflector
BTU	British thermal unit
CCS	Carbon capture and storage
C-FAR	Centre for Flow Assurance
CH_4	Methane
CO_2	Carbon dioxide
CPD	Constant pressure delivery
CRD	Constant rate delivery
CSMGem	Colorado School of Mines hyrate prediction software (Gibb's free energy minimisation)
CSMHYD	Colorado School of Mines hyrate prediction software
CT	Computer tomography
DAS	Data acquisition system
GC	Gas Chromatograph
GSC	Geological Survey of Canada
H_2CO_3	Carbonic acid
H_2O	Water
HCO_3^-	Hydrogen carbonate ion
HSZ	Hydrate stability zone
HWPVT	Heriot-Watt Hydrate and PVT prediction software
HydraFLASH	Hydrate and PVT prediction commercial software
IODP	Integrated Ocean Drilling Program
IPCC	Intergovernmental Panel on Climate Change
JNOC	Japan National Oil Company
JOGMEC	Japan Oil, Gas, and Metals National Corporation
LHA	Leonardite humic acid
LVDT	Linear Variable Differential Transformer
MD	Molecular dynamic
MDT	Modular Dynamic Tester

MEG	Mono ethylene glycol
MeOH	Methanol
MH21	Research Consortium for Methane Hydrate Resources in Japan
MHSZ	Methane hydrate stability zone
N_2	Nitrogen
NaCl	Sodium chloride
NMR	Nuclear Magnetic Resonance
NRCan	Natural Resources Canada
ODP	Ocean Drilling Program
OECD	Organisation for Economic Co-operation and Development
PR	Peng-Robinson
PRT	Platinum resistance thermometer
SAAD	Steam assisted antigravity drainage
SAGD	Steam assisted gravity drainage
sH	Structure H gas hydrate
sI	Structure I gas hydrate
sII	Structure II gas hydrate
SRK	Soave-Redlich-Kwong
STP	Standard temperature and pressure
STSFlash	Shell flash calculation software
TCD	Thermal Conductivity Detector
TCM	Trillion cubic meter
UBGH	Ulleung Basin Gas Hydrate
US DOE	United States Department of Energy
USGS	United States Geological Survey

Symbols

A_p	Surface area of hydrate particle
a_s	Effective surface area of gas-water interface
K'	Overall hydrate formation rate constant
$\dot{m}$	Gas mass flow rate
A	Pre-exponential constant / cross sectional area of porous media
a	Energy parameter in the EoS / empirical constant
b	Co-volume parameter in the EoS / empirical constant

C	Specific heat capacity / Langmuir constant
E	Activation energy
F	Number of degree of freedom / mole fraction of phase
f	Fugacity
H	Hydrate phase
h	Enthalpy
I	Ice phase
k	Coefficient of diffusion or reaction
K	Potential energy of interaction between two molecules / permeability
L	Liquid phase / length of core
M	Molecular weight
m	Constant / mass
N	Number of compoments / integer equal to 4, 5, 10 or 11
n	Number of moles / hydration number
P	Pressure
q	Volumetric flow rate
Q	Quadruple point
R	Universal gas constant / cavity radius
r	Distance from centre of cavity
R^*	Gas consumption rate during hydrate formation
S	Solid phase / saturation / solubility
T	Temperature
U	Superficial (gas) velocity
V	Vapour phase / velocity / volume
v	Molar volume
x	Mole fraction / mole fraction of component in the aqueous phase / phase composition
y	Mole fraction of component in the vapour phase
z	Feed composition / coordination number / gas compressibility factor

Greek Letters

μ	Chemical potential / viscosity
ρ	Density
Π	Number of phases
φ	Factor accounting for additional relationships between the variables in

	Gibbs' phase rule / fugacity coefficient
δ	Constant
Ω	Constant
τ	Temperature dependency factor
Δ	Difference
θ	Number of cavity
π	Pi
κ	Boltzmann's constant
ω	Cell potential
ε	Minimum potential energy
β	Hard-core radius
σ	Collision diameter
σ^*	Optimisation parameter ($\sigma^* = \sigma - 2\beta$)
ϕ	Porosity

Superscripts and Subscripts

i	Component / in
l	Phase
α	Phase α
β	Phase β / empty hydrate lattice
δ	Phase δ
0	Arbitrary reference state
1	Lower (quadruple) point
2	Upper (quadruple) point
a	Absolute
c	Critical / cavity / surface coating
d	Distinct (non-liquid water) liquid (phase) / diffusion
eq	Equilibrium (three phase)
f	Centre filling
g	Gas
G	Vapour phase
gg	Free methane gas
ggo	Methane gas injected
gh	Gas consumed for hydrate formation

gw	Methane gas in solution with water
H	Hydrate cavity
h	Hydrate
j	Hydrate forming component
m	Cavity type
max	Maximum value
n	Archie saturation exponent
o	Out / initial
p	Compressional (velocity) / pressure
r	Reduced / reaction
res	Residual
s	Shear (velocity) / sand
t	Time
tend	Time to end of hydrate formation
tot	Total
tr	Tripple point
v	Condenced gas components (phase)
w	Water / Water (phase) / liquid water in the aqueous (phase)
wh	Water consumed for hydrate formation
ww	Water injected

CHAPTER 1 INTRODUCTION

1.1 World Energy Demand

The world today is heavily dependent on fossil fuels for the supply of energy. These fossil fuels are non-renewable and are therefore subject to depletion. It is an established fact that conventional oil and gas reserves are fast depleting disproportionately with giant new discoveries, thus obviating the fact that the world is experiencing a shortage of energy supply. Global energy demand is increasing significantly due to population and economic growth. The 2013 International Energy Outlook by the United States Department of Energy (US DOE) projected a global energy consumption rise by 56% from 524 quadrillion BTU in 2010 to 820 quadrillion BTU in 2040 [1]. Growing non-OECD economies, notably China and India are the major contributors to the growing energy consumption. Their combined consumption has been projected to reach 28% of world energy consumption by 2030 [2]. As the world transits to a future where renewable is the energy mainstay, there has been tremendous progress in generating energy from non-fossil fuel sources. However, the amount generated is insignificant in meeting the energy demand. About 80% of world energy supply will still be sourced from carbon based fuels including natural gas, oil, and coal [3]. Combustion of these fuels will continue to emit CO_2, a greenhouse gas into the atmosphere increasing the atmospheric concentration of CO_2 and its attendant global warming effect. Natural gas is the cleanest burning of these three fuel sources and its use is set to grow highest among others. Thus, in the medium to long term it could serve as a link between now and a future where low to zero carbon energy reigns. Presently, about 80% of global natural gas consumption comes from conventional gas sources [4]. However, due to technological advances, contributions from unconventional sources including tight gas, shale gas, and coalbed methane have increased. To further increase the contribution from unconventional natural gas resources, there is need for development of natural gas hydrate reservoirs.

1.2 Gas Hydrates

Gas hydrates are non-stoichiometric ice-like compounds formed by trapping gas molecules in clathrates of water molecules under conditions of high pressure and low temperature. The water molecules are bonded together by hydrogen bonding forming

an unstable lattice structure (host) with empty spaces within. These spaces are then occupied by suitably sized (guest) molecules and are bonded to the water molecules by weak van-der-Waals force. This process makes the clathrates thermodynamically stable [5]. When the guest molecules are light hydrocarbon gases (methane, ethane, propane) or in combination with other non-hydrocarbon components of natural gas (carbon dioxide, nitrogen, sulphur (IV) oxide), the resulting hydrate is termed natural gas hydrate

1.2.1 Gas hydrates in history

Historical evolution of gas hydrate can be classified into three major phases. Sir Joseph Priestley [6] was the first to form hydrates in 1778 when studying the freezing of water in the presence of different gases. He formed *ice* (hydrate) when he bubbled sulphur (IV) oxide through water at temperatures below 8^{o}C. He also discovered that as the *ice* melts, it sank to the bottom of the water indicating that sulphur (IV) oxide hydrate is denser than water. Priestly however did not report his discovery. The first reported discovery was by Sir Humphry Davy [7] when in 1810 he discovered that chlorine could form solid compounds with water. Curiosity led to preparing and experimenting with new compound to identify other compounds that form hydrates.

The second phase began in the mid-1930s when Hammerschmidt [8] observed that natural gas hydrates blocked gas transmission lines at temperatures higher than ice point owing to the high pressures in which gas was transported in the pipelines. This discovery marks an important milestone in natural gas industry and birthed a new era of research. A major outcome of the new interest was the regulation of the water content in natural gas transmission lines. Continued research by Hammerschmidt [9], Deaton and Frost [10], Bond and Russel [11] , Kobayashi et al [12], and Woolfolk [13] involved investigation of the effect of inhibitors on hydrates. They tested chloride salts of calcium, sodium and potassium alongside methanol and monoethylene glycol. Over time, methanol became the most preferred inhibitor because of its ability to concentrate in the water phase after being vapourised into the gas at upstream.

The perception of hydrate as gas transmission pipeline nuisance changed into that of a potential energy resource when in the 1960s, vast quantities of methane hydrate were discovered in permafrost. This began from the Western Siberia permafrost in Russia in 1967 [14]. In the next decade, more discoveries were made in the permafrost sediments

of Northern Alaska [15], and the Mackenzie Delta in Canada [16]. With the realisation that the low temperature/high pressure condition necessary for hydrate formation and stability also existed in subsea sediments, efforts were made to explore and characterise hydrate deposits through deep sea drilling projects such as the Ocean Drilling Program (ODP) [17] and the Integrated Ocean Drilling Program (IODP) [18, 19]. Hydrate cores were recovered from among other areas, the Black Sea, U. S. east coast, Gulf of Mexico, Guatemala, and South America.

1.2.2 Structure of hydrates

Hydrates occur in different crystalline structures. The three most common types are structure I (sI), structure II (sII), and structure H (sH). Structure I and II were discovered by von Stackelberg [20, 21] and structure H was discovered much later in 1987 by Ripmeester [22]. These structures are composed of repetitive crystal units called 'cages' which are formed by hydrogen-bonded water molecules. The water cages come in two different sizes: large cages and small cages. The small cages forms the basic building block of the hydrate crystals in structures I and II. They consist of 12 faces of pentagonally bonded water molecules, hence the term 5^{12}. The 5^{12} cages are connected to each other through their vertices in structure I, and through their faces in structure II. These 5^{12} cages have spaces within their cavities that needs to be filled to prevent straining and breakage of the hydrogen bonds. The spaces are then filled by the larger hexagonally bonded /faced cages. Two of these big cages are needed in structure I, hence the use of $5^{12}6^2$ to denote the cavity structure of structure I hydrates. On the other hand, four of the big cages are needed in structure II hydrates; hence the term $5^{12}6^4$ to denote the cavity structure of structure II hydrates. These cages are occupied by suitable sized 'guest' molecules and are stabilised at favourable temperature and pressure conditions.

Structure I hydrates unit cell contains 46 water molecules forming a lattice size of 1.2 nm (12 Å). Its cavities are filled by small guest molecules with size in the range of 0.4-0.55 nm [23]. Examples include methane, ethane, and carbon dioxide. Exceptions to these are argon, krypton, oxygen, and nitrogen, with even smaller diameters typically less than 0.4 nm, but forms structure II hydrates.

Structure II hydrates unit cell contains 136 water molecules forming a lattice size of 1.73 nm (17.3 Å). Its cavities are filled by larger guest molecules with size range between 0.6-0.7 nm [23]. Examples include propane, iso-butane, and natural gas.

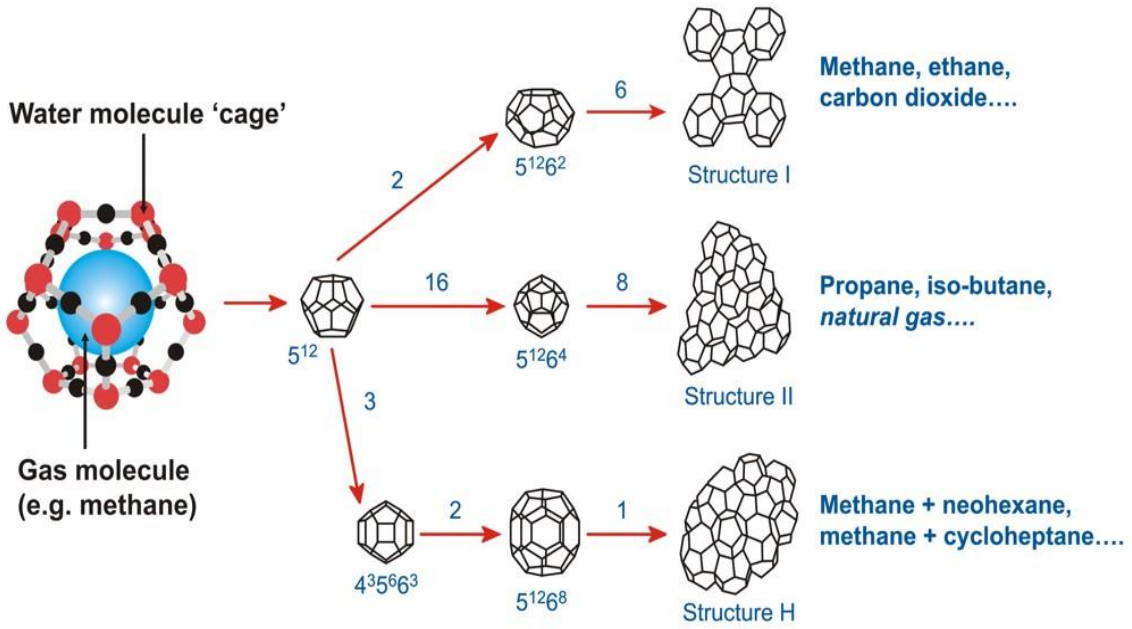

Figure 1.1 *Gas hydrate structure [24].*

34 water molecules form the unit cell of structure H hydrates whose hexagonal crystal has lattice parameters a = 12.26 Å and c = 10.17. Its lattice consists of three different types of cavities: three 5^{12}; two $4^35^66^3$; one $5^{12}6^8$. Unlike structure I and II, both small and large guest molecules are required to stabilise structure H hydrates. The small molecules such as methane, carbon dioxide, hydrogen sulphide occupies the small and large cavities while the larger molecules such as iso-pentane or neo-hexane occupies the large cavities [25].

Small guest molecules can fill both the small and large cages in a hydrate lattice. However, for hydrate formation with single large guest molecules, only the large cages are filled, leaving the small cages empty. At usual pressures, each cage accommodates one guest molecule. At unusual conditions such as exceptionally high pressures, it is possible to have multiple occupancy in the large cages if the guest molecules are very small such as hydrogen, argon, and other noble gases [26].

Structure I hydrates occurs predominantly in nature, structure II in man-made environments, and structure H can occur in either of the two [23]. Other unusual and

less common hydrate structures have also been discovered. Jeffrey [27] reported the existence of structures III-VII. Udachin et al. [28] also reported structure T in which the large cavities are all occupied by dimethyl ether molecules. Loveday et al. [29] reported the existence of structures MH-II and MH-III on one of the moons of Saturn (Titan) which remained stable up to 10 GPa pressures. They form a layer of almost 10km thick methane clathrate in the ice mantle of Titan. They opined that this layer could be the source of continuous replenishing of atmospheric methane in Titan.

1.2.3 Hydrate phase diagram

Given the presence of both water and the hydrate forming molecules in adequate quantities, temperature and pressure are two other factors that govern the formation, stability, and/or dissociation of hydrates. The curve connecting the dissociation temperatures and their corresponding pressures is the hydrate phase boundary. A simple example for methane hydrate is shown in **Figure 1.2**. The left of the phase boundary is the hydrate stability zone (HSZ) where methane hydrate (*H*), which is the solid phase is stable and could coexist with methane in the vapour phase (*V*) and liquid water (L_w) in the aqueous phase. To the right of the phase boundary, methane hydrate (*H*) is unstable, and dissociates into its constituent components: methane (*V*) and liquid water (L_w).

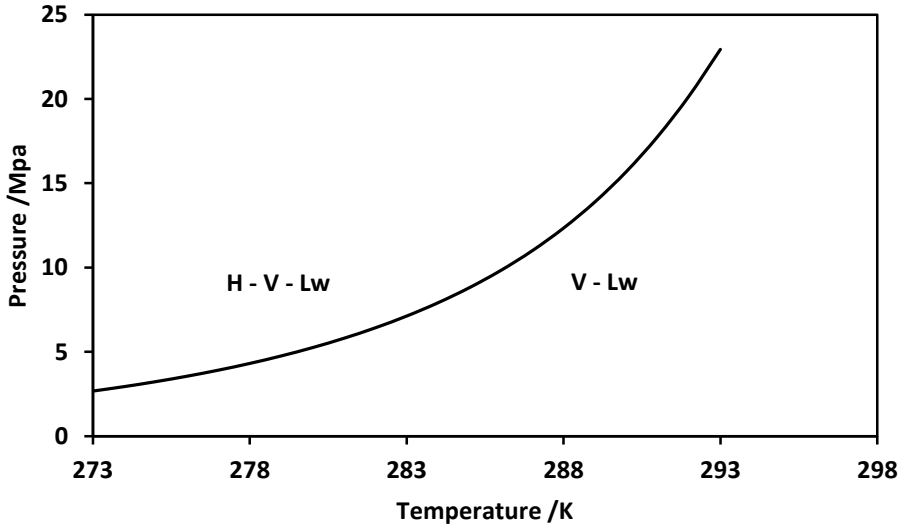

Figure 1.2 *Phase boundary of methane hydrate.*

1.3 Gas Hydrates in the Earth

Naturally occurring gas hydrate consisting mainly of methane hydrate and occurs in the earth crust. Major areas of occurrence are in the permafrost sediments and subsea sediments of the continental shelf. As stated in **Section 1.2**, four major factors govern the formation and stability of methane hydrate in these sediments: availability of methane gas, presence of water, low temperature, and high pressure. The most critical of these factors is the availability of methane gas. Water is seldom a limiting factor because of its abundance in nature while low temperature and high pressure conditions determine the extent of hydration of the sediments. The regions in which hydrate could form are illustrated in **Figure 1.3** and **Figure 1.4** for permafrost sediments and subsea sediments respectively as shown below.

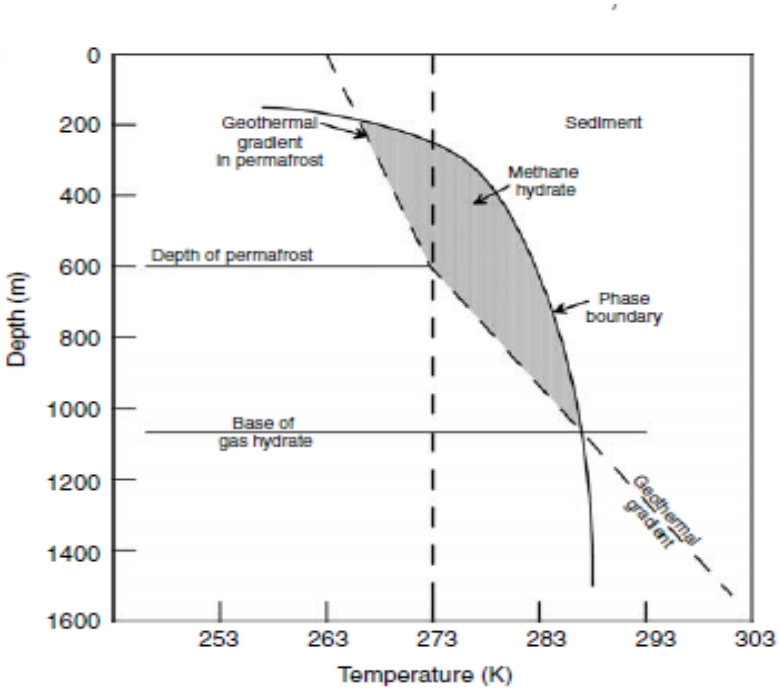

Figure 1.3 *Methane hydrate stability envelope (region) for permafrost sediments [25].*

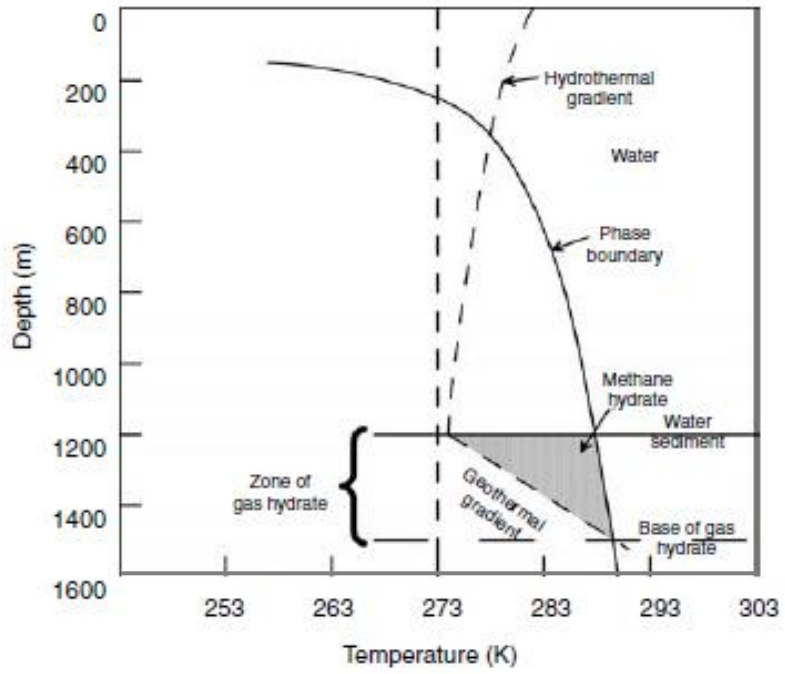

Figure 1.4 *Methane hydrate stability envelope (region) for marine sediments [25]*

The dashed lines are the lines of geothermal gradients. The dashed curve in the upper part of **Figure 1.4** represents hydrothermal gradient. The slopes of the lines changes at the base of the permafrost and at the interface of water and sediment for subsea sediments due to difference of thermal conductivity of the adjoining sediment. The solid curve is the phase boundary of methane hydrate with pressure converted to depth assuming hydrostatic conditions in both water and sediments. The points of intersection of the geothermal gradient lines and the phase boundary represents the upper and lower depths of the hydrate stability zone and the area bounded by the lines and the curve is the methane hydrate stability zone in permafrost sediments (**Figure 1.3**). In subsea sediments (**Figure 1.4**), the point of intersection of the geothermal gradient line and the phase boundary represents the lower boundary of the hydrate stability zone. The line at the water-sediment interface represents the upper boundary and the area bounded by the two lines and the curve is the hydrate stability region. Though the hydrothermal gradient curve and the phase boundary intersect and could represent the upper boundary of the hydrate stability zone. However, hydrate would not be stable in the region above the water-sediment boundary as there is no means to concentrate gas in seawater, also there is no means of retaining hydrate as hydrate is less dense than water.

Sources of methane for hydrate formation

There are two known sources of methane gas for hydrate formation: thermogenic methane and biogenic methane. Thermogenic methane gas [30, 31] is generated by *catagenesis* – the cracking of organic matter into hydrocarbons at depths. It is characterised by high temperatures of 450 K and above. Biogenic methane [32, 33] is produced by *bacteria methanogenesis* - bacterial conversion of organic matter to methane at shallow depths. Due to its shallow depth, it is characterised by low temperatures. In both cases, the generated methane migrates upwards to the hydrate stability zone, combines with water to form hydrates. Biogenic methane is dominant in hydrates. Thermogenic methane is more common with conventional natural gas reservoirs, but could also be an additional source for methane hydrate formation in some locations, as in the northern Gulf of Mexico [34–37].

Morphology of hydrates in sediments

Hydrate growth in sediments has been classified into four morphological types by R. D. Malone [38] as shown in **Figure 1.5**. In finely disseminated hydrate formations, as the name implies, hydrates are disseminated evenly in the sediment. Due to their nature, they could decompose easily upon little perturbation. A vast majority of methane hydrate in subsea sediments falls into this category. Nodular hydrates formations contain nodules of hydrates which may be up to 5 cm in diameter within sediments. Layered hydrate formations contain thin layers of sediments sandwiched between layers of hydrate in an alternating manner. Massive hydrates contain very thick hydrates of about 3-4 m with minimal sediments. Hydrate may make up to 95% of the bulk volume. This type of hydrate is either formed along fault margins where it fills up the space within the fault, or within sediments where it pushes the sediments apart as the massive hydrate grows.

Disseminated hydrate

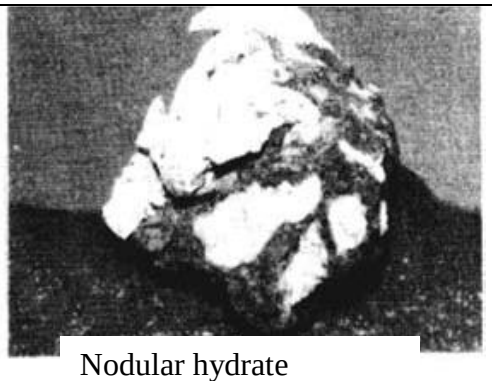

Nodular hydrate

Layered hydrate

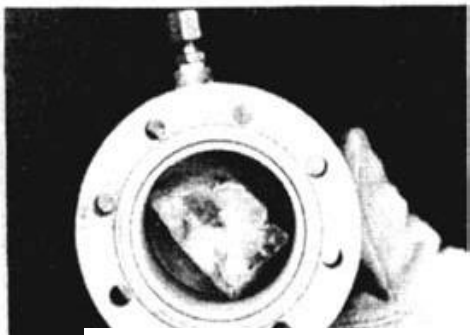

Massive hydrate

Figure 1.5 *Classes of hydrates in sediments based on morphology [38]*

Hydrate detection in the earth

Detection of gas hydrate in the earth can be achieved by acoustic imaging. A technique that has been used extensively is the Bottom Simulating Reflector (BSR). A BSR is a high amplitude reflector that results from a strong acoustic impedance/velocity contrast between gas hydrate bearing sediments above the reflector and the underlying free gas zone [39]. An important characteristic of BSR is that it approximately parallels the seafloor.

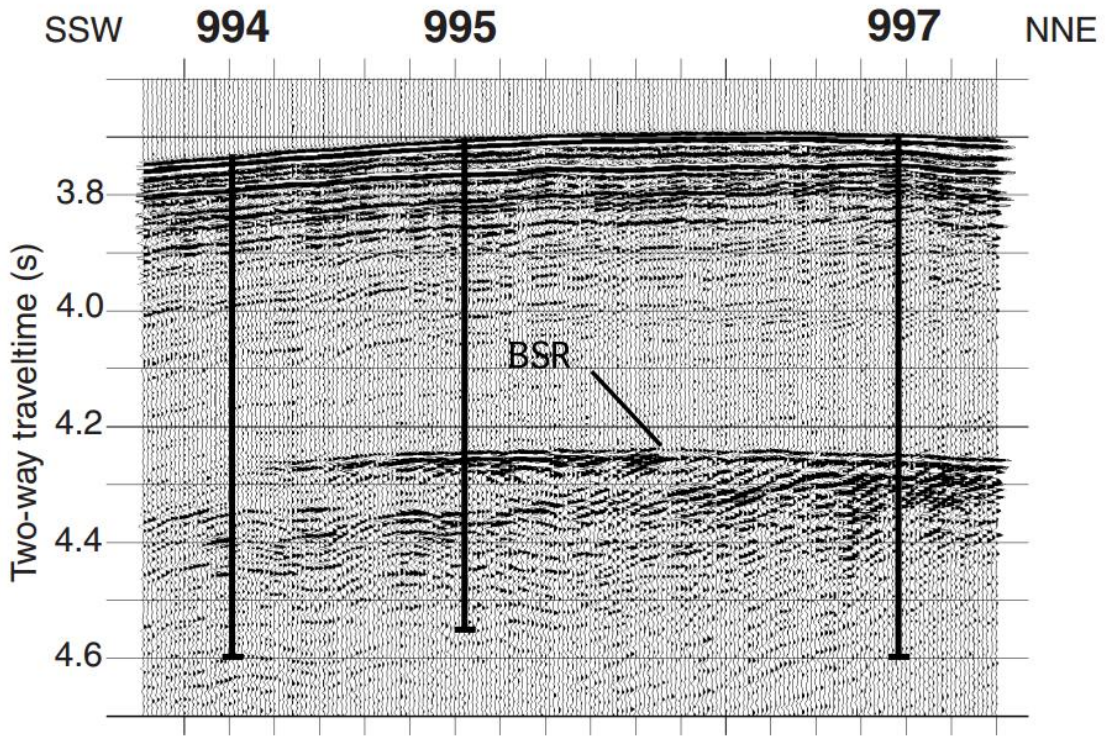

Figure 1.6 *Seismic profile across the Blake Ridge during transect drilling at sites 994, 995, and 997 of the Ocean Drilling Program (ODP) Leg 164* [40].

In this technique, sonic waves are propagated into the earth and the travel time of the reflected wave is recorded. Velocity contrast indicates change in density of the penetrated media. Thus, as the wave travels from one medium to another medium of different density, the velocity changes. For hydrate bearing sediments, this velocity changes as the wave travels from the hydrate host sediment to the underlying gas zone. This is denoted by a decrease in the sonic compressional velocity (V_p) and an increase in the shear velocity (V_s). Thus, the BSR corresponds to the zone at which the methane in the solid hydrate phase is in equilibrium with the gas phase [41]. This zone marks the depth of the hydrate stability zone (HSZ) therefore delineating the hydrate bearing sediment from the underlying gas zone. Though BSR have been extensively used as a definitive indicator of the presence of gas hydrate, gas hydrate has been found at locations lacking BSR [42]. To avoid over-reliance on one indicator for gas hydrates, Dai et al. [42] demonstrated the use of other seismic attributes such as gas chimneys and plumes, and seismic transparent or 'blank' zones to determine the occurrence of gas hydrate.

1.4 Hydrate - Geohazard Nexus

Gas hydrate has been reportedly connected to geohazards and consequently environmental hazard. Kvenvolden [43] put forward the explanation that follows. When gas hydrate forms, they occupy the interstitial pores of their host sediments, and act as a metastable cementation agent. Consequently, permeability to gas and water reduces as more hydrate forms and occupy large portions of the host sediment. Continued sedimentation leads to continued deeper burial of hydrate until it reaches the base of the hydrate stability zone. At the base of the hydrate stability zone, temperatures are such that hydrate is no longer stable. Thus, hydrate decomposes into gas and water, and the base of the gas hydrate stability zone becomes unconsolidated and over pressured due to gas release from the decomposing hydrate. This section becomes weak and could possibly fail upon gravitational loading, or seismic perturbation, resulting in submarine mudslides [44, 45]. He further noted hydrate dissociation could also be caused by lowering of sea level, or by increased seabed water temperatures. This described model has been noted to be responsible for the surficial slides and slump on the continental slope of West Africa [46, 47], slumps on the U S Atlantic continental slope [48], the Storegga Slide of Norway [49, 50]. The released methane gas escapes to the atmosphere. Another source of methane release to the atmosphere is from hydrate dissociation during strong earthquake as observed in the Nankai Trough, offshore Japan [51, 52]. Localised geohazard could also occur from human activities. For example, drilling through gas hydrate formation perturbs the equilibrium pressure and temperature conditions of the hydrate [53–55]. This can result in the release of gas plumes, damage to casing and other well site facilities. It could also cause subsidence and loss of integrity in the foundations of seabed installations. On possible future geohazard, Maslin [56] predicted that both marine and permafrost hydrate reservoirs will dissociate based on Intergovernmental Panel on Climate Change (IPCC) 2007 [57] suggestion that by the year 2100, mean surface temperature would rise by about 277 K. Thus, as the industry moves into greater water depths to exploit resources, great considerations should be given to gas hydrate dissociation associated geohazards.

1.5 Classification of Gas Hydrate Accumulations

Hydrate deposits have been classified into four based on their geologic and reservoir conditions [58, 59] as follows:

Class 1

This class of hydrate accumulation is comprised of two zones: a hydrate bearing interval, and underlying two phase fluid zone containing free gas and water. The hydrate bearing interval is characterised by low effective permeability due to very high hydrate saturations in its pore space. The bottom of the hydrate stability zone often coincides with the bottom of the hydrate interval. In terms of gas recovery, this type of hydrate deposit is the most desirable because of the hydrate thermodynamic proximity to the hydrate equilibrium condition. Thus, only a little perturbation in terms of pressure or temperature change is necessary to initiate hydrate dissociation [58].

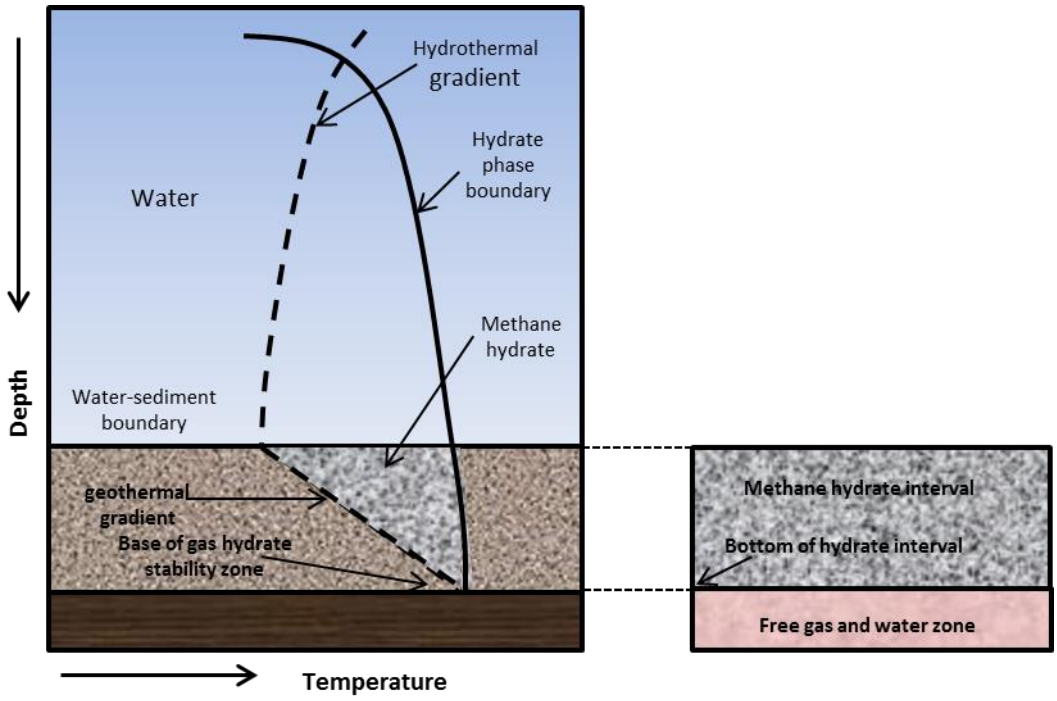

Figure 1.7 *Class 1 hydrate accumulation showing the bottom of the hydrate interval coinciding with bottom of the hydrate stability zone and the underlying free gas and water zone.(Adapted from [60]).*

Class 2

Class 2 hydrate accumulations also comprises of two zones: a hydrate bearing interval, and an underlying water interval with no free gas. In this class of hydrate accumulation, the bottom of the hydrate interval does not necessarily mark the bottom of the hydrate

stability zone as the entire hydrate interval may fall within the hydrate stability zone. In terms of gas recovery, depressurisation may appear to be more effective due to highly incompressible nature of water which leads to a strong pressure disturbance that is dissipated over a large area of the hydrate-water interface. However, numerical gas production studies by Moridis et al. [58] reveal that the favourable depressurisation regime could be easily hindered by adverse relative permeability conditions arising from the appearance and maintenance of a gas phase in a hitherto water filled zone. It has been reported that in single well configurations, gas recovery by depressurisation in this type of deposit could be accompanied by up to 98% water production [61].

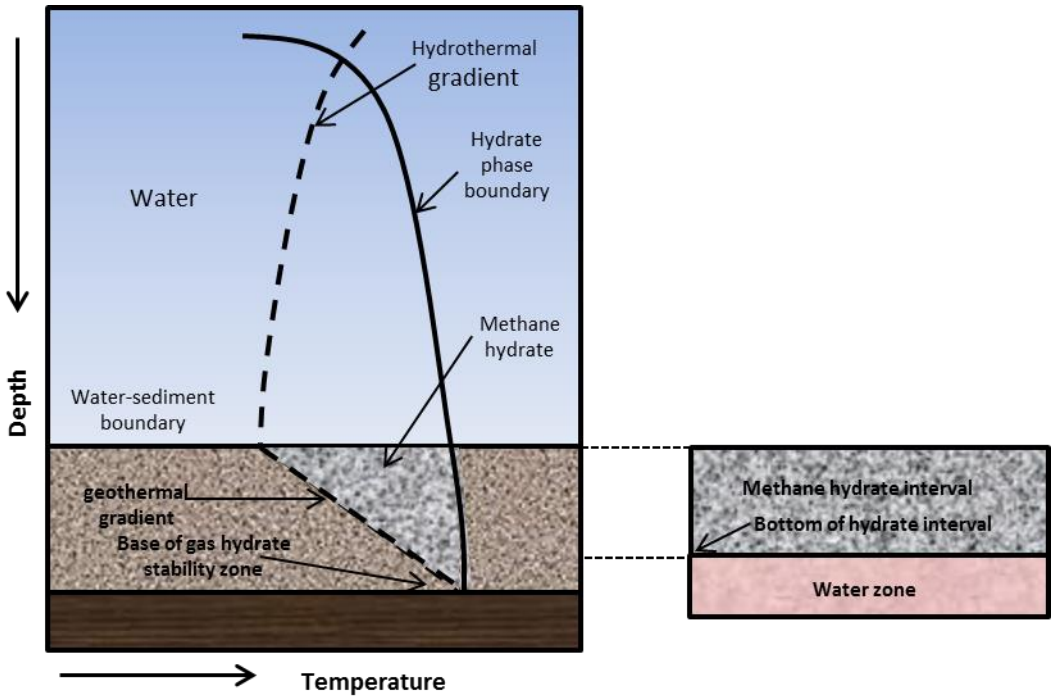

Figure 1.8 *Class 2 hydrate accumulation showing the bottom of the hydrate interval not coinciding with bottom of the hydrate stability zone, and the underlying water zone. (Adapted from [60]).*

Class 3

Class 3 accumulations, unlike Classes 1 and 2, are comprised of only one zone, the hydrate bearing interval, with no underlying fluid zone [59]. Also, the bottom of the hydrate interval does not necessarily mark the bottom of the hydrate stability zone as the entire hydrate interval may fall within the hydrate stability zone. Class 3 hydrate reserves typically have high hydrate saturation which reduces the effective permeability of gas and water especially in reservoirs with low intrinsic permeability. This make

depressurisation induced gas recovery not an attractive option. For this type of hydrate reserve, thermal stimulation appears an appropriate production technique.

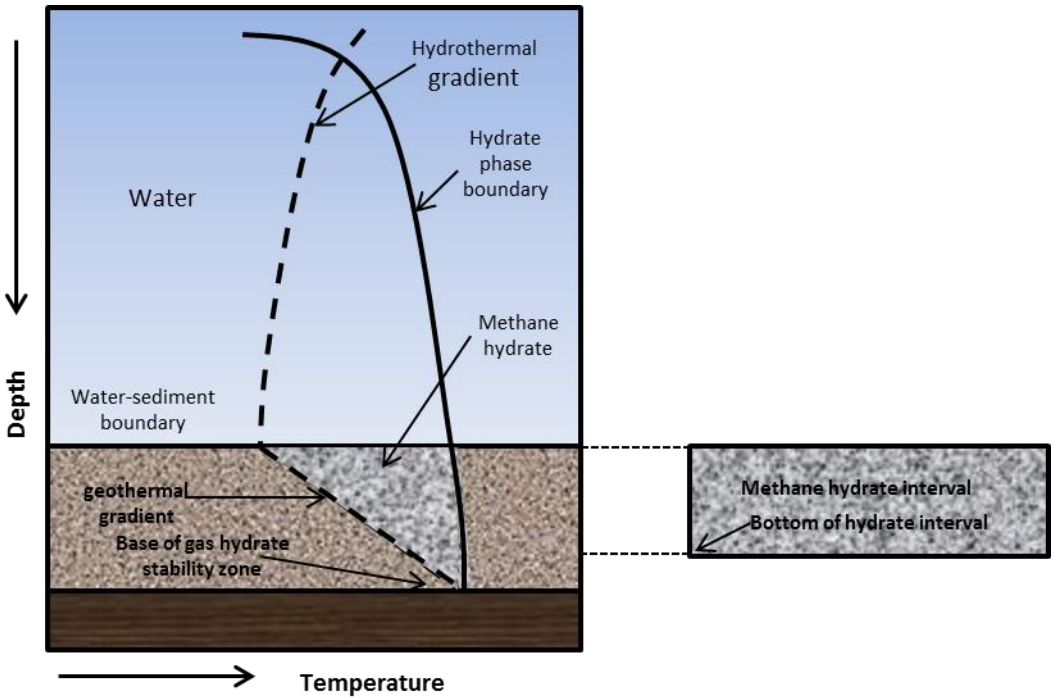

Figure 1.9 *Class 3 hydrate accumulation showing the bottom of the hydrate interval not coinciding with bottom of the hydrate stability zone, with no underlying water and/or free gas zone. (Adapted from* [60]*).*

Class 4

Class 4 accumulations are markedly different from the others in that they are dispersed and of low saturation, and not bounded by any confining strata [62]. They mostly occur in submarine hydrate deposits and are generally considered not a promising target for exploitation.

1.6 Hydrate Resource Assessment

They are geographically evenly distributed as seen in **Figure 1.10**. This has elicited active research and development activities into its development especially by conventional oil and gas resource lean countries like Japan and South Korea.

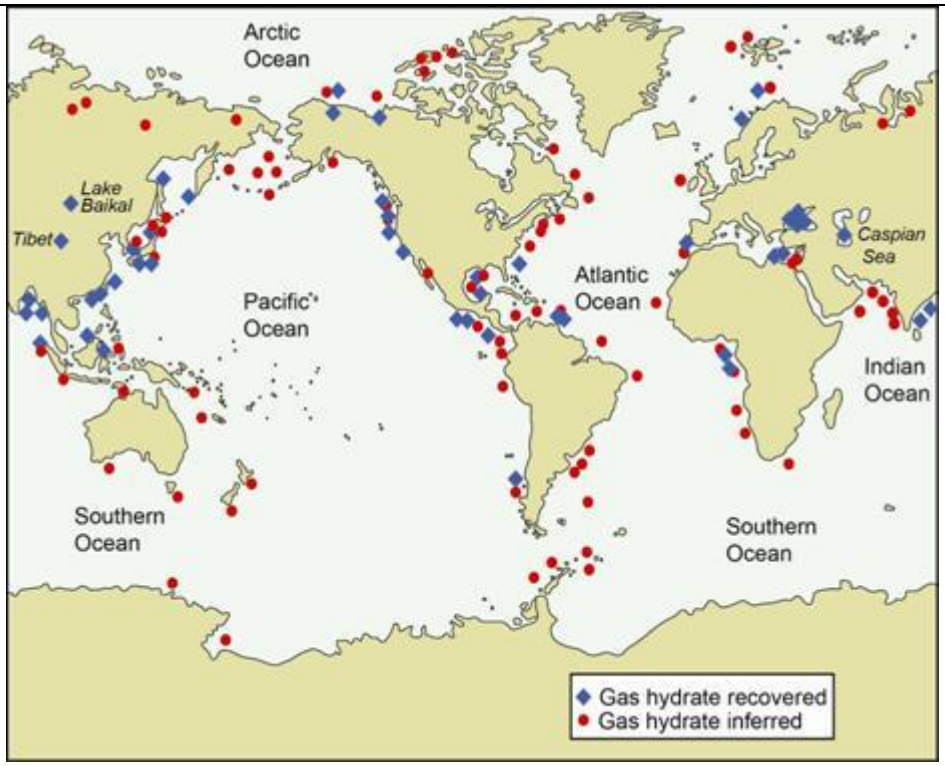

Figure 1.10 *Map showing locations of known and inferred gas hydrate accumulations [63].*

Since the discovery of gas hydrate as a potential energy resource, many attempts have been made at quantifying the amount of methane trapped as methane hydrate. Earlier estimates were based on a limited amount of fairly well known geological data on a local scale that was then extrapolated to a global scale. They were therefore highly speculative. One of the early estimates was by Trofimuk et al. [64] at 3053×10^{15} m^3 based on assumptions that hydrates could occur wherever conditions for formation and stabilisation exist. Soloviev [65] considered limiting factors such as availability of methane, limited porosity, and percentage of organic matter to give a more conservative estimate of 0.2×10^{15} m^3 of methane. However, from improved understanding and information extracted in-situ from field trials, estimates of methane in natural gas hydrates reservoirs has decreased significantly over time. Klauda and Sandler [66] in their improved approach incorporated the following into their model; a new thermodynamic model that takes into account the effects of pores and salts, local temperature and gradients in the oceans to determine the intersection of the geothermal gradient and the phase boundary, local organic sediment content to serve as input into the *methanogenesis* mass transfer model of Davie and Buffett [67, 68]. Based on these inputs, they gave a total global estimate, including very deep hydrate and very dispersed hydrate as $1.27\times10^{17}m^3$ methane (STP). Considering only continental margin gas

hydrate, they reduced their estimate to $4.4\times10^{16}m^3$ methane (STP). The most conservative in recent times is by Johnson [69] at 3×10^{15} m^3.

It should be noted however, that there is a difference between the amount of methane existing as hydrate and that which is technically recoverable. All the estimates reported above are for the amount of methane existing in the earth as hydrate. For a geological hydrate accumulation to be considered a potential resource, it must possess a minimum amount of gas concentration, often measured with gas yield in unit of m^3gas/m^3 sediment, and a significant total amount of gas. These properties must also compare favourably with those of existing medium or large gas reserves, either conventional or unconventional [70]. Technically recoverable volumes of gas in gas hydrate reservoirs have been put at approximately 3×10^{13} m^3 by Boswell and Collet [71].

1.7 Techniques for Methane Recovery from Hydrate Reservoirs

From the foregoing, it is evident that natural gas hydrate is a potential and abundant future source of energy. It is therefore imperative to develop techniques to exploit and recover methane from it. This however presents itself a daunting challenge, firstly due to the harsh conditions in its natural habitat. Also, it is markedly different from conventional and other unconventional natural gas sources. Conventional and other unconventional natural gas sources are trapped in place by geological structures (impermeable cap rock) and recovered by just sinking a well into the reservoir, and/or by creating additional conduit (hydraulic fracturing) in ultra-low permeability formations (tight gas and shale gas formations) [1]. Gas hydrates are solids in their natural state and does not need to be trapped, thus techniques to recover gas from them involves primarily in-situ dissociation and then creating a conduit (well) for gas flow. Three most commonly proposed recovery methods in literature are depressurisation, thermal stimulation, and inhibitor injection. Others include combination of processes, and gas injection.

Depressurisation

Gas production by depressurisation as the name imply lowering the reservoir pressure below the hydrate equilibrium pressure at the prevailing reservoir temperature [72–76]. This has been described as the most economical of the three methods as it does not

incur additional cost either in form of energy or chemicals. However, it is reportedly a slow process.

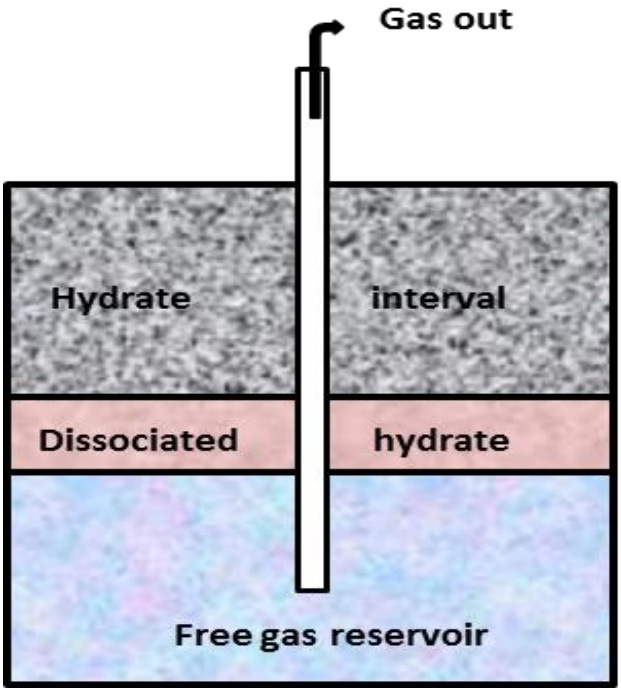

Figure 1.11 *Methane recovery from hydrate reservoir by depressurisation.*

Thermal stimulation

In thermal stimulation method, methane is recovered from natural gas hydrate by heating the reservoir to increase and shift the temperature away from the hydrate stability region leading to hydrate dissociation. Heat energy is supplied in the form of steam injection or hot water injection [77–81]. A major disadvantage of this technique is reduced efficiency due to the loss of heat energy during delivery from source to the reservoir. There is also the possible loss of heat to non-hydrate bearing zones and water handling issues due to excessive water production. To mitigate these challenges, alternative heat transfer approaches has been suggested. Islam [82] proposed electromagnetic heating in which electromagnetic heat sources are introduced downhole to provide localised heating. Castaldi et al. [83] also proposed in-situ combustion of methane from the methane hydrate reservoir.

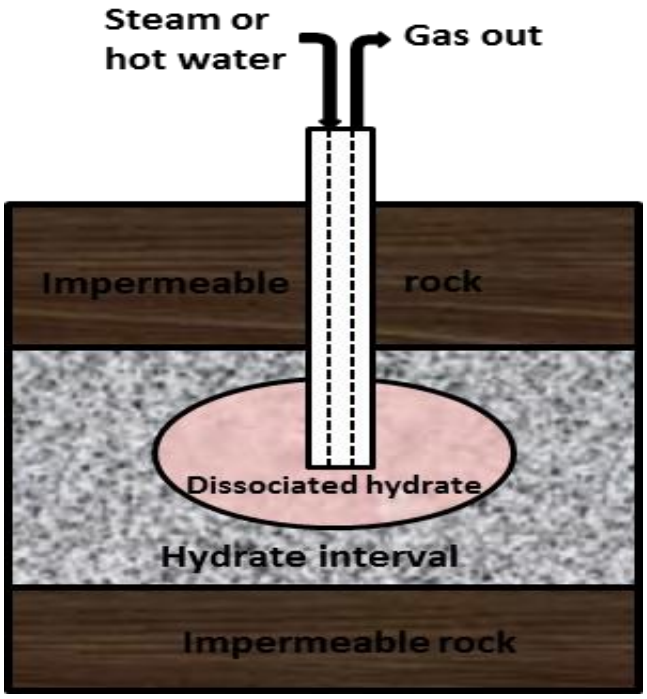

Figure 1.12 *Methane recovery from hydrate reservoir by thermal stimulation.*

Chemical inhibitor injection

Inhibitor injection works by altering the hydrate phase boundary to dissociate hydrate in-situ [84–89]. This it does by shifting the phase boundary to higher pressures and lower temperatures. As a gas recovery method from natural gas hydrate reservoirs, it is not well studied compared to depressurisation and thermal stimulation. This is owing to the fact that it is economically unwise considering the volume and cost of chemical needed and its toxicity to the environment. Chemical inhibition studies have so far been limited to hydrate dissociation in pipelines and surface facilities. Chemical inhibitors are classified into two main categories: thermodynamic inhibitors and kinetic inhibitors. Thermodynamic inhibitors such as momo ethylene glycol (MEG) and methanol (MeOH) alter the hydrate equilibrium condition, thereby dissociating hydrate. They are therefore more suitable for gas recovery in natural gas hydrate reservoir. On the other hand, kinetic inhibitors slows the rate of hydrate formation, hence they are of more interest in mitigating hydrate problems in pipelines and surface facilities.

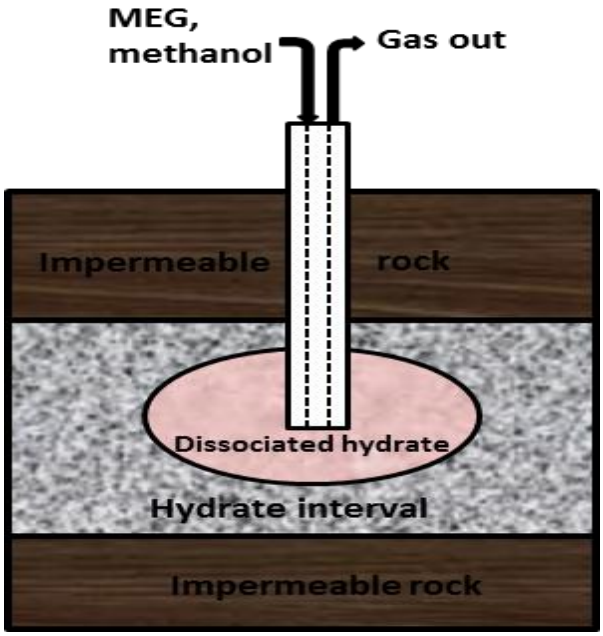

Figure 1.13 *Methane recovery from hydrate reservoir by inhibitor injection.*

Combination of processes

Combinations of two methods have also been proposed so that the effect of inherent deficiency in one method can be reduced by the other method. It has been reported that depressurisation, apart from being a slow method, also has the possibility of ice formation when rapidly done [90] thereby causing a reduction or complete blockage of permeability which affects the volume of gas produced. In thermal stimulation, a significant proportion of the heat energy supplied is lost to 'thief zones' (non-hydrate bearing zones). Also, the hydrate bearing zone must be of good porosity, about 15% or more for effective heat stimulation. Chemical inhibition process is expensive owing to the cost of the chemicals and also requires a good porosity. Some of these combined approaches mimics production techniques applied in conventional reservoirs and are mostly a combination of thermal stimulation and depressurisation. The huff and puff technique demonstrated by Li et al. [91] is a combination of thermal stimulation and depressurisation involving cycles of injection of hot fluid (water or steam), soaking, and gas production. According to the authors gas to water ratio of 55 m^3 of methane (STP)/m^3 of water justifies the economic feasibility of the process. Steam Assisted Gravity Drainage (SAGD) [92] and Steam Assisted Antigravity Drainage (SAAD) [93] have also been tested for gas recovery in natural gas hydrates in sediments in a combination of thermal stimulation, depressurisation, and brine injection. Both methods employ two horizontal wells; one injection and one production. In SAAD, the

production well is above the injection well and was reported to produce more gas and less water in comparison to SAGD.

Gas injection

Gas injection, especially CO_2 into natural gas hydrate reservoir for methane recovery has received tremendous attention [94–96]. In this regard, natural gas hydrate reservoirs could serve as a CO_2 sink by sequestering CO_2 as CO_2 hydrate in CO_2-CH_4 exchange process [97]. Hydrate phase equilibria depends on the type of gas occupying the hydrate cage. Seo et al. [98] in their study reported that comparing equilibrium conditions of pure CO_2 and methane gases, pure CO_2 hydrates form at higher temperature for a given pressure, or at a lower pressure for a given temperature. Lee et al. [99] demonstrated this by carrying out quantitative experiments to investigate the kinetics of CO_2-CH_4 exchange by injecting liquid CO_2 into methane hydrate. From their results they inferred the mechanism for methane production and identified the depth of the dissociation/exchange on hydrate particles. The process has also been reported to be thermodynamically feasible [100] as the heat released during CO_2-hydrate formation (exothermic, -57.98 kJ/mol) is larger than the heat absorbed during methane hydrate dissociation (endothermic, 54.49 kJ/mol). Nitrogen injection has been also used to dissociate methane hydrate. Panter et al. [101] purged gas hydrate plug in pipeline by injecting nitrogen gas. Also, Masuda et al. [102] flowed nitrogen through methane hydrate bearing limestone core. He observed that hydrate dissociated as the nitrogen gas passed through the core. Furthermore, mixtures of CO_2 and nitrogen has shown strong efficacy in dissociating methane hydrate [103–106]. Park et al. [107] quantified methane replacement using a mixture of CO_2 and nitrogen in comparison with CO_2 only. With the use of Raman spectroscopy, they reported that 23% of methane in methane hydrate was replaced by nitrogen and 63% of methane in methane hydrates was replaced by CO_2, thus recovering about 86% of methane in the hydrate, a significant increase on 64% that could be recovered by pure CO_2.

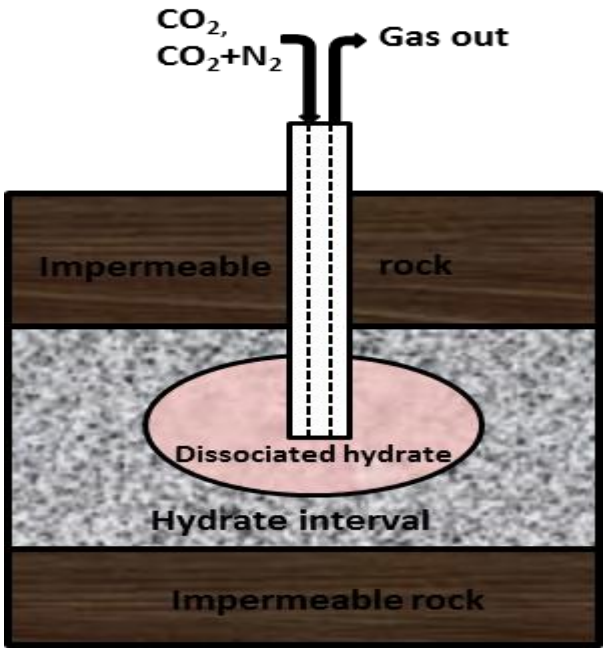

Figure 1.14 *Methane recovery from hydrate reservoir by gas injection.*

1.8 Field production Tests

Following several exploratory and scientific expeditions, and several laboratory and simulation studies, knowledge and understanding of gas hydrate have improved tremendously. Based on this, a number of onshore and offshore field production trials have been conducted. A brief summary is presented hereafter.

Messoyakha gas field

Messoyakha gas field in the Russian Arctic is the first reported production from a gas hydrate field. Its production date of 1969 predates most of the active research in natural gas hydrates. The field consists of a free gas layer underlying the hydrate layer [108]. Depressurisation technique was employed by producing gas from the free gas layer which reduces the reservoir pressure, causing the gas hydrate to dissociate and release more gas. Cumulative gas production to date from the field has been put at 12.9 BCM of which 5.4 BCM was contributed from hydrate decomposition.

Mount Elbert, Alaska

BP Exploration has been active in natural gas hydrate production research in the Alaska North Slope. This area has a significant concentration of natural gas hydrate reserves in

its permafrost with a total estimate of 2.4 TCM [109]. In 2007 in conjunction with US Department of Energy (U.S. DOE) and US geological Survey (USGS), they drilled a stratigraphic well to evaluate the potential of technical and commercial viability of gas resource from the Alaska North Slope gas hydrate accumulations. Results from their wireline Modular Dynamic Testing (MDT) analysis was in agreement with their pre-drill predictions [110].

Mallik Field, Canada

The Mallik field is situated in the Mackenzie delta, northwest Canada and it has seen active hydrate production testing since 2002 [111]. Hydrate saturations in excess of 80% of pore volumes in some locations has been reported. This makes the Mallik field one of the most concentrated hydrate field in the world. There have been two production tests in this site so far. The Mallik 2002 Gas Hydrate Production Research Well Program, a collaborative agreement between Japan National Oil Company (JNOC) and Geological Survey of Canada (GSC) tested the feasibility of gas production from a natural gas hydrate reservoir at the Mallik 5L-38 well site by quantifying the pressure drawdown response of a hydrate reservoir. They employed thermal stimulation method which involved hot brine injection. The test lasted for 124 hours and a total production of 468 m^3 of methane gas was produced. Their test results confirm the possibility of gas production from especially sand dominated hydrate reservoirs [112].

Also in 2007 and 2008, a consortium of researchers from Japan Oil, Gas and Metals National Corporation (JOGMEC), Natural Resources Canada (NRCan) conducted another production test at the Mallik 2L-38 well site using depressurisation method [113]. The main objective of the 2007 test was to complete the production and water injection wells, to install and test the monitoring systems, and to conduct a short term production test by depressurisation to gain understanding in readiness for the longer term test planned for 2008. The test period lasted only 60 hours with actual gas production time of about 30 hours. The 2008 test as noted earlier was for a longer term gas production. Applying depressurisation technique, the test lasted for 6 days, partly due to installation of sand screen at the perforated interval and application of stepwise depressurisation. Both water and gas were produced at 10-20 m^3 water/day and 2000-3000 m^3 gas/day. The 2007 test lasted for only 60 hours due to excessive sand production. For the 2008 test, the authors in their report opined that the initial high

permeability conduits that caused initial high gas production rate collapsed with time as hydrate dissociated, consequently causing a decline in production.

Ignik Sikumi Field, Alaska

The Ignik Sikumi gas hydrate field is located in the Prudhoe Bay Unit, Alaska North Slope. In May 2012, researchers from ConocoPhillips in collaboration with JOGMEC and U.S. DOE conducted the first field trial of CO_2-methane exchange mechanism for gas recovery from natural gas hydrate reservoir [114]. They injected approximately 6000 m^3 of a gas mixture composed of 23% CO_2 and 77% N_2 into the target hydrate bearing sediment. At the end of the test period, approximately 70% of the injected nitrogen was recovered while only 40 % of injected CO_2 was recovered indicating that CO_2-methane exchange occurred and CO_2 sequestered as CO_2-hydrate. Of the approximately 30000 m^3 of gas mixture produced, 24,210 m^3 was methane. Methane component of the gas mixture produced reached over 90% and the test lasted for six weeks.

MH-21 Nankai Trough, Japan

Following the successes achieved in onshore field production trials, the first offshore gas production gas production trial from natural gas hydrate reservoirs was conducted in 2013 by JOGMEC in the eastern Nankai Trough, off the Pacific Coast of Japan [115]. They employed depressurisation method by setting well bottom-hole pressure from 13.5 MPa to 4.5 MPa. The daily average gas production rate was 20,000m^3/d and a cumulative gas production of 120,000 m^3. The test lasted for 6 days and was reportedly suspended due to bad weather and sand production.

Challenges of the field production tests

Most reported field trials employ depressurisation as the principal technique for gas production. Exceptions are the Mallik 2002 Gas Hydrate Production Research Well Program in which thermal stimulation was tested and the Ignik Sikumi production test where CO_2 injection was tried for methane recovery. Besides the harsh habitat of methane hydrate reservoirs, a recurring problem in all reported field trial is excessive sand production.

Pressure changes and subsequent change in effective stress, and furthermore, hydrate dissociation leads to deformation and failure of formation [116]. This impacts on the geomechanical properties of the well and formation, thus negatively affecting sustained gas production due to permeability reduction, sand production and fines migration. Excessive sand production was reported as the main reason for early termination of the MH21 Nankai Trough production test and the Mallik 2007 production test and to a lesser extent, the Mallik 2002 production test. In the Ignik Sikumi production test, the major challenge was the early formation of CO_2-hydrate in the pores, reducing permeability, and consequently reducing methane production. This explains why the nitrogen component of the injected CO_2-N_2 mixture was as high as 77% to prevent CO_2-hydrate formation.

1.9 Gas Hydrate Application in Carbon dioxide Capture and Storage (CCS)

Carbon dioxide capture and storage (CCS) is the term used to describe the process that consists of the separation of CO_2 from point sources (industrial and energy related sources), transporting to a storage site, and long term isolation from the atmosphere [117]. It is one of the available options for reducing the atmospheric concentration of CO_2 resulting from human activities and its attendant climate change effect. Other options include increasing energy efficiency in power generation systems that involves fossil fuel combustion, switching to low carbon fuels, and increased use of renewables [118]. Potential storage sites includes geological formations such as depleted oil and gas reservoirs, unmineable coal beds, and deep saline formations, ocean storage (direct release into the water body or deep ocean floor). The highest proportion of the cost of any CCS scheme is due to CO_2 separation and compression [119]. Most fossil fuel combusting power plants use air instead of oxygen for combustion, this leads to effluent flue gas relatively low in CO_2 (15-19 mol% for coal-fired power plant and about 3 mol% in natural gas fired power plant) and a significant amount of nitrogen. Thus, it becomes difficult and expensive to capture CO_2 as a concentrated stream, the form in which it is required for most storage, conversion, and reuse applications [120]. Gas hydrate formation has been reported as a viable means of separating CO_2 from flue gas [121–124]. Therefore, direct injection of flue gas into methane hydrate reservoir reduces the extensive cost incurred in conventional CCS, sequester CO_2 as CO_2-hydrate while also recovering methane gas for energy uses.

1.10 Aims and Outline of Thesis

Given the abundant natural gas resource trapped in natural gas hydrate reservoirs, there have been intensified effort in the development of techniques to economically exploit the resource albeit in an environmentally safe manner. The major techniques for gas production from gas hydrate reservoirs and their inherent limitations have been discussed in **Section 1.7**. Also, the successes and challenges of the various field production trials were discussed in **Section 1.8**. The goal of this research therefore is to develop techniques that will potentially overcome the identified challenges. The reported techniques in the literature achieve gas production by destabilising the local equilibrium conditions thereby leading to methane hydrate decomposition, or by taking advantage of differences of phase equilibria in the case of injection. This research reports a novel technique of achieving a shift in the methane hydrate phase boundary thereby decomposing methane hydrate for methane recovery by direct flue gas injection while sequestering the CO_2 component of the flue gas as CO_2 hydrate or CO_2 mixed hydrate.

CHAPTER 1 gives a general introduction to gas hydrates, their occurrence in nature, and their exploitation as an energy resource. The aim of the thesis is also highlighted. The remainder of the thesis consists of seven chapters.

In **CHAPTER 2**, the theoretical background of hydrate systems is presented. The phase diagrams and phase behaviour of hydrate forming binary, ternary, and multicomponent systems were discussed using the Gibb's phase rule. Thermodynamic theory and modelling of hydrate systems were also presented. Furthermore, the theories of hydrate formation and dissociation were discussed in this chapter. **CHAPTER 3** reports the experimental investigation of the feasibility of the technique at various temperature-pressure conditions representative of typical gas hydrate reservoir. In **CHAPTER 4**, the effect of reservoir water salinity and saturation on hydrate formation and consequently on methane recovery using the proposed technique was investigated. **CHAPTER 5** extended the study further to the influence of reservoir rock property in relation to host sediment mineralogy on hydrate formation and on methane recovery using the proposed technique. The influence of the reservoir temperature-pressure conditions and the reservoir fluid and rock properties mentioned onCO_2 capture and storage was also investigated.

CHAPTER 6 extended the technique to the study of the feasibility of methane recovery by compressed air injection. In **CHAPTER 7**, gas permeation through gas hydrate-bearing system was studied. Finally, the conclusions of the research and recommendations for possible direction of future research on gas recovery from gas hydrate reservoirs were presented in **CHAPTER 8**.

CHAPTER 2 THEORETICAL BACKGROUND

2.1 Phase Diagrams of Hydrate Systems

Phase diagrams provide means of visualising the phase behaviour of systems. Systems are better studied when they are in equilibrium. A system is said to be in thermodynamic equilibrium when all phases present are in thermal, pressure (mechanical), and chemical equilibrium [25]. When thermodynamic condition is achieved, the chemical potential of a component i in the system is equal in all phases present in the system. That is,

$$\mu_i^{\alpha} = \mu_i^{\beta} = ...\mu_i^{\delta},\ i = 1, 2, ...N \qquad 2.1$$

where μ_i^l is the chemical potential of component i in phase l for $l = \alpha, \beta, ..., \delta$. **Equation 2.1** can be written for all components in the system. Thus, for a system with N components and Π phases, the total number of equilibrium equations (conditions) is $N(\Pi - 1)$. Also, the number of variables required to describe a system with N components and Π phase(s) is $2 + \Pi(N - 1)$. The number of degree of freedom F of a system is the difference of the number of variables $2 + \Pi(N - 1)$ and the number of equilibrium conditions $N(\Pi - 1)$ [126]:

$$F = N - \Pi + 2 \qquad 2.2$$

Equation 2.2 is the Gibbs' phase rule [126]. Possible additional relationships between the variables are accounted for by the introduction of φ to **Equation 2.2** as shown below:

$$F = N - \Pi + 2 + \varphi \qquad 2.3$$

These additional relationships occurs for example in binary azeotropes, and for systems at critical state [127]. For binary azeotropes where the moles of a component in the liquid phase and vapour phase is the same (i.e. $x_i = y_i$), then $\varphi = 1$. For fluids at critical state, the two coexisting phases becomes indistinguishable, therefore taken as one phase with $\varphi = 2$ [128]. The minimum number of phases Π in a system is $\Pi = 1$, thus the maximum value of F is:

$$F_{\max} = N + 1 \qquad 2.4$$

where $F_{\max}$ is the number of space dimension needed to completely describe the phase behaviour of a system with N components.

Unary system (Water)

The description of the unary system of water is essential for the study of the clathrate hydrate behaviour as the presence of water is a necessary condition for hydrate formation. For a unary system of water, $N = 1$, the maximum degree of freedom $F_{\max}$ is 2. Thus, the phase behaviour of the system can be represented in a 2-dimensional *P*-*T* plane. Phases that may occur in this system are ice (*I*), liquid water (L_w), and vapour (*V*). A schematic representation of the phase behaviour of water is shown in **Figure 2.1** for a temperature range of 200 to 700 K and pressure range of 1 to 100 MPa. The equilibrium lines *I*-L_w, *I*-*V*, and L_w-*V* represent a phase boundary and also indicate conditions at which two phases may coexist. The area bounded by any two equilibrium line represents the region in which only one phase could exist. The intersection of these equilibrium lines is the *tipple point*. At the triple point, three phases, *I*-L_w-*V* coexists in equilibrium and this occurs at unique pressure and temperature conditions P_{tr} and T_{tr} respectively. The *critical point* is the pressure and temperature condition at which two phases coexisting together becomes indistinguishable. For the unary system of water, the critical point occurs at the end of the L_w-*V* equilibrium line. At and above this point, L_w=*V*, the properties of both phases are equal.

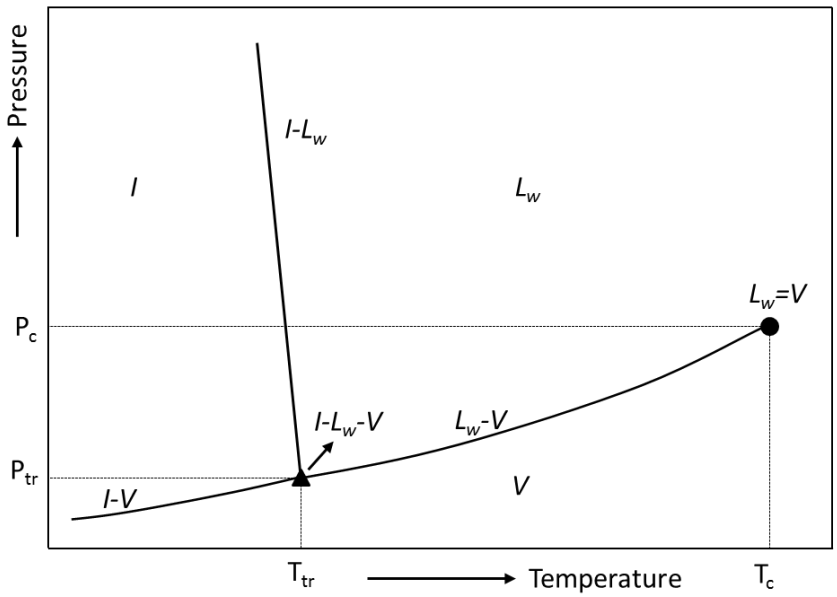

Figure 2.1 *Schematic diagram of the phase behaviour of unary system of water in a P-T plane (adapted from [125])*

Binary systems (water + hydrate-forming guest molecule)

For a binary system composed of water and a hydrate-forming guest such as methane, the number of components $N = 2$, applying **Equation 2.4**, $F_{\max} = 3$. Thus, three intensive properties (*P*, *T*, *x*) are required in a 3-dimensional plane to completely represent the phase behaviour. Since pressure and temperature are easily measurable, it is common to project the phase diagram of binary systems on *P-T* planes to study the equilibrium conditions of coexisting phases. Projections on *T-x* planes at constant pressure and *P-x* planes at constant temperature enables the study of compositions as functions of pressure and temperature. The number of phases that may occur in this system is remarkably higher than that of a unary system. Possible phases that may occur includes hydrate phase (*H*), the vapour phase (*V*), liquid water phase (L_w), a distinct liquid phase other than liquid water (L_d), solid phase of the guest molecule (*S*). The appearance of the distinct liquid phase (L_d) may be due to the liquefaction of a gaseous component at certain temperature, pressure, or composition, and complete immiscibility with water.

Two schematic phase diagrams are obtainable for binary systems of water and hydrate-forming gas in the hydrate stability region. The distinguishing feature of these phase diagrams is the critical temperature of the hydrate-forming gas [125]. Gases with

critical temperature below the triple point of water such as CH_4 and N_2, ($T_{c,CH_4} = 190.56K$, $T_{c,N_2} = 126.19K$) shows a gas-like behaviour while those with critical point above the triple point of water (273.16 K, 0.00062 MPa) such as CO_2 ($T_{c,CO_2} = 304.13K$) shows a liquid-like behaviour. Triple point of water $T_{tr,H_2O} = 273.16K$.

Figure 2.2 is a schematic diagram of the phase behaviour of binary system of a hydrate forming component (with critical temperature below the triple point of water) and water in a *P-T* plane. The quadruple point Q_1 is the point where four phases *I-H-L*$_w$*-V* coexists. It can be connected to the triple point of water by the three phase equilibrium curve *I-L*$_w$*-V*. ` The equilibrium curve *I-L*$_w$*-V* denotes the transition between water and ice without hydrate formation. The equilibrium curve *H-L*$_w$*-V* shows an exponential increase in pressure with increasing temperature. There is no upper limit to this equilibrium curve as gases that exhibits this behaviour has critical temperature far below the quadruple point Q_1 ($T_{c,CH_4} = 190.56K$, $T_{c,N_2} = 126.19K$, $T_{Q1,CH_4} = 272.9K$, $T_{Q1,N_2} = 271.9K$). It is of most interest in natural gas systems as it bounds the hydrate stability region at non-negative temperatures. The *I-H-V* line shows a decreasing pressure with increasing temperature. In the *I-H-L*$_w$ line, there is a steep increase in pressure with a small change in temperature due to high density and incompressibility of the phases present. The hydrate stability region is completely bound by the *I-H-V* and the *H-L*$_w$*-V* curves.

Figure 2.3 is a schematic diagram of the phase behaviour of binary system of a hydrate forming component (with critical temperature above the triple point of water) and water in a *P-T* plane. The major difference is the existence of a second quadruple point Q_2 (*H-L*$_w$*-L*$_v$*-V*) at which three other three phase equilibrium (*L*$_w$*-L*$_v$*-V*, *H-L*$_w$*-L*$_v$, and *H-L*$_v$*-V*) curves/lines emanates. The line *H-L*$_w$*-L*$_v$ shows a high increase in pressure due to the existence of incompressible phases. The *H-L*$_v$*-V* shows a slight change in pressure with temperature. It is of less importance as it exists within the boundaries bounded by *H-L*$_w$*-L*$_v$ and the *H-L*$_v$*-V*, falling within the hydrate stability zone. The hydrate stability region is completely bounded by the line *I-H-V* before Q_1, the curve *H-L*$_w$*-V* between Q_1 and Q_2, and line *H-L*$_w$*-L*$_v$ above Q_2. Temperature at Q_2 is often approximated as the maximum temperature at which hydrate can form. Hence the existence, beyond this point, of the equilibrium curve *L*$_w$*-L*$_v$*-V* without a hydrate phase.

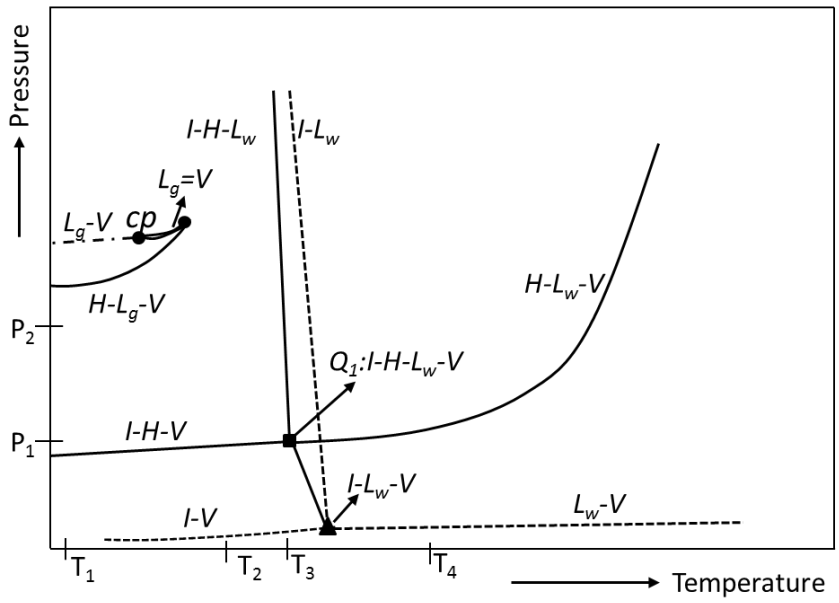

Figure 2.2 *Schematic diagram of the phase behaviour of binary system of water and a hydrate forming component (—) in a P-T plane. The phase diagram is representative of a gas with* $T_c<T_{tr,water}$ *eg. methane. The phase behaviour of the unary system of water (---) included for reference purpose.(adapted from [125]).*

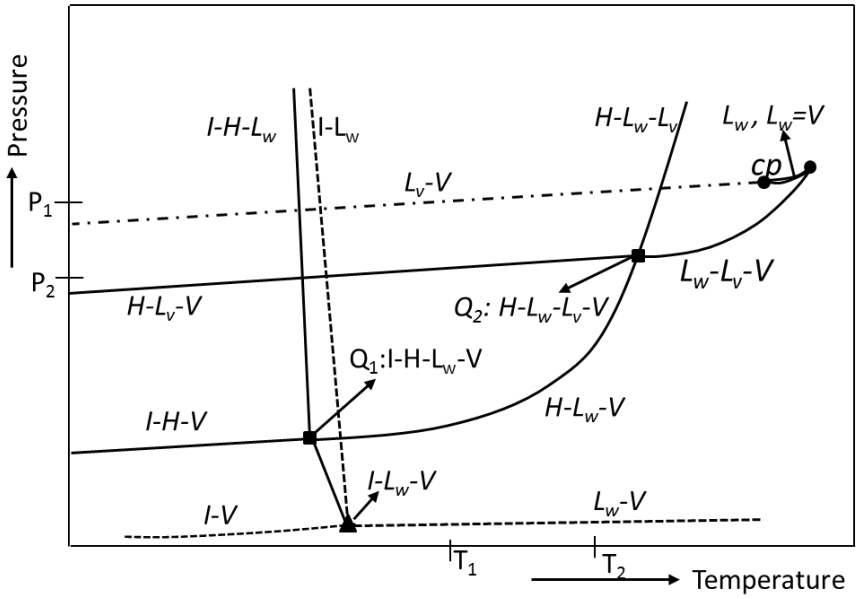

Figure 2.3 *Schematic diagram of the phase behaviour of binary system of water and a hydrate forming component (—) in a P-T plane. The phase diagram is representative of a gas with* $T_c>T_{tr,water}$ *eg. carbondioxide. The phase behaviour of the unary system of water (---) included for reference purpose.(adapted from[127]).*

Ternary and multicomponent systems

For ternary or multicomponent systems composed of more than two types of hydrate-forming guest molecules, the number of components $N \geq 3$, by **Equation 2.4**, $F_{\max} \geq 4$, thus requiring four or more dimensional plane to completely describe its phase behaviour. This is often not feasible. However, keeping some of the variables constant, a more elucidating representation of the phase diagram can be obtained. For ternary systems, the triangle diagrams in which pressure and temperature are kept constant, and prisms in which pressure or temperature is kept constant are used. Similarly, for multicomponent systems, fixing the composition of the each of the constituent components, the phase behaviour can be represented on a *P-T* plane. An example of hydrate-forming multicomponent system is natural gas whose phase behaviour diagrams are shown in **Figure 2.4**.

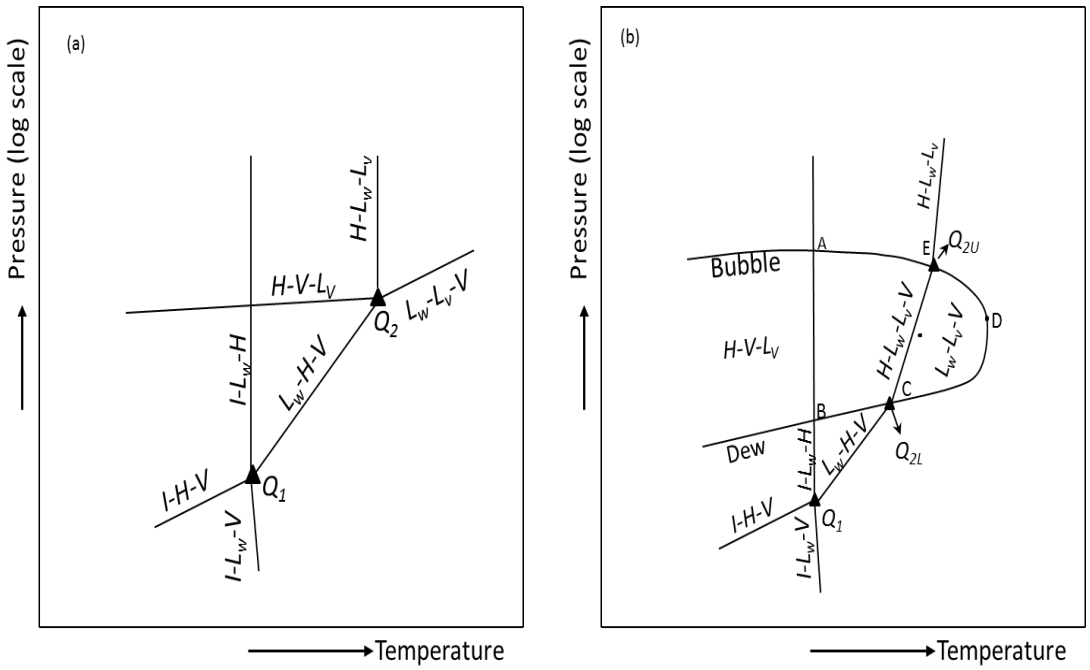

Figure 2.4 *Schematic diagram of the phase behaviour of multicomponent natural gas and water system (a) natural gas systems with light and heavy components (b) natural gas systems with heavy liquid hydrocarbon mixture (adapted from [25]).*

For natural gas systems with only light components, the phase behaviour is similar to that of binary system of a gas with $T_c < T_{tr,water}$ eg. methane and water can be approximated by the lower part of **Figure 2.4(a)** ,with only one quadruple point Q_1. For natural gas systems with heavier components such as propane and butane, a second

quadruple point Q_2 (**Figure 2.4(a)** exists from which there is the emergence of a condensed vapour phase L_v. The upper and lower quadruple points Q_1 and Q_2 are connected by the three-phase equilibrium line L_w-H-V. When a liquid hydrocarbon exists in the system, the line L_w-L_v-V in **Figure 2.4(a)** broadens to an area CDE in **Figure 2.4(b)**. The area is caused because a single hydrocarbon is no longer present, but rather created by a combination of hydrocarbon (and water) vapour pressures. Thus, the upper quadruple point Q_2 evolves into a four-phase equilibrium line H-L_w-L_v-V with upper and lower limits Q_{2U} and Q_{2L}.

2.2 Hydrate Thermodynamic Model

Thermodynamic modelling provides methods for calculating phase equilibria of hydrates. It affords a means of correlating and predicting all hydrate equilibrium regions in the phase diagrams. The thermodynamic model of van der Waal and Platteeuw [129] which was based on statistical thermodynamics laid the foundation for describing the phase behaviour of hydrate forming systems. They described the gas hydrate equilibrium state by taking the fact that at equilibrium, the chemical potential of water between the hydrate phase and the co-existing phases are equal.

The van der Waals and Platteeuw model has been used as the basis for different developments [130, 131]. Tohidi et al. [132] based on this thermodynamic approach developed a predictive model for hydrate inhibition in the presence of electrolytes. Martin [133] developed a simplified van der Waals and Platteeuw model for clathrates hydrates with multiple occupancy by assuming that guest molecules in cavities forms clusters in which molecules occupies fixed positions relative to each other. Chen and Guo [134] developed a simpler hydrate model by adopting a two-step hydrate formation mechanism; (1) a quasi-chemical reaction process to form basic hydrate, and (2) an adsorption of gas molecules into the empty linked cavities of basic hydrates. Hydrate models has also been developed into commercial softwares. Among them are HWPVT (Heriot-Watt University), HydraFLASH (Hydrafact Ltd.), CSMHYD (Colorado School of Mines), STFlash (Shell), CSMGem [135–138]. A description of a hydrate thermodynamic model is shown in the following section.

2.2.1 Multi-phase equilibrium

In a closed system consisting of N components and Π phases in equilibrium, the chemical potential of each component in all phases are equal as stated in **Equation 2.1**.

For an isothermal system, the chemical potential of component *i* in the vapour, liquid, or solid phase is related to the fugacity as:

$$\mu_i - \mu_{i,o} = RT \ln \frac{f_i}{f_{i,o}} \qquad 2.5$$

where μ_i and f_i represents the chemical potential and fugacity of component *i* at a given temperature *T* and pressure *P*. $\mu_{i,o}$ and $f_{i,o}$ are the chemical potential and fugacity respectively of component *i* at an arbitrary reference state of pressure and composition. *R* is the universal gas constant. Since $\mu_{i,o}$ and $f_{i,o}$ are inter-related, the equilibrium criteria in terms of chemical potential can then be re-written in terms of fugacities as:

$$f_i^{\alpha} = f_i^{\beta} = ...f_i^{\delta}, (i = 1, 2, ..., N) \qquad 2.6$$

For a system with *N* components, $N(\Pi - 1)$ equations of fugacity equality are obtained for a general case, where all the system species are presented in each phase. Taking a mass balance for a closed system, the following $N + \Pi$ equations must be fulfilled:

$$z_i = \sum_{l=\alpha}^{\delta} F^l x_i^l, \quad (i = 1, 2, ..., N) \qquad 2.7$$

$$\sum_{l=1}^{N} x_i^l = 1, \quad l = \alpha, \beta, ..., \delta \qquad 2.8$$

where z_i is the feed composition of component *i* (mole fraction), x_i^l is the mole fraction of component *i* in phase *l*, and F^l is the mole fraction of phase *l* in the system.

The $(N+1)\Pi$ equations in total as given in **Equations 2.6** to **2.8** are then used to solve the equilibrium problem, given an equal number unknowns. The unknowns may be $[x_i^l, F^l]$ for $(i = 1, 2, ..., N)$ and $(l = \alpha, \beta, ..., \delta)$ at specified temperature *T* and pressure *P*.

2.2.2 Vapour and liquid phases

The fugacities of component *i* in the vapour (*V*), liquid hydrocarbon (L_2) and aqueous (L_1) phases can be calculated by a cubic equation of state (EoS):

$$f_i = x_i \varphi_i P \qquad 2.9$$

where f_i, x_i, and φ_i are the fugacity, mole fraction, and fugacity coefficient of component *i* and *P* is the system pressure.

Previous hydrate modelling studies [132, 139] used the Valderrama modification of Patel-Teja (VPT) EoS to estimate fluid fugacities. However, the petroleum industry favours the Soave-Redlich-Kwong (SRK) [140] and the Peng-Robinson (PR) [141].

The general description of the SRK and PR EoS is as shown below:

$$P = \frac{RT}{v-b} - \frac{a}{\left(v+\delta_1 b\right)\left(v+\delta_2 b\right)} \qquad 2.10$$

where *P*, *v*, *T*, and *R* represents the pressure, molar volume, temperature, and universal gas constant. The constants δ_1 and δ_2 is 1 and 0 in the SRK EoS, and 2.414 and -0.414 in the PR EoS respectively.

a and *b* are terms related to the molecular attraction and repulsion, given by:

$$a = \Omega_{ac} \frac{R^2 T_c^{\,2}}{P_c} \tau \qquad 2.11$$

$$b = \Omega_b \frac{RT_c}{P_c} \qquad 2.12$$

where T_c and P_c are the critical temperature and critical pressure. Ω_{ac} and Ω_b are constants equal to 0.42747 and 0.08664 in the SRK EoS, and 0.45724 and 0.07780 in the PR EoS.

The term τ in **Equation 2.11** shows the temperature dependency of the attraction term as it is a function of the reduced temperature and the acentric factor. The function was suggested by Soave [140] and later selected by Peng and Robinson [141]. It is given as:

$$\tau = \left[1 + m\left(1 - T_r^{0.5}\right)\right]^2 \qquad 2.13$$

$T_r = T/T_c$ where T_r is the reduced temperature. m is a constant for each component.

2.2.3 Solid (hydrate) phase

The statistical thermodynamic theory proposed by van der Waals and Platteeuw [142] have been used to model hydrate phase equilibrium. They modelled hydrate phase using the ideal solid solution theory. The model assumed that the Langmuir adsorption is analogous to hydrate forming molecule enclathration into the hydrate cavity.

The fugacity of water in the hydrate phase is estimated by:

$$f_w^H = f_w^\beta \exp\left(-\frac{\Delta\mu_w^{\beta-H}}{RT}\right) \qquad 2.14$$

where f_w^{β} is the fugacity of water in the empty hydrate lattice. $\Delta\mu_w^{\beta-H}$ is the difference of chemical potential for water between the empty hydrate lattice $\Delta\mu_w^{\beta}$ and the hydrate phase $\Delta\mu_w^{H}$.

Estimation of f_w^{β}

The fugacity of water in the empty hydrate lattice f_w^{β} is given by:

$$f_w^{\beta} = f_w^{L_1/I} \exp\left(-\frac{\Delta\mu_w^{\beta-L_1/I}}{RT}\right) \qquad 2.15$$

where $f_w^{L_1/I}$ is the fugacity of pure water or ice. $\Delta\mu_w^{\beta-L_1/I}$ is the difference of chemical potential for water between the empty hydrate lattice and pure water or ice.

The term in parenthesis, $\frac{\Delta\mu_w^{\beta-L_1/I}}{RT}$ is given by:

$$\frac{\Delta\mu_w^{\beta-L_1/I}}{RT} = \frac{\Delta\mu_w^{o}}{RT_o} - \int_{T_o}^{T} \frac{\Delta h_w^{\beta-L_1/I}}{RT^2} dT + \int_{0}^{P} \frac{\Delta v_w^{\beta-L_1/I}}{RT} dP \qquad 2.16$$

where the subscript *o* represents reference property, $\Delta\mu_w^{o}$ is the reference chemical potential difference between water in the empty hydrate lattice and pure water in the ice phase at 273.15 K. $\Delta h_w^{\beta-L_1/I}$ and $\Delta v_w^{\beta-L_1/I}$ are the molar enthalpy difference and the molar volume difference, respectively between and empty hydrate lattice and water or ice.

$\Delta h_w^{\beta-L_1/I}$ in **Equation 2.16** is generally calculated by:

$$\Delta h_w^{\beta-L_1/I} = \Delta h_w^{o} + \int_{T_o}^{T} \Delta C_{p,w} dT \qquad 2.17$$

Δh_w^o is the difference of enthalpy between the hydrate lattice and ice at the ice point and zero pressure and $\Delta C_{p,w}$ is the heat capacity difference between the empty hydrate lattice and the pure liquid water. $\Delta C_{p,w}$ can be calculated using the following empirical correlation [143–145]:

$$\Delta C_{p,w} = -37.32 + 0.179\left(T - T_o\right), \quad T > T_o \qquad 2.18$$

Estimation of $\Delta\mu_w^{\beta-H}$

The chemical potential difference between water in the empty hydrate lattice and the hydrate phase is given as [146]:

$$\Delta\mu_w^{\beta-H} = RT\sum_m \theta_m \ln\left(1 + \sum_j C_{jm} f_j\right) \qquad 2.19$$

where θ_m is the number of type *m* cavity for each water molecule in the unit cell, f_j is the fugacity of the hydrate forming component *j* and C_{jm} is the Langmuir constant and is calculated as [144, 147]:

$$C_{jm} = \frac{4\pi}{\kappa T}\int_0^R \exp\left(-\frac{\omega(r)}{\kappa T}\right) r^2 dr \qquad 2.20$$

where κ is the Boltzmann's constant, $\omega(r)$ is the spherically symmetric cell potential in the cavity, with *r* measured from the centre of the cavity.

$\omega(r)$ depends on the intermolecular potential function adopted for describing the encaged guest molecule-water interaction. van der Waals and Platteeuw in their original work used the Lennard-Jones 6-12 [148, 149] potential function to estimate the cell potential. The Lennard-Jones potential function is more applicable to mono-atomic and spherical molecules. McKoy and Sinanoglu [150] suggested that the Kihara is better suited for both larger and non-spherical molecules.

The Kihara potential functions are as shown below:

$$K(r) = \infty, \quad (r = 2\beta) \tag{2.21}$$

$$K(r) = 4\varepsilon\left[\left(\frac{\sigma - 2\beta}{r - 2\beta}\right)^{12} - \left(\frac{\sigma - 2\beta}{r - 2\beta}\right)^{6}\right], \quad (r > 2\beta) \tag{2.22}$$

where $K(r)$ is the potential energy of interaction between two molecules, ε is the depth of the energy well, that is, the minimum potential energy, β is the hard-core radius, σ is the collision diameter, that is, the distance when $\mathrm{K} = 0$.

The overall cell potential $\omega(r)$ can be calculated as:

$$\omega(r) = 2z^{H}\varepsilon\left[\frac{(\sigma^{*})^{12}}{R_c^{11} r}\left(\delta^{10} + \frac{\beta}{R_c}\delta^{11}\right) - \frac{(\sigma^{*})^{6}}{R_c^{5} r}\left(\delta^{4} + \frac{\beta}{R_c}\delta^{5}\right)\right] \tag{2.23}$$

where z^{H} is the coordination number of the hydrate cavity, ε is the characteristic energy and R_c represents the cavity radius. σ^{*} is given as $\sigma^{*} = \sigma - 2\beta$ where σ is the collision diameter. The general expression for δ^{N} where N is an integer and equal to 4, 5, 10, or 11 is given as:

$$\delta^{N} = \frac{1}{N}\left[\left(1 - \frac{r}{R_c} - \frac{\beta}{R_c}\right)^{-N} - \left(1 + \frac{r}{R_c} - \frac{\beta}{R_c}\right)^{-N}\right] \tag{2.24}$$

2.3 Hydrate Formation

The formation of clathrate hydrates is analogous to a crystallisation process. It is essentially a two stage process: hydrate nucleation, and hydrate growth [151–157].

2.3.1 Hydrate nucleation

Hydrate nucleation is said to be occurring when small clusters of water and gas, that is, hydrate nuclei grow and achieve a critical size. When the critical size is achieved, the

nucleus is stable and subsequently leads to the formation of hydrate. Published results by Nerheim et al. [158] and Englezos et al. [152] has shown that the radius of a stable hydrate nuclei should be between 25-170 Å.

Hydrate formation is a phase transformation process. It requires a supersaturated environment to occur. The supersaturation which is the driving force is often in terms of gas overpressure. Thus, the extent of supersaturation determines the number of hydrate nuclei that will form. The driving force reduces during nucleation and hydrate growth as the system approaches equilibrium which is described by a minimum energy. The time difference between the creation of supersaturation and the formation of a new phase is the induction time [159]. The induction time can be estimated through the pressure-time plot of a hydrate forming system as shown in **Figure 2.5**.

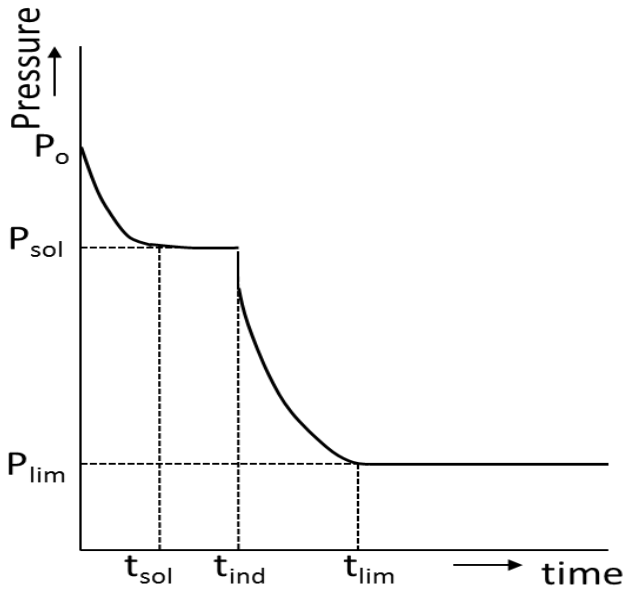

Figure 2.5 *Typical pressure profile with time for a hydrate formation experiment (adapted from [160]).*

The dissolution of the gas in the aqueous phase causes the first pressure drop from P_o to P_{sol} at a corresponding time of t_{sol}. Between t_{sol} and $t_{ind,}$ the pressure stabilises. The duration of the pressure stability is the induction time marked by t_{ind}. Beyond the t_{ind}, a sudden pressure drop is observed as hydrate starts to form. This point is known as the turbidity point. The pressure decrease continues as more gas is consumed for hydrate formation until the pressure reaches $P_{lim.}$ Beyond P_{lim} the pressure remains constant indicating that hydrate formation is complete. The duration of induction is then calculated as:

$$Induction\ time = t_{ind} - t_{sol} \qquad 2.25$$

Long and Sloan [161] in a series of experiments to investigate the site of nucleation for natural gas and carbondioxide hydrate nucleation in a sapphire tube, reported that hydrate nucleation occurs at the water-gas interface. This assertion was also supported for methane hydrate by Huo et al. [162], Ostergaard et al [163], Taylor [164], for carbon dioxide hydrate by Fujioka et al. [165], Kimuro et al. [166], Hirai et al. [167], and Mori et al. [168].

2.3.2 Hydrate growth

The hydrate growth stage is the stage during which the stable hydrate nuclei grow into solid hydrates. During this process, mass and heat transfer dominates. However, most of the nucleation parameters including displacement from equilibrium conditions, surface area, agitation, water history, and gas consumption continue to be important. Vysniauskas and Bishnoi [151, 169] were the first to quantitatively describe and model the formation kinetics of gas hydrates. Their study obtained kinetic data by contacting gas with water at temperatures above the freezing point of water and constant pressures. They developed a semi empirical model in which hydrate formation rate was determined from gas consumption rate.

$$R^* = Aa_s \exp\left(-\frac{\Delta E}{RT}\right)\exp\left(-\frac{a}{\delta T^b}\right)P^\gamma \qquad 2.26$$

where R^* is the gas consumption rate during hydrate formation, A is the pre-exponential constant, a_s is the effective surface area of gas-water interface, ΔE is the activation energy for hydrate formation, *a* and *b* are empirical constants to account for the effect of supercooling to consumption rate.

Englezos et al. [152] proposed an intrinsic kinetic model with only one adjustable parameter to describe the kinetics of hydrate formation. Their model was based on the theory of crystallisation and used the two-film theory to model to mass transfer across the water-gas interface. In the two-film theory model as depicted in **Figure 2.6**, it is assumed that the solid hydrate particle is surrounded by an adsorption (reaction) layer, then followed by a stagnant liquid diffusion layer. The authors proposed a two-step

process for hydrate growth: diffusion of dissolved gas from the bulk liquid phase to the crystal (hydrate)-liquid interface through a laminar diffusion layer around the particle, and the reaction at the interface which involves adsorption of gas molecules into the water cavity of the hydrate.

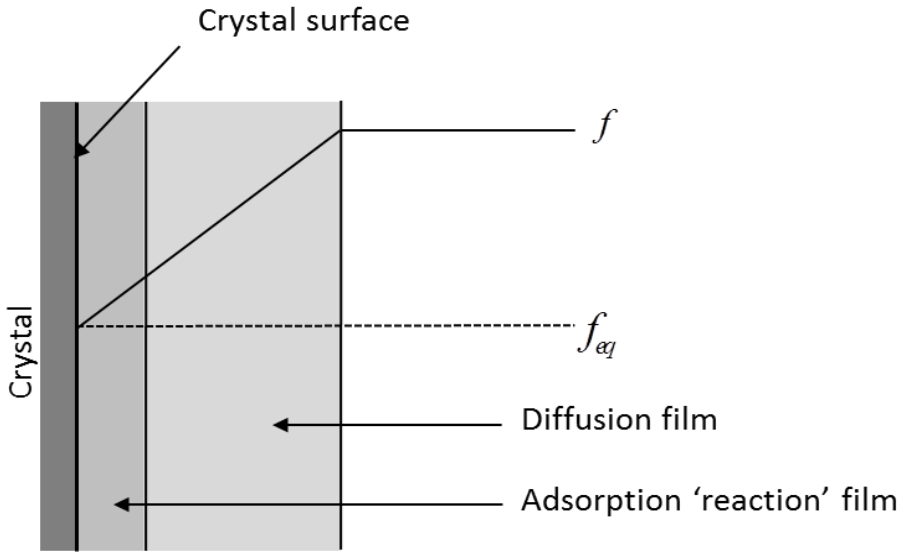

Figure 2.6 *Schematic representation of the two-film theory (adapted from [152]).*

Their model assumed that there is no mass accumulation in the diffusion layer, thus the rates in the two layers are equal. Hence, the rate of growth hydrate particle in terms of the overall driving force is:

$$\left(\frac{dn}{dt}\right)_p = K' A_p \left(f - f_{eq}\right) \qquad 2.27$$

where $\left(dn/dt\right)_p$ is the number of moles of gas consumed for hydrate formation per time, A_p is the surface area of hydrate particle, f is fugacity of the gas, f_{eq} gas fugacity at three phase equilibrium, K' is the overall hydrate formation rate constant and it is expressed in terms of coefficients of diffusion k_d and reaction k_r as:

$$\frac{1}{K'} = \frac{1}{k_r} + \frac{1}{k_d} \qquad 2.28$$

2.4 Hydrate Dissociation

Hydrate dissociation is of extreme importance in gas production from natural gas hydrate reservoirs. It is the basis of all gas recovery techniques from gas hydrate reservoirs. Hydrate dissociation is an endothermic process, thus requiring external supply of heat to break the hydrogen bonds holding the water molecules, and also the van der Waals interaction forces between the guest molecule and the water cavity to decompose the hydrate into gas and water. The different methods to dissociate hydrate have been discussed in **Section 1.7**. Extensive experimental and modelling studies have been reported on hydrate dissociation. Kim et al. [170] suggested that hydrate decomposition may be viewed as a two-stage process: the destruction of the clathrate lattice at the particle surface, and the desorption of the guest molecule from the surface. They developed an intrinsic kinetic model for hydrate dissociation. Comparison of experimental data with modelling results has shown that heat transfer is the dominant process in hydrate dissociation rather than intrinsic kinetics [171–173]. Hong et al. [172] suggested that intrinsic kinetics control the early stages of hydrate dissociation. But due to heat removal during decomposition, a temperature gradient exists between the interface and the hydrate zone, conducting heat from the hydrate zone to the interface. Thus, heat transfer dominates at the latter stages of hydrate dissociation. Gupta [174] in his nuclear magnetic resonance (NMR) studies of methane hydrate dissociation also suggested that intrinsic kinetics is not likely to play a dominant role in the dissociation process.

2.5 Summary

The theoretical background of hydrate forming system has been described. The Gibb's phase rule was used to describe the phase diagrams of unary, binary, ternary and multicomponent systems. The phase behaviour of hydrate forming binary, ternary and multicomponent systems were described using the phase diagrams. The thermodynamic theory of hydrate systems was discussed and a typical thermodynamic model described. Furthermore, the theories of the kinetics of hydrate formation vis-à-vis, nucleation and growth, and hydrate dissociation was also discussed.

CHAPTER 3 FLUE GAS INJECTION FOR METHANE RECOVERY FROM METHANE HYDRATE RESERVOIRS

3.1 Introduction

Methane production from methane hydrate reservoirs using the classical production techniques has been extensively studied. Despite the benefits of methane recovery using these techniques, they come with inherent disadvantages. Depressurisation is a slow process and has the possibility of ice formation if done rapidly thereby reducing permeability and ultimate recovery. Thermal stimulation has the challenge of energy inefficiency with regard to heat loss, while chemicals such as methanol and ethylene glycol are toxic to the environment if used as inhibitors for methane production. Furthermore, there is the problem of water handling due to excess water production, and possible surficial slide arising from loss of formation integrity due to hydrate dissociation. Gas injection such as CO_2, or CO_2 + nitrogen binary mixture for methane recovery provides a viable alternative as methane hydrate reservoir could simultaneously serve as a CO_2 sink and methane source. Many researchers have studied CO_2-methane exchange in topics including thermodynamic feasibility [175–178], phase equilibria [179–181], and kinetics [99, 176, 178, 182]. Many of the reported experiments in literature were conducted with bulk phase methane hydrate [183–186]. Temperature and pressure conditions range from 268.15 K to 278 K, and 2.67 MPa to 6 MPa respectively. Reported recoveries were in the range of 12% and 90% of methane in methane hydrate. Hydrate growth and dissociation characteristics in the bulk phase is markedly different from that in porous media. The physical properties and surface chemistry may affect hydrate formation/dissociation in sediments with regards to thermodynamic conditions, formation/dissociation kinetics, and spatial distribution [187]. Based on this, a few studies on CO_2-methane exchange were conducted using sand, sandstone, and quartz sand to simulate the porous media [177, 188]. Experimental temperatures and pressures range from 277 K to 283 K, and 3 MPa to 13 MPa respectively. Methane recovery achieved range from 3.4% to 40.7%, a significant reduction compared with bulk phase experiments.

Binary mixtures of CO_2 and nitrogen have been proposed. Nitrogen is a hydrate former, thus it is expected that its inclusion in the exchange process will lead to increased methane replacement and recovery. A number of authors used different ratios of CO_2-

nitrogen mixtures to investigate methane replacement by this binary mixture. For a 20:80 mixture of CO_2 + nitrogen, Park et al. [189], at 274.15 K reported 85% and 92% recoveries at 3.5 MPa and 12 MPa respectively, Shin et al. [190] at 274.4 K and 12 MPa reported a 92% recovery, and Seo et al. [191] at 274 K and 10 MPa achieved 48% recovery. For a 50:50 mixture of CO_2 + nitrogen, Seo et al. [191] at 274 K and 10 MPa achieved 51% recovery. Masuda et al. [192] in their study used a 60:40 CO_2 + nitrogen mixture, temperature range of 277 K – 280 K, and 7 MPa. They achieved only 30% methane recovery.

These authors all focussed mainly on CO_2 – methane and CO_2 + nitrogen – methane replacement. This study showcases a novel technique that achieves methane recovery from methane hydrate in porous media by shifting the methane hydrate equilibrium phase boundary by flue gas injection. Kinetics of methane recovery in the presence of flue gas was studied. The technique was combined with conventional depressurisation to enhance methane recovery. The technique has the benefit of being non-destructive as methane molecules in the hydrate lattice is replaced by CO_2 to form CO_2-hydrate or CO_2-methane mixed hydrate, thus sequestering the CO_2 component of the flue gas. This mitigates concerns about huge volumes of produced water. Furthermore, the use of CO_2 + nitrogen mixture improves methane recovery efficiency. The amount of CO_2 that can be sequestered using this technique is reduced compared with pure CO_2 injection as the CO_2 component of flue gas is only a small fraction. However, the additional cost incurred for CO_2 separation and purification in conventional carbon capture and storage (CCS) is eliminated. Experiments were conducted at 273.2 K, 278 K, 283 K, and 284 K and the corresponding methane hydrate equilibrium pressures at these temperatures. Temperatures were chosen to cover the range of thermodynamic conditions obtained in methane hydrate reservoirs.

3.2 Experimental Apparatus

All experiments were conducted at the Centre for Flow Assurance (C-FAR) at the Institute of Petroleum Engineering, Heriot-Watt University. The Ultrasonic rig was modified for use in the experiments. **Figure 3.1** is a schematic view of the experimental rig. It consists of a high pressure cylindrical cell made of stainless steel, a Linear Variable Differential Transformer (LVDT), Quizix pump, hydraulic hand pump, a data acquisition system (DAS), and a cryostat. The maximum internal length of the cell after

assembling is 18.16 cm and an internal diameter of 7.5 cm. Thus, the maximum inner volume of the cell is 800 cm^3. The cell is rated to withstand a maximum working pressure of 40 MPa, exceeding the pressure range of interest in this study. The cell is housed in a cooling jacket and its temperature is controlled by a cryostat and measured by a thermal probe consisting of a Platinum Resistance Thermometer (PRT) with an accuracy of 0.1 K. The thermal probe was calibrated with a PREMA Precision Thermometer 3040 over a range of 273.15 K to 298.15 K. The thermal probe is inserted into the cooling jacket to measure cell temperature. The cell pressure is measured by a pressure transducer with an accuracy of 0.05 MPa. The pressure and temperature are continuously recorded on a computer. The top-cap of the cell is fixed while the bottom-cap is fitted with a movable piston that can be moved forward or backward by the injection or withdrawal of hydraulic fluid with the aid of the hydraulic hand pump. The piston movement helps to increase or reduce the pore pressure/cell volume without injecting or removing fluid from the cell, thus maintaining a closed system. A displacement meter (Linear Variable Differential Transformer, LVDT) is fitted to the tail rod of the piston to measure the piston displacement. This enables the estimation of the exact volume of the cell at any instant. Pore pressure, temperature, pump pressure, overburden pressure, and piston displacement are logged every 60 seconds using LabView programme and recorded on a computer (PC) via a data acquisition system (DAS). Test fluids and samples for analysis are injected and collected through valves on the bottom-cap and top-cap.

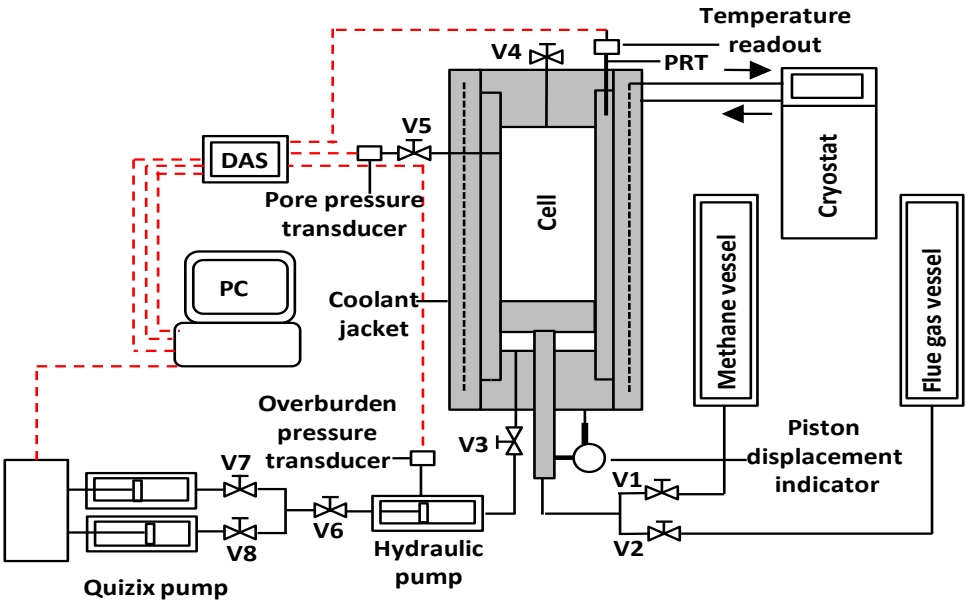

Figure 3.1 *Schematic diagram of experimental rig.*

3.3 Materials

Research grade methane with certified purity of 99.9995 vol% supplied by BOC Limited was used

Flue gas composed of 86 Mol% nitrogen and 14 mol% CO_2 typical of coal-fired power plants was synthesised. Both the nitrogen and CO_2 were certified with purity of 99.9995 vol% and were supplied by BOC Limited.

Deionised water produced with ELGA DV 25 water purification system.
Silica sand from Fife (Scotland) was used as the porous medium. X-Ray diffraction analysis of the Fife sand samples show that it is composed of basically four minerals; quartz, microcline, calcite, and kaolinite. The mineralogical composition of eight samples analysed is shown in **Table 3.1**.

Table 3.1 *Mineralogical composition of Fife sand*

Sample	Quartz /%	Microcline /%	Calcite /%	Kaolinite /%
1	100	Trace	0	0
2	97	3	0	0
3	97	3	0	Trace
4	97	3	0	Trace
5	97	3	Trace	Trace
6	97	3	0	Trace
7	97	3	Trace	Trace
8	97	3	0	Trace

The particle size distribution of the sand was analysed using Malvern Mastersizer, shown in **Figure 3.2**. It measures the particle size distribution based on the principle of laser scattering. The particle size distribution is shown in **Table 3.2** and graphically in **Figure 3.2**. The particle size distribution range from 1.2 µm to 600 µm with a mass medium of 256.54 µm and specific surface area of 0.0236 m^2/g.

Figure 3.2 *Malvern Mastersizer particle size distribution analyser*

Table 3.2 *Particle size distribution for the silica (Fife, Scotland) sand used in the experiments*

Size/ µm	Ratio/ mass%	Size/ µm	Ratio/ mass%	Size/ µm	Ratio/ mass%	Size/ µm	Ratio/ mass%	Size/ µm	Ratio/ mass%
600	0.9	166	3.0	46.2	0.3	12.8	0.1	3.55	0.0
544	1.2	151	2.1	41.8	0.2	11.6	0.1	3.22	0.0
493	1.9	137	1.5	37.9	0.2	10.5	0.1	2.92	0.0
446	3.3	124	1.3	34.3	0.2	9.52	0.0	2.64	0.0
404	5.2	112	1.0	31.1	0.1	8.63	0.0	2.39	0.0
366	7.6	102	0.8	28.2	0.1	7.82	0.0	2.17	0.0
332	10.2	92.1	0.7	25.5	0.1	7.08	0.0	1.97	0.1
301	12.0	83.4	0.6	23.1	0.1	6.42	0.0	1.78	0.1
273	12.6	75.6	0.5	21	0.1	4.82	0.0	1.61	0.1
247	11.3	68.5	0.5	19	0.1	5.27	0.0	1.46	0.1
224	8.2	62.1	0.4	17.2	0.1	4.77	0.0	1.32	0.1
203	5.7	56.2	0.4	15.6	0.1	4.33	0.0	1.2	0.1
184	4.1	50.9	0.3	14.1	0.1	3.92	0.0		
Mass medium = 256.54 µm				Specific surface area = 0.0236 m^2/g					

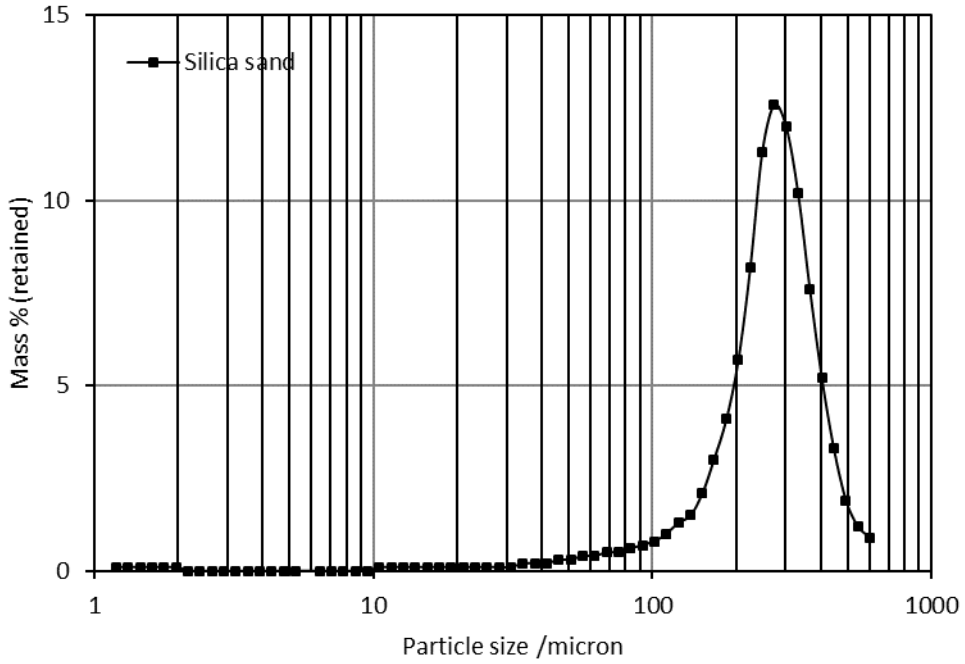

Figure 3.3 *Particle size distributions of the sand used in graphical form.*

3.4 Experimental Procedure

3.4.1 Test conditions

The experiments were conducted using the silica sand to simulate the porous medium to investigate the feasibility of flue gas injection technique for methane recovery from gas hydrate reservoir. The experiments were designed to understand three fundamental issues: how methane hydrate decomposes upon exposure to flue gas, how flue gas affects depressurisation process, and the possibility of CO_2 sequestration while methane hydrate is decomposing. To understand these issues, experiments were conducted at different temperature-pressure conditions. Experiments 1, 2, and 3 were set inside both methane and CO_2 HSZs while Experiment 4 was set outside the CO_2 HSZ but inside the methane HSZ. Temperatures were set at 273.2 K, 278 K, 283 K, and 284 K for Experiments 1, 2, 3, and 4 respectively. These covers the typical range of thermodynamic conditions obtainable in the gas hydrate stability zones of naturally occurring natural gas hydrate reservoirs. The experiments were designed to achieve vapour phase composition of 50:50 mol% methane and flue gas at equilibrium after flue gas injection. Therefore, pressures were also set to corresponding equilibrium pressures at the given temperatures and desired vapour phase composition. **Table 3.3** is a summary of the Experimental conditions. **Figure 3.4** shows the hydrate equilibrium

phase boundaries and the pressure and temperature conditions for the experiments. The equilibrium pressure at each test temperature and target vapour phase composition, the hydrate equilibrium phase boundaries and consequently the hydrate stability zones were predicted by HWPVT, an in-house software developed by the Centre for Gas Hydrate Research at the Institute of Petroleum Engineering, Heriot-Watt University for hydrate and allied calculations.

Table 3.3. *Summary of experimental conditions*

Experiment	Temperature/K	Pressure/MPa
1	273.2	4.15
2	278.0	6.89
3	282.0	11.00
4	284.0	14.04

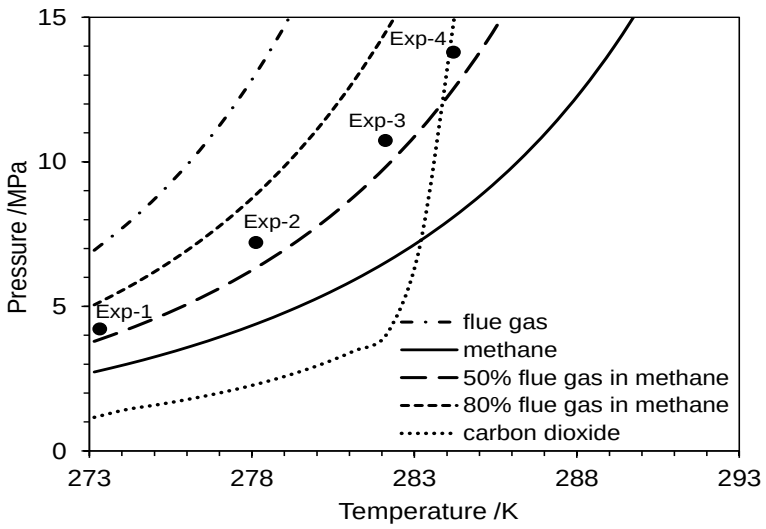

Figure 3.4 *Phase boundaries of methane-, nitrogen-, and CO_2-hydrates, phase boundaries of vapour phase compositions of 50:50 mol% flue gas + methane; 80:20 mol% flue gas + methane in equilibrium with methane hydrate, and the test conditions.*

3.4.2 Sample preparations

3.4.2.1 Flue gas synthesis

Flue gas used was typical of coal-fired power plants, composed of 86:14 mol% nitrogen and CO_2. The mass of CO_2 and nitrogen to give the desire composition of flue gas given the volume (of the transfer vessel) and target pressure was determined. The determined mass of CO_2 was transferred first into the transfer vessel, then nitrogen was

transferred next and pressurised to the target pressure. The prepared mixture was then analysed using a Gas Chromatograph (GC Varian 3600) to ensure the accuracy of the composition of the prepared flue gas mixture.

3.4.2.2 Partially water saturated sand

The dry sand sample was thoroughly mixed with distilled and deionised water to partially saturate it. The desired saturation was achieved at an initial water saturation of 14.4 mass% water.

3.4.3 Methane hydrate synthesis

The prepared wet sand was loaded into the cell in batches of small quantities, while thumping after each batch to ensure that the wet sand is properly packed to avoid vugs. This continued until the sediment reached the position of the end of the top cap. The cell was then sealed with the top cap and vacuumed. The sediment was then compacted by applying an overburden pressure of 3.5 MPa by injecting fluid behind the piston with the aid of the hydraulic hand pump. The desired amount of methane was then injected into the cell through valve V1, the cell temperature was then set to 298 K via the cryostat, data logging by LabVIEW was then commenced, while the cell was allowed time to equilibrate. Once pressure and temperature equilibrium was achieved, cell temperature was reduced to 273.2 K via the cryostat to initiate hydrate formation. As temperature reduces, pressure reduces in relation to temperature. Hydrate begins to form at a point where abrupt change in pressure is noticed and continues until there is no longer any noticeable change in pore pressure. The onset of hydrate formation appeared at the point where there was a change in slope of the pressure profile during cooling (approximately at 281 K, 16 MPa in **Figure 3.5**). Hydrate growth continued until there is no noticeable change in pressure, signifying the completion of hydrate formation. (**Figure 3.6**).

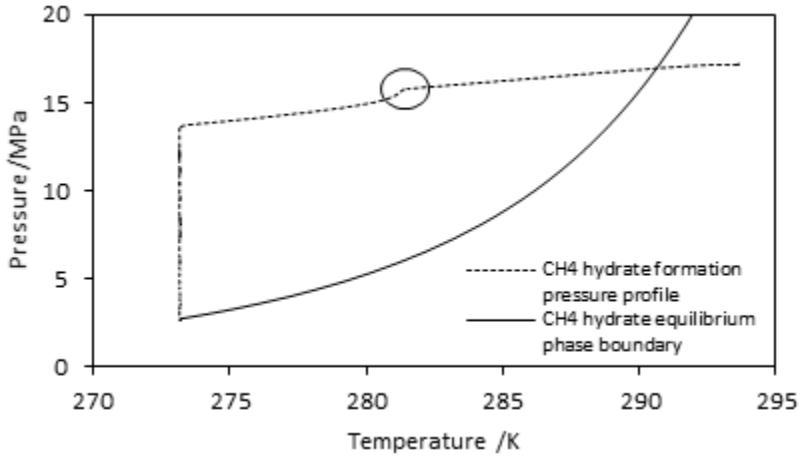

Figure 3.5 *Methane hydrate equilibrium phase boundary and methane hydrate formation pressure profile. The circled part shows the abrupt change in slope of pressure profile indicating the onset of hydrate formation at approximately 281 K and 16 MPa.*

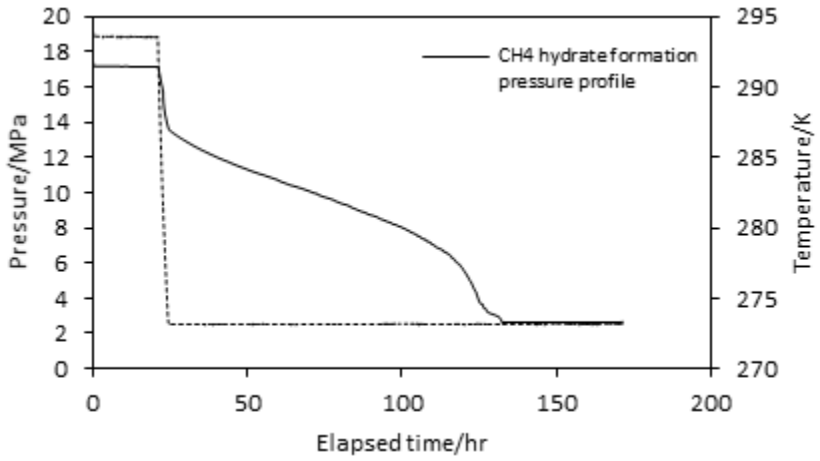

Figure 3.6 *Methane hydrate formation temperature and pressure profile with time. Hydrate formation was completed at 140 hours after which the system pressure remains relatively constant.*

3.4.4 Flue gas injection

Upon completion of methane hydrate formation at the desired experimental temperature, the synthesised flue gas was injected into the cell through valve V2 to pressurise the system to about 10 times the equilibrium pressure after hydrate formation. This was done to reduce the proportion of unconsumed methane in the gas phase to the barest minimum. The vapour phase was then purged to reduce the system pressure to just higher than equilibrium pressure of flue gas at the test temperature. The system was then allowed to equilibrate. At this point it was assumed that no hydrate dissociation occurred, vapour phase sample was then taken and analysed using a Gas

Chromatograph (GC Varian 3600) to ascertain the initial composition of the vapour phase before the commencement of methane recovery.

3.4.5 Methane recovery

Methane recovery was initiated by setting the system pressure to the desired equilibrium pressure as predicted, by purging out the gas mixture (resident methane + injected flue gas) from the cell until the desired pressure was achieved. This shifted the methane hydrate phase boundary away from equilibrium. Consequently, methane hydrate dissociated and methane was released as the system is approaching a new equilibrium with the changing gas composition. A programmable (Quizix) pump was used to maintain the system at the desired target pressure. Samples from the vapour phase were collected and analysed at intervals using the GC. This continued until the ratio of each component in the vapour became relatively constant. This signified that a new equilibrium had been reached. In order to increase the amount of methane recoverable after decomposition has stopped, depressurisation was initiated. This was done in four pressure steps. The first two steps were both inside the methane and CO_2 HSZs. The third step was outside the methane HSZ but inside the CO_2 HSZ. These steps were to allow for complete decomposition of methane hydrate. The final step was at a point outside the CO_2 HSZ. This was done to ascertain the formation of CO_2-hydrate formation and consequently CO_2 sequestration. In each step the system pressure was maintained by the Quizix pump while the system was allowed to reach equilibrium.

3.4.6 GC analysis

The gas samples collected from the test cell were analysed for composition using a GC Varian 3600. The carrier gas is Helium and the detector type is TCD (Thermal Conductivity Detector). The TCD measures the variations in the thermal conductivity of the effluent gas from the column of the GC and compares it to that of the reference flow of carrier gas (helium). The column temperature was set constant at 323 K for 10 minutes during which 3 injections were made and thereafter ramped up to 378 K for one minute at the rate of 323 K/min to vapourise the content of the column. To accurately quantify the proportion of each component of the vapour phase of the test cell at any instant, the GC was calibrated. Known volumes (100 µL, 200 µL, 300 µL, 400 µL), and consequently the moles of pure components (nitrogen, carbondioxide, and methane)

were injected into the GC. This gave their signature chromatograms, retention times, and their corresponding peak areas. A typical chromatogram of the gas mixtures analysed is shown in **Figure 3.7**. The moles of each component at the different volumes were then plotted against their corresponding peak areas to obtain their calibration curves and equations. The equations are then used to estimate the relative amount of their corresponding components in the vapour phase. When summed together, the proportion of each component of the vapour phase in relation to the total of all the components can be estimated.

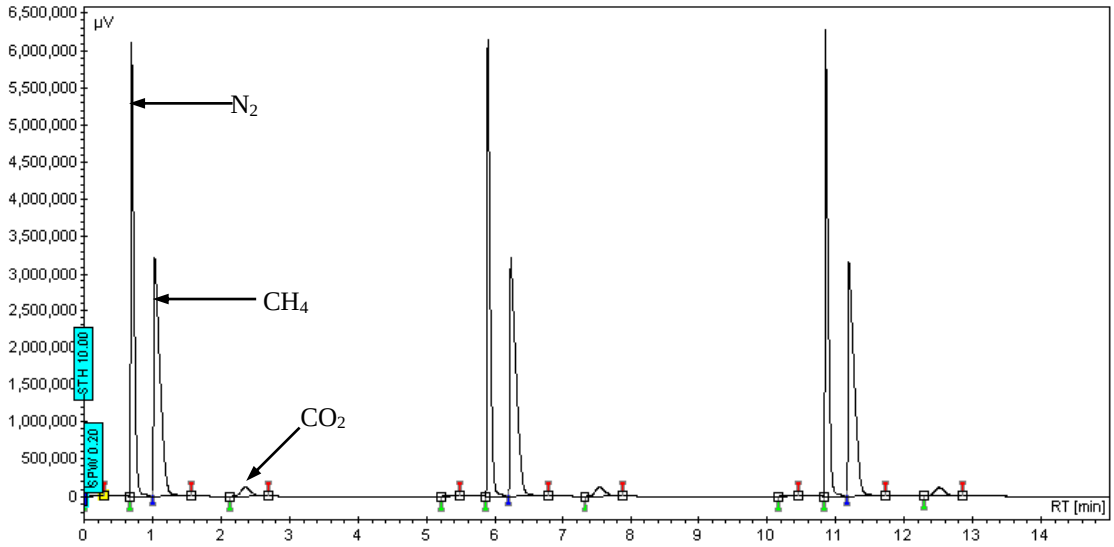

Figure 3.7 *Chromatogram of a gas mixture containing nitrogen, methane, and carbon dioxide.*

(a)

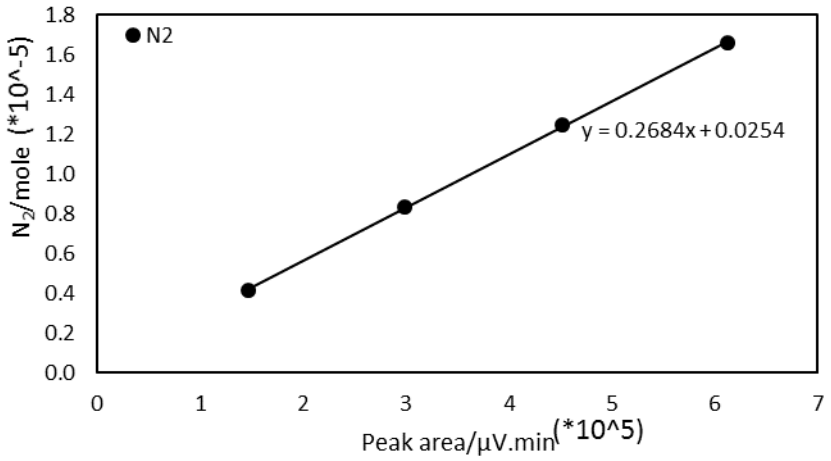

(b)

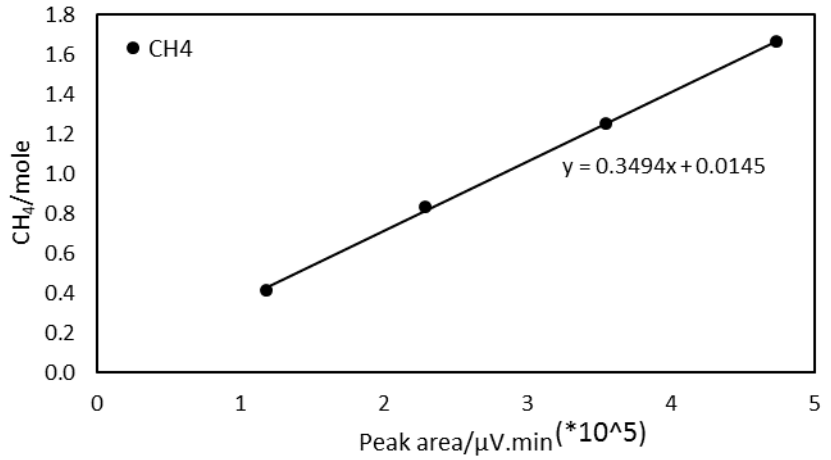

(c)

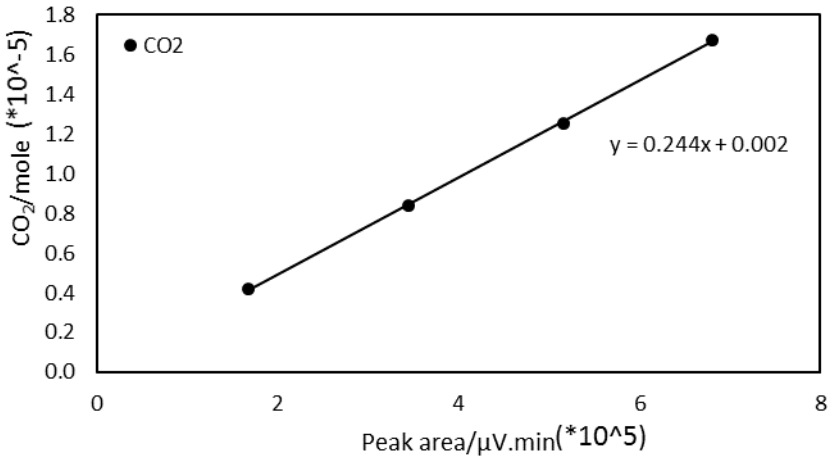

Figure 3.8 *Calibration lines of (a) nitrogen, (b) methane, and (c) carbondioxide showing their moles as functions of their respective peak areas.*

3.5 Results and Discussions

Four experiments were conducted to investigate the feasibility of flue gas injection method for methane recovery from methane hydrate reservoirs. The fundamental issues studied are; methane hydrate decomposition behaviour upon exposure to flue gas; effect of flue gas injection on the depressurisation process; and the possibility of the CO_2 component of the flue gas to be sequestered in hydrate form while methane is being released from the hydrate.

Table 3.4 summarises the properties and initial parameters of the sediment samples before flue gas injection including porosity ϕ, hydrate saturation S_h, remaining methane gas saturation S_g and remaining water saturation S_w

Table 3.4 *Properties and initial parameters of the hydrate bearing sediment samples*

Experiment	1	2	3	4
Height (cm)	15.08	14.77	14.77	14.6
Diameter (cm)	7.5	7.5	7.5	7.5
Volume (cm^3)	666.1	652	652.1	644.7
Porosity (vol%)	42.1	43.1	43.1	43.2
Dry mass (g)	1076.6	1076.6	1076.6	1076.6
Grain density (g/cm^3)	2.64	2.64	2.64	2.64
Wet mass (g)	1231.8	1231.8	1231.8	1231.8
Initial water saturation (mass%)	14.4	14.4	14.4	14.4
Wet density (g/cm^3)	1.85	1.89	1.89	1.91
Hydrate saturation (vol%)	54	43.8	36.8	31.3
Gas saturation (vol%)	34.3	36.1	37.4	38.1
Water saturation (vol%)	11.7	20.1	25.8	30.5

3.5.1 Decomposition kinetics

Analysis of the composition of the vapour phase was used to monitor the release of methane from the hydrate phase into the vapour phase after flue gas injection. Vapour phase samples were collected at 0 mins, 15 mins, 45 mins, 1hr 15 mins, and 4hr 45 mins initially to monitor the initial rapid change in composition. Subsequently, samples were taken and analysed at 24 hr interval as the composition change slowed and gradually stopped. **Error! Reference source not found.** to **Error! Reference source not found.** in **APPENDIX C** shows the vapour phase composition with time for Experiments 1 to

4 respectively. **Figure 3.9** (Experiment 1) illustrates the typical kinetic process of methane hydrate decomposition after flue gas injection. From A to B lasting 0 to 5 hours (Stage 1), rapid dissociation of methane hydrate occurred leading to a surge in the vapour phase methane concentration from 15.9 mol% to 42.9 mol%. From B to C lasting from 5 to 262.72 hours (Stage 2), the rate of decomposition of methane hydrate reduced; consequently the rate of increase of vapour phase methane concentration slowed and gradually became relatively stable. From C to D (Stage 3), the system was depressurised in steps releasing more methane from the methane hydrate. Similar trend was observed for Experiment 2, 3, and 4 respectively. Stages 1 and 2 are henceforth referred to as the Kinetic recovery phase while Stage 3 is referred to as the depressurisation recovery phase.

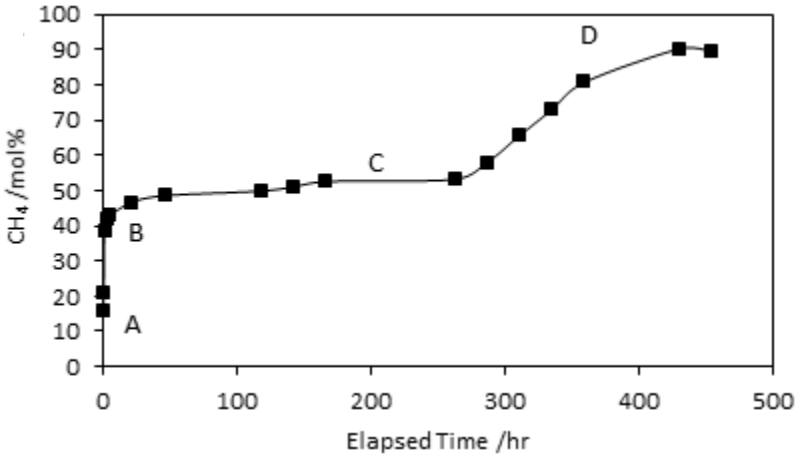

Figure 3.9 *Methane recovery stages after flue gas injection for Experiment 1*

3.5.1.1 Kinetic recovery phase

In the kinetic phase, it was desired to achieve an overall vapour phase composition of 50 mol% methane. This was achieved as the phase boundary shifted in the presence of flue gas from a flue gas rich region to a methane rich region at the set pressure as methane hydrate decomposed. **Figure 3.10** to **Figure 3.13** shows the shifting phase boundaries during the kinetic phase for Experiments 1 - 4 respectively. This phase boundary shift continued as methane hydrate continued to decompose until a new equilibrium is reached corresponding to the set pressure at the experimental temperature. The evolution of the vapour phase methane concentration is shown in **Figure 3.14**. The two methane release trends described in **Figure 3.9** (Stage 1 and Stage 2) is evident in **Figure 3.14.** Vapour phase methane concentration rose from 15.9

mol % to 38.6 mol% in Stage 1, and from 38.6 mol% to 53. 3 mol% in Stage 2 for Experiment 1. For Experiment 2, it rose from 7.6 mol% to 31.6 mol% in Stage 1 and from 31.6 mol% to 49.2 mol% in Stage 2. For Experiment 3, it rose from 11.5 mol% to 35.7 mol% in Stage 1 and from 35.7 mol% to 46.9 mol% in Stage 2. In Experiment 4, vapour phase methane concentration rose from 21.5 mol % to 35.4 mol% in Stage 1, and from 35.4 mol% to 46.8 mol% in Stage 2. A summary of these including the time duration of each stage is shown in **Table 3.5**.

Table 3.5 *Initial and maximum vapour phase methane concentration in stages 1 and 2 of the kinetic recovery phase, experimental conditions, and elapsed time*

					CH_4 /mol%	
Experiment	Recovery Stage	T/K	P/MPa	Time/hr	Initial	Final
1	1	273.2	4.13	0.9	15.9	38.6
	2	273.2	4.13	163.8	38.6	53.3
2	1	278.0	6.89	2.2	7.6	31.6
	2	278.0	6.89	140.9	31.6	49.2
3	1	282.0	11.02	4.2	11.5	35.7
	2	282.0	11.02	186.3	35.7	46.9
4	1	284.0	14.03	2.8	21.5	35.4
	2	284.0	14.03	88.1	35.4	46.8

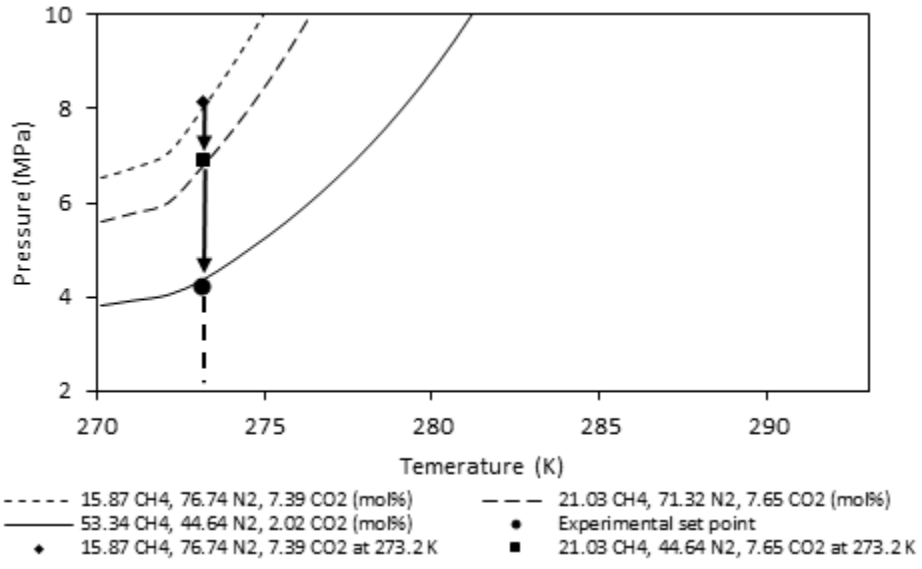

Figure 3.10 *Shifting system phase boundaries for Experiment 1 from flue gas rich region (◆) 15.87 CH_4, 76.74 N_2, 7.39 CO_2 (mol%)) to methane rich region (●) 53.34 CH_4, 44.62 N_2, 2.02 CO_2 (mol%)).*

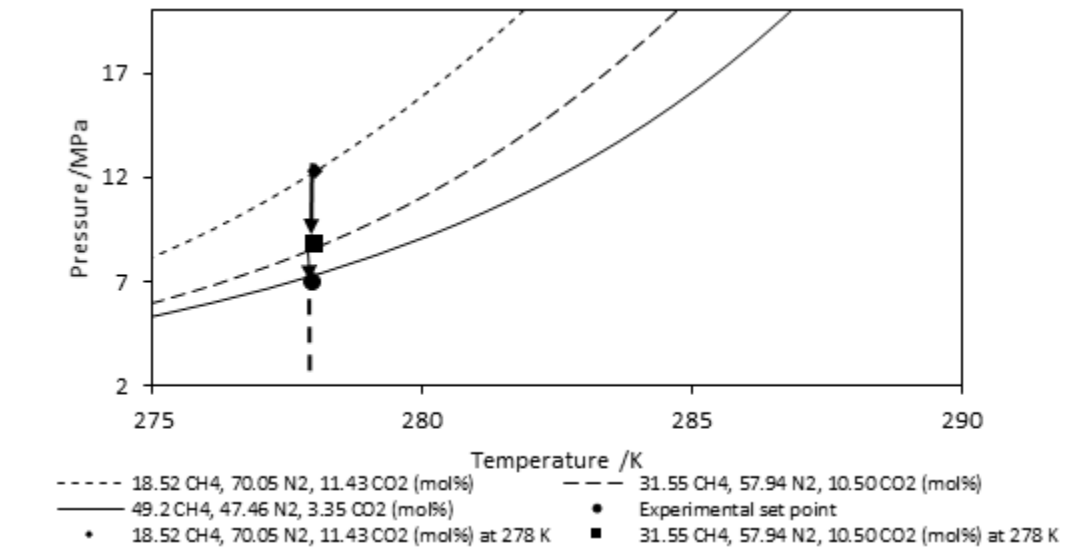

Figure 3.11 *Shifting system phase boundaries for Experiment 2 from flue gas rich region (◆) 18.52 CH_4, 70.05 N_2, 11.43 CO_2 (mol%)) to methane rich region (●) 49.52 CH_4, 47.46 N_2, 3.55 CO_2 (mol%))*

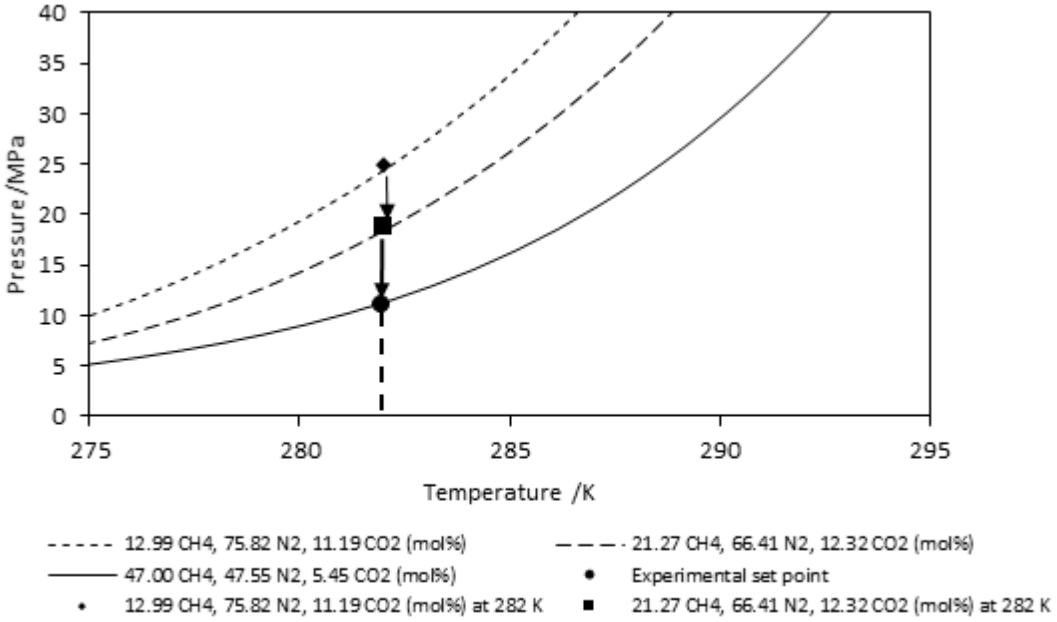

Figure 3.12 *Shifting system phase boundaries for Experiment 3 from flue gas rich region (◆) 12.99 CH_4, 75.82 N_2, 11.19 CO_2 (mol%)) to methane rich region (●) 47.00 CH_4, 47.55 N_2, 5.45 CO_2 (mol%)).*

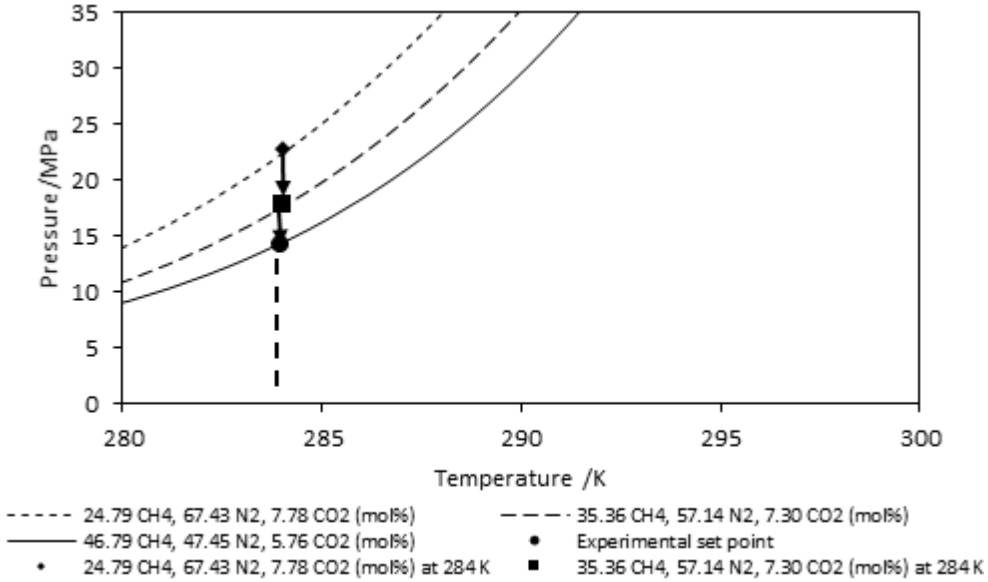

Figure 3.13 *Shifting system phase boundaries for Experiment 2 from flue gas rich region (◆) 24.79 CH_4, 67.43 N_2, 7.78 CO_2 (mol%)) to methane rich region (●) 46.79 CH_4, 47.45 N_2, 5.76 CO_2 (mol%))*

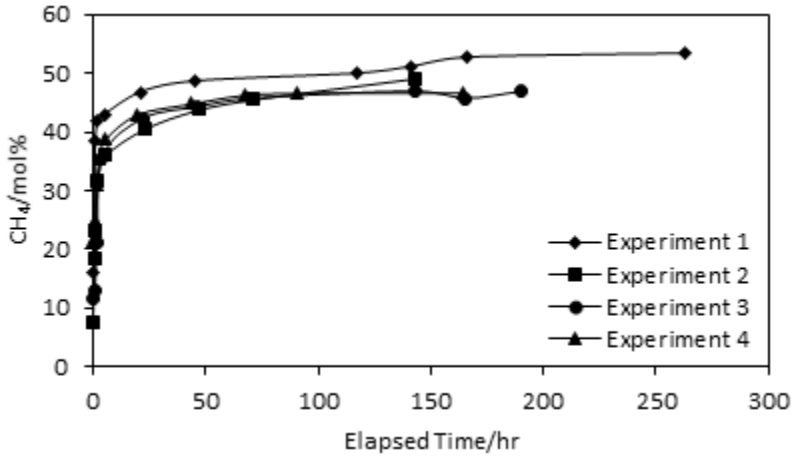

Figure 3.14 *Evolution of the vapour phase methane concentration during the kinetic recovery phase*

3.5.1.2 Kinetics of methane recovery

The vapour phase methane concentrations were used to study kinetics of methane release from the hydrate phase into the vapour phase. **Table 3.6** shows the rate of methane release for stages 1 and 2 of the kinetic recovery phase, amount recovered and percentage recovery in relation to the amount of methane initially in hydrate.

Percentage methane recovery was calculated as follows:

$$\%\ methane\ recovery = \frac{(n_{CH4,G})_t - (n_{CH4,G})_{res}}{(n_{CH4,H})_{tend}} \quad 3.1$$

where $(n_{CH4,G})_t$ is the mole of methane in the vapour phase at any time t during the kinetic recovery phase, $(n_{CH4,G})_{res}$ is the mole of residual methane in the vapour phase at the commencement of the kinetic recovery phase, and $(n_{CH4,H})_{tend}$ is the mole of methane consumed for hydrate formation.

The rate of methane release from the hydrate phase for stages 1 and 2 is given by

$$\frac{dn_{CH4}}{dt} = \frac{(n_{CH4,G})_{t+\Delta t} - (n_{CH4,G})_{t=0}}{\Delta t} \quad 3.2$$

where $(n_{CH4,G})_{t+\Delta t}$ is the mole of methane in the vapour phase at the end of the stage, $(n_{CH4,G})_{t=0}$ is the mole of methane in the vapour phase at the commencement of the stage, and Δt is the time duration of the stage.

Mole of methane in the vapour phase at any time t was estimated by:

$$(n_{CH4,G})_t = y_{CH4}\frac{P_g V_g}{zRT} \quad 3.3$$

where y_{CH4} is the mole fraction of methane in the vapour phase, P_g is the gas pressure, V_g is the gas volume, z is the gas compressibility factor, R is the universal gas constant, and T is temperature.

It is seen from **Table 3.6** that methane release rate was high in stage 1 with values ranging from 0.0544 mol/hr, 0.0565 mol/hr, 0.0894 mol/hr, and 0.101 mol/hr for Experiments 1 to 4 respectively. On the other hand, the rate of methane release was relatively low in stage 2, with values ranging from 0.00018 mol/hr, 0.00049 mol/hr, 0.00061 mol/hr, and 0.00102 mole/hr for Experiments 1 to 4 respectively. This shows two orders of magnitude less than the rate in stage 1.

Table 3.7 to **Table 3.10** shows the cumulative amounts of methane released and their corresponding percentage recovery for Experiments 1 to 4 respectively. Graphical representations of these two values as seen in **Figure 3.15** and **Figure 3.16** shows two distinct trends for both the cumulative amount of methane released and the corresponding percentage recovery. For Experiments 1 and 2 conducted at low temperatures (273.2K and 278K), the amount of methane released from the hydrate phase into the vapour phase is lower, reaching a maximum of 0.280 moles and 0.268 moles respectively. This corresponds to recoveries of 24.9% and 26.9% respectively for Experiments 1 and 2. On the other hand, for Experiments 3 and 4 conducted at higher temperatures of (282K and 284K), the cumulative amount of methane released is considerably higher, reaching a maximum of 0.492 moles and 0.489 moles respectively. This corresponds to recoveries of 71.3% and 84.5% respectively for Experiments 3 and 4. From these observations, it is evident that temperature is an important factor in the kinetics of methane recovery from methane hydrate in porous media.

Hydrate decomposition is an endothermic process; thus, it is expected that higher temperatures favours the kinetics of methane hydrate dissociation. The endothermic nature of hydrate decomposition is seen in **Figure 3.17** which shows the temperature profile with time for the first 5 hours of methane recovery in Experiments 1 and 3. It is seen that within the first 10 minutes, temperature drops. This drop in temperature is accompanied by fast methane release, but the drop-in temperature lasted only a short time as heat transfer from the coolant in the cryostat to the cell returns the cell the experimental temperature. Thus, hydrate decomposition by heat transfer is negligible; moreover, the system is maintained at constant temperature and pressure. Therefore, the continued methane release could be attributed to the difference in the concentration of methane in the hydrate phase and the vapour phase, albeit in the presence of flue gas.

Table 3.6 *Rates of methane recovery, amount recovered, and percentage recovery for at the end of the kinetic phase*

Experiment	T/K	CH_4 release rate /mol/hr		CH_4 initially in hydrate /mole	CH_4 recovered /mole	CH_4 recovery (%)
		Stage 1	Stage 2			
1	273.2	0.0544	0.00018	1.128	0.28	24.9
2	278.0	0.0565	0.00049	1.121	0.278	28
3	282.0	0.0894	0.00061	0.69	0.493	71.3
4	284.0	0.101	0.00102	0.575	0.489	84.5

***Table 3.7**.Methane released, % methane recovery with time, and elapsed time for Experiment 1*

Elapsed Time /hr	CH_4 released /mol	% CH_4 recovery
0.0	0.098	8.7
0.5	0.182	16.2
1.7	0.202	18.0
4.6	0.209	18.6
21.1	0.240	21.3
45.0	0.253	22.5
117.2	0.261	23.2
141.2	0.266	23.6
165.5	0.274	24.4
237.3	0.280	24.9

***Table 3.8**.Methane released, % methane recovery with time, and elapsed time for Experiment 2*

Elapsed Time /hr	CH_4 released/mol	% CH_4 recovery
0.0	0.091	9.1
0.5	0.128	12.8
1.5	0.179	18.0
4.9	0.205	20.6
21.4	0.229	23.1
45.3	0.248	24.9
69.3	0.258	25.9
141.4	0.278	28.0
165.2	0.268	26.9

***Table 3.9**.Methane released, % methane recovery with time, and elapsed time for Experiment 3*

Elapsed Time /hr	CH_4 released/mole	% CH_4 recovery
0.0	0.000	0.0
1.1	0.111	16.0
3.5	0.311	45.1
20.5	0.413	59.9
44.6	0.445	64.4
68.0	0.468	67.8
140.9	0.493	71.3
164.5	0.471	68.3
188.8	0.492	71.3

Table 3.10 *Methane released, % methane recovery with time, and elapsed time for Experiment 4*

Elapsed Time /hr	CH_4 released/mol	% CH_4 recovery
0.0	0.008	1.5
0.6	0.131	22.6
2.0	0.226	39.0
4.8	0.293	50.7
19.2	0.389	67.2
42.6	0.43	74.3
66.6	0.466	80.5
90.1	0.476	82.3
115.5	0.489	84.5

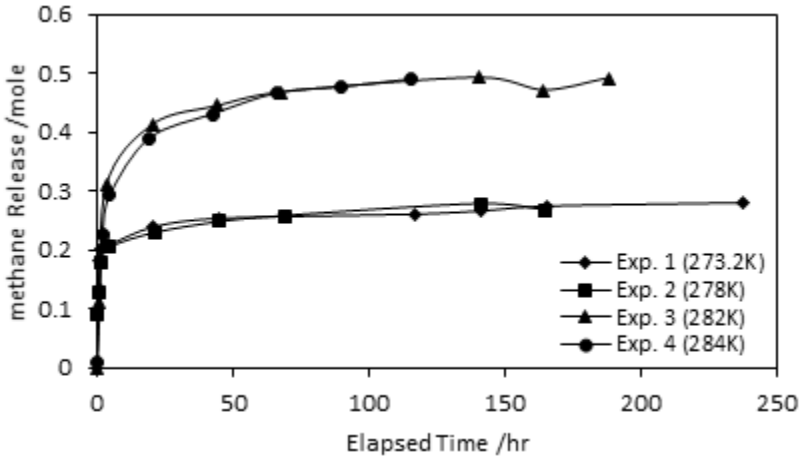

Figure 3.15 *Amount of methane released from the hydrate phase into the vapour phase for Experiments 1 to 4.*

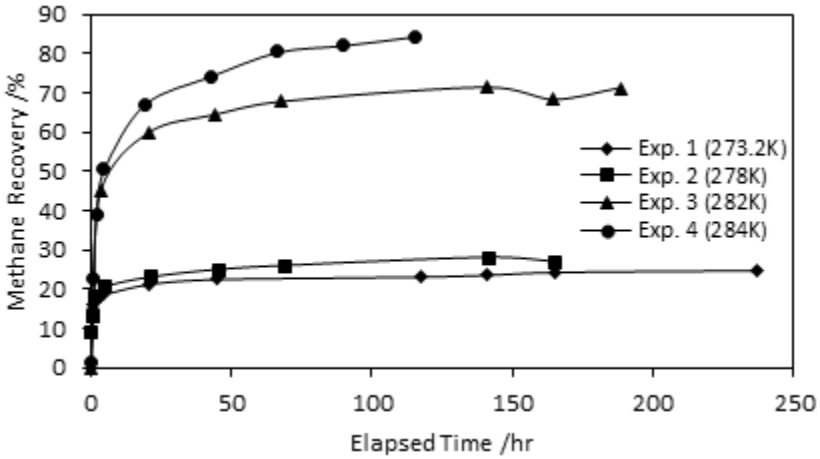

Figure 3.16 *Percentage methane recovery for Experiments 1 to 4.*

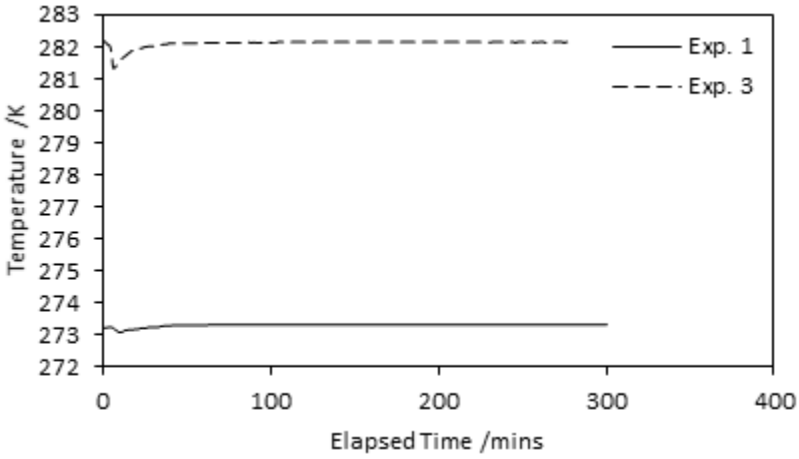

Figure 3.17 *Temperature profile of 0 to 5 hour for Experiments 1 and 3.*

3.5.1.3 Depressurisation

The pressure and temperature conditions in the kinetic recovery phase were set to achieve vapour phase composition of 50:50 mol% methane and flue gas. As described in **Section 3.4.5**, depressurisation was initiated at the end of the kinetic phase to enhance methane recovery from methane hydrate. A steady increase in the vapour phase methane concentration was observed as shown in the lower part of **Error! Reference source not found.** to **Error! Reference source not found.** in **APPENDIX C** for Experiments 1 to 4 respectively and peaked at 90.5 mol%, 89.7 mol%, 66.8 mol% and 48.2 mol% respectively as shown in **Table 3.11**. **Figure 3.18** illustrates methane recovery during depressurisation in the presence of flue gas. The dotted vertical lines represent methane hydrate dissociation pressures at the corresponding experimental pressures. It is seen that in the presence of flue gas, methane hydrate decomposed well inside the methane hydrate stability zone (MHSZ) as shown by the continued increase in vapour phase methane concentration before the methane hydrate decomposition pressure is reached. For instance, depressurising in the presence of flue gas achieved a vapour phase methane concentration of 65.7 mol% at 3.5 MPa, 0.75 MPa above the dissociation pressure of 2.75 MPa at 273.2 K (Experiment 1), 60 mol% was achieved at 5.11 MPa, 0.8 MPa above methane hydrate dissociation pressure of 4.31 MPa at 278 K (Experiment 2), 55 mol% was achieved at 7.77 MPa, 1.35 MPa above methane hydrate dissociation pressure of 6.42 MPa at 282 K (Experiment 3). In Experiment 4, methane hydrate was almost completely decomposed during the kinetic recovery phase. Thus, no significant increase in vapour phase methane concentration was observed before the

system pressure was reduced below the methane hydrate dissociation pressure of 7.9 MPa at 284 K.

From the foregoing, it is evident that flue gas injection leads to methane hydrate decomposition at pressures well above the methane hydrate dissociation pressure at given temperatures. This showcases the possibility of reducing the extent of depressurisation in hydrate reservoirs to dissociate methane hydrate. Reduced depressurisation consequently leads to reduced pressure difference (drawdown) between the reservoir and the production well, hence reducing the driving force for water and fines migration. Moreover, the extra pressure reduces/eliminates the need for external pumps to lift the produced water to allow for gas flow [117, 192]. This could substantially improve the feasibility of the depressurisation method for gas hydrate reservoirs with severe conditions such as low permeability Class 1 hydrate reservoirs, Classes 2 and 3 hydrate accumulations that are deep inside the hydrate stability zone, and hydrate reservoirs with disperse hydrate accumulations [58].

Table 3.11 *Depressurisation pressure range, initial and final vapour phase methane concentration during the depressurisation phase.*

Experiment	T/K	Depressurisation P/MPa	CH_4/mol% Initial	Final
1	273.2	4.13-1.03	53.3	90.5
2	278.0	6.89-1.72	49.2	89.7
3	282.0	10.96-3.10	47.0	66.8
4	284.0	14.03-3.45	46.8	48.2

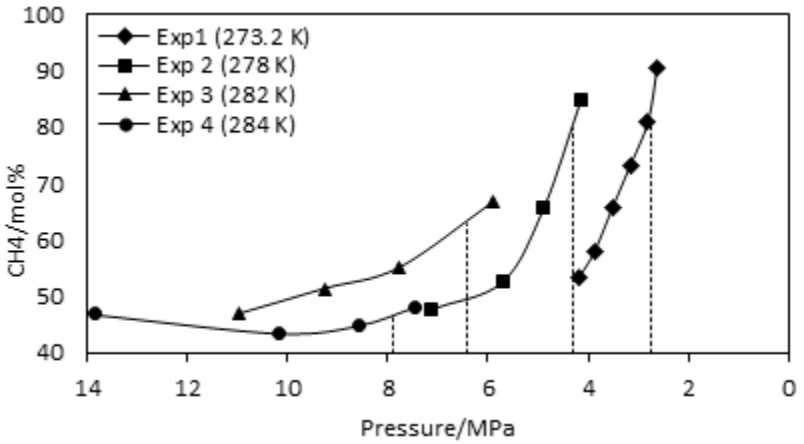

Figure 3.18 *Vapour phase methane concentration during depressurisation in the presence of flue gas. Dotted vertical lines represent decomposition pressure of methane hydrate at the experimental temperatures. Methane hydrate starts to decompose well inside the methane hydrate stability zone.*

3.5.2 CO_2 sequestration

The potential of flue gas injection method for CO_2 capture and storage in gas hydrate reservoirs was studied. The ratio $CO_2/(CO_2+N_2)$ shown in **Error! Reference source not found.** to **Error! Reference source not found.** in **APPENDIX C** and in **Figure 3.19** is an indicator of the absolute quantity of CO_2 in the vapour phase. This enables the determination of CO_2 involved in the formation of CO_2-hydrate or CO_2-mixed hydrate. The possible mixed hydrates that could be formed are CO_2-CH_4 hydrate, and N_2-CO_2-CH_4 hydrate. The vapour phase concentrations of CO_2, nitrogen, and methane are plotted in **Figure 3.19** to study the kinetics if CO_2-involved hydrate formation.

In Stages 1 and 2 methane hydrate dissociated continuously as its phase equilibrium was broken by the injected flue gas. Release of methane from the hydrate phase into the vapour phase reduces the concentration of CO_2 and nitrogen in the vapour phase. Also, the ratio $CO_2/(CO_2+N_2)$ reduced continuously in Stages 1 and 2. This shows that the amount of CO_2 in the vapour phase is reducing due to its conversion to hydrate. The amount of CO_2 reduced to its minimum at the end of Stage 2 when the system reached a new thermodynamic equilibrium. In contrast, in Stage 3 during depressurisation, the ratio $CO_2/(CO_2+N_2)$ continuously increased indicating that the vapour phase CO_2 content is increasing, especially in Experiments 1 to 3. This suggests the decomposition of the CO_2 mixed hydrates formed in Stages 1 and 2. The N_2-CO_2-CH_4 hydrate would be decomposed before the system was depressurised out of the methane HSZ, on the other hand, CO_2-CH_4 hydrate would not completely dissociate until the system was depressurised outside the CO_2 HSZ. However, observing the methane concentration curves in **Figure 3.19**, the maximum methane concentrations, 90.5 mol% (2.62 MPa, 273.2K) observed at the second to the last point in **Figure 3.19 (a)** for Experiment 1, 89.7 mol% (2.99 MPa, 278K) observed at the third to the last point in **Figure 3.19 (b)** for Experiment 2, 66.8 mol% (5.88 MPa, 282K) observed at the fourth to the last point in **Figure 3.19 (c)** for Experiment 3, and 46.79 mol% (13.87 MPa, 284K) observed at the fourth to the last point in **Figure 3.19 (d)** for Experiment 4 shows that methane hydrate and CO_2-CH_4 mixed hydrate were completely dissociated at those points. Maximum CO_2 concentration 4.99 mol% (0.85 MPa, 273.2K), 5.1 mol% (1.72 MPa, 278K), and 7.61 mol% (3.79 MPa, 282K) was observed at the last points on the CO_2 curves of **Figure 3.19 (a)**, **(b)** and **(c)** for Experiments 1 to 3 respectively. These points were outside the CO_2 HSZ and indicate the complete decomposition of CO_2-

hydrate. Such rise in vapour phase CO_2 concentration was not observed in Experiment 4 (**Figure 3.19 (d)**) as evident in the relatively constant CO_2 concentration profile and the ratio $CO_2/(CO_2+N_2)$. Experiment 4 temperature was set just outside the CO_2-hydrate phase boundary (**Figure 3.4**), thus there was little or no CO_2- or CO_2-mixed hydrate.

Table 3.12 shows the amount of CO_2 in the vapour phase captured as CO_2 hydrates. The amount of CO_2 sequestered, which is the difference between the amounts of CO_2 at the beginning and at the end of the kinetic phase is 0.0252 mole, 0.0384 mole, and 0.0659 mole for Experiments 1 to 3 corresponding to 70.4%, 68.5%, and 48.1% of CO_2 in the vapour phase at the beginning of the kinetic phase. For Experiment 4, the difference between the amounts of CO_2 at the beginning and at the end of the kinetic phase is 0.0191mole corresponding to 14.8% of CO_2 at the start of the kinetic phase. This further confirms that there is little or no CO_2 sequestration in Experiment 4.

The CO_2 hydrate formation, aside the benefit of capturing and storing CO_2 from flue gas in the hydrate reservoir formation, it could also reduce the impact of methane hydrate decomposition on wellbore and seafloor stability. The results further suggest that (reservoir) conditions in terms of the CO_2 HSZ plays a significant role in CO_2 capture and sequestration from flue gas. The deeper the condition inside the CO_2 HSZ, the stronger the driving force to promote the formation of more CO_2 hydrate, CO_2-CH_4 hydrate, and N_2-CO_2-CH_4 hydrate. Considering also the sharp turn in the CO_2 hydrate phase boundary at about at about 282 K, it can be suggested that hydrate reservoirs at low temperatures are better choices for CO_2 capture and storage by flue gas injection technique.

(a)

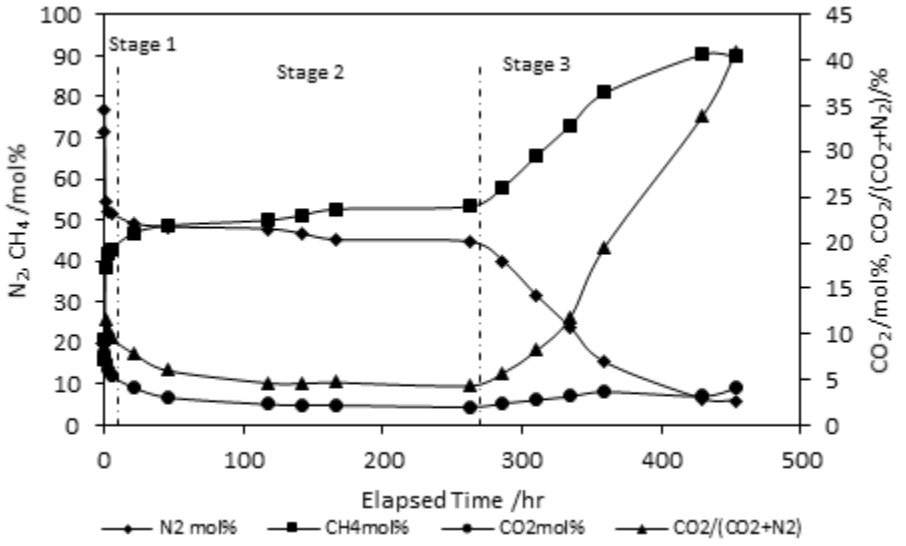
Stage 1
Stage 2
Stage 3
N_2, CH_4 /mol%
CO_2/mol%, $CO_2/(CO_2+N_2)$/%
Elapsed Time /hr
N2 mol%
CH4mol%
CO2mol%
CO2/(CO2+N2)

(b)

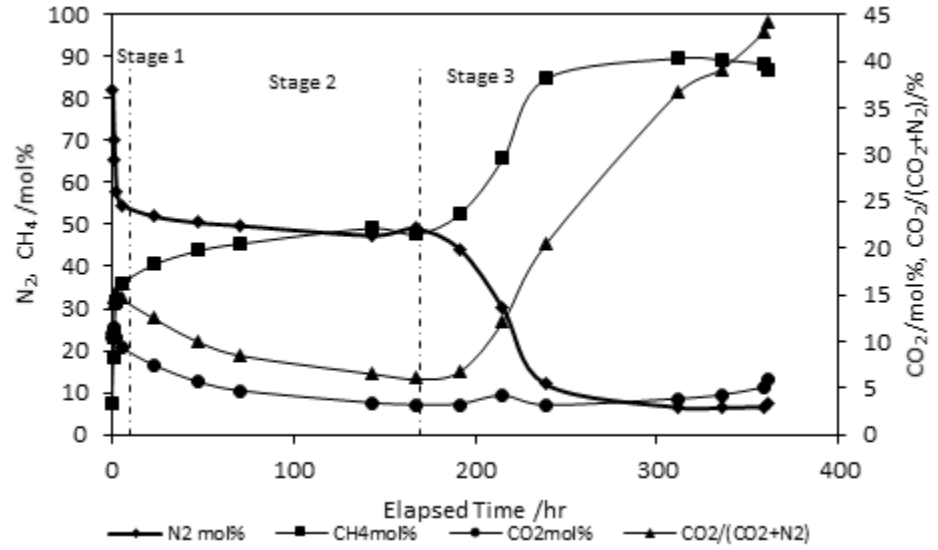
Stage 1
Stage 2
Stage 3
N_2, CH_4 /mol%
CO_2/mol%, $CO_2/(CO_2+N_2)$/%
Elapsed Time /hr
N2 mol%
CH4mol%
CO2mol%
CO2/(CO2+N2)

(c)

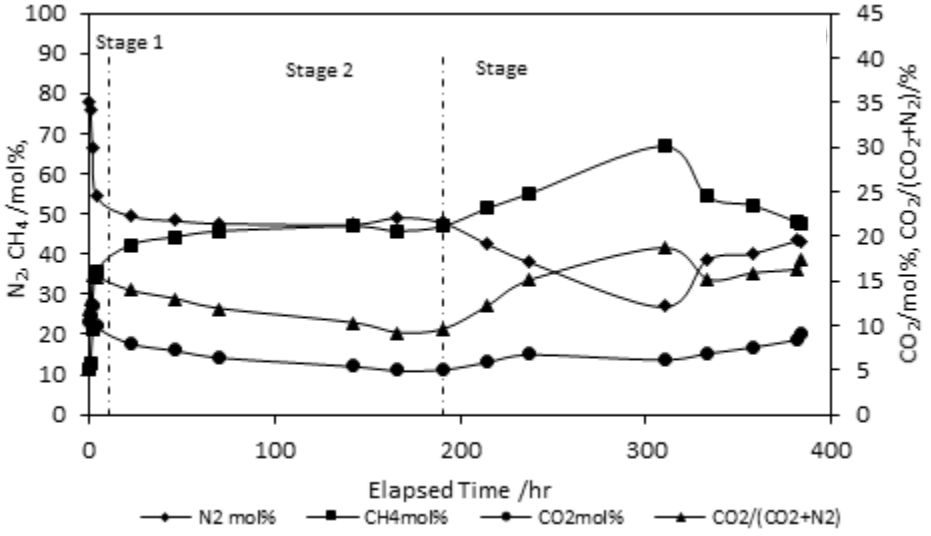
Stage 1
Stage 2
Stage
N_2, CH_4 /mol%,
CO_2/mol%, $CO_2/(CO_2+N_2)$/%
Elapsed Time /hr
N2 mol%
CH4mol%
CO2mol%
CO2/(CO2+N2)

(d)

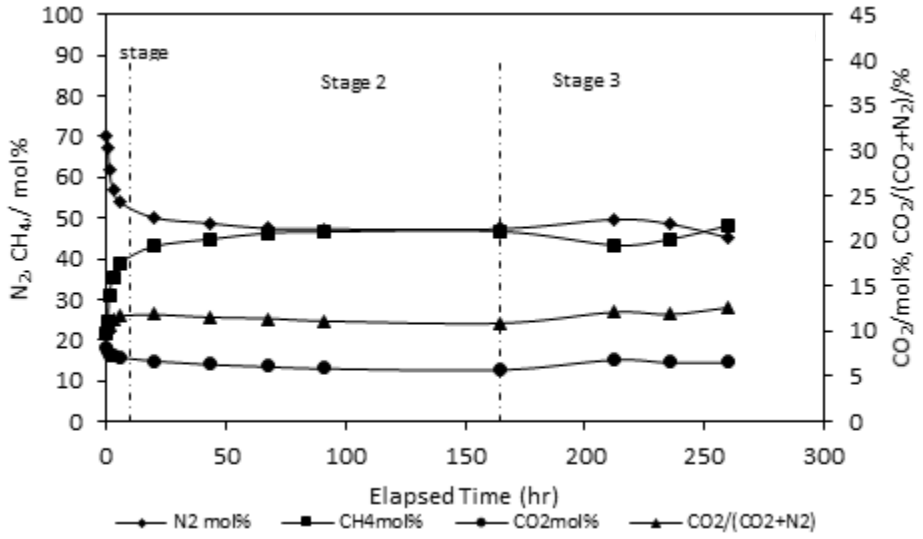

Figure 3.19 *Vapour phase concentrations of methane, nitrogen, and CO_2 after flue gas injection and during depressurisation. The ratio $CO_2/(CO_2+N_2)$ shows the absolute content of CO_2 in the flue gas component of the vapour phase at any instant. (a), (b), (c) and (d) represent Experiments 1, 2, 3 and 4 respectively.*

Table 3.12 *Amount of CO_2 in the vapour phase captured and stored as hydrates.*

Experiment		CO_2 in vapour phase/mole		CO_2 in hydrate	
	T/K	Initial	Final	phase/mole	%
1	273.2	0.0358	0.0106	0.0252	70.4
2	278.0	0.0561	0.0177	0.0384	68.5
3	282.0	0.1369	0.071	0.0659	48.1
4	284.0	0.1287	0.1096	0.0191	14.8

3.6 Summary

The feasibility of methane recovery and CO_2 sequestration by flue gas injection into methane hydrate reservoirs was demonstrated. Four experiments were conducted within the temperature range of 273.2 K to 284 K and pressure range of 4.2 MPa to 13.8 MPa to cover the typical methane hydrate reservoir conditions. Experiments 1, 2, and 3 were conducted inside both the methane and CO_2 HSZs while Experiment 4 was conducted inside the methane HSZ but slightly outside the CO_2 HSZ. Flue gas injection resulted in rapid dissociation of methane hydrate by shifting the methane hydrate stability zone.

The kinetic recovery phase enabled the study of methane recovery rates in the presence of flue gas. Two recovery trends were observed in this phase; a fast methane release stage lasting only a few hours occasioned by rapid methane hydrate decomposition, and a slow methane release stage lasts for a longer time as the system approaches a new

thermodynamic equilibrium. These trends were evident in the vapour phase methane concentrations, calculated cumulative amount of methane release, and the corresponding percentage methane recovery. The vapour phase methane concentrations reached about 50 mol% in the four experiments within the typical methane hydrate reservoir conditions.

Temperature effect was significant in both methane hydrate formation and methane recovery. Given approximately same pressure and temperature at the start of hydrate formation, higher hydrate saturations were achieved for Experiments 1 and 2 conducted at 273.2 K and 278 K respectively while lower hydrate saturations were achieved for Experiments 3 and 4 conducted at 282 K and 284 K respectively. For methane recovery, recoveries for Experiments 3 and 4 conducted at higher temperatures were higher than those of Experiments 1 and 2 conducted at low temperatures. Thus, high temperature favours the thermodynamics as well as the kinetics of methane recovery.

Further depressurisation in the presence of flue gas enhanced methane recovery. Vapour phase methane concentration reached up to 80 mol% depending on the experimental temperature and pressure. Depressurisation in the presence of flue gas enabled methane hydrate decomposition resulting in methane-rich vapour phase at pressures above the methane hydrate dissociation pressures at the experimental temperature. The CO_2 component of the flue gas formed CO_2-hydrate and CO_2 mixed hydrates including N_2-CO_2-CH_4 hydrate and CO_2-CH_4 hydrate during methane recovery after flue gas injection. Up to 70% of CO_2 in the vapour phase was converted and stored in the sediment as hydrates depending on the experimental temperature and pressure.

It is concluded that the technique has considerable potential to improve the economic viability of methane recovery from gas hydrate reservoirs and CO_2 capture and storage as hydrates in geological formations.

CHAPTER 4 INFLUENCE OF WATER SALINITY ON METHANE RECOVERY BY FLUE GAS INJECTION

4.1 Introduction

Formation of gas hydrates requires the presence of suitable guest gas molecules, high pressure and low temperature environment, and most importantly water. Gas hydrates in nature occurs in permafrosts and marine sediments. Available water in these environments is saline and could have significant impact on the formation, morphology, distribution and saturation of gas hydrates, and consequently, also on the dissociation behaviour of the gas hydrates. The most common salt in the formation water is NaCl. The inhibition effect of salt to hydrate formation is well reported [193–195]. Hydrate inhibition by salt is a function of the degree of ionisation, and the number of ions formed by each salt molecule and this further depends on the type and concentration of the salt [196, 197]. These ions interact and interfere with the hydrogen bonds with water molecules thereby reducing the activity of water and its ability to form water cages in which the guest gas molecules are hosted. The effect of varying concentrations of NaCl on the equilibrium phase boundary have been reported by many authors [198–204]. Tohidi et al. [196] studied the effect of salt on the equilibrium concentration of gas components of a hydrate system. They observed that the presence of salt reduces the solubility of methane, and inhibit hydrate formation. They showed that the H-L_w-L_v curve for a 3.5 mass% NaCl solution is at a lower temperature compared to pure water.

All the earlier referenced works were exclusively for hydrae formation and dissociation in bulk phase. For a better understanding of methane recovery from natural gas hydrate reservoirs, it is necessary these studies be extended to porous media. Hydrate formation characteristics is markedly different in porous media compared to bulk solutions. Besides heat and mass transfer that is common to bulk phase and porous media, other possible reasons could be due to the interactions between the fluid molecules and the hydrophilic mineral surface, and the energy required to maintain capillary equilibrium [187]. Also, properties such as particle size, pore size distribution, pore volume, porosity, and permeability also affects hydrate formation in porous media [201–206].

A few studies on the influence of salinity on hydrate formation and dissociation in porous media have been reported in open literature. Husebo et al. [207] studied methane hydrate formation in sandstone cores partially saturated with varying degrees of salinity.

They reported that salinities lower than regular seawater levels show a significant impact on the fill fraction of methane hydrate in porous media. For salinities higher than regular seawater, the drop in fill fraction is significant. Mekala et al. [208] in their study of formation and dissociation kinetics of methane hydrate formation in seawater and silica sand observed a 72% water conversion to hydrate with pure water, and only 11.6% water conversion to hydrate for seawater. They concluded that the presence of salt in porous, besides being a thermodynamic inhibitor, could also act as a kinetic inhibitor based on the observed reduced rate of hydrate formation. Yang et al. [182] conducted similar experiment using CO_2. They also observed a reduced water conversion to CO_2-hydrate in the presence of salt. They further noted that the presence of salt show no kinetic inhibition during hydrate formation but had a slight impact on dissociation kinetics.

The level of salinity in a natural gas hydrate reservoir increases with depth [207]. Furthermore, the stability of natural gas hydrates in reservoirs also depends amongst other factors on the surrounding fluids. For instance, in subsea environments, sediment are normally highly saturated with seawater [196], whereas in permafrost sediments, water saturation is only partial. Therefore, this chapter investigates the impact of varying degrees of salinity on hydrate formation and more importantly, its effect on methane recovery in the presence of flue gas. Additionally, the impact of water saturation was investigated by conducting experiments using both excess gas and excess water methods of hydrate formation.

4.2 Experimental Section

4.2.1 Experimental apparatus

Excess gas tests

The experimental rig for experiments conducted with the excess gas hydrate formation method is similar to that described in **Section 3.2**. The modification made was the disconnection of the Quizix pump as there was no need for pressure maintenance in these experiments. The modified rig is shown in **Figure 4.1**.

Excess water tests

For excess water hydrate formation tests, the Quizix pump was connected to the cell via two additional lines to the bottom and top of the cell through valves V6 and V7 as shown in **Figure 4.2**. The purpose of the Quizix pump was to inject water into the sediment in the cell.

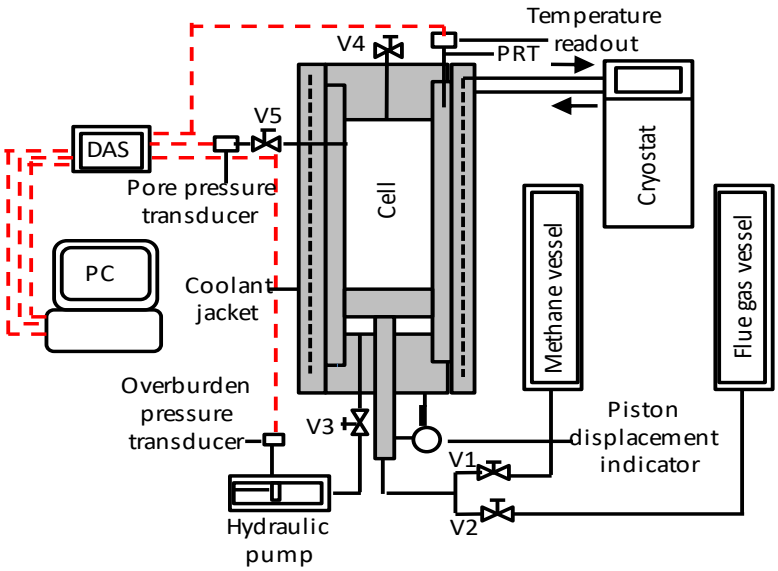

Figure 4.1 *Schematic diagram of experimental rig for the excess gas method. The dashed red lines represent cables for electronic communications while the black solid lines represent conduits for fluid flow.*

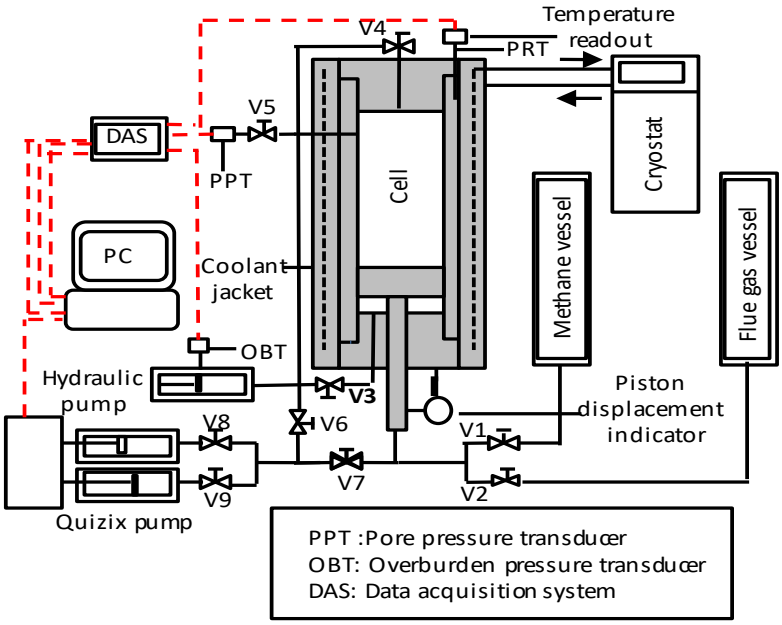

Figure 4.2 *Schematic diagram of experimental rig for the excess water method. The dashed red lines represent cables for electronic communications while the black solid lines represent conduits for fluid flow.*

4.2.2 Experimental materials

Methane gas, flue gas, water, and silica sand used in these experiments are as described in **Section 3.3** of **CHAPTER 3**.

4.2.3 Experimental procedure

4.2.3.1 Test conditions

Table 4.1 is a summary of experimental conditions. Experiments 5, 6, 7 were conducted using the excess gas method for methane hydrate formation with water salinities of 0, 3, and 10 NaCl wt % respectively. Experiments 8, 9, and 10 were conducted using the excess water hydrate formation method with water salinities also of 0, 3, and 10 NaCl wt % respectively.

Table 4.1 *Summary of experimental conditions*

Experiment	Hydrate Formation Method	Temperature (K)	Pressure (MPa)	Salinity (NaCl wt%)
5	Excess gas	273.2	4.0	0
6		273.2	4.2	3
7		273.2	8.5	10
8	Excess water	273.2	10.3	0
9		273.2	10.4	3
10		273.2	10.3	10

4.2.3.2 Sample preparation

Flue gas synthesis and partially water saturated sand preparation were as described in **Sections 3.4.2.1** and **3.4.2.2** of **CHAPTER 3**.

4.2.3.3 Methane hydrate synthesis

Methane hydrate formation for the varying degrees of water salinity for the excess gas method follows the same procedure as described in **Section 3.4.3**. Methane hydrate formation using excess water method follows a different procedure and is described in the following paragraphs.

In the excess water methane hydrate formation method, the dried silica sand was loaded into the cell in batches of small quantities and thumped after each batch to ensure there

are no cavities in the sediment. The sediment quantity was chosen such that when completely loaded into the cell, it is just at the same position as the top cap when the system is covered. The cell was then sealed and vacuumed. To compact the sediment, an overburden pressure of 3.5 MPa was applied by injecting fluid behind the piston through valve V3 (**Figure 4.2**) with the aid of the hydraulic hand pump. The desired amount of methane was then injected into the cell through valve V1. Next, the prepared salt solution was injected into the cell with the aid of the Quizix pump set at a constant rate delivery (CRD) of 3 ml/min to reach the desired target pressure of 10.34 MPa. The salt solution was injected from top and bottom (valves V6 and V7 in **Figure 4.2**) alternately to ensure even distribution. When the desired target pressure was reached, the Quizix pump was set to constant pressure delivery (CPD) to maintain the system at the target pressure. The system was left overnight to ensure complete water saturation. The cell temperature was then set to 273.2 K to initiate hydrate formation and Quizix pump data logging was commenced while the pump is still set at CPD to maintain a constant pressure of 10.34 MPa by injecting salt solution into the cell. The rate of methane consumption and hydrate formation is monitored by the rate of water injection into the cell. This rate was initially high indicating hydrate formation. Hydrate formation was deemed to be complete when the change in the rate of water injection became negligible. The process lasted for 7-14 days. Upon the completion of hydrate formation, the Quizix pump is disconnected from the cell by shutting off valves V6 and V7.

4.2.3.4 Flue gas injection and methane recovery

The flue gas injection following the completion of hydrate formation and methane recovery follows the same procedure as described in **Sections 3.4.4 and 3.4.5** respectively.

4.3 Results and Discussions

A series of six experiments were planned to study the impact of water salinity on the formation of methane hydrate and consequently on the methane recovery in the presence of flue gas. Hydrate formation was conducted using both the excess gas method and the excess water method to simulate limited water environment such as permafrost sediments and excess water environments such as marine sediments. **Table 4.2** shows the properties and initial parameters of the sediment samples before flue gas

injection including porosity ϕ, hydrate saturation S_h, remaining methane gas saturation S_g and remaining water saturation S_w.

Table 4.2 *Properties and initial parameters of the hydrate bearing sediment samples*

Experiment	5	6	7	8	9	10
Height (cm)	14.69	14.69	14.34	14.7	14.85	14.6
Diameter (cm)	7.5	7.5	7.5	7.5	7.5	7.5
Volume (cm^3)	649.29	645.52	633.51	649.75	655.99	645.11
Porosity (vol%)	43.6	44.7	52.8	40.28	39.4	50.9
Dry mass (g)	1076.6	1076.6	1076.6	1076	1076	1076
Grain density (g/cm^3)	2.64	2.64	2.64	2.64	2.64	2.64
Wet mass (g)	1231.8	1231.8	1231.8	-	-	-
Initial water saturation (mass%)	14.4	14.4	14.4	-	-	-
Wet density (g/cm^3)	1.89	1.9	1.94	-	-	-
Hydrate saturation (vol%)	44.7	45.8	37.2	29.8	21.8	7.5
Gas saturation (vol%)	35.8	37.1	44.9	31.1	24.4	37.1
Water saturation (vol%)	19.5	17.1	17.9	39.1	53.8	55.4

4.3.1 Formation behaviour of methane hydrate in water and NaCl solutions

As stated in **Section 2.3**, hydrate formation is a two-stage process: hydrate nucleation and hydrate growth. Hydrate nucleation is exothermic; thus, nucleation events are identified by a sharp rise in temperature of the hydrate forming system.

Figure 4.3 shows the temperature and pressure profiles of the hydrate forming systems in excess gas environment and varying degree of water salinity. For hydrate formation in pure water system (0 mass% NaCl solution), significant nucleation event was observed as shown by the sustained spike in the temperature profile *(T1)* from 100 to 170 hr. A short period of nucleation was observed for the system with 10 mass% NaCl *(T3)* from 0 to 50 hr. No significant spike in temperature was observed for the system with 3 mass% NaCl *(T2).* This may be due to inadequate insensitivity of the thermal probe suggesting slow hydrate formation. The pressure profiles *P1*, *P2*, and *P3* is indicative of gas uptake during the hydration formation experiments for systems with 0, 3, and 10 mass% NaCl respectively. The high drop in pressure profile *P1* shows that gas uptake in the pure water system was very significant, and reduces with increasing salinity as seen in *P2* and *P3* for systems with 3 and 10 mass% NaCl respectively.

Further comparison for methane hydrate formation with pure water and saline solutions were made based on methane hydrate growth rate as shown in **Figure 4.4**. Two trends were observed in the growth rate: a high rate of formation at early time followed by a period of slow growth marked by a change in slope of the curve. Change in slope was observed at 4 days for the pure water system and at 2 days for both saline systems. After the change in slope, hydrate growth rate was significantly lower for pure water system than for saline systems. For experiment with 3 mass% NaCl, a sustained high growth rate was observed from day 2 to day 4, then reduced tending to same rate as that of 10 mass% NaCl from day 6 onward. The sustained high rate of hydrate growth consumed water thereby increasing the salinity of the remaining water as reported by Husebo [207] consequently causing the growth rate to be identical to that of 10 mass% NaCl.

These observations suggest that the presence of salt (NaCl) causes kinetic inhibition in hydrate forming systems. These observations has also been reported by Dholabhai et al. [209] for bulk systems and by Chong et al. [210] for porous media. The presence of salt (NaCl) in the aqueous phase causes a mass transfer resistance between the gas phase and the aqueous phase as water molecules cluster around the ions of the salt, causing a salting-out effect. This reduces the solubility of the gas in water thereby suppressing hydrate nucleation and growth.

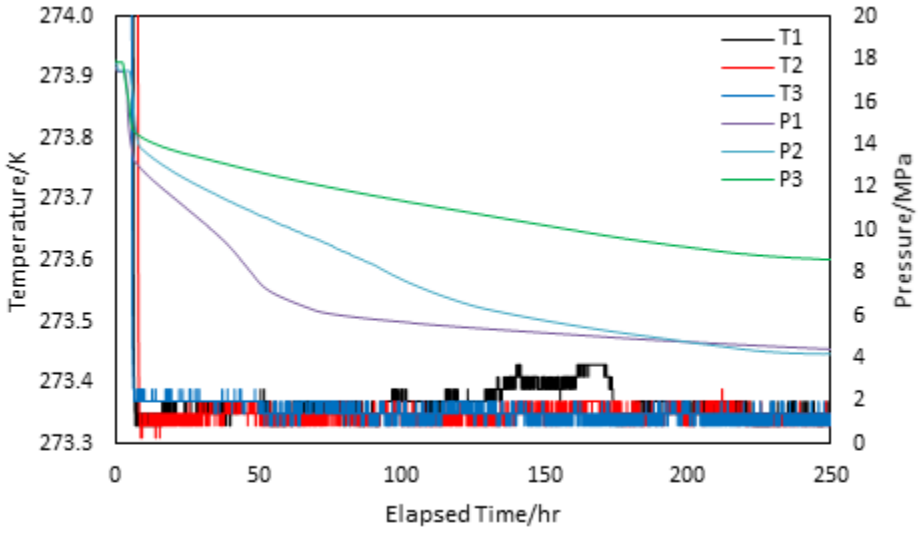

Figure 4.3 *Temperature and pressure profiles of methane hydrate formation during Experiments 5, 6, and 7 respectively. T1, T2, T3 and P1, P2, P3 represents temperature and pressure profiles for systems with 0, 3, and 10 mass% NaCl respectively.*

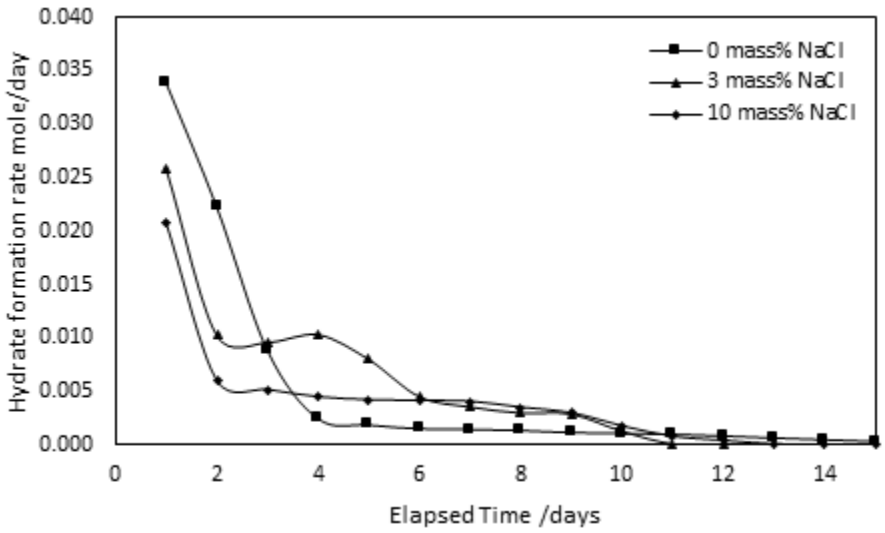

Figure 4.4 *Hydrate formation rates for systems with 0, 3, and 10 mass% NaCl solution.*

For hydrate formation in excess water environment, the rate water injection into the system was used as an indicator for gas consumption and hydrate growth. **Figure 4.5** shows the water injection rate with time during hydrate formation. Similar trend was observed as with excess gas environment; a high injection rate at initial time signifying high gas uptake followed by a period of relatively low injection rate. As expected, significantly higher gas uptake was observed for the system with pure water (0 mass% NaCl) compared with 3 and 10 mass% NaCl systems showing hydrate inhibition activity of salts.

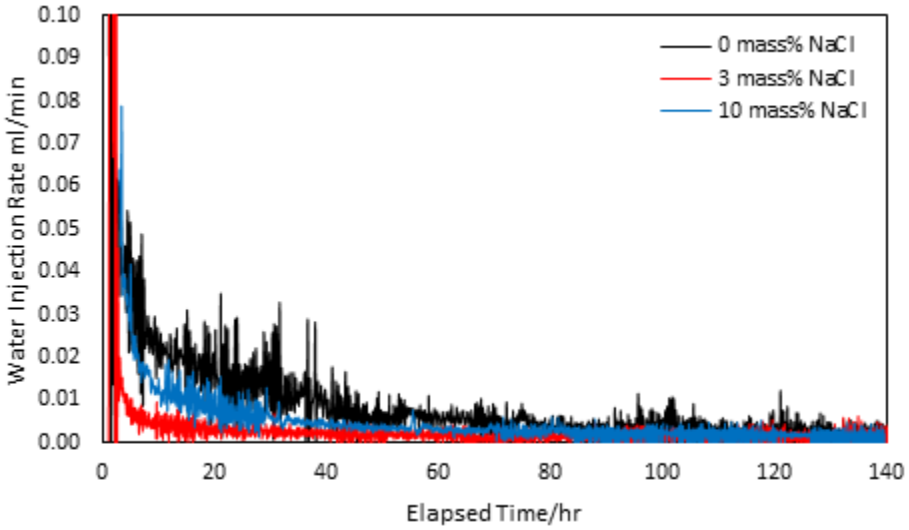

Figure 4.5 *Water injection rates for hydrate formation in excess water environment during Experiments 8, 9, and 10 respectively.*

Figure 4.6 shows quantitatively the conversion of methane to hydrate as a percentage of the amount of the amount of methane gas injected for hydrate formation. It is seen that for excess gas and excess water methods, the presence of 3 mass% NaCl in the aqueous phase has only a slight impact on the conversion of methane to hydrate as comparable conversions of 82.1% and 80.9% were achieved for systems with 0 and 3 mass% NaCl respectively for the excess gas method and 54.9% and 53.1% respectively for the excess water method. This may be attributable to the phenomenon observed in **Figure 4.4** where for 3 mass% NaCl system, a sustained high hydrate growth rate from day 2 to day 4. It is believed that this increased methane conversion to hydrate substantially before the system became excessively saline due to water consumption, decreasing the activity of water which consequently limits further hydrate formation. For the 10 mass% NaCl system, a significant drop in the methane conversion to hydrate was observed as evidenced by 53.6% and 29.5% conversion for excess gas and excess water environments respectively. This is due to the concentration of the salt (NaCl) ions being high enough that the water is more stable as liquid water than hydrate water.

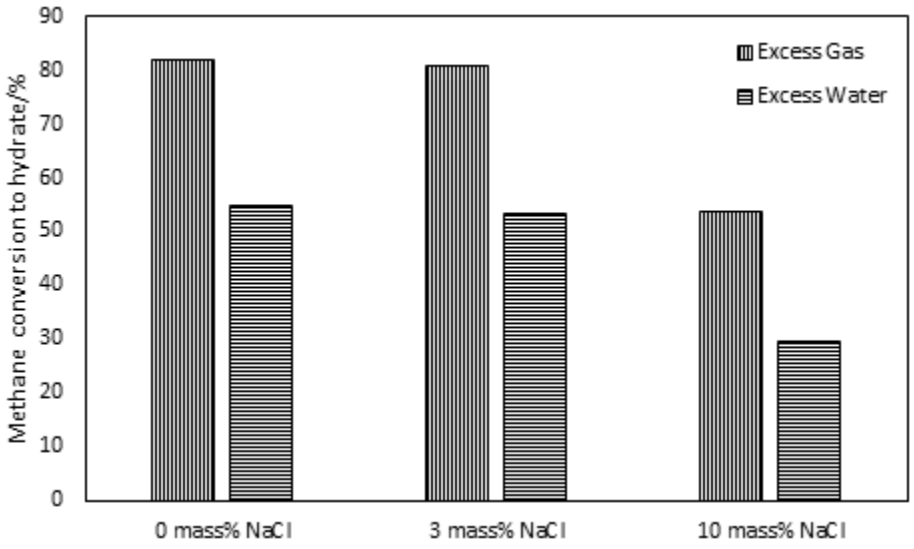

Figure 4.6 *Methane conversion to hydrate for excess gas and excess water hydrate formation methods with varying degrees of water salinity.*

4.3.2 Decomposition kinetics

The vapour phase composition was used to monitor the decomposition of methane hydrate after flue gas injection. The vapour phase compositions for experiments 5 – 10 are shown in Error! Reference source not found. to Error! Reference source not found. in **APPENDIX D**. The typical kinetic process of methane hydrate decomposition is

described as shown in **Figure 3.9**. Similar trends as reported in **Section 3.5** were observed. **Figure 4.7** shows the evolution of vapour phase methane concentration after flue gas injection. Methane hydrate dissociated rapidly in the first 5 hours leading to a high increase in the vapour phase methane concentration of 48.4, 46.6, 48.9 mol% for Experiments 5, 6, 7 and 65.6, 84.5, 83.1 mol% for experiments 8, 9, 10. This was followed by a phase of slow decomposition lasting about 60 hours. Vapour phase methane concentrations of 51.7, 51.5, 54.6 mol% and 59.5, 85.9, 88.6 mol% were achieved for Experiments 5, 6, 7 and 8, 9, 10 at the end of this phase. For the experiments with excess gas, the vapour phase methane compositions for systems with 0 and 3 mass% NaCl are identical. This implies that the presence of 3 mass% NaCl in the aqueous phase has no significant impact on methane hydrate decomposition. However, for the system with 10 mass% NaCl in the aqueous phase, slightly higher vapour phase methane compositions were achieved. This may be attributed to the reduced hydrate saturation achieved due to strong inhibition during hydrate formation. For the experiments with excess water, as the name implies, excess water environments limit the amount of methane gas available for hydrate formation. Consequently, lower saturations of 29.8, 21.8, and 7.5% were achieved for 0, 3, and 10 mass% NaCl respectively. It is also seen that for the excess water system, vapour phase methane concentration for the saline systems are significantly higher than for the pure water system. It has been shown that at low hydrate saturations, methane hydrate decomposition by flue gas is extremely fast as seen in Experiments 3 and 4 in contrast to slightly slower decomposition observed for higher saturations. Overall, a comparison of vapour phase methane achieved in both environments shows that methane concentrations in the excess gas environments are generally lower than those in excess water environments. As discussed earlier, this is still due to reduced hydrate saturation in excess water environment and its consequent ease of decomposition arising from such low saturations.

Table 4.3 is a summary of vapour phase methane concentrations and methane release rates at the end of Stages 1 and 2 of methane hydrate decomposition. It is evident that a high proportion of methane was recovered during Stage 1. The rate of methane release in Stage 1 is more than 100 times higher than is Stage 2, hence the astronomical rise in vapour phase methane concentration during Stage 1.

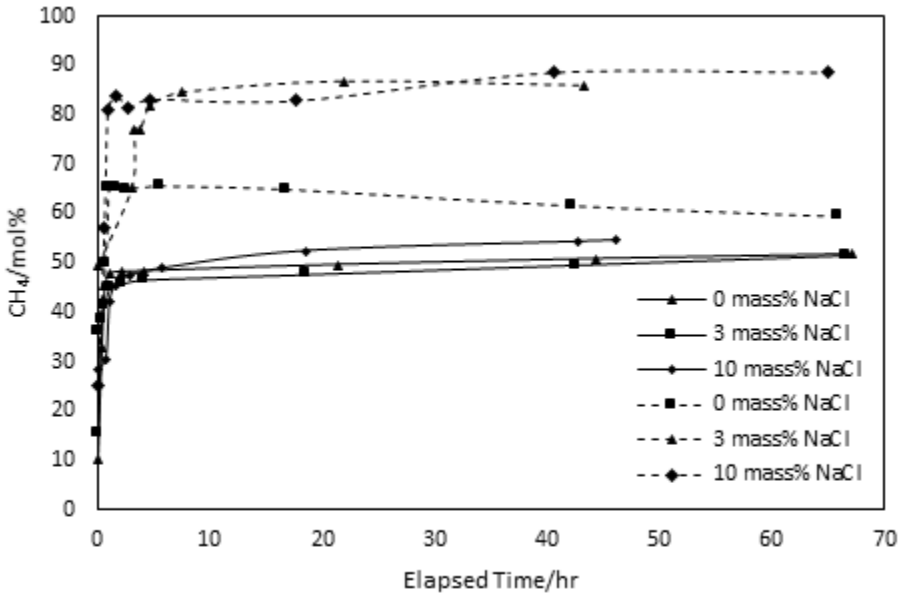

Figure 4.7 *Evolution of the vapour phase methane concentration after flue gas injection. Thick lines represent experiments with excess gas hydrate formation method. Dashed lines represent experiments with excess water hydrate formation method*.

Table 4.3 *Vapour phase methane concentration, methane release rates, and CO_2 ratio during methane recovery (Stages 1 and 2).*

Experiment	Hydrate Formation Method	Stage	CH_4 (mol%)			$CO_2/(CO_2+N_2)$ (%)	
			Initial	Final	Rate (mol/hr)	Initial	Final
5	Excess gas	1	10.2	47.8	0.0886	13.7	15.2
		2	47.8	51.7	0.00043	15.2	6.9
6		1	15.3	45.7	0.0296	16.9	19.6
		2	45.7	51.5	0.00044	19.6	13.9
7		1	28.3	45.6	0.1751	17.6	18.2
		2	45.6	54.6	0.0014	18.2	18.8
8	Excess water	1	36.11	65.3	0.095	13.6	15.4
		2	65.3	59.5	0.00095	15.4	11.7
9		1	49.3	81.9	0.025	15.4	26.4
		2	81.9	85.9	0.0015	26.4	29.1
10		1	25.1	81.6	0.0638	13.3	17.9
		2	81.6	88.6	0.0019	17.9	15.3

4.3.3 Influence of water salinity on methane recovery by depressurisation

Similar to **Section 3.5.1.3**, depressurisation was initiated in a series of pressure steps after thermodynamic equilibrium was achieved at the end of Stages 1 and 2 to enhance methane production. Each pressure step lasted about 24 hours to ensure the system reached equilibrium.

Figure 4.8 (a) and **(b)** shows the vapour phase methane concentration during depressurisation for the experiments with excess gas and excess water respectively. The dashed vertical lines represent the methane hydrate dissociation pressure of systems with 0, 3, and 10 mass% NaCl respectively at the corresponding experimental temperature. It is seen that the presence of 3 and 10 mass% NaCl in the aqueous phase increased the methane hydrate dissociation pressure from 2.72 MPa (0 mass% NaCl) to 3.11 MPa and 4.29 MPa respectively. In **Figure 4.8 (a)** for Experiment 5 (0 mass% NaCl), as high as 72 mol% methane is present in the vapour phase at 3.3 MPa, that is 0.58 MPa above the methane hydrate dissociation pressure. At the third pressure step, dissociation pressure of 2.72 MPa had been reached and 90 mol% methane is present in the vapour phase showing complete hydrate dissociation. For Experiments 6 and 7, despite increased methane hydrate dissociation pressure due to the presence of 3 and 10 mass% NaCl in the aqueous phase, maximum vapour phase methane concentration of 80.5 mol% and 65.7 mol% were achieved after three and two pressure steps respectively at 3.3 MPa and 4.8 MPa respectively, that is 0.2 MPa and 0.5 MPa above the methane hydrate dissociation pressures at the corresponding experimental conditions. In **Figure 4.8 (b)**, 75.2 mol% vapour phase methane concentration was achieved after two depressurisation steps at 3 MPa, 0.3 MPa above the methane hydrate dissociation pressure for Experiment 8 (0 mass% NaCl). For Experiments 9 and 10, maximum vapour phase concentrations of 76.2 mol% and 61.8 mol% were achieved at 3.6 MPa and 5.3 MPa respectively after only one depressurisation step at 0.5 MPa and 1 MPa above the methane hydrate dissociation pressure. Limited amount of methane was available for hydrate formation in the excess water systems, this also limited the hydrate saturation achieved during hydrate formation. Thus, a large proportion of methane have already been recovered during Stages 1 and 2. Given sufficient hydrate saturation, predictions by HydraFLASH shows that up to 80 mol% vapour phase methane concentration could be achieved in both Experiments 9 and 10 at 3.2 MPa, 0.09 MPa above methane hydrate dissociation pressure for Experiment 9 and 4.47 MPa, 0.18 MPa above methane hydrate dissociation pressure for Experiment 10. From the foregoing, it is seen that the presence of salt (NaCl) though negatively affecting hydrate saturation achievable during hydrate formation is nonetheless beneficial to methane recovery by depressurisation in the presence of flue gas. It increased the dissociation pressure of methane hydrate with increasing salt (NaCl) concentration, but also aids faster and complete decomposition of methane hydrate by flue gas with increasing salt (NaCl)

concentration. This is more so for Experiments 9 and 10 (excess water) where complete decomposition was achieved at 0.5 MPa and 1 MPa above the methane hydrate dissociation pressure. This could be very beneficial for methane recovery from gas hydrate reservoir especially in marine sediments with dispersed hydrate deposits.

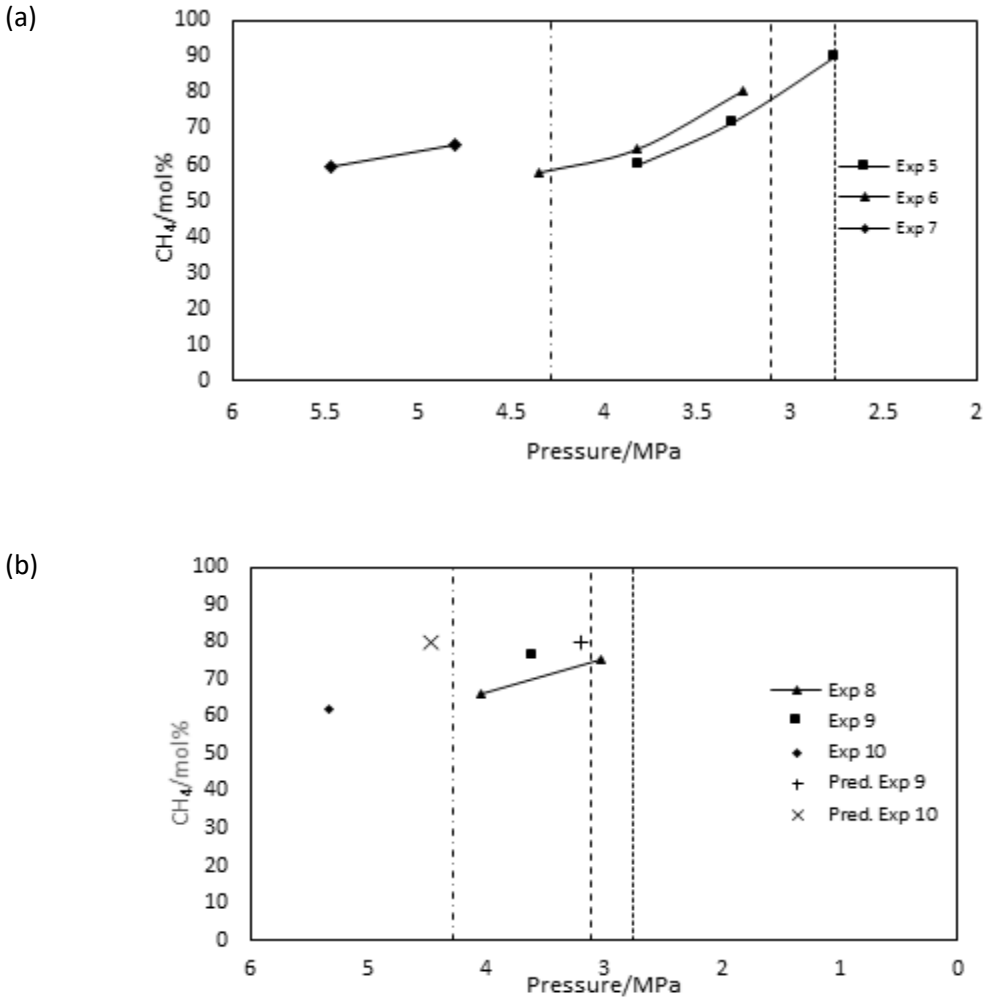

Figure 4.8 *Vapour phase methane concentration during depressurisation in the presence of flue gas. (a) and (b) represents experiments with excess gas and excess water hydrate formation methods respectively. Dotted vertical lines (---→(– – –) (– · – · ·) represents decomposition pressure of methane hydrate for 0, 3, and 10 mass% NaCl systems at 273.2 K respectively. Methane hydrate starts to decompose well inside the methane hydrate stability zone. (+) and (×) represents model predictions (80 mol%) of vapour phase methane concentration by HydraFLASH given sufficient hydrate saturation.*

4.3.4 Influence of water salinity on CO_2 sequestration

Flue gas injection into methane hydrate reservoirs offers the possible benefit of CO_2 capture and storage in hydrate form. The ratio $CO_2/(CO_2+ N_2)$ was used to indicate the absolute content of CO_2 in the flue gas component of the vapour phase. A reduction in the value of the ratio implies that CO_2 is involved in CO_2-hydrate or CO_2-mixed hydrate

formation. Possible CO_2-mixed hydrates that could be formed are CO_2-CH_4 and N_2-CO_2-CH_4 mixed hydrates. **Figure 4.9** and **Figure 4.10** showing the vapour phase concentrations of methane, nitrogen, and CO_2 for experiments with excess gas and excess water respectively enables the analysis of the kinetics of CO_2-involved hydrate formation. In Stages 1 and 2, methane concentration rose continuously due to methane hydrate decomposition as its equilibrium is broken by the injected flue gas. Consequently, the concentration of CO_2 and N_2 decreases. Also, the ratio $CO_2/(CO_2+N_2)$ reduced suggesting that CO_2 molecules were involved in hydrate formation. The CO_2 content reduced to a minimum when a new thermodynamic equilibrium was reached at the end of Stage 2. During depressurisation (Stage 3), the ratio $CO_2/(CO_2+N_2)$ rose continuously indicating that CO_2 is being released from the decomposing CO_2 mixed hydrates formed during Stages 1 and 2. As mentioned in **Section 3.5.2**, the N_2-CO_2-CH_4 was first to dissociate before the system was depressurised outside the methane hydrate stability zone (HSZ). The CO_2-CH_4 mixed hydrate and CO_2 hydrate would be completely dissociated once the system was depressurised outside the CO_2 HSZ. Hence the slight increase in CO_2 concentration in the vapour phase at the end of depressurisation. **Table 4.4** shows the rate and amount of CO_2 captured in the hydrate phase during Stages 1 and 2. The initial concentration was determined at the start of the recovery experiment after the purge of the remaining methane gas after methane hydrate formation and the final concentration determined when equilibrium was reached at the end of Stage 2 prior to depressurisation. For the excess gas tests, 59.8% of CO_2 in the vapour phase was captured and stored in hydrate form at the end of Stage 2 in Experiment 5. As expected due to kinetic inhibition of CO_2 hydrate formation by NaCl, the amount of CO_2 captured reduced to 42.5% and 22.6% for systems with 3 (Experiment 6) and 10 (Experiment 7) mass% NaCl in the aqueous phase respectively. This is also evidenced by the high rate of CO_2 entrapment in the hydrate phase in Stages 1 and 2 of Experiment 5. The high rate was observed only in Stage 1 for Experiments 6 and 7. In the excess water tests, a reverse trend was observed. 36.4%, 45.6%, and 68.5% of CO_2 in the vapour phase was captured in the hydrate phase for systems with 0 (Experiment 8), 3 (Experiment 9), and 10 (Experiment 10) mass% NaCl in the aqueous phase respectively. Given the excess water environment and CO_2 solubility in water, it is expected that a significant amount of CO_2 will dissolve in the aqueous phase. However, the increasing CO_2 consumption with salinity suggests that reduction in CO_2 in the 3 and 10 mass% NaCl systems is not only due to CO_2 hydrates formation.

Besides CO_2 involved in hydrate formation, CO_2 solubility in water should decrease with increasing salinity due to salting out effect [211, 212] thus, increasing the concentration of CO_2 in the vapour phase. It is believed that different types of carbon species including hydrogen carbonate ion (HCO_3^-) and carbonic acid (H_2CO_3) would be present in the excess water and would be converted to carbonate (CO_3^{2-}) provided that NaCl was present in excess [213]. This could be a possible reason for the reduced vapour phase CO_2 concentration with increasing salinity besides CO_2 involved in hydrate formation. This is especially true given the high CO_2 in Experiment 10 (10 mass% NaCl). This could be a subject of future investigation. From the foregoing, it is evident that besides methane production, saline excess water environments as obtainable in marine sediments and deep saline aquifers are excellent candidates for CO_2 sequestration both in hydrate form and otherwise.

(a)

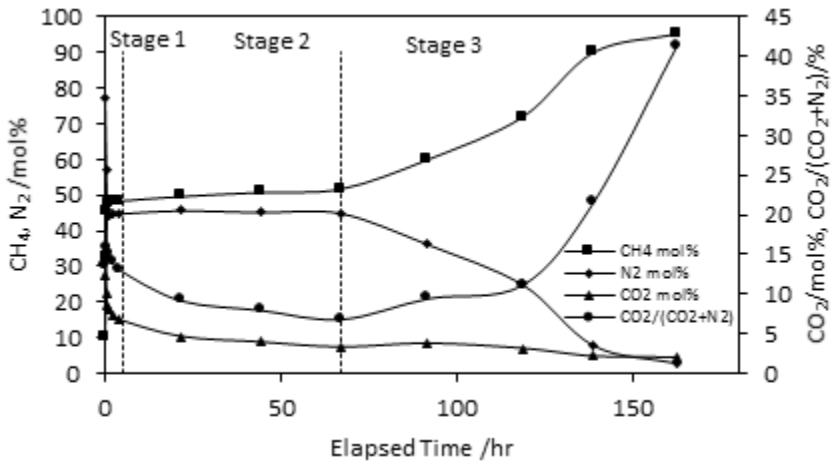

(b)

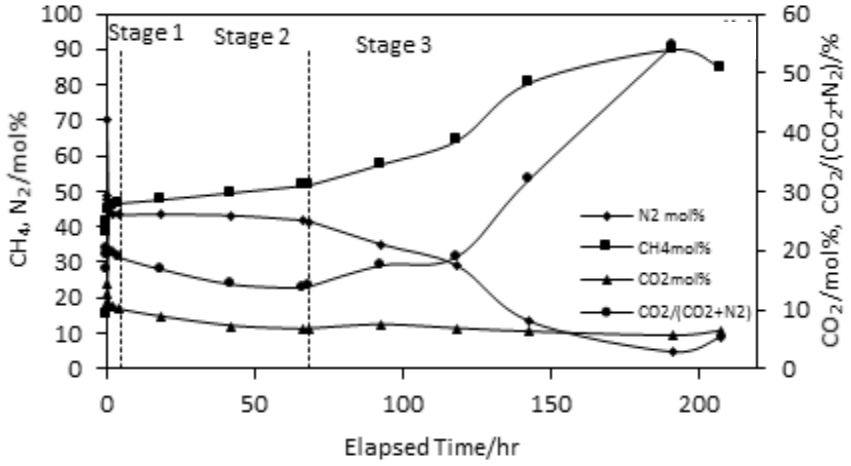

(c)

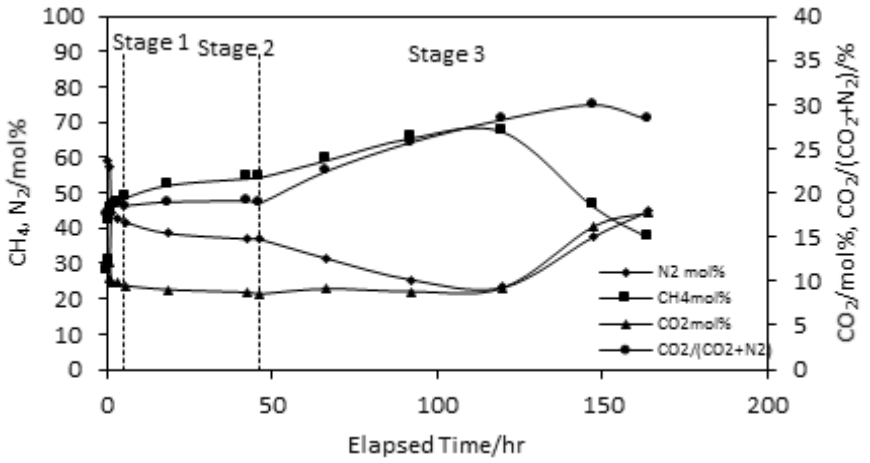

Figure 4.9 *Vapour phase concentrations of methane, nitrogen, and CO_2 after flue gas injection and during depressurisation for experiments with excess gas hydrate formation method. The ratio $CO_2/(CO_2+N_2)$ shows the absolute content of CO_2 in the flue gas component of the vapour phase at any instant. (a), (b), and (c) represent experiments with 0, 3, and 10 mass% NaCl in the aqueous phase respectively.*

(a)

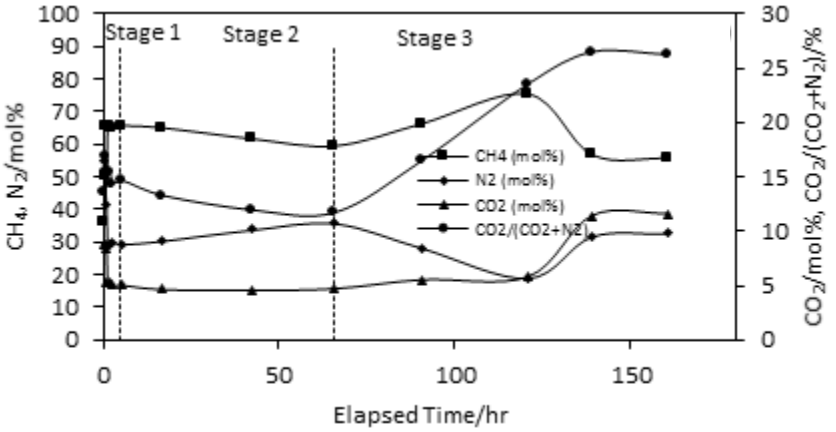

(b)

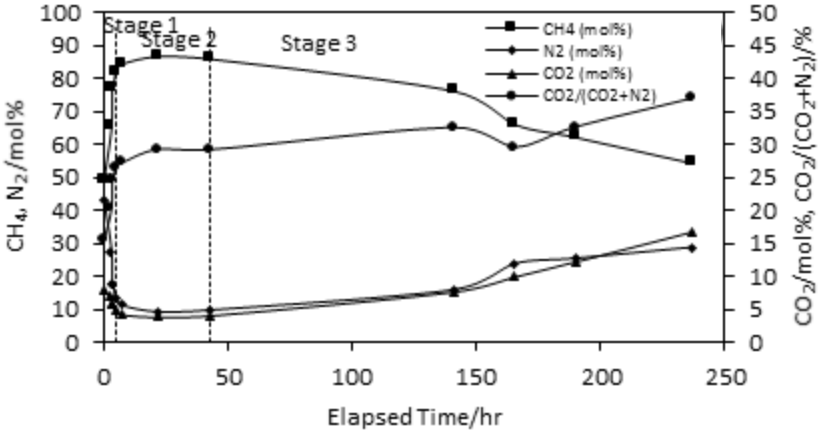

(c)

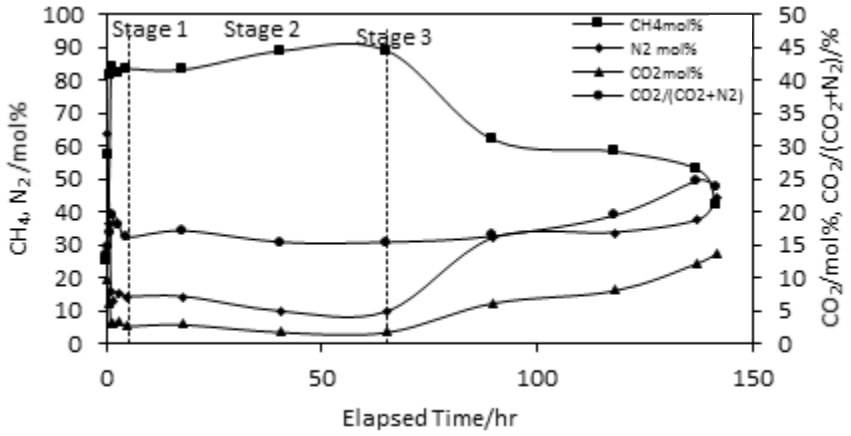

Figure 4.10 *Vapour phase concentrations of methane, nitrogen, and CO_2 after flue gas injection and during depressurisation for experiments with excess water hydrate formation method. The ratio $CO_2/(CO_2+N_2)$ shows the absolute content of CO_2 in the flue gas component of the vapour phase at any instant. (a), (b), and (c) represent experiments with 0, 3, and 10 mass% NaCl in the aqueous phase respectively.*

Table 4.4 *Kinetics of CO_2 hydrate formation and the amount of CO_2 captured in the hydrate phase during Stages 1 and 2.*

Experiment	Hydrate formation method	CO_2 consumption rate/ mol/hr		CO_2 in vapour /mole		CO_2 in hydrates	
		Stage 1	Stage 2	Initial	Final	(mole)	(%)
5	Excess gas	0.00298	0.0048	0.03560	0.01430	0.0213	59.8
6		0.00255	0.000304	0.06708	0.03858	0.0285	42.5
7		0.00363	0.00025	0.10602	0.08203	0.0240	22.6
8	Excess water	0.00805	0.000035	0.04796	0.03052	0.0174	36.4
9		0.00564	0.000004	0.02246	0.012225	0.0102	45.6
10		0.00428	0.00015	0.04854	0.015313	0.0332	68.5

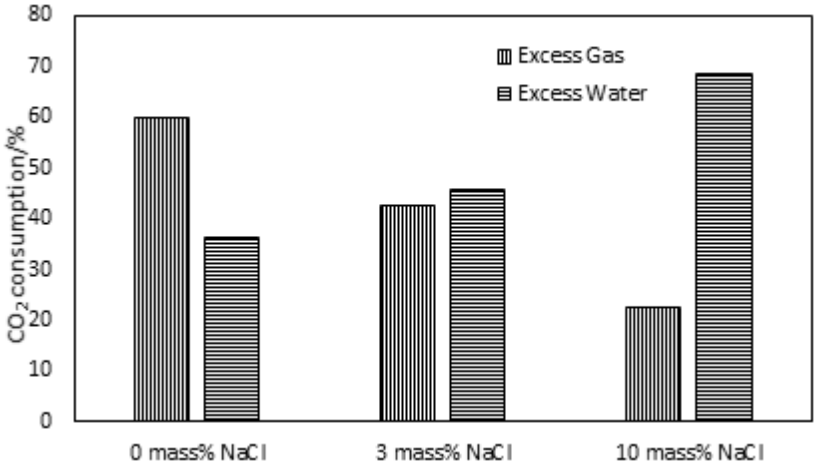

Figure 4.11 *CO_2 consumption after flue gas injection in the excess gas and excess water environments with varying degrees of water salinity.*

4.4 Summary

The influence of water salinity on methane hydrate formation and consequently methane recovery by flue gas injection was studied. Three experiments each with 0, 3, and 10 mass% NaCl in the aqueous phase were conducted using the excess gas and excess water hydrate formation methods to simulate permafrost and marine sediments. Significant nucleation and methane gas uptake was observed in pure water system in the excess gas hydrate formation method. Hence, hydrate growth rate was higher for pure water system compared to systems with 3 and 10 mass% NaCl. In the system with 3 mass% NaCl, high growth rate was sustained from day 2 to day 4 until the remaining water became saline enough to suppress continued hydrate growth. Similarly, in excess water environment, methane gas consumption was higher for pure water system than for the 3 and 10 mass% NaCl systems. Overall, the presence of NaCl has a kinetic inhibition effect on methane hydrate growth. However, a quantitative comparison of methane conversion to methane hydrate shows that 3 mass% NaCl in the aqueous phase has only slight impact on methane conversion as comparable conversions were achieved with pure water systems in both excess gas and excess water environments.

At the new thermodynamic equilibrium after flue gas injection, vapour phase methane concentrations for pure water system and 3 mass% NaCl system were identical for the excess gas tests showing that 3 mass% NaCl has a negligible impact on methane hydrate decomposition in the presence of flue gas. Higher vapour phase methane concentration was achieved for the 10 mass% NaCl system due to ease of methane hydrate decomposition arising from reduced methane hydrate saturation achieved during methane hydrate formation. In excess water environments, reduced methane hydrate saturations were achieved due to limited amount of methane gas. Vapour phase methane concentration achieved after flue gas injection were similar and significantly higher in the saline systems than in the pure water system. The ease of methane hydrate decomposition at low hydrate saturations by flue gas enabled almost complete methane recovery in saline excess water environments. In both excess gas and excess water environments, methane recovery rate in Stage 1 was more than 100 time higher than in Stage 2.

The presence of 3 and 10 mass% NaCl in the aqueous phase increased the dissociation pressure of methane hydrate from 2.72 MPa to 3.11 and 4.29 MPa respectively, it nonetheless aided in fast and complete decomposition of methane hydrate at pressures

above the methane hydrate dissociation pressure. In the excess gas tests, as high as 72 mol% of methane was present in the vapour phase at the second depressurisation step at 3.3 MPa for the pure water system. Complete decomposition was achieved at the third pressure stage of 2.72 MPa which is the methane hydrate dissociation pressure. 3 and 10 mass% NaCl in the aqueous phase enabled complete methane hydrate decomposition at 0.2 and 0.5 MPa above the methane hydrate decomposition pressure respectively. In excess water environments, complete methane hydrate dissociation was achieved after two depressurisation steps in the pure water system at 0.3 MPa above methane hydrate dissociation pressure, and only after one depressurisation step for 3 and 10 mass% NaCl systems at 0.5 and 1 MPa above methane hydrate dissociation pressures respectively.

The benefit of CO_2 capture and storage in hydrate form in the presence salt (NaCl) was also examined. In the excess gas environment, CO_2 captured and stored in the hydrate phase decreased with increasing NaCl concentration in the aqueous phase showing kinetic inhibition of CO_2-hydrates formation by NaCl. A contrasting trend was observed in the excess water environment where the amount of CO_2 captured and stored increased with increasing NaCl concentration. Due to excess water environment and the fairly significant CO_2 solubility in water, more CO_2 is dissolved in the aqueous phase. Also, the increasing CO_2 consumption with increasing salinity suggests that CO_2 reduction in the vapour phase in excess water environment may not be due only to CO_2 involvement in hydrate formation but also in the formation of sodium carbonates. It is concluded that aside from methane production, saline water environments seem excellent candidates for CO_2 capture and storage.

CHAPTER 5 INFLUENCE OF SEDIMENT MINERALOGY ON METHANE RECOVERY BY FLUE GAS INJECTION

5.1 Introduction

Hydrate stability condition is generally dependent on the compositions of the gas and aqueous phases in bulk conditions. In the presence of porous media, additional factors including pore and grain size [187, 214], sediment mineralogy and water content [215] could also have a significant influence on hydrate stability. Their effect could be so significant that the discrepancy observed between the estimated base of gas hydrate stability zone (BGHS) and the observed BSR in the Ocean Drilling Project (ODP) Leg 164, at Blake Ridge (1995) reported by Matsumoto et al. [216] were thought to be due to hydrate stability inhibition by strong capillary forces in the fine-grained sediments [217].

Knowledge of the effects of porous media on hydrate stability has been advanced experimentally. Handa and Stupin [206] reported that water activity may have a direct effect on stability conditions of gas hydrates. They also showed that dissociation pressure of methane and propane in fine pores of porous media was higher than for same in the bulk phase. Uchida et al. [214, 218] investigated the effect of pore sizes of 4nm to 100nm on the dissociation of gas hydrates. Their results indicated that water activity is a function of pore size and that dissociation temperature decreased with decreasing pore size. Clennell et al. [187] in their conceptual model hydrate growth in marine sediments postulated that hydrate growth is inhibited in fine-grained sediments by a combination of factors including reduced water activity, and excess internal energy, which they thought of as capillary pressure, of small crystals confined in pores. Anderson et al. [219] reported that this capillary pressure, if high enough leads to a depression in hydrate decomposition temperature.

The host sediments of natural gas hydrates are composed mainly of sands, clays, and/or organic matter. Uchida et al. [220] in a further study measured the decomposition conditions of methane hydrates during formation-decomposition cycles using sand, sandstone, and clay as the porous media and compared their results with that obtained for hydrate formation-decomposition cycles in glass beads of identical particle size. Their results indicated that dissociation temperatures at given pressure for sand and sandstone were lower than that of bulk phases by as much as 0.5 K, and even lower for

kaolinite clay, up to 1.5 K , further confirming the effect of pore size on hydrate stability. They further confirmed that decomposition temperature depression was more pronounced for smaller initial water saturation. Identical results obtained with glass beads experiments suggests that surface texture and mineral components had less significant influence on hydrate formation and dissociation behaviour of sediments with no significant swelling when in contact with water. Clay types with significant swelling when in contact with water affects hydrate formation and decomposition in ways different from sand and sandstone. The influence of clay particles on hydrate formation in sediments is variable due to their characteristic low permeability and varying water activity in their pores.

There have been only a few experimental studies on hydrate formation and dissociation in clay, perhaps due to difficulties in working with wet clays [215, 221, 222]. Cha et al. [221] reported that the inclusion of a third surface (bentonite – a swelling clay) in a methane-water hydrate system provides a large surface area for ordered strong water adsorption. The ordered adsorption of water molecules onto the clay surfaces approximates part of a hydrate lattice which makes it easier for hydrate formation. Thus, the presence of clay could act as a thermodynamic promoter. Kotkoskie et al. [222] observed hydrate formation in a bentonite based drilling mud at a pressure as low as 2.8 MPa at 290 K, further confirming the promotion effect of bentonite clay on hydrate formation.

In recent years, advancement in molecular dynamic (MD) simulation has helped to improve understanding of the mechanism of crystal growth and by extension, mechanism of hydrate nucleation and growth in porous media at microscopic scale. Park and Sposito [223] using Monte Carlo and molecular dynamics simulation were able to observe that stable methane hydrate forms and stabilise in the interlayers of hydrated Na-montmorillonite at pressure as low as 1 MPa and 300 K. Yan et al. [224] also conducted molecular dynamic simulations of the nucleation and growth of methane hydrate in the presence of the surface and nanopores of clay. They found out that hydrate formation is more complex in porous media than in the bulk phase and there is a relationship between hydrate growth and molecular diffusion in the nanopores of clay. Also, the hydroxylated edge sites of the clay surfaces could be a source of methane molecules to facilitate nucleation. In the same vein, Ji et al. [225] captured the effect of organic matter-leonardite humic acid (LHA) occurring in clays on methane hydrate

growth in the interlayers of Na-montmorillonite. They observed that LHA exhibited kinetic inhibition on hydrate formation on clay minerals. Methane adsorption on LHA aggregate made it difficult for methane to form hydrate directly near the LHA surface or to be adsorbed by water cages already formed in the surrounding region.

Hydrate formation in sand is well studied. However, there is paucity of knowledge on hydrate formation and dissociation in clay sediments. It is well known that many naturally occurring gas hydrate reserves seldom lay in sediments that are 100% sand, but in sediments with varying proportions of clay. This chapter reports the investigations on the effects of clay on methane hydrate formation and its consequence on methane recovery by flue gas injection. The impact of water saturation was also investigated by conducting experiments using partially water saturated sediment (excess gas method) and fully water saturated sediment (excess water method). Sediment from the Leg 311 of the Integrated Ocean Drilling Programme (IODP) was used as the porous media. It is silty and clayey and could approximate clay in texture and other physical attributes. It is also a good representation of the host sediment of naturally occurring gas hydrate.

5.2 Experimental Section

5.2.1 Experimental apparatus and materials

The experimental rig for the excess gas and excess water tests are already described in **Section 4.2.1.** The materials used except the IODP sediment remains the same. The mineralogical composition of the IODP sediment is shown in **Table 5.1**. The particle size distribution is shown in **Table 5.2** and **Figure 5.1**. The particle size distribution range from 0.15 μm to 80 μm with a mass medium of 28.1 μm and specific surface area of 0.48 m^2/g.

Table 5.1 *Mineralogical composition of the IODP sediment*

Mineral		mass%
Silicates	quartz	29.2
	plagioclase	34.3
	K-feldspar	2.3
	amphibole	5.3
	pyroxene	1.4
carbonates	calcite	1.6
	dolomite	Not detected
	Fe folomite (ankerite)	<0.5
Phyllosilicates (clay minerals)	mica'	12
	kaolinite	Not detected
	chlorite	7.1
	smectite	5.3
Others	magnetite	Not detected
	hematite	Not detected
	halite	1.1

Table 5.2 *Particle size distribution for the IODP sediment used in the experiments*

Size/ µm	Ratio/ mass%	Size/ µm	Ratio/ mass%	Size/ µm	Ratio/ mass%	Size/ µm	Ratio/ mass%	Size/ µm	Ratio/ mass%
80.0	9.7	20.1	2.8	5.07	1.1	1.28	0.6	0.32	0.2
71.9	8.6	18.1	2.5	4.56	1.2	1.15	0.5	0.29	0.2
64.7	6.6	16.3	2.2	4.1	1.3	1.03	0.5	0.26	0.1
58.2	5.1	14.6	2.0	3.69	1.3	0.93	0.5	0.23	0.1
52.3	4.3	13.2	1.7	3.32	1.2	0.83	0.5	0.21	0.1
47.1	3.8	11.8	1.6	2.98	1.1	0.75	0.4	0.19	0.1
42.3	3.5	10.7	1.5	2.68	1.1	0.68	0.4	0.17	0.1
38.1	3.2	9.58	1.4	2.41	1.0	0.61	0.4	0.15	0.1
34.2	2.8	8.62	1.3	2.17	0.9	0.55	0.3		
30.8	2.6	7.75	1.2	1.95	0.8	0.49	0.3		
27.7	2.7	6.97	1.2	1.75	0.8	0.44	0.3		
24.9	2.8	6.27	1.2	1.58	0.7	0.40	0.2		
22.4	3.0	5.64	1.2	1.42	0.6	0.36	0.2		
Mass medium = 28.1 µm						Specific surface area = 0.48 m^2/g			

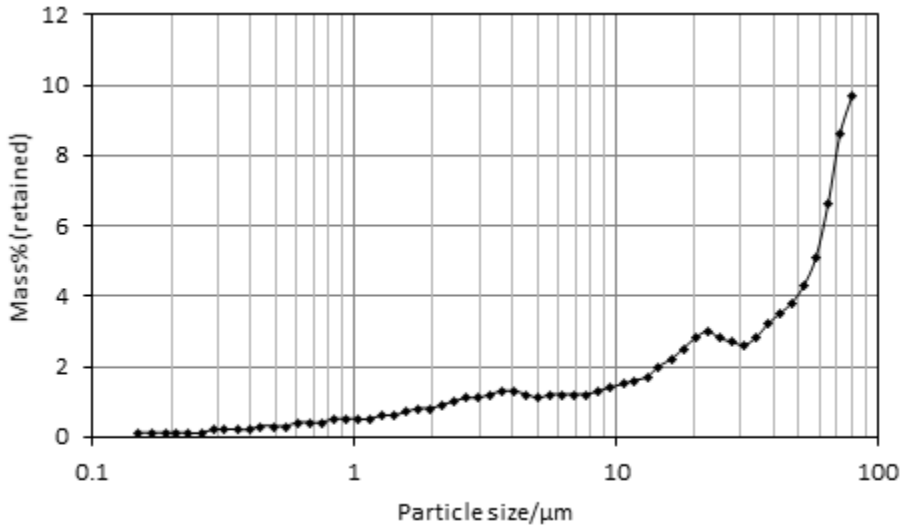

Figure 5.1 *Particle size distributions of the IODP sediment used in graphical form.*

5.2.2 Experimental procedure

The experimental procedure including sample preparation, methane hydrate synthesis follows the same processes as described in **Sections 3.4.2** and **3.4.3** for the excess gas test. For the excess water test, methane hydrate synthesis is as described **Section 4.2.3.3.** Flue gas injection and methane recovery for both tests follows the same procedure as described in **Sections 3.4.4**, and **3.4.5.** The IODP sediment used was dried in the oven at 293 K for 24 hours, and pulverised before use.

5.3 Results and Discussions

One experiment each was conducted with the IODP sediment using the excess gas and excess water hydrate formation methods to simulate limited water environment as obtainable in permafrosts and excess water environment as obtainable in marine sediments. Results were compared with Experiments 5 and 8 conducted with silica sand in excess gas and excess water environments respectively to highlight the peculiarities of clayey sediments with regard to hydrate formation and its influence on methane recovery by flue gas injection. **Table 5.3** shows the properties and initial parameters of the sediment samples before flue gas injection.

Table 5.3 *Properties and initial parameters of the hydrate bearing sediment samples*

	Excess Gas Environment		Excess Water Environment	
	Silica Sand	IODP Sediment	Silica Sand	IODP Sediment
Experiment	5	11	8	12
Height (cm)	14.69	14.21	14.7	14.32
Diameter (cm)	7.5	7.5	7.5	7.5
Volume (cm^3)	649.29	627.58	649.75	632.61
Porosity (vol%)	43.6	50	40.3	56.1
Dry mass (g)	1076.6	985.44	1076	887.1
Grain density (g/cm^3)	2.64	2.7	2.64	2.7
Wet mass (g)	1231.8	1231.8	-	-
Initial water saturation (mass%)	14.4	25	-	-
Wet density (g/cm^3)	1.89	1.96	-	-
Hydrate saturation (vol%)	44.7	7.5	29.8	2.4
Gas saturation (vol%)	35.8	20.1	31.1	41.8
Water saturation (vol%)	19.5	72.4	39.1	55.8

5.3.1 Effect of sediment mineralogy on hydrate formation

Figure 5.2 shows the temperature and pressure profile during hydrate formation in excess gas environment using silica sand and IODP sediment as the porous media. Observing the temperature profile, an early onset of nucleation is seen in the IODP sediment (*TC*) compared to the experiment with silica sand (*TS*). From **Table 5.1**, it is seen that 24.4% of the IODP sediment is phyllosilicates containing smectite (montmorillonite), a swelling clay. As reported in **Table 5.3**, a water mass ratio of 25 mass% was necessary to achieve the desired partial saturation in the IODP sediment compared to 14.4 mass% for silica sand. The increased water mass ratio is due to water molecules being adsorbed in an orderly manner and incorporated into the inter-layer space of clay sheets, thus increasing the volume of clay. The ordered adsorption sets up water structures that are favourable to hydrate crystals leading to a hydrate promotion effect. This may be the reason for the early onset of nucleation observed in the IODP sediment. However, despite the early onset of nucleation, the pressure profile which is an indication of gas uptake for hydrate formation shows a significantly reduced gas uptake for the IODP sediment (*PC*) in comparison to the gas uptake for silica sand system *(PS).* It has been reported that pore size impacts negatively on hydrate formation [214, 218]. Reduced pore size in clay sediments leads to reduced water activity consequently leading to thermodynamic inhibition. Furthermore, hydrate

crystal increases in volume during growth. The high compressibility of clay particles with the application of overburden pressure may also reduce the space available for hydrate growth especially outside of the inter-layers. On the other hand, silica sand absorbs less water. Thus, hydrate would form with water existing in the inter-granular spaces. **Figure 5.3** which compares the rate of methane consumption during hydrate formation further shows a higher rate of methane consumption for silica sand system compared with the IODP sediment.

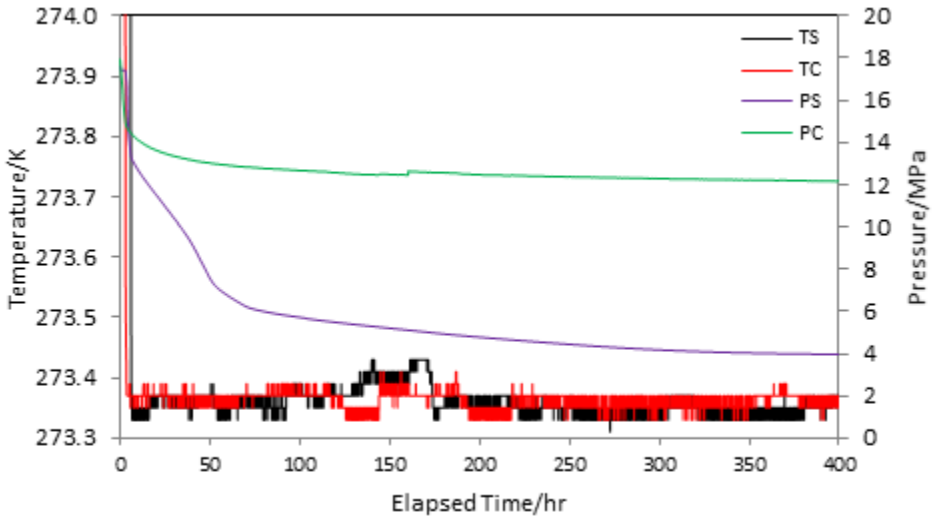

Figure 5.2 *Temperature and pressure profiles of methane hydrate formation during Experiments 5 and 11 respectively using excess gas hydrate formation method. TS, TC, PS, and PC represent temperature and pressure profiles for systems silica sand and IODP sediment respectively.*

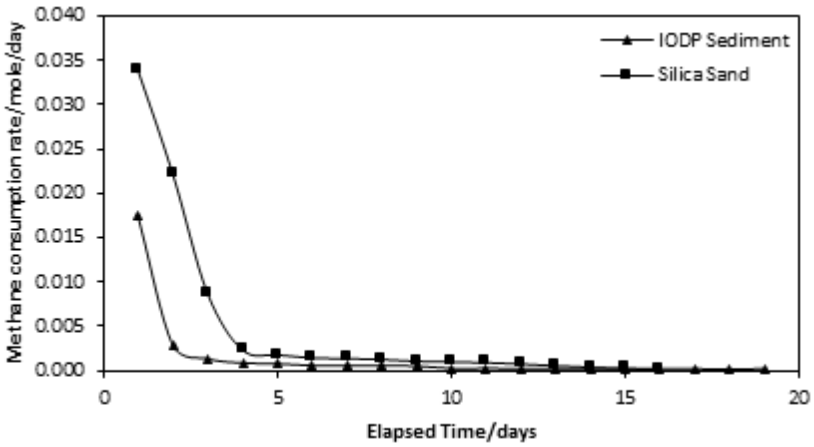

Figure 5.3 *Methane consumption rate during hydrate formation for Experiments 5 and 11 respectively using excess gas method.*

In excess water environment, the rate of water injection is indicative of gas uptake during hydrate formation. As expected, a high injection rate at initial time followed afterwards by a relatively low injection rate was observed as shown in **Figure 5.4**. Overall, it is seen that water injection rate is higher for silica sand sediment than the IODP sediment at all times. This is so as silica sand has larger particle size (mean particle diameter is 256.5 μm for the Fife sand used in this test), absorbs less water, and less compressible. Thus, silica sand allows the injection of water as much water as possible while also providing enough pore space to contain the water, consequently little or no inhibition to hydrate growth and accumulation. On the other hand, the IODP sediment has smaller particle size (mean particle diameter is 28.1 μm), absorbs more water and expands in volume. The volume expansion coupled with the high compressibility with the application of overburden pressure significantly reduces the available pore space for water accumulation.

Estimates of methane conversion to hydrate as shown in **Figure 5.5** further buttress these observations. In the excess gas environment, 82% conversion was achieved in the silica sand sediment compared to 29% in the IODP sediment. In the excess water environment, 55% conversion was achieved in silica sand sediment compared to only 7% in IODP sediment. Clay particles have been shown to have promotion tendencies in dilute clay-water systems due to absence of confinement. Seo et al. [226] reported that the inter-layer spacing between clay particles increased from 12.65 Å to 15.38 Å to 16.06 Å for pure clay powder, clay-water suspension, and clay-methane hydrate intercalate respectively. However, in bulk clay sediments, this expansion may not be possible especially in the presence of over- and/or underburden pressure. It can be concluded that in bulk clay sediments, clay may have both promotion and inhibition effects. A weak promotion effect at the onset of hydrate formation due to ordered adsorption of water into the inter-layer sheets of clay promoting hydrate nucleation, then an inhibition effect in the long run due to limitation to volume expansion to accommodate the growing hydrate crystal due to confinement.

A comparison of the water saturation at the end of hydrate formation in the IODP sediments shows that, contrary to observations in silica sand, water saturation is higher in the excess gas method than in the excess water method. In the excess gas method, the IODP sediment was pre-mixed with water to the desired partial saturation before loading in the cell. Thus, the injected methane gas is in contact with water in all parts

of the system. In the excess water method, dry IODP sediment was loaded in the cell, followed by water injection. Despite water injection at intervals from the bottom, middle and top of the cell, even distribution was not achieved. This is because the IODP exhibits swelling clay attributes. Thus, it absorbs water and swells, and coagulates under compaction by the overburden pressure. This coagulation and compaction reduces the permeability of the sediment thus hindering access to methane gas at portions away from the injection ports. Hence, hydrate formation was limited to only parts of the sediment in contact with water. This behaviour is in consonance with that reported by Ruffine [227]. In his experiments on hydrate formation with varying proportion of clay in sand using excess water method, he observed that for 40.3 mass% clay in sand, a great proportion of the core was dry after hydrate formation. Besides the peculiarities of hydrate formation in clayey sediments discussed earlier, this may also be a contributing factor to the low hydrate saturation achieved in the excess water method for the IODP sediment.

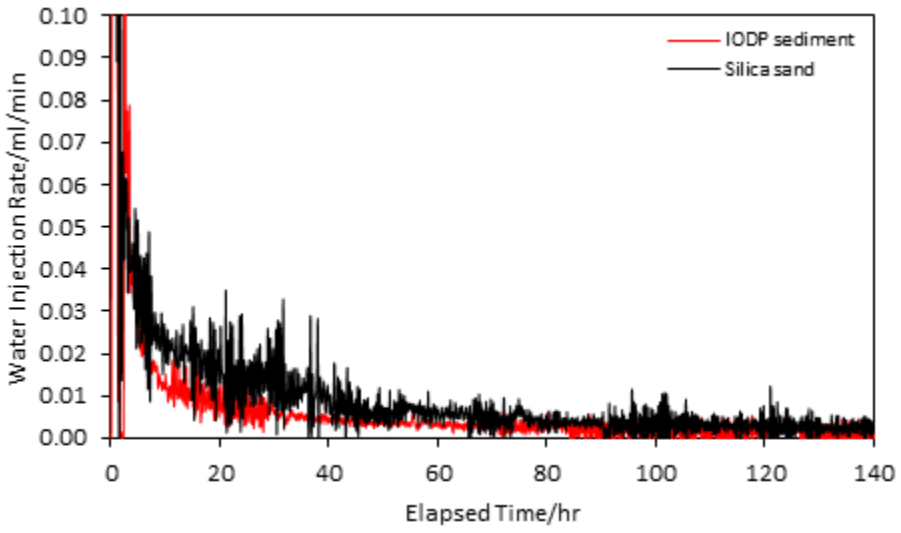

Figure 5.4 *Water injection rates for hydrate formation in excess water environment during Experiments8, 8, and 12 respectively.*

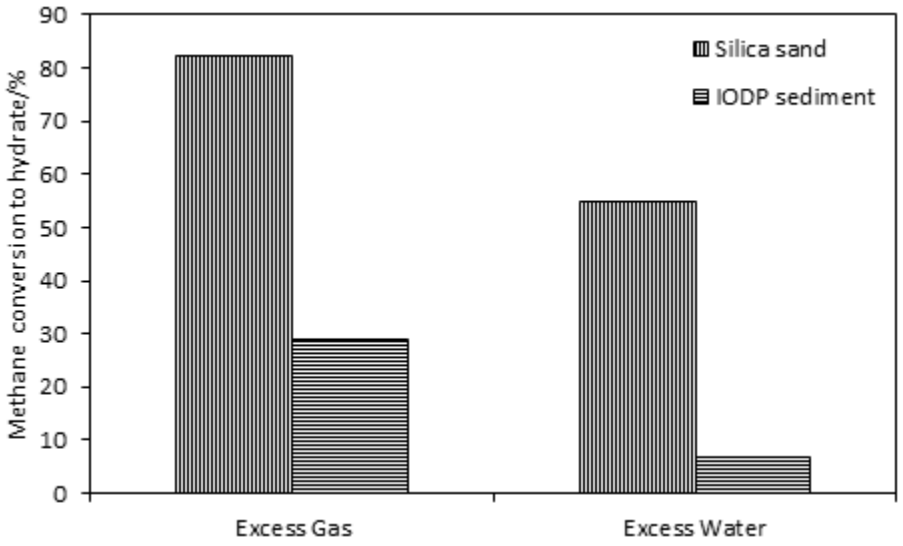

Figure 5.5 *Methane conversion to hydrate for excess gas and excess water hydrate formation methods in silica sand and IODP sediment.*

5.3.2 Effect of sediment mineralogy on methane hydrate decomposition in the presence of flue gas

The vapour phase methane concentrations for Experiments 11 and 12 conducted with IODP sediment are shown in **Error! Reference source not found.** and **Error! Reference source not found.** in **APPENDIX E**. The kinetic process of methane hydrate decomposition is already described in **Figure 3.9**. **Figure 5.6** is the evolution of vapour phase methane concentration after flue gas injection. In the excess gas environment, vapour phase methane concentration of 52 mol% was achieved in silica sand sediments while for the IODP sediment, it was 58 mol%. This is attributed to hydrate saturation achieved during hydrate formation. As explained in **Section 5.3.1**, lower hydrate saturation was achieved in the IODP sediment. Hydrate decomposition is a fast process compared to hydrate formation. It has also been demonstrated that at low hydrate saturation, decomposition in the presence of flue gas is extremely fast. In the excess water environment, vapour phase methane concentrations reached 60 mol% in both silica sand and IODP sediments. Once more, the fast decomposition in the presence of flue gas is due to low hydrate saturation achieved during hydrate formation in excess water environment.

Table 5.4 is a summary of the vapour phase methane concentrations, methane release rates, and the ratio $CO_2/(CO_2+N_2)$ as an indicator of the CO_2 involvement in hydrate formation. Similar to the observation in **Section 4.3.2**, the rate of methane release is at least 100 times higher in Stage 1 than in Stage 2 for all experiments except Experiment

12 conducted with IODP sediment in excess water environment. This is understandable as the rate of methane release in Stage 1 (0.0164 mole/hr) is significantly low compared to other experiments due to extremely low hydrate saturation achieved during hydrate formation. In both excess gas and excess water tests, it is seen that the rate of methane release in silica sand is higher in both Stages 1 and 2 than in the IODP sediment. It can be said that silica sand offers no inhibition to methane hydrate decomposition. As it absorbs little or no water, methane hydrate in its large pore spaces decomposes readily in the presence of flue gas. For the IODP sediment, despite the reduced hydrate saturation achieved during hydrate formation, bulk clay sediments may also offer some restrictions to hydrate decomposition especially in confined sediments. Methane hydrate formed outside the clay inter-layers may decompose readily in the presence of flue gas; however, the intercalated methane hydrate may decompose at a slightly slower rate because they are formed with the ordered water molecules strongly adsorbed to the surfaces of the inter-layer clay sheets.

In Experiments 8 (silica sand) and 12 (IODP sediment), despite the low hydrate saturations achieved during hydrate formation, it is seen in **Table 5.4** that the initial vapour phase methane concentration at the start of the recovery experiment is 36.1 mol% and 47.1 mol% respectively. This is due to technical difficulty in the presence of water which may cause significant hydrate dissociation when setting the system pressure to the desired experimental pressure for methane recovery. This initially high methane concentration reduces the relative ratio of CO_2 in the vapour phase, consequently the low ratio of $CO_2/(CO_2+N_2)$ (5.6%) in Experiment 12. Also, the substantial high vapour phase methane concentration at the end of Stages 1 and 2 in Experiments 8 and 12 (excess water) is attributable to pressure limitation in terms of flue gas injection due to the incompressible nature of water. This limitation makes the methane ratio relatively high.

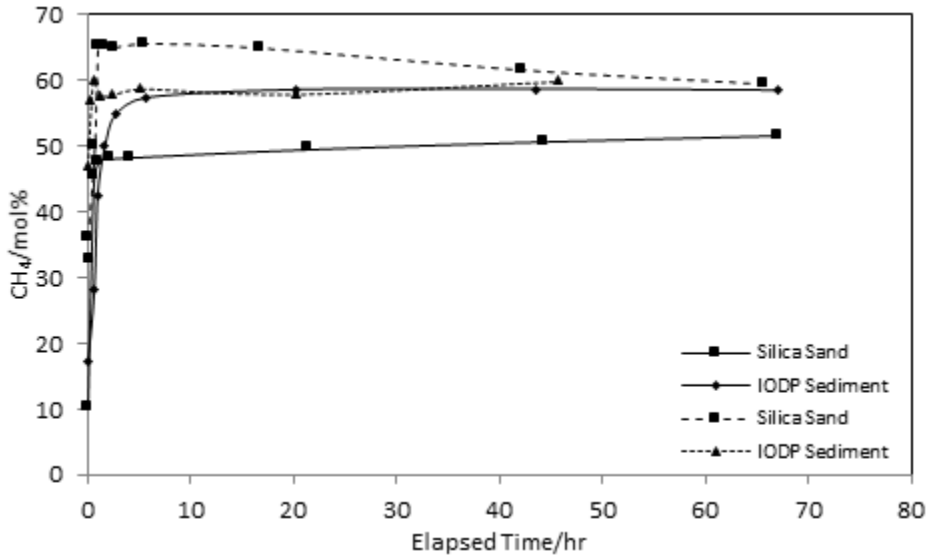

Figure 5.6 *Evolution of the vapour phase methane concentration after flue gas injection for experiments with Silica sand and IODP sediment as the porous media respectively. Thick lines represent experiments with excess gas hydrate formation method. Dashed lines represent experiments with excess water hydrate formation method.*

Table 5.4 *Vapour phase methane concentration, methane release rates, and CO_2 ratio during methane recovery (Stages 1 and 2).*

Experiment	Hydrate Formation Method	Stage	CH_4 (mol%)			$CO_2/(CO_2+N_2)$ (%)	
			Initial	Final	Rate (mol/hr)	Initial	Final
5	Excess gas	1	10.2	47.8	0.0886	13.7	15.2
(Silica Sand)		2	47.8	51.7	0.00043	15.2	6.9
11		1	17.4	54.8	0.048	17.8	10.9
(IODP Sediment)		2	54.8	58.5	0.00038	10.9	2.6
8	Excess water	1	36.11	65.3	0.095	13.6	15.4
(Silica Sand)		2	65.3	59.5	0.00095	15.4	11.7
12		1	47.1	57.9	0.0164	5.6	7.7
(IODP Sediment)		2	57.9	60	0.00055	7.7	4.4

5.3.3 Effect on sediment mineralogy on methane recovery by depressurisation in the presence of flue gas

Figure 5.7 shows the vapour phase methane concentrations during depressurisation in the presence of flue gas in excess gas and excess water environments respectively. The dashed lines represent the pure methane hydrate dissociation pressure at the experimental conditions. In **Figure 5.7(a)** for excess gas environment, in the experiment with silica sand (Experiment 5), as discussed in **Section 4.3.3,** 72 mol% methane is present in the vapour phase at 3.3 MPa, that is, 0.54 MPa above the pure

methane hydrate dissociation pressure. By the third pressure step, the methane hydrate dissociation had been reached and up to 90 mol% methane is present in the vapour phase. For the IODP sediment, 65 mol% methane was achieved during depressurisation and remained relatively unchanged after two depressurisation steps. This implies that up to 65 mol% methane could be achieved at 3.5 MPa, which is 0.74 MPa above the pure methane hydrate dissociation pressure. In **Figure 5.7(b)** for excess water environment, in the silica sand sediment, up to 75 mol% methane is present in the vapour phase after two depressurisation steps down to 3.3 MPa, which is 0.24 MPa above the pure methane hydrate dissociation pressure. For the IODP sediment, maximum vapour phase methane concentration of 91 mol% was achieved after two depressurisation steps down to 2.9 MPa, that is, 0.14 MPa above methane hydrate dissociation pressure. Though IODP sediment may have hindered hydrate growth during hydrate formation, and also led to reduced rate of dissociation in the presence of flue gas due to excessive compaction owing to its small particle size, and also confinement. It is seen from the foregoing that it has no negative impact on methane hydrate decomposition during depressurisation. This is because during depressurisation, system pressure is reduced, consequently the effect of over-pressure, and over- and/or underburden pressure is reduced. Thus, both intercalated methane hydrate and that formed outside of the inter-layers and in the pore spaces dissociates with less restriction/inhibition. Also in all cases, it is seen that substantial methane hydrate dissociation occurred at pressures above the methane hydrate dissociation pressure at the experimental temperature as evidenced by the high vapour phase methane concentrations.

(a)

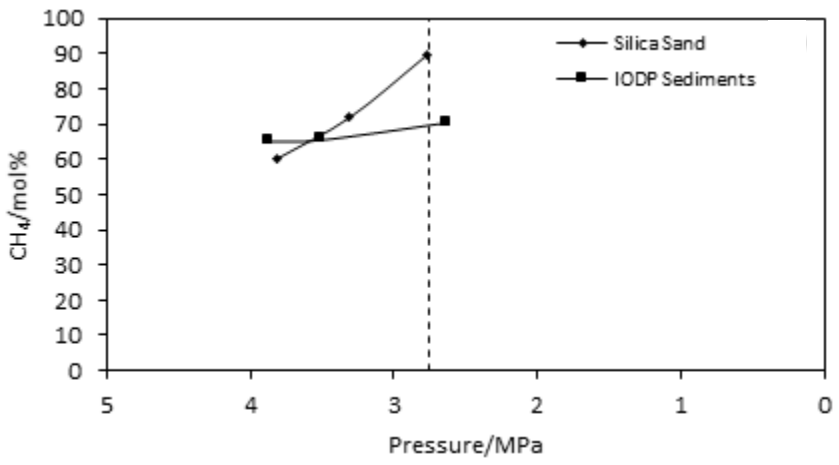

(b)

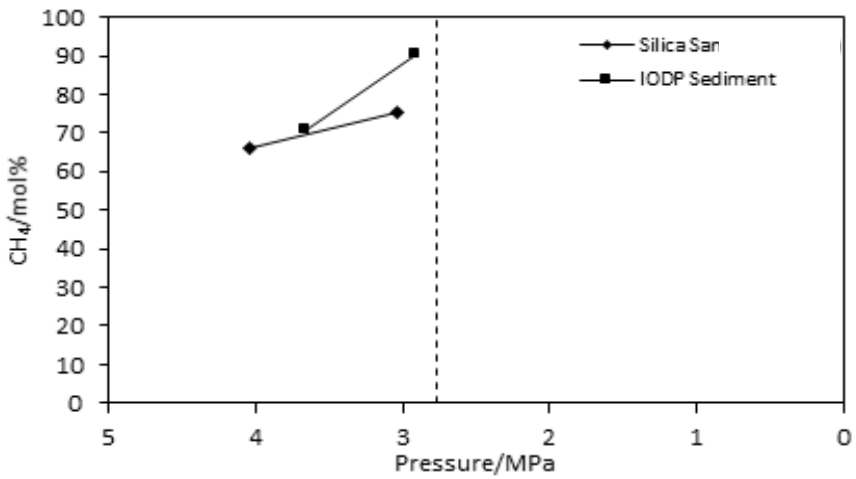

Figure 5.7 *Vapour phase methane concentration during depressurisation in the presence of flue gas. (a) and (b) represents experiments with excess gas and excess water hydrate formation methods respectively. Dotted vertical lines represents dissociation pressure of pure methane hydrate at the experimental temperature of 273.2 K. Methane hydrate starts to decompose well inside the methane hydrate stability zone.*

5.3.4 Effect of sediment mineralogy on CO_2 sequestration

The capture and storage of the CO_2 component of flue gas in hydrate form and the different forms of CO_2-mixed hydrate that could be formed has been discussed in **Section 3.5.2**. **Figure *5.8*** and **Figure *5.9*** shows the changing vapour phase concentration of methane, nitrogen and CO_2 for experiments with silica sand and IODP sediments in excess gas and excess water environments. They are similar in trend to those in **Figure *4.9*** and **Figure *4.10*** and the processes leading to this trend are already discussed in **Section 3.5.2**. **Table 5.5** shows the rate and amount of CO_2 captured in the hydrate phase during Stages 1 and 2. The initial concentration was determined at the start of the recovery experiment after the purge of the remaining methane gas after methane hydrate formation and the final concentration determined when equilibrium was reached at the end of Stage 2 prior to depressurisation. In the excess gas environment, it is seen that the rate of CO_2 consumption for hydrate formation is higher in the IODP sediment compared to silica sand. This leads to about 90% of CO_2 initially in the vapour phase being captured in the hydrate phase as opposed to about 60% in the silica sand sediment. This is attributed to the promotion effect caused by the ordered adsorption of water that sets up water structures favourable for hydrate formation. It is also enhanced by the relative ease of CO_2 replacement of methane in hydrate cages. In the excess water environment, a reverse trend is observed. The rate of CO_2 consumption for hydrate formation is lower in the IODP sediment in comparison to silica sand. As noted in **Section 5.3.1**, more water was injected into the silica sand

sediment during methane hydrate formation owing to availability of pore space due to its large particles and low compressibility. Therefore, more methane hydrate was formed, and consequently, higher CO_2 hydrate formation. On the other hand, less water was injected during methane hydrate formation in the IODP sediment as explained in **Section 5.3.1**. The IODP sediment has smaller particle size, absorbs more water and expands in volume. The volume expansion coupled with the high compressibility with the application of over- and/or underburden pressure significantly reduces the available pore space for water accumulation. Hence, the low methane hydrate saturation achieved during methane hydrate formation, and consequently, the low CO_2 consumption for CO_2 hydrates formation. Moreover, limitation in the quantity of flue gas that could be injected into the system due to incompressibility of water in the excess water system limits the amount of CO_2 in the system and consequently, the amount of CO_2 consumed for CO_2 hydrate formation.

The CO_2 consumption in the four cases is represented graphically in **Figure 5.10**. From the foregoing and the graph, it can be suggested that, based on sediment mineralogy, permafrost sediments with significant proportion of clay is a good candidate for CO_2 capture and sequestration in hydrate form.

(a)

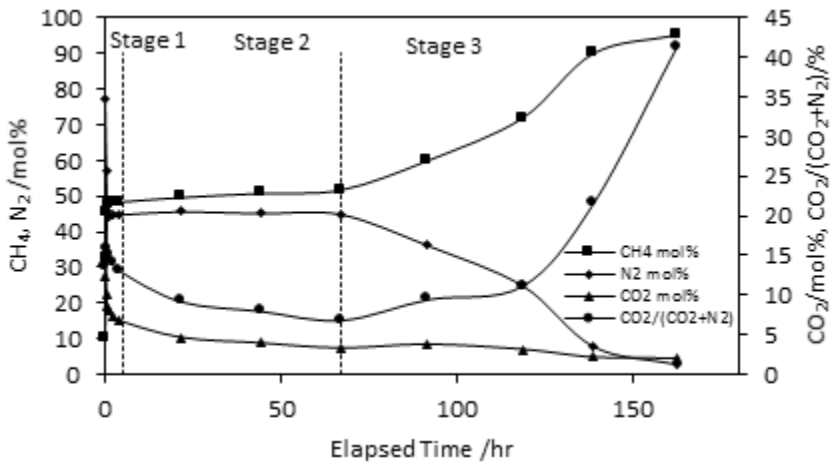

(b)

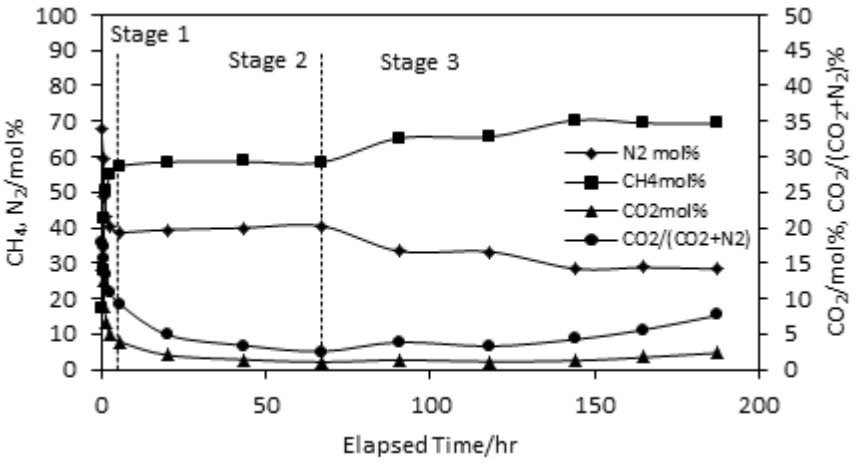

Figure 5.8 *Vapour phase concentrations of methane, nitrogen, and CO_2 after flue gas injection and during depressurisation for experiments with excess gas hydrate formation method. The ratio $CO_2/(CO_2+N_2)$ shows the absolute content of CO_2 in the flue gas component of the vapour phase at any instant. (a) and (b) represent experiments with silica sand and IODP sediment respectively as the porous media.*

(a)

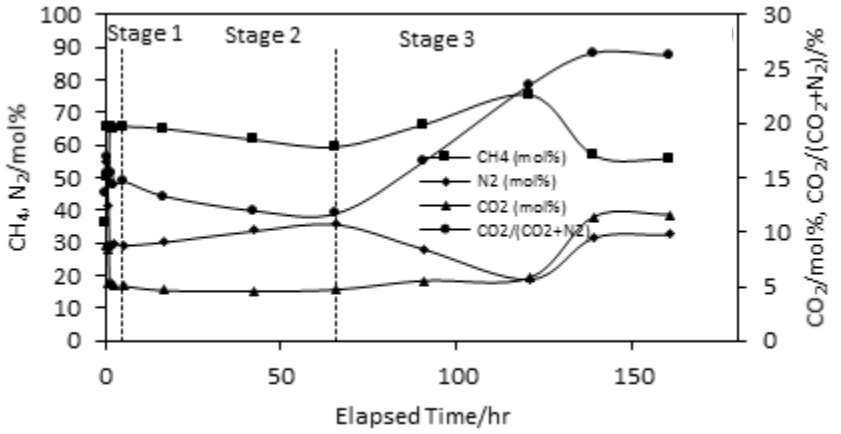

(b)

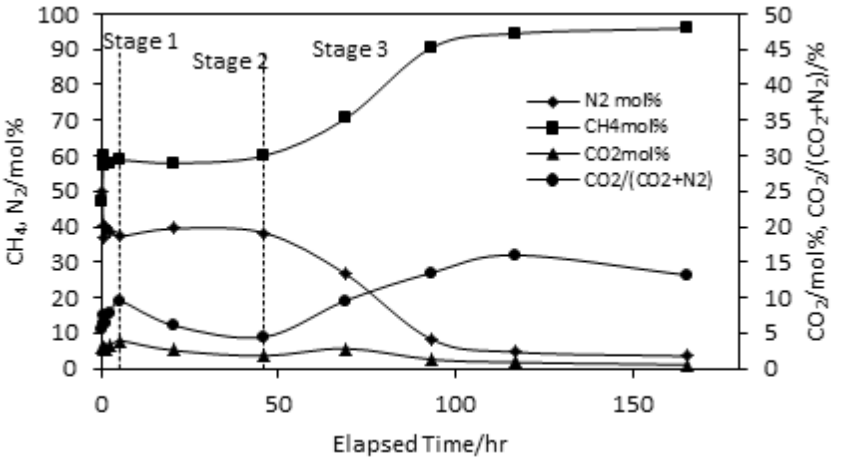

Figure 5.9 *Vapour phase concentrations of methane, nitrogen, and CO_2 after flue gas injection and during depressurisation for experiments with excess water hydrate formation method. The ratio $CO_2/(CO_2+N_2)$ shows the absolute content of CO_2 in the flue gas component of the vapour phase at any instant. (a) and (b) represent experiments with silica sand and IODP sediment respectively as the porous media.*

Table 5.5 *Kinetics of CO_2 hydrate formation and the amount of CO_2 captured in the hydrate phase during Stages 1 and 2.*

Experiment	Hydrate formation method	CO_2 consumption rate/ mol/hr		CO_2 in vapour /mole		CO_2 in hydrates	
		Stage 1	Stage 2	Initial	Final	(mole)	(%)
5	Excess	0.0029	0.0048	0.037	0.014	0.021	59.8
11	gas	0.012	0.00017	0.046	0.0047	0.042	89.9
8	Excess	0.0081	0.000035	0.048	0.031	0.017	36.4
12	water	0.002	0.00034	0.017	0.012	0.0043	25.7

Note: Experiments 5 and 8 were conducted using silica sand while Experiments 11 and 12 were conducted using IODP sediment.

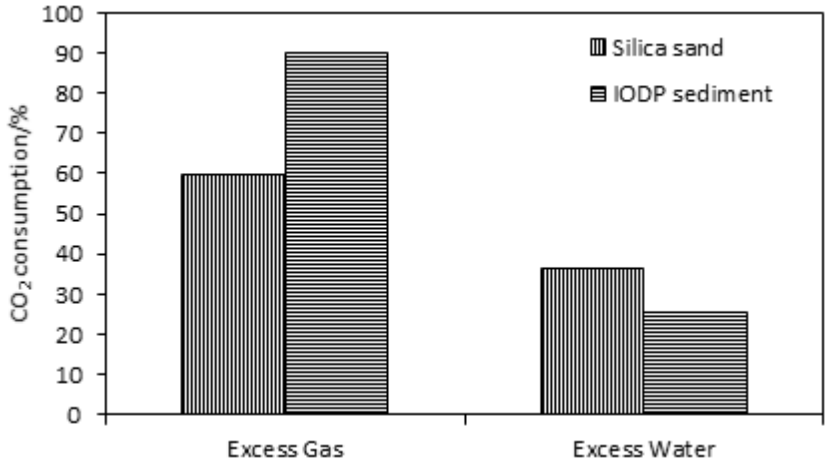

Figure 5.10 *CO_2 consumption after flue gas injection in the excess gas and excess water environments for silica sand and IODP sediments.*

5.4 Summary

The effect of sediment mineralogy on methane hydrate formation, and methane recovery by flue gas injection was investigated. One experiment each was conducted with real sediments from the Leg 311 of the Integrated Ocean Drilling Programme (IODP) using the excess gas and excess water hydrate formation methods to simulate permafrost and marine sediments. The IODP sediment is rich clay in and could approximate clayey sediment. Results were compared with experiments at similar conditions conducted with silica sand.

In the excess gas method, the early onset of nucleation of nucleation in the IODP sediment indicates that clay particles have a promotion effect on hydrate formation in the early times. However, the rate of hydrate growth reduced significantly at later times due to reduced water activity arising from reduced pore size. The high compressibility

of clay particles also reduced the space available for hydrate growth. In the silica sand, there is no known inhibition of any sort resulting from sediment mineralogy on hydrate growth. Consequently, methane conversion to hydrate of 82% was achieved in the silica sand, and only 29% in the IODP sediment. In the excess water method, water injection rate was higher in the silica sand sediment due to its reduced compressibility and water absorption, thus providing space for free water accumulation. The IODP sediment absorbs more water, and it is also highly compressible, thus providing limited space for free water accumulation. Also, the coagulation and compaction of parts of the sediment close to water injection ports reduces the permeability of the sediments to water and hinders free water access to the inner parts of the sediment away from the water injection ports. Consequently, only 7% methane conversion to hydrate was achieved in the IODP sediment compared to 55% in the silica sand sediment.

Vapour phase methane concentration at equilibrium after flue gas injection reached 52 mol% in silica sand and 58 mol% in the IODP sediment in the excess gas environment. It was 60 mol% for both silica sand and IODP sediment in the excess water environment despite low methane hydrate saturations achieved in the two experiments. The relatively high methane concentration is attributed to pressure limitation in terms of the quantity of flue gas injected due to the incompressibility of water. The high methane concentrations were due to near complete decomposition of methane hydrate by flue gas at low methane hydrate saturations. The rate of methane release is at least 100 times higher in stage 1 than in stage 2 with the exception of Experiment 12 (IODP sediment in excess water environment) due to extremely low methane hydrate saturation achieved during hydrate formation. Comparisons of methane release rates in both excess gas and excess water environments shows that the rate is higher in silica sand than in IODP sediment, suggesting that the IODP sediment has a slight inhibition effect on methane hydrate dissociation.

Enhanced methane release was achieved by depressurisation in the presence of flue gas. The presence of flue gas enabled methane decomposition at pressures above the methane hydrate decomposition at the experimental temperature. In the excess gas environment, up to 72 mol% of methane is present in the vapour phase at 3.3 MPa, 0.54 MPa above the methane hydrate dissociation pressure in the silica sand sediment. 65 mol% methane was in the vapour phase after two depressurisation steps at 3.5 MPa, 0.74 MPa above the methane hydrate dissociation pressure in the IODP sediment. In

the excess water environment, up to 75 mol% methane was achieved in the vapour phase in silica sand sediment after two depressurisation steps at 3.3 MPa, 0.24 MPa above the methane hydrate dissociation pressure. For the IODP sediment, 91 mol% methane was in the vapour phase after two depressurisation steps at 2.9 MPa, 0.14 MPa higher than the methane hydrate dissociation pressure. Depressurisation reduced the effect of over pressure in the IODP sediment, enabling the decomposition of methane hydrate within and outside the clay interlayers.

The influence of sediment mineralogy on the capture and storage of the CO_2 component of the flue gas was also investigated. 90 % of CO_2 in the vapour phase was captured and stored as CO_2 hydrate in the IODP sediment in excess gas environment while it was 60% in silica sand. This confirms that IODP sediment have a promotion effect on CO_2 hydrate formation coupled with the relative ease of CO_2 replacement of methane in hydrate. In the excess water environment, CO_2 capture and storage was low in the IODP sediment due to inadequate free water for CO_2 hydrate formation and limited flue gas injection due to water incompressibility. It is concluded that if sediment mineralogy is considered permafrost sediments with significant proportion of clay is a good candidate for CO_2 capture and storage as CO_2 hydrate.

CHAPTER 6 ENHANCED DEPRESSURISATION FOR METHANE RECOVERY BY COMPRESSED AIR INJECTION

6.1 Introduction

Methane hydrate reservoirs have distinctive geological characteristics based on their geological location. For instance, the natural gas hydrate reservoir on the Alaska North Slope has a temperature and pressure of about 278 K and 7 MPa, the Ulleung Basin Gas Hydrate Site (UBGH) has a temperature and pressure range of 288 – 293 K and 20 – 22 MPa [228]. Flue gas injection technique for methane recovery with its accompanying CO_2-CH_4 exchange has been shown to be feasible and adaptable to pressure and temperature conditions of most methane hydrate reservoirs [229, 230]. However, in harsher environments, it is possible for the components of the injected flue gas, especially CO_2, to change from the gaseous phase to liquid phase. This could reduce the rate of soaking and migration of the injected gas. The fluctuation between phases destabilises injection and diffusion and consequently reduce the rate and yield of methane recovery.

Sources of flue gas are seldom close to the point of injection into natural gas hydrate reservoir thus, requiring additional costs in pipelines to transport from source to site. On the other hand, air is abundant and readily available anywhere needed. Kang et al. [231] recovered methane gas from bulk phase methane hydrate by air and CO_2/air injection in a methane-air and methane-CO_2/air exchange process. In this chapter, the use of a novel technique involving air injection for methane recovery from methane hydrate reservoirs based on shift in the methane hydrate equilibrium phase boundary is reported. Aside the potential benefit of low cost methane production, the technique also ensures sustained high pressure production that helps to avoid water production and sand migration. Nitrogen and oxygen, the major components of air has been shown to dissociate methane hydrate as demonstrated by Haneda et al. [232] and Panter et al. [101].

6.2 Experimental Section

6.2.1 Experimental apparatus and materials

The experimental apparatus and materials used are as described in **Sections 3.2** and **3.3** with flue gas substituted with compressed air. Compressed air used was synthesised and composed of 80 mol% nitrogen and 20 mol% oxygen. Nitrogen and oxygen used were supplied by BOC Limited with certified purities of 99.9995%.

6.2.2 Experimental procedure

6.2.2.1 Test conditions

Three experiments were conducted using silica sand as the porous medium. Experiments 13, 14, and 15 were conducted at 273.2 K, 278 K, and 283 K respectively to cover the typical range of temperatures obtainable in naturally occurring hydrate reservoirs and also to investigate the effect of temperature on the kinetics of the recovery process. The experiments are composed of two parts; the first part was designed to demonstrate the possibility of methane recovery by stepwise depressurisation in the presence of air/nitrogen. They were designed such that at the end of the last pressure stage, a vapour phase composition of 60:40 mol% methane and air will be achieved when the system reaches equilibrium after air injection. The second part aims to enhance methane recovery by continuous depressurisation,

6.2.2.2 Sample preparation, methane hydrate synthesis, and air injection

The partially water saturated sand preparation, methane hydrate synthesis, and air injection followed the same procedure as described in **Sections 3.4.2**, **3.4.3**, and **3.4.4.**

6.2.2.3 Methane recovery

After air injection into the porous media containing methane hydrate, purging of excess gas (mixture) reducing the system pressure to just above the equilibrium pressure of air hydrate at the experimental temperature, the system was allowed to equilibrate, and methane recovery was commenced. Methane recovery was done in multi-pressure stages. In each stage, the system was set to the target pressure corresponding to the desired vapour phase composition at equilibrium by returning the piston, which

expanded the cell volume, reducing the system pressure without any need for fluid withdrawal from the test cell. The time at which the desired target pressure was reached in each stage was taken as time zero, that is, the commencement of methane recovery for that stage. Samples from the vapour phase were taken and analysed for composition using a GC (Varian 3600). Cell pressure drops during sampling by a maximum of 0.015 MPa which does not lead to any significant change in the system. Sampling and compositional analysis in each stage continued until there was no noticeable change in the vapour phase composition of methane. At this point, the system was considered to have reached equilibrium.

6.2.2.4 GC analysis

Due to the difference in the components of the vapour phase in these experiments – nitrogen, oxygen and methane as compared to nitrogen, methane, and CO_2 in the flue gas experiments, a new calibration was done for GC analysis of the vapour phase composition. The calibration method was same as described in section 3.4.6. However, due to similarities in the elution times of nitrogen and oxygen at high temperatures, complete separation of their chromatographs could only be achieved at a low temperature value of 243 K. Consequently, complete elution of the three components lasted 8 minutes, and about 25 minutes for 3 injections. The column temperature was set constant at 243 K for 25 minutes during which 3 injections were made and thereafter ramped up to 378 K for one minute at the rate of 323 K/min to vapourise the content of the column. **Figure 6.1** below shows the calibration lines of the components of the vapour phase.

(a)

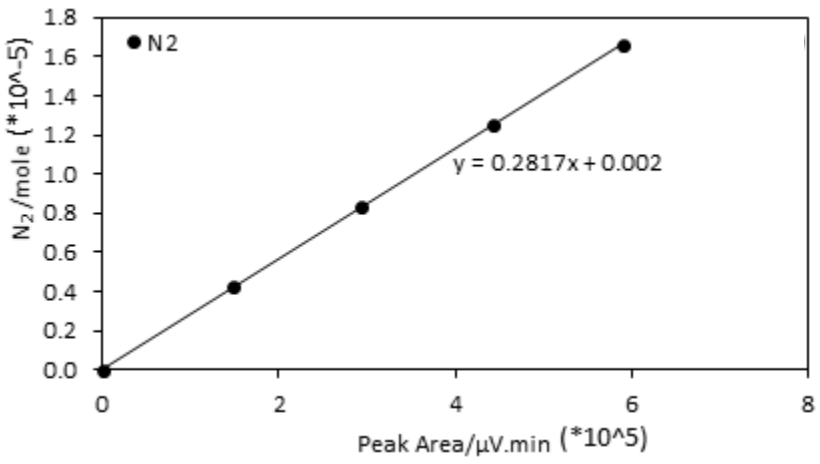

(b)

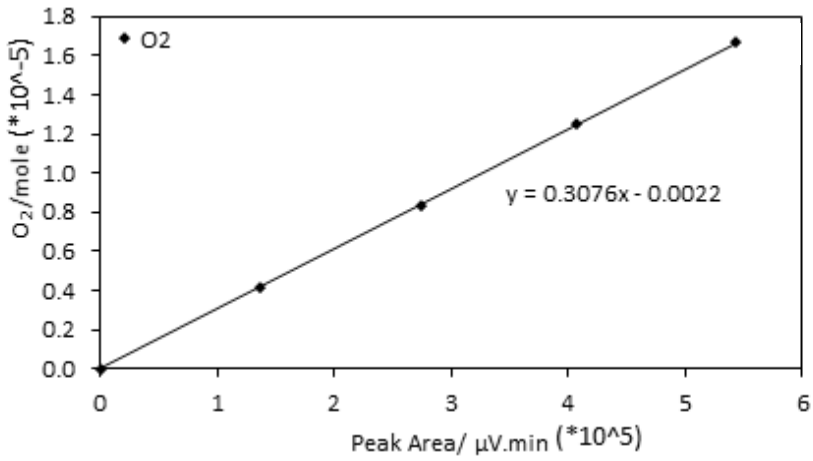

(c)

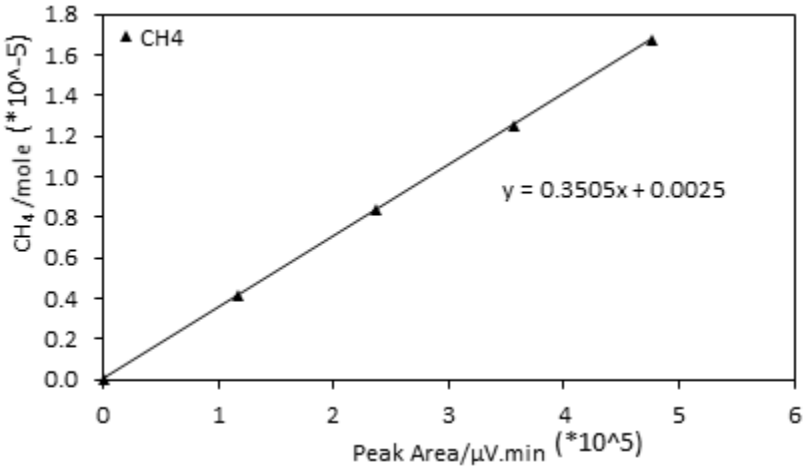

Figure 6.1 *Calibration lines of (a) nitrogen, (b) oxygen, and (c) methane showing their moles as functions of their respective peak areas.*

6.3 Results and Discussions

As stated earlier, three experiments were conducted to investigate the feasibility of air injection for methane recovery from methane hydrate bearing sediments. Two fundamental issues were investigated: methane hydrate decomposition behaviour in the presence of air, and the effect of air injection on the depressurisation process.

Table 6.*1* is a summary of the properties and initial parameters of the sediment samples before air injection including porosity ϕ, hydrate saturation S_h, remaining methane gas saturation S_g and remaining water saturation S_w.

Table 6.1 *Properties and initial parameters of the hydrate bearing sediment samples*

Experiment	13	14	15
Height (cm)	14.69	14.69	14.68
Diameter (cm)	7.50	7.50	7.50
Volume (cm^3)	649.4	649.2	648.4
Porosity (vol%)	46.40	48.30	46.00
Dry mass (g)	1076.6	1076.6	1076.6
Grain density (g/cm^3)	2.64	2.64	2.64
Wet mass (g)	1231.8	1231.8	1231.8
Initial water saturation (mass%)	14.4	14.4	14.4
Wet density (g/cm^3)	1.90	1.90	1.90
Hydrate saturation (vol%)	49.2	51.0	39.3
Gas saturation (vol%)	38.7	40.4	40.1
Water saturation (vol%)	12.1	8.6	20.6

6.3.1 Multi-stage depressurisation

Changing vapour phase composition with time was used to monitor the release of methane from the hydrate phase into the vapour phase after air injection. Methane recovery process consists of multiple stages of depressurisation. In each pressure stage, samples were taken at 0 mins, 15 mins, 45 mins, 1hr 15 mins, and 4hr 45 mins to monitor the fast release of methane from the hydrate phase at the early times. Subsequently, samples were taken at 24 hour intervals as methane release slows and gradually ceased. **Table F1** to **Table F3** in **APPENDIX F** shows the vapour phase composition with time for Experiments 13 to 15. **Figure 6.2** (Experiment 14) illustrates the typical kinetic process of methane hydrate decomposition after air injection. The experiments are composed of two parts; the first part was designed to demonstrate the feasibility of methane recovery by multi-stage depressurisation in the presence of air. It was designed to achieve 60 mol% methane in the vapour phase. The second part was to enhance methane recovery by continuous depressurisation. The time at which the desired set pressure was reached was taken as time zero, that is, the commencement of methane recovery at that pressure stage. In each stage, initially fast methane hydrate decomposition was observed as shown by the nearly vertical portion of the curves. This was followed by a slow decomposition which eventually ceases with time. Similar trend was also observed in Experiments 13 and 15. Graphical representation of the vapour phase concentrations is shown in **Figure 6.3** to **Figure 6.5**. The dotted vertical lines separate sections A-F and F-G. The figures show that the air component of the

vapour phase varies inversely with that of methane. The ratio $N_2/(N_2+O_2)$ was used to monitor the composition of the individual components of air in the vapour phase. It is also seen from **Figure 6.3** to **Figure 6.5** that $N_2/(N_2+O_2)$ remains constant throughout the duration of the experiments. This indicates that there is no preferential inclusion of one of the components of air into the hydrate phase over the other as nitrogen and oxygen possess similar characteristics.

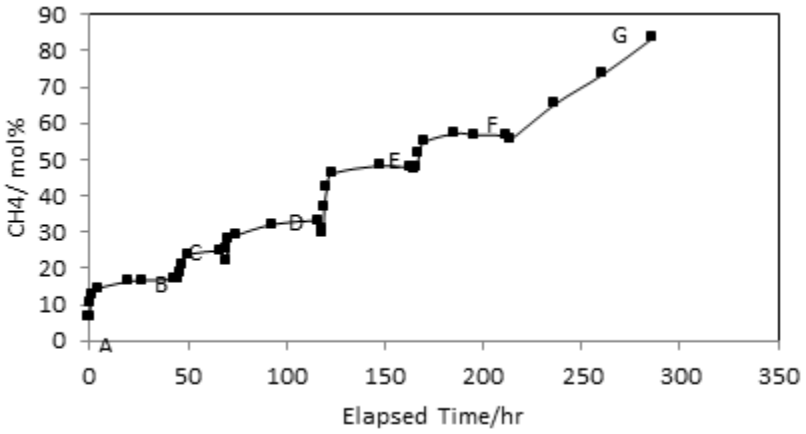

Figure 6.2 *Methane recovery stages after air injection for experiment 6*

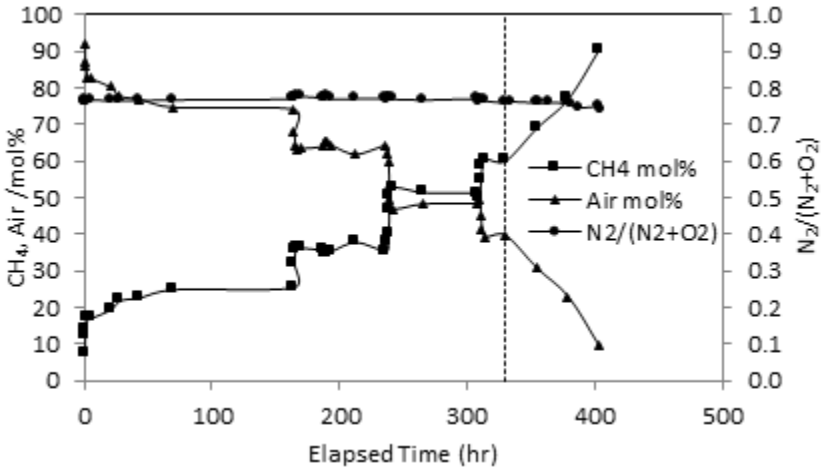

Figure 6.3 *Vapour phase methane and air concentrations, $N_2/(N_2+O_2)$ at 273.2K (Experiment 13).*

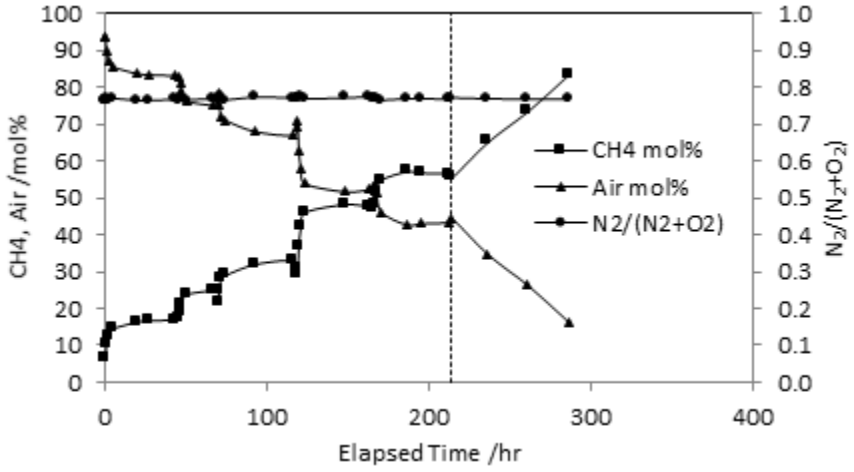

Figure 6.4 *Vapour phase methane and air concentrations, $N_2/(N_2+O_2)$ at 278K (Experiment 14).*

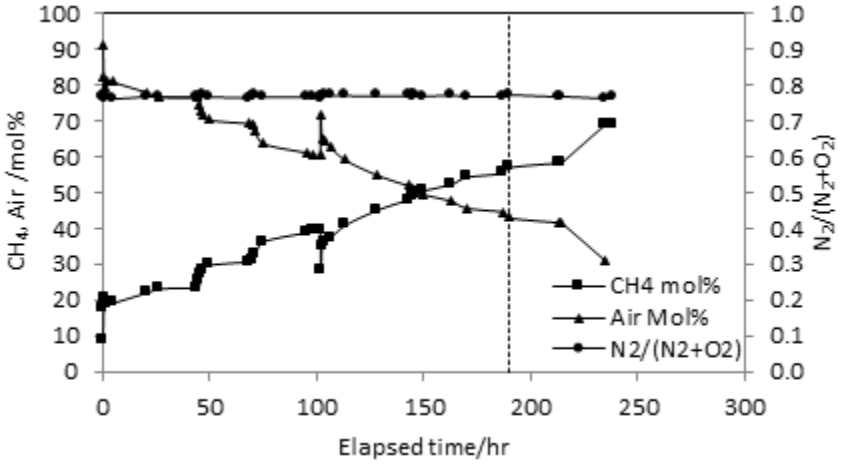

Figure 6.5 *Vapour phase methane and air concentrations, $N_2/(N_2+O_2)$ at 283K (Experiment 15).*

6.3.2 Methane recovery ratios

The kinetics of methane recovery after injection of compressed air was investigated in the multi-stage phase where it was desired to achieve a vapour phase composition of 60 mol% methane in the presence of air in an isochoric system. Given the expected vapour phase composition, the target pressure was predicted by HydraFLASH. Methane hydrate decomposition was achieved by equilibrium phase boundary shift in the presence of air from an air rich region to a methane rich region.

Table 6.2 below shows the initial pressure, target/desired set pressure, pressure reached at equilibrium, and vapour phase methane concentration achieved in each of the pressure stage for the experiments.

Table 6.2 *Initial pressure, target pressure, equilibrium pressure, and vapour phase methane concentration*

Experiment	Stage	Initial P (MPa)	Desired Set P (MPa)	P at equilibrium (MPa)	CH_4 (mol%)
13 (273.2 K)	1	15.00	11.38	8.04	25.7
	2	8.00	6.25	6.59	35.8
	3	6.60	5.73	5.93	38.6
	4	5.97	4.16	4.84	51.4
	5	4.84	3.92	4.22	60.3
14 (278 K)	1	23.61	17.32	16.69	16.9
	2	16.69	12.29	12.92	24.9
	3	12.92	10.49	11.03	32.9
	4	11.12	7.38	8.44	56.5
	5	8.44	6.65	7.27	56.5
15 (283 K)	1	38.51	26.98	26.93	23.5
	2	26.93	18.76	19.85	30.6
	3	19.85	15.94	16.63	39.2
	4	16.79	11.79	13.39	47.9
	5	13.39	10.45	11.22	55.3

It is seen from **Table 6.2** that at the end of Stage 5 in each of the experiments, having successively brought the system to the target pressure for the desired vapour phase methane concentration and allowing enough time for the system to reach equilibrium afterwards, the maximum vapour phase methane concentration was 60.3 mol%, 56.5 mol%, and 55.3 mol% respectively for Experiments 13, 14, and 15.

Since the experiments were set in an isochoric system, methane release from methane hydrate should be indicated by both the increasing vapour phase methane concentration and increasing system pressure. An interesting phenomenon was observed in the equilibrium pressure at the end stage 1 in the three experiments as seen in **Table 6.2**. It is seen that equilibrium pressure reached at the end of Stage 1 is less than target/set pressure to initiate methane hydrate decomposition.

Upon setting the system pressure to desired set point in the first stage, it is expected that system pressure increase continuously due to rapid methane hydrate decomposition and subsequent methane release into the vapour phase. However, it was observed that as the system pressure drops below the air phase boundary, for instance 23.61 MPa in Experiment 14 down to 17.32 MPa, there was an initial surge in pressure as expected owing to rapid methane hydrate decomposition. This increase in pressure lasted only a short time, then followed gradual decrease in system pressure (**Figure 6.6**) despite

increasing vapour phase methane concentration. It is believed that after the initial methane hydrate decomposition and surge in pressure, methane hydrate decomposition reduced. At this point the system is dominated by the inclusion of the components of air into the hydrate phase as the system pressure is close to air hydrate phase boundary at the experimental temperature. Thus, the continued increase in the vapour phase methane concentration is as a result of the reduction in the amount of the air component of the vapour phase rather than methane hydrate decomposition.

This is in contrast to the observations in Stages 2-5 in the three experiments where, as expected equilibrium pressure reached at the end of each stage increased from the target/set pressure due to methane release into the vapour phase. The pressure profiles for stages 1- 5 in Experiments 13-15 are shown in **Figure 6.7** to **Figure 6.9** respectively.

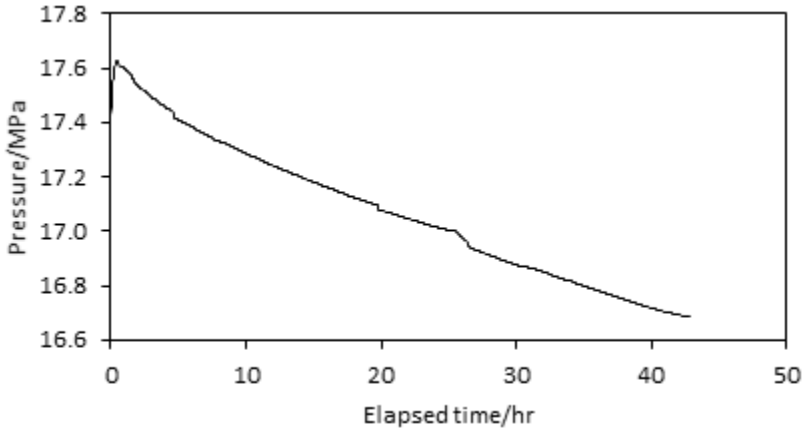

Figure 6.6 *Pressure profile during stage 1 of the kinetic recovery phase in Experiment 14 showing pressure reduction.*

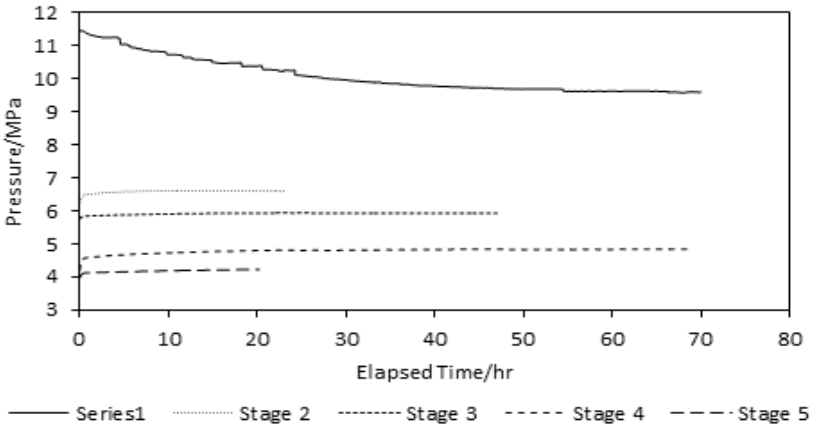

Figure 6.7 *Pressure profiles for stages 1-5 for Experiment 13(273.2K)*

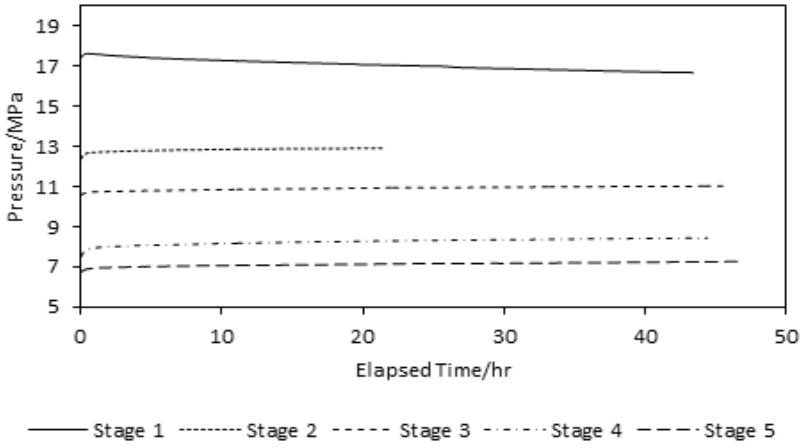

Figure 6.8 *Pressure profiles for Stages 1-5 for Experiment 14(278K)*

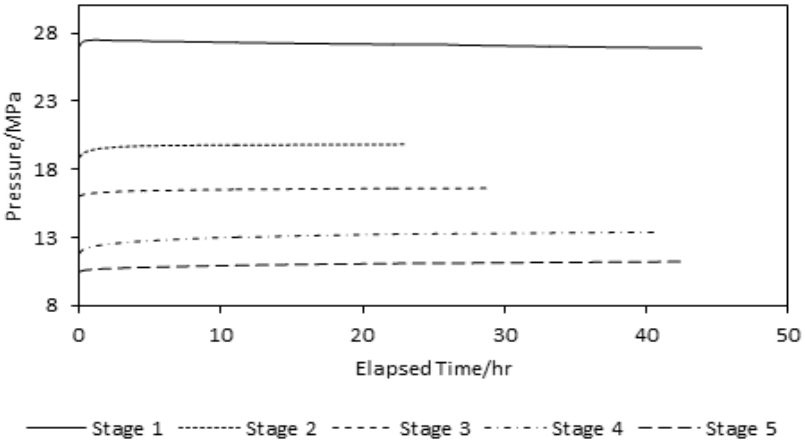

Figure 6.9 *Pressure profiles for Stages 1-5 for Experiment 15(283K)*

The evolution of the vapour phase methane concentration is shown graphically in **Figure 6.10**. As seen in the figure, methane recoveries in each of the successive pressure stages are distinct from each other and continue to increase to the last pressure stage. Two recovery trends can be observed in each individual curve; an initial fast methane recovery followed by a slower recovery that tend to a plateau as the system approaches equilibrium. The fast recovery, as noted earlier is caused by a shift in the methane hydrate equilibrium phase boundary in the presence of air leading to rapid dissociation of methane hydrate which continues and starts to slow down as the system approaches a new thermodynamic equilibrium.

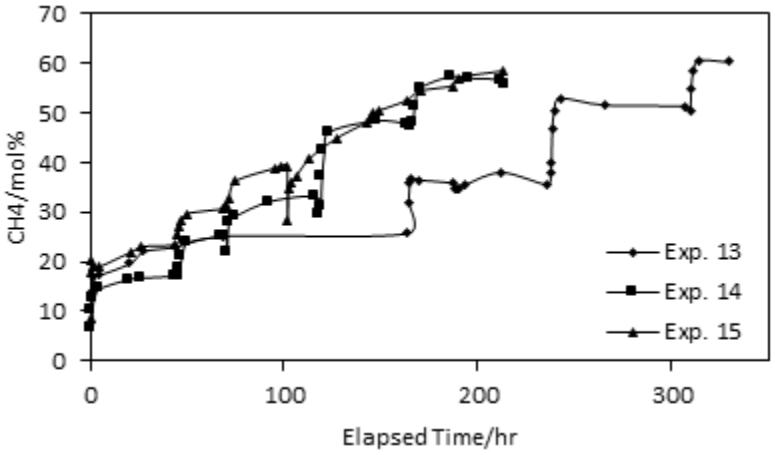

Figure 6.10 *Evolution of the vapour phase methane concentration during the multi-stage depressurisation phase for Experiments 13, 14, and 15.*

6.3.3 Kinetics of methane recovery in the presence of air

Figure 6.11to **Figure 6.13** show quantitatively, the amount of methane released in each stage of the multi-stage depressurisation recovery phase. The amount released was cumulated from stage 1 to stage 5 in each of the experiments. It could be seen that methane release could also be divided into two sub-stages; a first sub-stage in which methane release was rapid and a second sub-stage in which methane release slows down and gradually reduces with equilibrium. For example, in Stage 1 of the multi-stage depressurisation phase at 278 K (Experiment 14), of a total of 0.15 mole of methane released as shown in **Figure 6.14**, 0.12 mole was released during the first 5 hours, representing 80% of total mole released. The remaining 0.13 mole representing only 20% of total mole released was released for the rest of the time as the system reaches a new thermodynamic equilibrium.

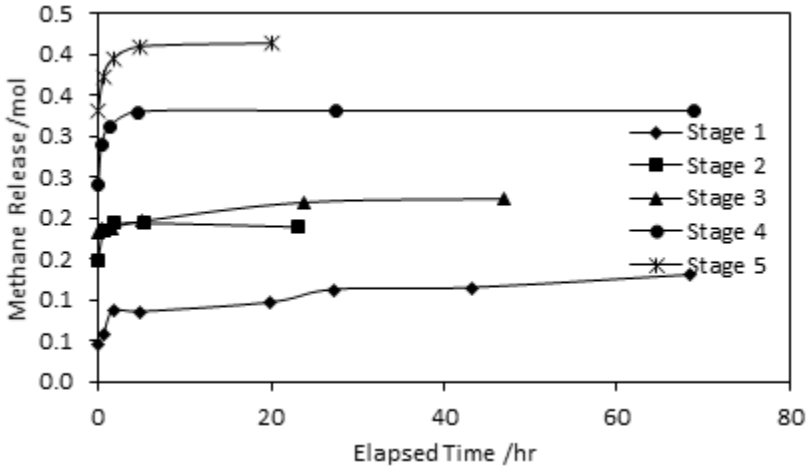

Figure 6.11 *Amount of methane released from the hydrate phase into the vapour phase in each of the pressure stages for Experiment 13.*

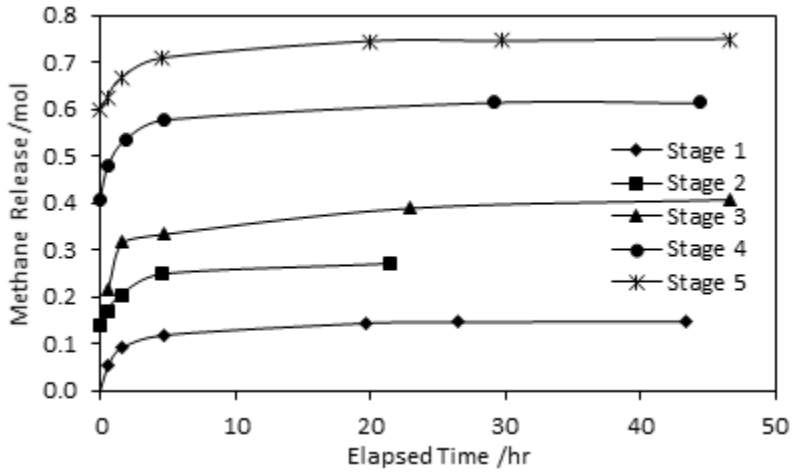

Figure 6.12 *Amount of methane released from the hydrate phase into the vapour phase in each of the pressure stages for Experiment 14.*

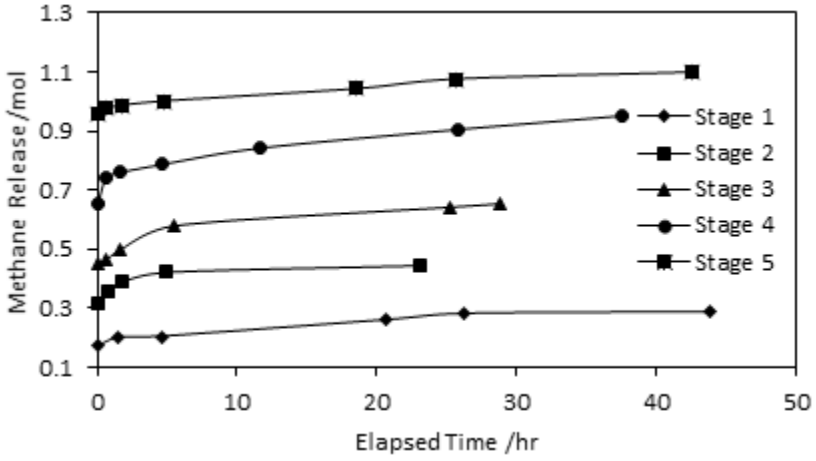

Figure 6.13 *Amount of methane released from the hydrate phase into the vapour phase in each of the pressure stages for Experiment 15.*

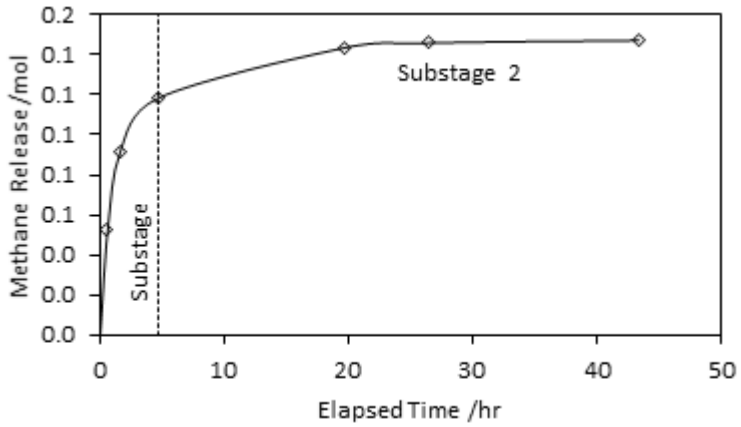

Figure 6.14 *Methane release in stage 1 of the kinetic recovery phase at 278K (Experiment 14).*

The percentage methane recovery and the rates of recovery in the sub-stages are estimated using **Equations 3.1** and **3.2**.

Table 6.3 *Summary of recovery experiments during the multi-stage depressurisation phase showing rate of methane recovery, amount of methane released from methane hydrate and percentage methane recovery*

		Methane release rate/mol/hr			
Experiment	Stage	Sub-stage 1	Sub-stage 2	Amount released (mole)	Percentage methane recovery/%
	1	0.0246	0.0007	0.10	9.2
	2	0.0227	0.0003	0.19	17.5
13	3	0.0034	0.0008	0.22	20.5
(273.2 K)	4	0.0455	0.0005	0.33	30.4
	5	0.0343	0.0008	0.41	38.0
	1	0.0555	0.0013	0.15	12.6
	2	0.0416	0.0027	0.27	23.3
14	3	0.0904	0.0017	0.41	35.0
(278 K)	4	0.0646	0.0015	0.61	52.8
	5	0.0441	0.0023	0.75	64.4
	1	0.116	0.0034	0.29	33.1
15	2	0.0418	0.0013	0.45	51.4
(283 K)	3	0.0301	0.0033	0.66	75.4
	4	0.0613	0.0052	0.84	96.9

Amount of methane released from methane hydrate during the first depressurisation phase of recovery increased from 0.10 mole to 0.41 mole at 273.2 K (Experiment 13), 0.15 mole to 0.75 mole at 278 K (Experiment 14), and 0.29 mole to 0.84 mole at 283 K (Experiment 15). These correspond to recoveries of 38.0%, and 64.4% for Experiments 13 and 14 respectively, and by the fourth stage of Experiment 15, 96.9% recovery had

been achieved. This is in spite of the vapour phase methane concentration at the end of the kinetic phase being slightly higher at 60.3 mol% at 273.2 K (Experiment 13), while it is 56.5 mol% at 278 K (Experiment 14) and 55.3 mol% at 283 K (Experiment 15) respectively as reported in **Table 6.2**. The increasing amount of methane recovery with temperature is attributed to hydrate equilibrium pressure. At higher temperatures, the hydrate equilibrium pressure is higher, implying a higher gas phase density. Therefore, to achieve a given vapour phase methane concentration, more methane needs to be released from the hydrate at higher temperature than at lower temperatures. Methane hydrate synthesis was carried out such that about 50% methane hydrate saturation was achieved at the end of methane hydrate formation in all experiments.

The evolutions of the percentage methane recoveries are shown in **Figure 6.15** to **Figure 6.17**. As expected, they follow the same trend as methane release and are cumulated from stage 1 to stage 5 in each experiment. As seen in **Figure 6.17** (Experiment 15), at 16 hours into stage 4, 100% recovery had been achieved. This shows as explained earlier that high temperatures favours methane hydrate decomposition and consequently, methane recovery.

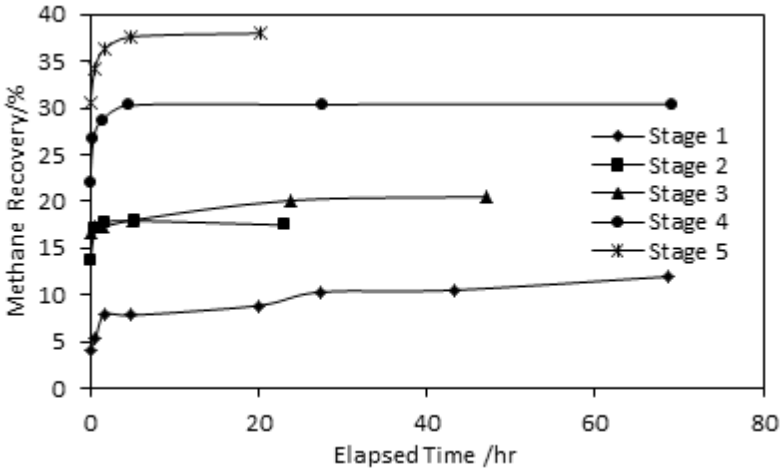

Figure 6.15 *Percentage methane recovery for each of the stages during the multi-stage depressurisation recovery phase at 273.2 K (Experiment 13).*

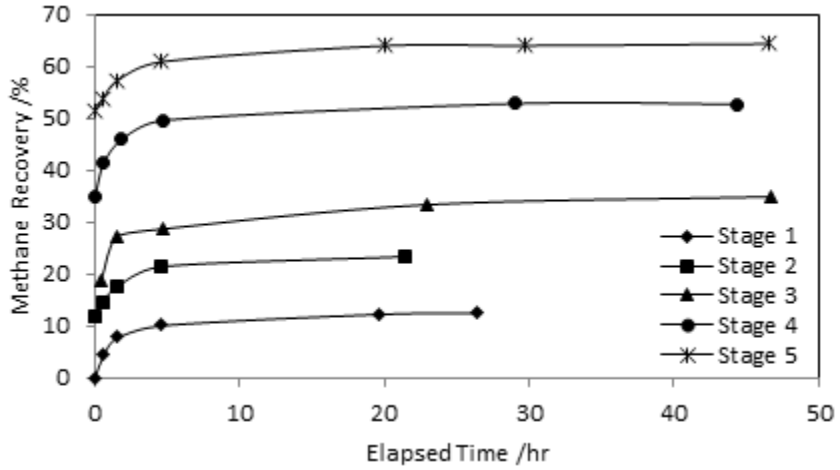

Figure 6.16 *Percentage methane recovery for each of the stages during the multi-stage depressurisation recovery phase at 278 K (Experiment 14).*

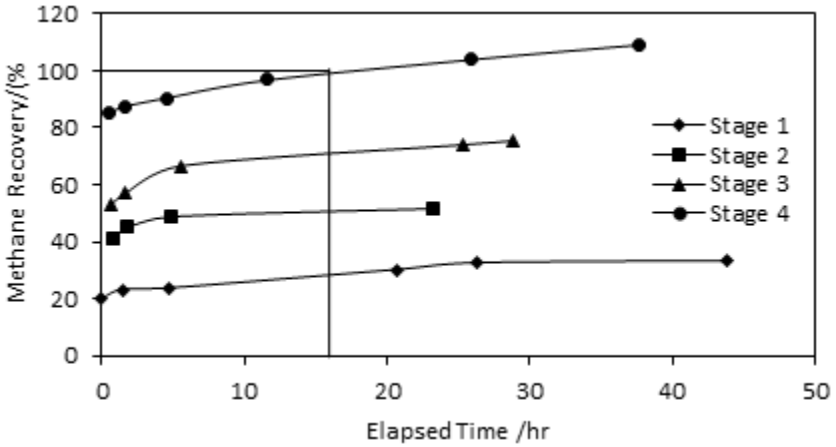

Figure 6.17 *Percentage methane recovery for each of the stages during the multi-stage depressurisation recovery phase at 283K (Experiment 15).*

6.3.4 Depressurisation for enhanced recovery

For complete hydrate decomposition and maximum methane recovery after the kinetic studies of the multi-pressure depressurisation phase, the system was subjected to extended depressurisation in steps. Each depressurisation step lasted 24 hours to ensure equilibrium was reached. **Figure 6.18** is a plot of vapour phase methane concentrations during the entire depressurisation phases. The dashed vertical lines represent the dissociation pressure lines of methane hydrate at the corresponding experimental temperatures. In Experiments 14 and 15, the maximum vapour phase methane concentrations, 84 mol% and 69 mol% respectively were achieved before the methane hydrate dissociation pressure was reached. This indicates that in the presence of compressed air, methane hydrate was completely decomposed at 4.87 MPa in

Experiment 14 (i.e. 0.56 MPa above methane hydrate dissociation pressure at 278 K), and 7.52 MPa in Experiment 15 (i.e. 0.4 MPa above methane hydrate dissociation pressure at 283 K). For Experiment 13, complete methane hydrate decomposition was not achieved before system pressure drops below the methane hydrate phase boundary. However, vapour phase methane concentration exceeded 77.1 mol%. Complete methane hydrate decomposition was however achieved when system pressure dropped beyond methane hydrate dissociation pressure (2.72 MPa at 273.2 K) as evidenced by maximum vapour phase methane concentration of 90.5 mol%.

From the foregoing, it is evident that the injection of compressed air into methane hydrate-bearing sediment leads to methane hydrate decomposition at pressures above the methane hydrate dissociation pressures at the prevailing temperatures. A major benefit of this technique is cost saving due to the abundant availability of air. In terms of methane recovery, the technique leads to minimisation of the extent of depressurisation required to decompose methane hydrate, that is, the reservoir does not need to be depressurised below the methane hydrate dissociation pressure. The minimised depressurisation leads to reduced drawdown between the production well and the reservoir, consequently, reduced water and sand flow to the well. The high pressure gas production could also minimise the requirement for external pumps to lift produced water as obtainable in conventional depressurisation. Furthermore, this technique has the potential to improve the feasibility of methane recovery by depressurisation in gas hydrate reservoirs, especially in severe reservoir conditions such as low permeability or low hydrate saturations.

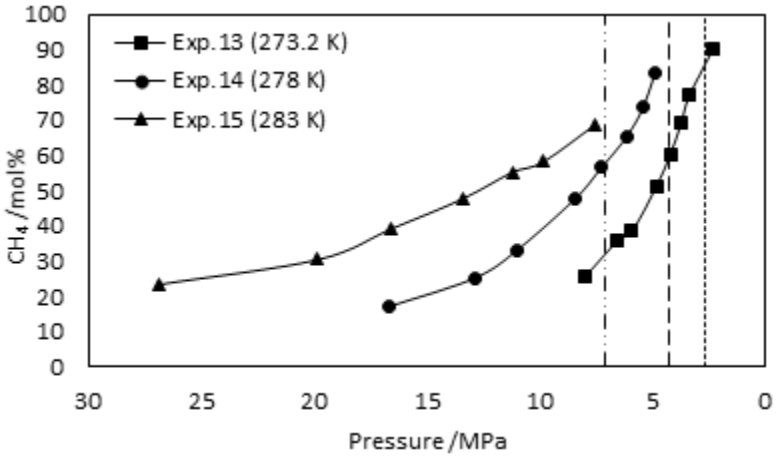

Figure 6.18 *Vapour phase methane concentration during the entire depressurisation phases in the presence of compressed air. Dotted vertical lines (·····) (– – – –) (— · · — ·) represents decomposition pressure of methane hydrate at 273.2 K, 278 K, and 283 K respectively. Methane hydrate starts to decompose well inside the methane hydrate stability zone.*

6.4 Summary

A series of experiments were conducted to study the feasibility of methane recovery from methane hydrate reservoirs by compressed air injection. This is of importance in the quest for the development of economically viable and environmentally responsible technique for recovering the vast quantities of methane trapped in the earth as methane hydrate. Compressed air injection enabled methane recovery in a multi-stage depressurisation process. The first phase was designed to study the kinetics of methane release from methane hydrate in the presence of air and the second phase was to maximise methane recovery. Methane recovery was achieved by shifting the methane hydrate equilibrium phase boundary to accommodate the presence of air, consequently decomposing methane hydrate. In each pressure stage, two trends of methane release were observed; a fast release stage indicated by a surge in vapour phase methane concentration owing to rapid decomposition of methane hydrate, followed by a slow release stage as the system approaches to a new thermodynamic equilibrium.

Methane release kinetics increases with temperature as indicated by the percentage methane recovery of 37.99%, 64.36% for Experiment 13 (273.2 K) and Experiment 14 (278 K). It was 96.86% by the fourth pressure stage of Experiment 15 (283 K). Vapour phase composition analysis indicates that there is no preferential inclusion of either component of air into the hydrate phase. Decrease in system pressure was observed in the first pressure stage in all experiments despite increasing vapour phase methane

concentration. In the other pressure stages, system pressure increases as expected. This implies that when system pressure was just below the air phase boundary at the experimental temperature, inclusion of air into the hydrate phase dominates, but when the system pressure is far away from the air phase boundary, methane hydrate decomposition dominates.

Depressurisation was used to enhance methane recovery at the end of the kinetic recovery phase. The presence of compressed air enabled complete decomposition of methane hydrate at pressures above the dissociation pressures of methane hydrate at the prevailing experimental temperatures. Complete decomposition was achieved at 4.87 MPa in Experiment 14 (0.56 MPa above methane hydrate dissociation pressure at 278 K), 7.52 MPa in Experiment 15 (0.4 MPa above methane hydrate dissociation pressure at 283 K).

Compressed air injection enabled high pressure production of methane from methane hydrate bearing sediment. High pressure production would reduce the drawdown between the reservoir and the production well. This will consequently reduce the flow of free water and sand migration to the production well. It could also facilitate the application of conventional depressurisation operation to produce methane from Class 1, Class 2, and Class 3 hydrate deposits.

CHAPTER 7 EXPERIMENTAL STUDY OF GAS PERMEATION THROUGH GAS HYDRATE-BEARING SEDIMENTS

7.1 Introduction

Natural gas production from natural gas hydrate reservoirs is gaining unprecedented attention due to its reputation as a potential future source of low carbon energy. Consequently, a lot of research effort is targeted at developing techniques to commercially produce gas from natural gas hydrates in an environmentally sustainable manner. Many laboratory experiments have demonstrated the feasibility of different recovery processes. Also, a few pilot tests have been carried out with varying degrees of success. However, to fully understand, design, and operate a natural gas hydrate reservoir, there is need to develop simulators that will accurately predict the behaviour of gas recovery over a long period.

Inherent challenges in achieving this are the uncertainties in hydrate dissociation phenomena (process) in porous media and the preponderance of unknown parameters. Chief among these parameters is the permeability of the porous media in the presence of hydrates. Permeability of hydrate bearing sediments reduces due to porosity reduction as hydrate nucleates and grows in the porous medium. This permeability reduction varies in extent depending on hydrate formation sites in the porous medium. If hydrate forms a coat on the surfaces of grains, permeability reduction is minimal and its effect on fluid flow is also minimal [233]. If a hydrate forms in the middle of pores, its effect on fluid flow is pronounced and permeability reduces to zero if pore body is completely blocked [233]. Thus, permeability in the presence of hydrate changes as hydrate dissociates. This change imparts directly on pressure communication, fluid flow and ultimately, gas production from hydrate bearing sediments.

Permeability measurements using natural core samples in in-situ conditions from hydrate bearing sediments is often difficult to achieve [234, 235]. Pressure coring [236] helps to maintain the samples at near in-situ conditions but does not completely eliminate sample disturbance during coring. Also, creep and diffusion processes may cause hydrate re-distribution and alter physical properties of the cores when pressure cores are stored for a long time [234]. Laboratory synthesis of artificial hydrate cores is therefore a viable alternative for permeability measurements and studies. It has the flexibility of synthesising hydrates with characteristics of interest such as saturations

and preparation processes. Different hydrate synthesis processes have been reported in literature; ice seeding [237, 238]; excess gas method [206], excess water method [239], dissolved gas method [240]. Hydrate formation method have been reported to have strong influence on the hydrate formation sites in the porous medium [239]. For this study, excess gas method was used for the following reasons: low water saturation was desired, ease of achieving desired hydrate saturation, and most importantly because the tests were intended for gas permeability measurements.

Kneafsey et al., [235] performed gas permeability measurements on partially saturated sand packs under confining stress. They measured gas permeability for wet, frozen, hydrate-bearing, and dry samples. Using computer tomography (CT) scanning, they observed processes that are spatially dependent. They reported decreasing effective permeability as the pore spaces in their sample became increasingly occupied as they measured permeability from wet to hydrate bearing for each sample. Kleinberg et al. [233] used NMR to study hydrate formation, hydrate growth, and its effect on relative permeability of water. They reported that at substantial hydrate saturation, NMR relaxation time measurements showed that hydrate preferentially replaced water in the largest pores rather than coating grain surfaces. The relative permeability to water reduced significantly. The extent of the reduction, they noted agreed with hydrate formation in pore bodies rather than on grain surfaces. Kumar et al. [241] measured gas permeability using carbondioxide hydrate formed in packed glass beads. They compared their experimental data with values from empirical correlations. They observed a critical hydrate saturation of 35%. Below this, hydrate tends to form on grain surfaces and above this hydrate from at the centre of pores.

In the absence of sufficient experimental data, empirical models have been used in numerical simulators. These models, though helpful, shows wide variations with measured data due to assumptions made in their development. Furthermore, they do not account for differences in hydrate formation processes, sediment mineralogy, and compaction as obtainable in natural environments.

This chapter investigates the gas permeability-pressure relationship in unconsolidated silica sand, silica sand-montmorillonite cores, and solid sandstone core as the basis for understanding the behaviour in hydrate bearing cores and the effect of mineralogy on gas flow. Gas permeation in varying hydrate saturations in both the unconsolidated

silica sand-montmorillonite cores and in solid sandstone core were studied for peculiarities of gas flow in hydrate bearing sediments. The measured gas permeabilities were compared with predictions of existing permeability reduction models for performance analysis and discussed.

7.2 Experimental Section

7.2.1 Materials

Methane, distilled water, and silica (Fife) sand as described in **Section 3.3** were used in the experiments. Montmorillonite from supplied by 'The Clay Cure' was used. The montmorillonite has an average particle diameter of 10.5 μm and a specific surface area of 0.566 m^2/g. The particle size distribution is shown in **Table 7.1** and **Figure 7.1**.

Table 7.1 *Particle size distribution of the montmorillonite used in the experiments*

Size (μm)	Ratio (mass%)	Size (μm)	Ratio (mass%)	Size (μm)	Ratio (mass%)	Size (μm)	Ratio (mass%)	Size (μm)	Ratio (mass%)
80.0	0.7	20.1	3.4	5.1	2.8	1.3	0.7	0.3	0.1
71.9	0.9	18.1	3.4	4.6	2.7	1.2	0.6	0.3	0.1
64.7	1.2	16.3	3.3	4.1	2.6	1.0	0.5	0.3	0.1
58.2	1.6	14.6	3.3	3.7	2.4	0.9	0.4	0.2	0.1
52.3	1.9	13.2	3.2	3.3	2.3	0.8	0.4	0.2	0.1
47.1	2.2	11.8	3.1	3.0	2.1	0.8	0.4	0.2	0.1
42.3	2.5	10.7	3.0	2.7	2.0	0.7	0.3	0.2	0.0
38.1	2.8	9.6	3.0	2.4	1.8	0.6	0.3	0.2	0.0
34.2	3.0	8.6	3.0	2.2	1.5	0.6	0.3	0.1	0.0
30.8	3.1	7.8	2.9	2.0	1.4	0.5	0.3	0.1	0.0
27.7	3.2	7.0	2.9	1.8	1.2	0.4	0.2	0.1	0.0
24.9	3.3	6.3	2.9	1.6	1.0	0.4	0.2	0.1	0.0
22.4	3.4	5.6	2.8	1.4	0.8	0.4	0.2		
Mass medium = 10.5 μm				Specific surface area = 0.566 m^2/g					

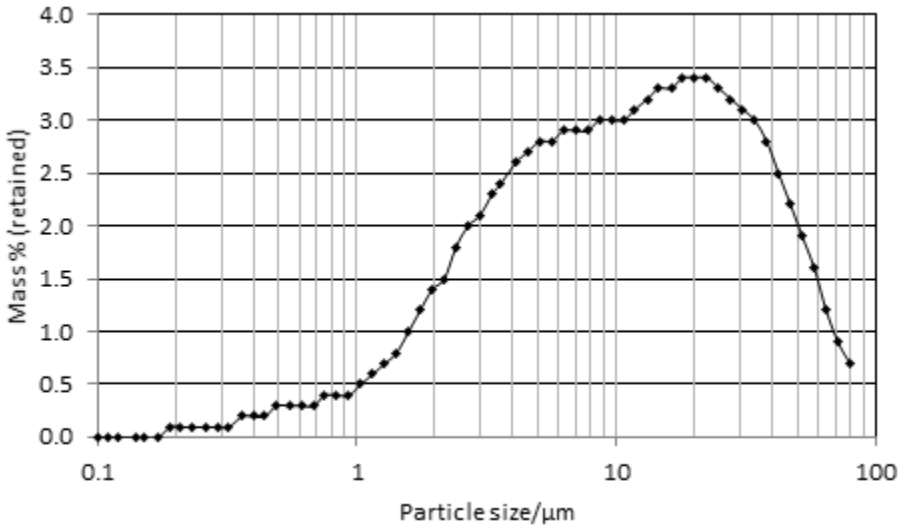

Figure 7.1 *Particle size distributions of the montmorillonite used in graphical form.*

7.2.2 Experimental apparatus and set-up

The core holder used for permeability measurements is shown schematically in **Figure 7.2**. It is made of cylindrical stainless steel pressure vessel of 4 cm and 10.8 cm inner and outer diameter respectively and a total length of 34 cm. It also has two threaded stainless steel endcaps, one for each end. The endcaps have 1/8" diameter holes to serve as connections for fluid inlet and exit. Inside the pressure vessel is a Viton rubber sleeve of 4 cm internal diameter and 19.5cm in length. The Viton rubber sleeve serves to hold the packed sand. The sleeve is connected to both endcaps as shown in **Figure 7.2**. Two ports are provided on the body of the pressure vessel, one midway through the length of the vessel to provide radial confining pressure and the other, near one end of the vessel to provide axial confining pressure if needed.

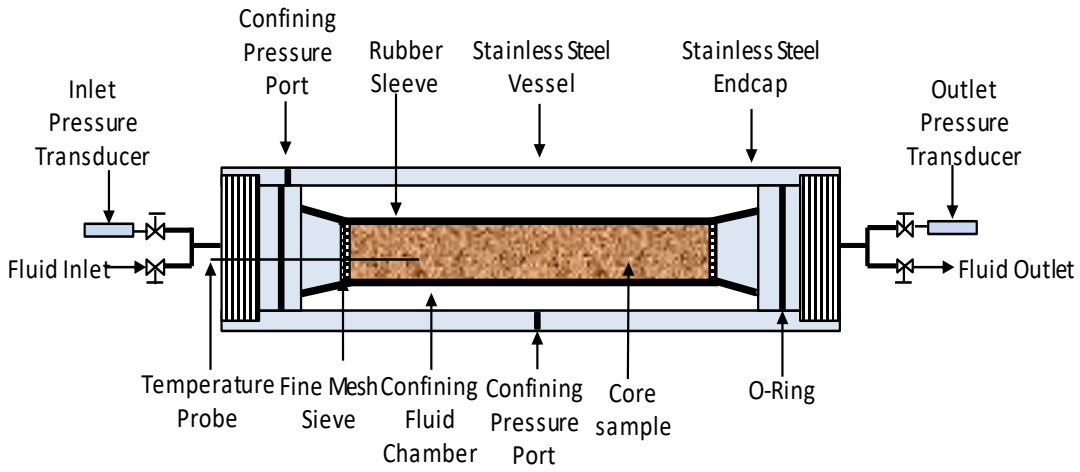

Figure 7.2 *Schematic of core holder used for permeability measurement.*

Figure 7.3 shows the experimental set-up for permeability measurements. A copper coil was wound round the pressure vessel and connected to the cryostat for cooling fluid circulation. The pressure vessel was then completely immersed in the water bath that was completely lagged to prevent heat interaction with the environment. Quizix pump was connected to the pressure port at the middle of the cell through valve V7 to inject confining fluid (water) into the confining fluid chamber and to maintain a constant confining pressure. The confining pressure was always maintained at 3.5 MPa higher than the pore pressure as the seal sealing the Viton rubber sleeve and the endcaps could break if the pore pressure exceeds the confining pressure. Methane gas from the methane bottle is injected into the core sample in the sleeve through the inlet valve V1 and exits through the outlet valve V3. The methane gas is pre-cooled to approximately the temperature of the water bath by passing it first through a 1m length of 1/8" pipe wound into a coil (not shown in the diagram-**Figure 7.3** to avoid complications) and immersed in the water bath before entering into the cell. A back-pressure regulator is connected to the exit line to maintain the pore pressure above the hydrate dissociation pressure during permeability measurements. Gas exiting the back-pressure regulator then flows into a gas flow meter to measure the flow rate and then vented. Two Quartzdyne pressure transducers measures the inlet and outlet pressure. A PRT thermal probe attached to the body of the vessel measures the system temperature. Data from the pressure transducers, the thermal probe, and the Quizix pump are acquired by the data acquisition system (DAS) and stored in the PC.

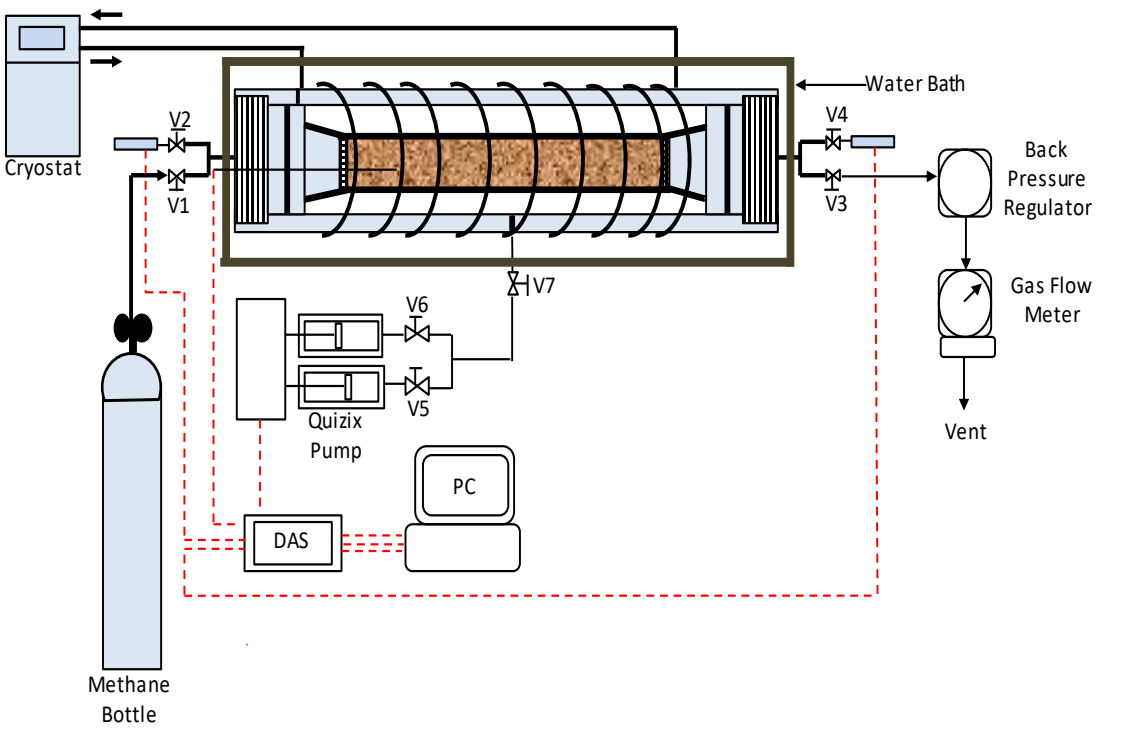

Figure 7.3 *Schematic diagram of the experimental set-up for permeability measurement. The dashed red lines represent cables for electrical communications while the black solid lines represent conduits for fluid flow.*

7.2.3 Experimental procedure

7.2.3.1 Gas permeability measurement in the absence of hydrate

The silica sand used is Fife (Scotland) sand. Its properties are already described in **Section 3.3**. The silica sand used was dried in the oven at 343 K for 24 hours. The endcap of the inlet end of the pressure vessel with the fine mesh sieve was put in the Viton rubber sleeve and placed upright. A given quantity of sand, partially saturated with water was packed into the cell. The sand was fed into the sleeve in layers and the desired packing was achieved using a cylindrical pestle rod. Then another fine mesh sieve was put at the open end of the core, the core was put in the pressure vessel, and the endcaps fixed to hold the core in place. The gas entry line from the methane bottle was then connected. Also, the exit line was connected to the gas flow meter via the back-pressure regulator. The pressure vessel was immersed in the water bath, and vacuumed. The back-pressure regulator was set to 3.45 MPa while also setting the inlet pressure to 3.45 MPa using the regulator on the methane supply vessel, while valves V1 and V3 were closed so as to disconnect the core from gas sources. Confining pressure was then applied incrementally via the Quizix pump while also injecting methane gas

into the core until the pore pressure was 3.45 MPa and the confining pressure was 6.9 MPa. The inlet and outlet valves were then fully opened to allow for gas flow. When constant flow rate was achieved, the inlet and outlet pressures were recorded to estimate the differential pressure across the core and the effective permeability to gas using **Equation 7.6**.

7.2.3.2 Methane hydrate formation in the porous media

Same mass of sand used in permeability measurement in the absence of hydrate was used in all other experiments. The sand was moistened with distilled water to achieve a predetermined water saturation. Then packing into the Viton rubber sleeve, and vacuuming was done following the same procedure described in **Section 7.2.3.1** above. Confining pressure was then applied incrementally while injecting methane gas into the core to the desired pressure for hydrate formation. The confining pressure was maintained at 3.5 MPa above the pore pressure via the Quizix pump. The system temperature was then set to 293 K and allowed to equilibrate. When equilibrium was achieved, the system temperature was set to 273.2 K to initiate methane hydrate formation. As the pore pressure reduced gradually due to gas consumption for hydrate formation, the confining pressure was also reduced accordingly to maintain the 3.5 MPa difference. This continued until pressure change becomes insignificant signifying the completion of hydrate formation.

7.2.3.3 Gas permeability measurement in the presence of hydrate

Permeability to gas in the presence of methane hydrate was measured for varying methane hydrate saturations. Upon completion of hydrate formation, the back-pressure regulator was set to 3.45 MPa to maintain a constant back pressure. For pore pressure in excess of 3.45 MPa after hydrate formation, the excess gas was released, and for pore pressure less than 3.45 MPa, gas was injected from the methane supply vessel. This ensures that the pore pressure was above the three phase (*Lw-H-V*) methane hydrate equilibrium phase boundary at 273.2 K at which no hydrate dissociation occurs. The inlet pressure was set to 3.45 MPa with the aid of the regulator on the methane supply cylinder. The inlet and outlet valve were then closed to allow the system to attain pressure equilibrium. After equilibrium was attained, both valves were opened for gas flow through the core. When flow rate stabilized, the inlet and outlet pressure were

recorded to estimate the differential pressure across the core. The permeability to gas of the core was then computed using **Equation 7.6**.

7.3 Gas Permeability Calculation

The superficial gas velocity can be assumed to obey assumed to obey Darcy's law and expressed as:

$$U_g = -\frac{K_g}{\mu_g}\frac{dP_g}{dL} \qquad 7.1$$

Where U_g is the superficial gas velocity in cm^3/sec, K_g is the gas phase permeability in *darcy*, D, μ_g is the gas viscosity in centipoise, cp, and P_g is the gas pressure in atmosphere, atm.

The mass flow rate of gas is defined as:

$$\dot{m} = \rho_g U_g A \qquad 7.2$$

Where A is the cross sectional area of the porous media, and ρ_g is the density of gas.

It is assumed that the gas obeys ideal gas law, then

$$\rho_g = \frac{P_g M_w}{RT_g} \qquad 7.3$$

Where M_w is the gas is molecular weight, R is the universal gas constant and T_g is the gas temperature.

From mass conservation equation at steady state:

Mass flow into core = Mass flow out of core

$$\rho_{gi} U_{gi} A = \rho_{go} U_{go} A = \rho_{stp} q_{stp} \qquad 7.4$$

Where the subscripts *i* and *o* denotes in and out, ρ_{stp} is the gas density at standard temperature and pressure, and q_{stp} is the gas flow rate flow rate at standard temperature and pressure. Standard temperature and pressure is taken as 298.15 K and 1 atm (101.3 KPa).

Substituting **Equations 7.1** and **7.3** into **Equation 7.4** gives

$$P_g\left(-\frac{K_g}{\mu_g}\frac{dP_g}{d_L}\right)=P_{stp}\frac{q_{stp}}{A} \qquad 7.5$$

Integrating both sides of the equation and re-arranging gives:

$$K_g=\frac{2\mu_g P_{stp} q_{stp} L}{A\left(P_{gi}^2-P_{go}^2\right)} \qquad 7.6$$

Equation 7.6 was used to estimate gas permeability where μ_g is the gas viscosity in cp, P is the gas pressure in atm, q is the volumetric flow rate in cm^3/sec, L is the length of the core in cm, and A is the cross sectional area of the core in cm^2. It should be noted that the gas permeability depends on the squared pressure owing to the compressibility of the gas.

7.4 Experimental Results and Discussions

Gas flow characteristics of hydrate-bearing sediments were studied by permeability measurements in the presence and absence of hydrates. Two sediments composed of 100 mass% silica sand and 95 mass% silica sand + 5 mass% montmorillonite was used in the experiments. The introduction of 5 mass% montmorillonite was to enable the investigation of the effect on sediment mineralogy on gas flow. The initial properties of the unconsolidated core samples are summarised in **Table 7.2**.

Table 7.2 *Properties and initial parameters of the unconsolidated core samples used*

	100% Silica sand	95% Silica Sand+5% Montmorillonite			
Experiment	17	18	19	20	21
Height (cm)	15.5	15.5	15.5	15.5	15.5
Diameter (cm)	3.9	3.9	3.9	3.9	3.9
Volume (cm^3)	185.2	185.2	185.2	185.2	185.2
Grain density (g/cm^3)	2.65	2.65	2.65	2.65	2.65
Dry mass (g)	350	350	350	350	350
Volume of sediment (cm^3)	132.2	132.2	132.2	132.2	132.2
Porosity	28.6	28.6	28.6	28.6	28.6
Wet mass (g)	400	400	400	400	400
Gravimetric moisture content (mass%)	14.3	14.3	14.3	14.3	14.3
Wet density (g/cm^3)	2.16	2.16	2.16	2.16	2.16
Hydrate saturation (%)	0	0	32.6	35.8	47.5

7.4.1 Permeability-pressure relationship

Permeability measurements were conducted in the absence of hydrate for both types of sediment at incremental inlet pressures. **Figure 7.4(a)** and **(b)** shows the plots of differential pressure against permeability for both silica sand and silica sand-montmorillonite systems respectively. From these figures, it is seen that gas pressure affects gas flow characteristics of sediments differently depending on sediment mineralogy. **Figure 7.4(a)** shows that gas permeability increases linearly with differential pressure in silica sand sediment. On the other hand, in **Figure 7.4(b)**, it is seen that for the silica sand-montmorillonite sediment, gas permeability reduces with increasing differential pressure. The rate of reduction decreases with increasing differential pressure and tends to a constant of about 40 mD as the differential pressure continued to increase. Silica sand has large particle diameter (256.54 μm) and higher resistance to compaction by confinement, thus the reduction in intergranular and interconnected pore space is limited, hence restriction to gas flow is limited. On the other hand, the observation with the silica sand-montmorillonite sediment suggests that the onset of gas flow causes redistribution in the sediment mixture. The finer montmorillonite particles are redistributed in the bigger intergranular pore spaces of the silica sand. The redistribution formed fine pores. In such fine pores, Klinkenberg effect resulted in decreasing gas permeability with increasing differential pressure. From that point onward, gas permeability tends to a relatively constant value even with increasing differential pressure. This behaviour needs to be further studied as it could give

valuable insights into permeability variations in sandy sediments with varying proportions of clay for proper characterisation of gas flow in such sediments.

(a)

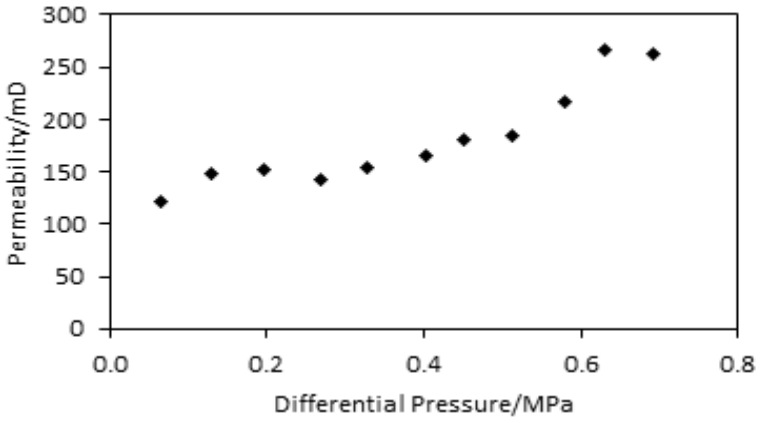

(b)

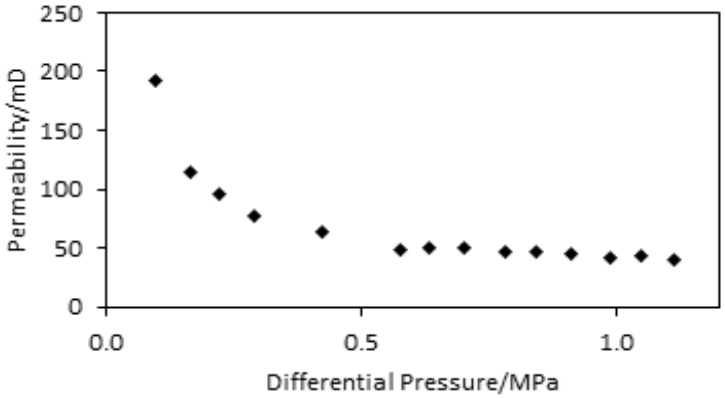

Figure 7.4 *Permeability changes with pressure, (a) represents silica sand system, and (b) represents silica sand-montmorillonite system.*

7.4.2 Permeability in the presence of hydrate

Permeability measurements were also conducted for the same silica sand-montmorillonite mixture in the presence of varying saturations of methane hydrate. Measurements were done for sediments with 33, 36, and 48 vol% hydrate saturations. **Figure 7.5(a)**, **(b)**, and **(c))** shows the measured gas permeabilities at 33, 36, and 48 vol% hydrate saturations respectively. An established trend is observed in which gas permeability increased initially reaching a maximum, then decreases gradually with increasing differential pressure. Maximum values obtained are 0.25 mD, 0.58 mD, and 1.71 mD for 33, 36, and 48 vol% hydrate saturations respectively. This observation may be attributed to two phenomena. Firstly, is hydrate heaving, a term used to

describe the slight pushing apart of sediment particles by the growing hydrate. The second is the capillary effect. Capillary sealing occurs in porous media with heterogeneous pore structures. The capillary sealing efficiency is measured by breakthrough pressure. The breakthrough pressure is the excess pressure of the non-wetting fluid phase (methane gas) at which the wetting phase is displaced enough to create a continuous flow path for the non-wetting phase. The flow path created is initially comprised of the largest interconnected pore spaces. Continued increase in pressure creates additional flow paths for the non-wetting fluid, thus increasing its permeability and saturation in the core. At this stage, the flow paths are less focused but more divergent, and the flow is no longer capillary dominated but viscous dominated. Beyond this point, the Klinkenberg effect became significant so that gradual decrease in the measured permeability observed as the differential pressure was increasing. **Figure 7.6** is a comparison of gas permeability in silica sand-montmorillonite core with and without hydrate. It is seen that gas permeability in the absence of hydrate is two to three orders of magnitude greater than gas permeability in the presence of hydrate. This is expected as hydrate occupation reduces the interconnected pore spaces in the core. However, an interesting phenomenon observed in the presence of hydrate is increasing gas permeability with increasing hydrate saturation. This is attributed to hydrate heaving noted earlier. It is believed the more the hydrate saturation, the stronger the effect of heaving, hence increasing permeability with increasing hydrate saturation.

(a)

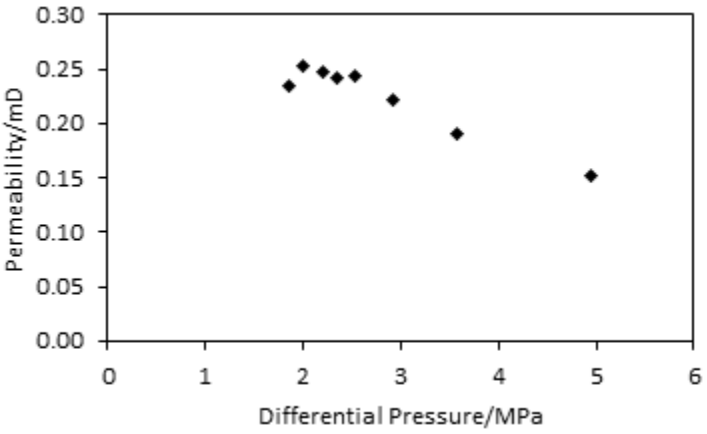

(b)

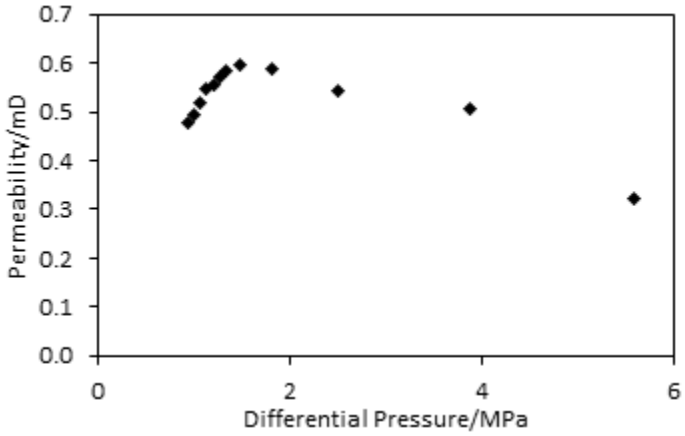

(b)

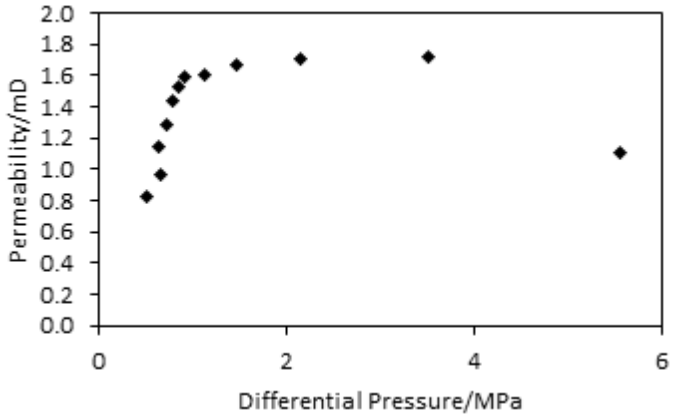

Figure 7.5 *Gas Permeability at varying hydrate saturations. (a), (b), and (c) represents silica sand-montmorillonite sediments with 33, 36, and 48 vol% hydrate saturations respectively.*

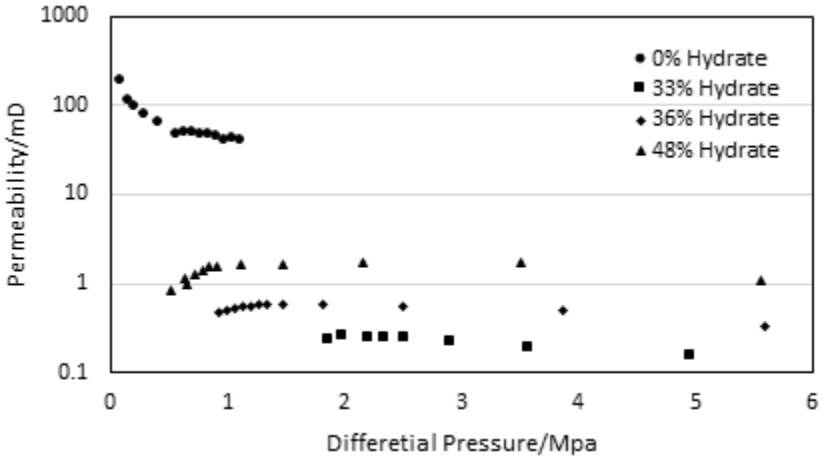

Figure 7.6 *Comparison of gas permeabilities in the presence of varying hydrate saturations and in the absence of hydrate.*

7.4.3 Permeability measurement in solid sandstone core

To investigate whether the observations in **Section 7.4.2** were as a result of particle migration or capillary force under variable pressure, the experiments were repeated with solid sandstone core of similar dimensions with the unconsolidated core. **Table 7.3** shows a summary of the initial parameters of the solid sandstone core sample.

Table 7.3 *Properties and initial parameters of the solid sandstone core samples used*

	Wet core	Hydrate -Bearing	
Experiment	22	23	24
Height (cm)	15.2	15.2	15.2
Diameter (cm)	3.8	3.8	3.8
Volume (cm^3)	172.3	172.3	172.3
Grain density (g/cm^3)	2.55	2.55	2.55
Dry mass (g)	355.6	355.6	355.6
Porosity	18.2	18.2	18.2
Wet mass (g)	372.7	372.7	372.7
Gravimetric moisture content (mass%)	4.8	4.8	4.8
Wet density (g/cm^3)	2162.9	2162.9	2162.9
Hydrate saturation (%)	0.00	15.0	44.0

Figure 7.7 shows gas permeability changes with pressure for the sandstone core sample without hydrate. It is seen that permeability increases with increasing differential pressure. This is similar to the observation in **Figure 7.4** (a) for unconsolidated silica sand core sample. **Figure 7.8** is a graph of gas permeability against differential pressure in the solid sandstone core with varying hydrate saturation. It is seen that gas

permeability decreases with increasing differential pressure, tending to a relative constant with continued increase in differential pressure. This could be explained to be due to the presence of fine pores after hydrate formation. In these fine pores, Klinkenberg effect also became significant. Therefore, the gradual decrease in gas permeability observed as the differential pressure was increasing. From the foregoing, it can be said that the strong capillary effect observed in the unconsolidated core sample is due to the presence of montmorillonite. Montmorillonite is a strong absorbent of water; this causes its particles to be strongly bonded together. Moreover, due to its small particle size, it could also fill up the large pore spaces created by silica sand particles. It is also observed in **Figure 7.9** that gas permeability decreases with increasing hydrate saturation as expected. This suggests that hydrate heaving is not significant in consolidated sediments. Furthermore, it is observed that gas permeability in the non-hydrate bearing core is 1 to 2 orders of magnitude higher than in the hydrate bearing core. As mentioned earlier, this is expected given that the presence of hydrate in the pore spaces reduces their interconnectivity. It is also seen that the differential pressure in the non-hydrate bearing core is about 2 orders of magnitude lesser than in the hydrate bearing core. The presence of hydrate requires a higher excess pressure to achieve breakthrough, and the restriction to flow also requires a higher differential pressure to achieve reasonable gas flow.

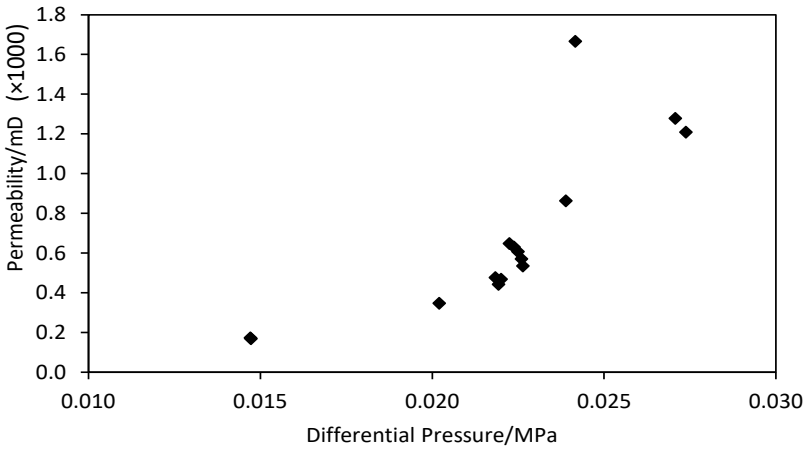

Figure 7.7 *Permeability changes with pressure in solid sandstone core sample in the absence of hydrate.*

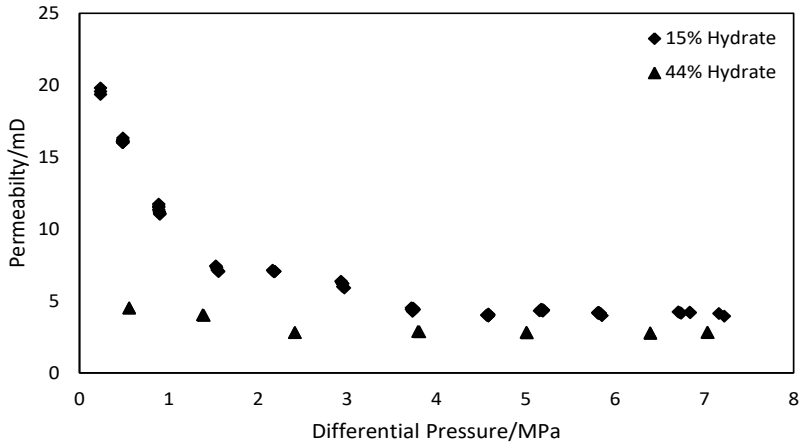

Figure 7.8 *Gas Permeability at varying hydrate saturations in solid sandstone core sample. (a) and (b) represents core samples with 15 and 44 vol% hydrate saturations respectively.*

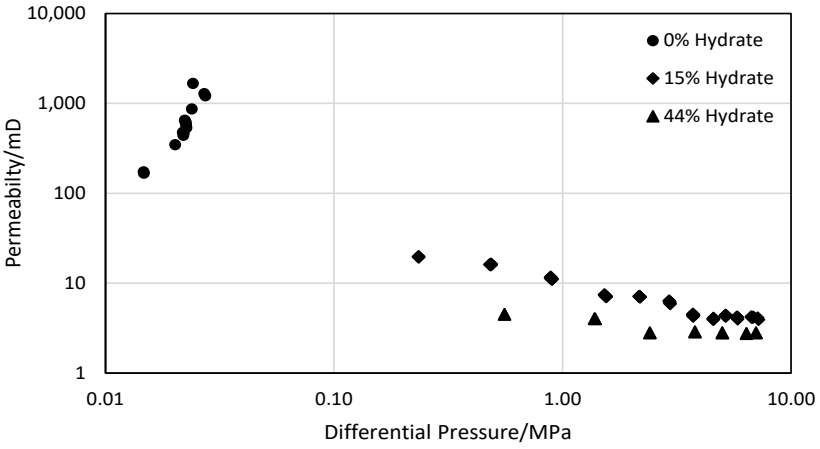

Figure 7.9 *Comparison of gas permeabilities in the presence of varying hydrate saturations and in the absence of hydrate for solid sandstone core.*

7.5 Permeability Reduction Models

In addition to gas hydrate saturation, the permeability of a hydrate-bearing porous medium depends on the site of hydrate formation in the pore space [242]. Kleinberg et al. [233] considered the limiting case of hydrate being an infinitesimal film of solid. If the film coats the pore walls, the effect on fluid flow is minimal. If the film is thick enough to divide the elliptical flow channel into two separate ducts, fluid flow rate will decrease by as much as a factor of four. If on the other hand, the film blocks the entire cross section of the pore, then permeability is reduced to zero. Two common models are used in literature to predict permeability reduction in hydrate-bearing porous media: the parallel capillary models and the Kozeny grain models [233]. Each model further divides to grain coating and pore filling.

7.5.1 Parallel capillary model

The Parallel Capillary model assumes that the porous medium is composed of a bundle of straight and parallel cylindrical capillaries.

Capillary wall coating

If hydrate coats the walls of the capillaries, the permeability of the porous medium at any given hydrate saturation is given by:

$$K_{c(S_h)} = K_a \left(1 - S_h\right)^2 \qquad 7.7$$

Where $K_{c(S_h)}$ is the gas permeability at a given hydrate saturation, K_a is the absolute permeability in the absence of hydrate, and S_h is the hydrate saturation.

Capillary centre filling

If hydrate fills the centres of the capillaries, the permeability of the porous medium at any given hydrate saturation is given by:

$$K_{f(S_h)} = K_a \left[1 - S_h^2 - \frac{\left(1 - S_h\right)^2}{ln\left(\frac{1}{S_h^{0.5}}\right)}\right] \qquad 7.8$$

7.5.2 Kozeny grain model

The Kozeny grain model more appropriately represents the porous medium as composed of packed grains with irregular pore spaces, longer and tortuous flow paths.

Grain coating

If hydrate coats the grain surfaces, the permeability of the porous media at any given hydrate saturation is given by:

$$K_{c(S_h)} = K_a \left(1 - S_h\right)^{n+1} \qquad 7.9$$

Where n is the Archie saturation exponent, $n = 1.5$ for $0 < S_h < 0.8$.

Pore filling

If hydrate occupies the pore centres, the permeability of the porous medium is given by:

$$K_{f(S_h)} = K_a \left[\frac{\left(1 - S_h\right)^{n+2}}{\left(1 + S_h^{0.5}\right)^2} \right] \qquad 7.10$$

Where $n = 0.7S_h + 0.3$.

7.6 Prediction Performance of Permeability Reduction Models

The presence of hydrate alters the pore structure of sediments and reduces the permeability of hydrate bearing sediments; hence the need for permeability reduction models to account for the presence of hydrate. **Figure 7.10** shows comparison for the Kozeny grain models. It is seen that for both the unconsolidated silica sand-montmorillonite core (**Figure 7.10(a))** and the solid sandstone core (**Figure 7.10(b)**), both the surface coating and the pore centre filling models over-predicts. Similarly, in the comparison for the Parallel Capillary model as seen in **Figure 7.11**, for the unconsolidated and the solid core samples, the models over-predicts. However, it is seen that for both the Kozeny grain model and the Parallel Capillary model, the pore centre and the capillary centre filling models performs better than the grain coating and the capillary wall coating model. Though this may be connected to the hydrate formation method adopted. A further look at the pore/capillary centre filling models of both Kozeny grain and Parallel Capillary models shows that the Parallel Capillary model better approximates the measured permeability data.

The disparity observed between the measured permeability data and model predictions may be due to the models' inability to account for pore structure change due to hydrate formation and hydrate heaving, and possible fines migration as observed in the experiments. It is worth mentioning that this study is only a preliminary one and a basis

for a more comprehensive study on the observed phenomena and improved permeability models.

(a)

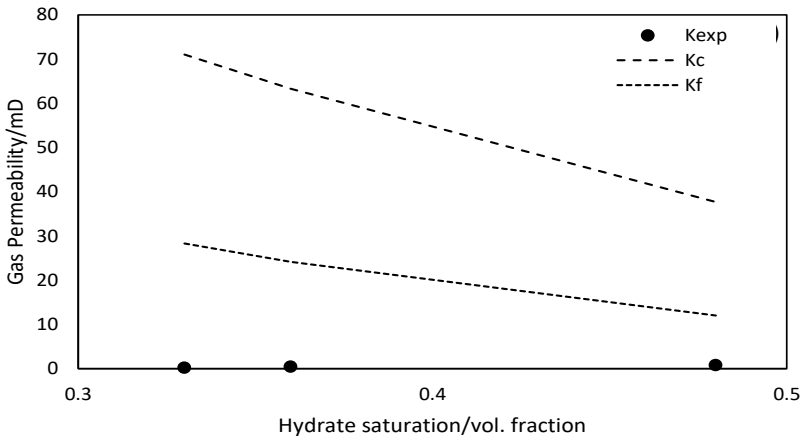

(b)

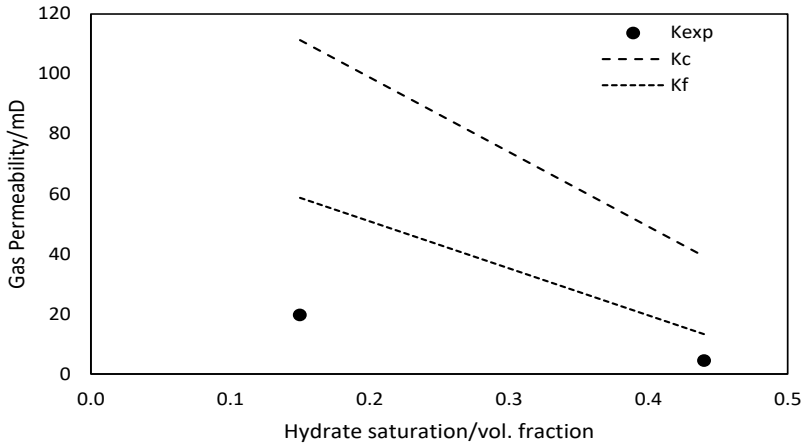

Figure 7.10 *Comparison of the measured permeability* $K_{\exp}$ *with Kozeny grain models for grain coating* K_c *and pore filling* K_f *. (a) represents unconsolidated silica sand-montmorillonite core samples and (b) represents solid sandstone core sample.*

(a)

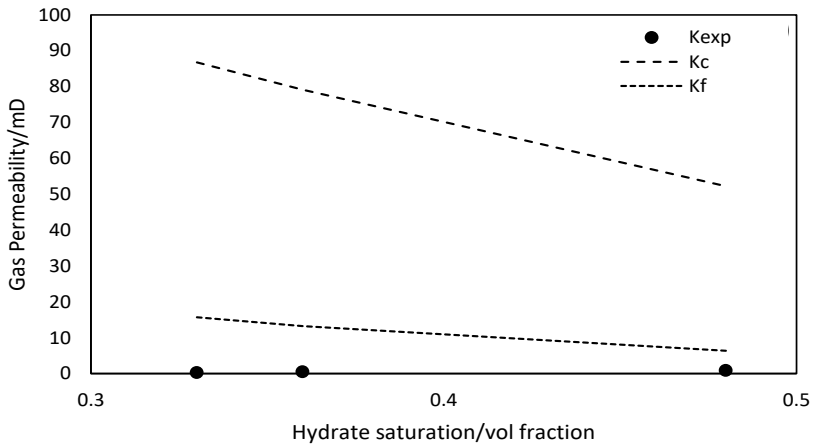

(b)

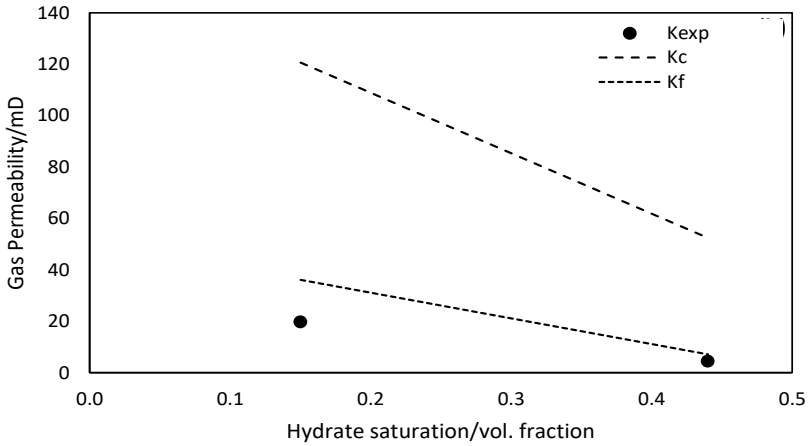

Figure 7.11 *Comparison of the measured permeability* K_{exp} *with Parallel Capillary models for grain coating* K_c *and pore filling* K_f *. (a) represents unconsolidated silica sand-montmorillonite core samples and (b) represents solid sandstone core sample.*

7.7 Summary

Peculiarities of gas flow in hydrate bearing sediments was studied through gas permeability measurements in hydrate bearing and non-hydrate bearing core samples using a standard core-holder. Permeability measurements of non-hydrate bearing cores were made on unconsolidated silica sand, and 95 wt% silica sand + 5 wt% montmorillonite, and a solid sandstone core. Gas permeability dependence on pressure was investigated. For hydrate-bearing cores, unconsolidated 95 wt% silica sand + 5 wt% montmorillonite and a solid sandstone core were used. In the non-hydrate bearing unconsolidated silica sand and the solid sandstone cores the capillaries were broken easily due to the presence of large interconnected pore spaces which offers reduced restriction to flow thereafter, hence, the increasing permeability with increasing

differential pressure. With 5 wt% montmorillonite in the non-hydrate bearing silica sand, gas permeability reduced gradually tending to a relative constant with continued increase in differential pressure. This behaviour was attributed to montmorillonite particle redistribution in the larger pore spaces of the silica sand. This redistribution led to the formation of fine pores after which Klinkenberg effect becomes significant leading to reduced permeability with increasing pressure.

In the presence of varying saturations of hydrate in the unconsolidated silica sand-montmorillonite core, gas permeability increased initially after gas breakthrough of capillary pores and later reduced gradually as Klinkenberg effect becomes significant. In the hydrate bearing solid sandstone core, gas permeability reduced gradually with increasing differential pressure after breakthrough. Capillary effect is less significant as evidenced by the ease of gas breakthrough. However, the presence of hydrate reduced the available pore space consequently reducing flow paths. Thus, permeability reduced with increasing pressure due to Klinkenberg effect. The impact of hydrate heaving increased with increasing hydrate saturation in unconsolidated silica sand-montmorillonite core, hence the increasing permeability with increasing hydrate saturation. Due to consolidation, hydrate heaving does not occur in the sandstone core, hence the decreasing gas permeability with increasing hydrate saturation.

Predictions of the Kozeny grain models and the Parallel Capillary models for both the surface coating and centre filling were compared with measured permeability values. In both model types, both the surface coating and the centre filling over predicts, with the centre filling showing a slightly improved performance over the surface coating models. Comparison of the centre filling in both the Kozeny grain model and the Parallel Capillary model shows that the Parallel Capillary model also shows a slightly improved approximation to the measured permeability values than the Kozeny grain model.

These reported observations highlights the deviation of gas permeation in hydrate bearing sediments, the inadequacy of the permeability reduction models, and the need for improved models that takes into account these peculiarities for improved reliability of gas hydrate reservoir simulators.

CHAPTER 8 CONCLUSIONS AND RECOMMENDATIONS

8.1 Introduction

The research reported in this thesis was mainly aimed at the development of novel techniques for methane recovery from gas hydrate reservoirs by flue gas injection and also to study the potential of CO_2 capture and storage as hydrates in the hydrate reservoirs. The study involved laboratory simulation of methane hydrate reservoirs at representative reservoir conditions using a high pressure cell and subsequent injection of flue gas to demonstrate the feasibility of the technique (**CHAPTER THREE**). The flue gas used was laboratory synthesised and composed of 86% nitrogen and 14 % CO_2, typical of flue gas from coal fired power plants. The impact of water salinity on hydrate formation and subsequently on methane recovery by flue gas injection was examined in both excess gas and excess water environments in **CHAPTER FOUR**. Furthermore, the impact of water salinity and saturation on CO_2 capture and storage was examined. In **CHAPTER FIVE**, the influence of host sediment mineralogy on hydrate formation and subsequent methane recovery as well as CO_2 capture and storage by flue gas injection was studied for both excess gas and excess water environments. **CHAPTER SIX** extended the technique to the study of the feasibility of methane recovery by compressed air injection. The peculiarities of gas flow in hydrate bearing sediments through permeability measurements in both hydrate-bearing and non-hydrate-bearing unconsolidated and solid cores were studied in **CHAPTER SEVEN**. Findings of the research are summarised in the section below. Recommendations and outlook on the future investigations are also presented.

8.2 Conclusions

It is acknowledged that techniques for gas recovery from gas hydrate reservoirs have been extensively studied and reported. Also, a few field trials have been conducted. However, the major challenge still facing the use of these techniques is that they are not economically feasible despite their technical successes. This research therefore proposed and studied flue gas injection and compressed air injection as possible techniques with potential cost benefits that could improve the economic feasibility of gas recovery from gas hydrate reservoirs.

Flue gas injection broke the equilibrium of methane hydrate and caused a shift in the methane hydrate stability zone, leading to rapid methane hydrate decomposition. In the typical methane hydrate reservoir conditions of 273.2 K to 284 K and 4.15 MPa to 14.04 MPa in which the experiments were conducted, up to 50 mol% methane was present in the vapour phase at the new thermodynamic equilibrium.

After a new thermodynamic equilibrium was reached, depressurisation was conducted to further enhance methane recovery. Methane hydrate decomposed well inside the methane hydrate stability zone (MHSZ) in the presence of flue gas. Up to 65.7 mol% methane was achieved in the vapour phase at 3.5 MPa, 0.75 MPa above the dissociation pressure of 2.75 MPa at 273.2 K (Experiment 1), 60 mol% was achieved at 5.11 MPa, 0.8 MPa above methane hydrate dissociation pressure of 4.31 MPa at 278 K (Experiment 2), 55 mol% was achieved at 7.77 MPa, 1.35 MPa above methane hydrate dissociation pressure of 6.42 MPa at 282 K (Experiment 3). Methane recovery ncreased with increasingexperimental temperature. Thus, it is concluded that high temperature favours both the kinetics and thermodynamics of methane recovery.

The potential of CO_2 sequestration was verified as the CO_2 component of the injected flue gas formed CO_2 hydrate and CO_2-mixed hydrates after flue gas injection. 70.4%, 68.5% and 48.1% of CO_2 in the vapour phase was captured and stored as hydrates in Experiments 1, 2, and 3 respectively. The amount of CO_2 stored decreased progressively with increasing experimental temperature due to higher equilibrium pressure at higher temperatures requiring more gas in the vapour phase. CO_2 capture and storage was insignificant in Experiment 4 conducted slightly outside the CO_2 HSZ (284 K, 14.04 MPa). This suggests that for CO_2 capture and storage, conditions inside both the CH_4 and CO_2 HSZs are favourable, especially low temperatures.

Compressed air injection in the same manner as flue gas injection broke the equilibrium of methane hydrate, causing a shift in the methane HSZ resulting in rapid decomposition of methane hydrate to release methane. Very fast methane hydrate decomposition in the presence of compressed air enabled the implementation of multi-stage depressurisation and allowed for methane recovery at high pressures.

The multi-stage depressurisation was done in two phases; the first phase was designed to study the kinetics of methane release in the presence of air while the depressurisation continued in the second phase for maximum methane recovery. Two methane release

trends were observed; a fast methane release stage owing to shift in methane HSZ followed by a slow release stage as the system tends to a new thermodynamic equilibrium. The kinetics of methane release is favoured by temperature as 38%, 65% and 97% methane recoveries were achieved in the first phase of the multi-stage depressurisation for Experiments 13, 14 and 15 conducted at 273.2 K, 278 K and 283 K respectively. In the first pressure stage of the multi-stage depressurisation, system pressure reduced despite increasing methane concentration in the vapour phase. This was attributed to nitrogen and oxygen incorporation into the hydrate phase as the set pressure was too close the air-hydrate equilibrium pressure at the experimental condition.

In the second phase, complete/near complete methane hydrate decomposition was achieved as evidenced by the high vapour phase methane concentrations achieved. Up to 77 mol% of methane was achieved in the vapour phase in Experiment 13 (273.2 K) at 3.37 MPa, 0.65 MPa above the methane hydrate dissociation pressure. For Experiment 14 (278 K), it was 84 mol% methane at 4.87 MPa, 0.56 MPa above the methane hydrate dissociation pressure. 69 mol% methane was achieved at 7.52 MPa, 0.4 MPa above the methane hydrate dissociation pressure.

These techniques have several advantages over other techniques reported in literature. Secondary hydrate formation which is a prevalent problem especially in CO_2 injection method could be avoided by both flue gas and compressed air injection. Direct injection of flue gas has the added benefit of capture and storage of CO_2 as CO_2 hydrates while simultaneously recovering methane. This could potentially lead to huge cost saving when compared to the cost of conventional carbon capture and storage (CCS). From a technical perspective, both flue gas and compressed air injection leads to high pressure production. High pressure production helps to maintain reservoir energy. This could help save cost in terms of pumping facilities, and also reverse the energy penalty associated with the conventional techniques of depressurisation and thermal stimulation. Moreover, high pressure production could help to reduce the extent of depressurisation. The minimised depressurisation could be beneficial especially for low permeability reservoirs and also for hydrate reservoirs whose conditions are far inside the HSZ. Moreover, high pressure production could also help to reduce pressure drawdown. This could help in mitigating the problem of sand migration that leads to blockage of equipment. Multi-stage depressurisation as

implemented in compressed air injection could allow for controlled depressurisation. Controlled depressurisation could help to mitigate sand production problem, especially in highly unconsolidated sediments. Additionally, it could also help to control excessive water production.

The impact of formation water salinity on hydrate formation and consequent methane recovery by flue gas injection was studied for both excess gas and excess water environment. Methane consumption for hydrate formation was significant for pure water systems in both excess gas and excess water hydrate formation methods. Reduced rate of methane consumption was observed increasingly for systems with 3 and 10 mass% NaCl in the aqueous phase, showing that the presence of NaCl has a kinetic inhibition effect on methane hydrate formation. Quantitatively, methane conversion to hydrate in the 3 mass% NaCl system is comparable to that of pure water systems in both excess gas and excess water environments. This suggests that the presence of 3 mass% NaCl in the aqueous phase has only a slight impact on methane hydrate nucleation and growth.

Methane hydrate dissociation and consequently vapour phase methane concentration at the new thermodynamic equilibrium after flue gas injection were similar for pure water and 3 mass% NaCl systems in the excess gas environment, implying that 3 mass% NaCl in the aqueous phase leads to no significant enhancement in methane hydrate decomposition in the excess gas environment. However, in the 10 mass% NaCl system, higher vapour phase methane concentration was achieved arising from reduced hydrate saturation due to strong kinetic inhibition to hydrate growth during hydrate formation. In excess water environment, vapour phase methane concentrations after flue gas injection were similar and higher in the 3 and 10 mass% NaCl systems than in the pure water system. This is attributed to ease of dissociation in the presence of flue gas due to reduced hydrate saturation achieved during hydrate formation. Additionally, vapour phase methane concentration is relatively high as less flue gas was injected due to pressure limitation arising from water incompressibility. 3 and 10 mass% NaCl in the aqueous phase increased the dissociation pressure of methane hydrate from 2.72 MPa for pure water system to 3.11 MPa and 4.29 MPa respectively. Complete/near-complete decomposition of methane hydrate was achieved when the system was depressurised in the presence of flue gas. Maximum vapour phase methane concentrations of 81 mol% and 65 mol% were achieved in 3 and 10 mass% NaCl systems respectively at three and

two depressurisation steps at 0.2 MPa and 0.5 MPa above the methane hydrate dissociation pressures at the experimental temperature. For pure water systems, maximum methane concentration of 75 mol% was achieved after two depressurisation steps at 0.3 MPa above the methane hydrate dissociation pressure. For the systems with 3 and 10 mass% NaCl, maximum methane concentrations of 76 mol% and 62 mol% were achieved after only one depressurisation step at 0.5 MPa and 1 MPa respectively above the methane hydrate dissociation pressures at 3 and 10 mass% NaCl systems.

CO_2 captured and stored as hydrate decreased with increasing NaCl concentration implying that NaCl exhibits kinetic inhibition to CO_2-hydrate formation in excess gas environment. In excess water environment, CO_2 captured and stored increased with increasing NaCl concentration. It is believed that besides CO_2 involved in hydrate formation, CO_2 formed HCO_3 and H_2CO_3 which were converted to CO_3^{2-}. This contributed to the significant reduction in the CO_2 content of the vapour phase. It is suggested that aside from methane production, saline environments with high water saturations are excellent candidates for CO_2 capture and storage.

Furthermore, the effect of host sediment mineralogy on methane hydrate formation and methane recovery by flue gas injection was also investigated. Real sediment from the Leg 311 of the Integrated Ocean Drilling Programme (IODP) which approximates clayey sediment was used to conduct methane hydrate formation and methane recovery experiments in both excess gas and excess water environments. Results were compared with experiments conducted in similar conditions with silica sand. Clay particles have a promotion effect on hydrate nucleation due to ordered adsorption of water molecules in the interlayer sheets of clay as evidenced by the early onset of nucleation in the excess gas hydrate formation method. However, reduced water activity arising from reduced pore size and the high compressibility of clay reduced the rate and space available for hydrate growth. Such inhibition effects were not observed with silica sediment, hence, the 82% methane conversion to hydrate achieved as compared to only 29% achieved in the IODP sediment. In the excess water hydrate formation method, 55% methane conversion to hydrate was achieved in silica sand while only 7% was achieved in IODP sediment. This is attributed to high water injection rate into silica sand due to reduced compressibility and less water absorption. The IODP sediment absorbs more water, increases in volume, and also highly compressible, thus providing limited space for free water accumulation.

Fast methane hydrate dissociation by flue gas was observed in both silica sand and IODP sediment. Methane concentration reached 52 mol% in silica sand in the excess gas environment. It reached as high as 58 mol% in IODP sediment in excess gas environment and 60 mol% in both silica sand and IODP sediment in excess water environment due to near complete methane hydrate decomposition by flue gas at low hydrate saturations. Comparisons of dissociation rates in both excess gas and excess water environments shows that hydrate dissociation rate is higher in silica sand than in IODP sediment. This suggests that methane hydrate dissociation could be slightly hindered in clayey sediments.

Gas flow characteristics in hydrate bearing sediments were studied through gas permeability measurements in hydrate-bearing and non-hydrate-bearing consolidated and unconsolidated cores. Effect of sediment mineralogy was also investigated by the addition of 5 wt% montmorillonite into the silica sand sediment. Gas permeability was found to be pressure dependent. The dependence on pressure varied with sediment mineralogy. Gas permeability increased with increasing pressure in the non-hydrate-bearing unconsolidated silica sand and the solid sandstone core. This is attributed to weak capillary effect caused by large interconnected pore spaces. 5 wt% montmorillonite in the unconsolidated silica sand core caused the permeability to gas to reduce gradually tending to a constant value with increasing differential pressure. This is thought to be due to the redistribution of the smaller montmorillonite particle in the larger pore spaces of the silica. In the resulting fine pores, Klinkenberg effect causes the permeability to reduce with increasing differential pressure.

In the range of hydrate saturation investigated, gas permeability in the unconsolidated silica sand-montmorillonite core increased initially after breakthrough of capillary pores and later reduced gradually as Klinkenberg effect becomes significant. A contrasting observation was made in the hydrate-bearing solid sandstone core. Gas permeability decreased with increasing hydrate saturation. This is also due to weak capillary effect in the absence of narrow pore throats and flow paths. It is concluded that capillary effect is significant when pore throats are narrow as observed in the silica sand-montmorillonite core. Hydrate heaving phenomenon caused gas permeability increase with increasing hydrate saturation in the unconsolidated silica sand-montmorillonite core. In contrast, gas permeability decreased with increasing hydrate saturation in

consolidated sandstone core as expected. It is believed that hydrate heaving effect is negligible in solid cores.

Prediction performance of existing permeability reduction models was preliminarily tested by comparing with measured permeability data using the surface coating and the centre filling models of the Kozeny grain and the Parallel capillary family models. In the two model families, both the surface coating and the centre filling models over-predicts. However, the centre filling shows a slightly improved performance over the surface coating models. Focusing on the centre filling model in both the Kozeny grain and the Parallel Capillary shows that the Parallel Capillary model also shows a slightly improved approximation to the measured permeability values than the Kozeny grain model.

These observations highlight the previously non-reported gas flow peculiarities in hydrate-bearing sediment and the inadequacy of the permeability reduction models. This obviates the need for development of improved models that takes into account these characteristics for reliability improvement in gas hydrate reservoir simulators.

8.3 Recommendations

The research reported in this thesis has shed light on the economic feasibility of methane recovery from the abundant natural gas hydrate reserves by flue gas injection. It has also contributed new insights into CO_2 sequestration as hydrates at various reservoir rock and fluid conditions. Furthermore, it highlights the feasibility of methane recovery from gas hydrate reservoirs by enhanced depressurisation following compressed air injection. Additionally, for better understanding of gas flow in hydrate bearing porous media which could aid in improvements in the design of gas recovery projects and development of improved hydrate reservoir simulators, previously non-reported peculiarities of gas flow in hydrate bearing sediments were brought to fore. However, inherent gap in understanding requiring further studies have been identified.

The experimental rig was designed to be a closed system in which produced gas remains in-situ. Modifying the rig would for continuous injection of flue gas/air and removal of the resulting gas mixture while maintaining a constant cell pressure. The use of an inline GC would enable real time sampling and analysis of gas phase composition. This would greatly enhance the study of the kinetics of methane hydrate

decomposition in the presence of flue gas/air. The improved understanding from this would be beneficial in the development of kinetic models.

An important area for future research is the model development for methane hydrate dissociation in the presence of flue gas. A few simulators have been developed that can simulate gas production from hydrate reservoirs. The TOUGH+HYDRATE code is the most prominent. [243] developed by Moridis and co-workers at the Lawrence Berkeley National Laboratory, Berkeley, California. It can model the non-isothermal hydrate dissociation, phase behaviour, and fluid flow in gas-hydrate bearing sediment. It includes both equilibrium and kinetic models of hydrate formation and dissociation. Their model can account for up to four components (water, methane, hydrate, and inhibitor) in four phases (gas, liquid, ice, and hydrate). Their model has been used to describe hydrate dissociation mechanisms including depressurisation, thermal stimulation, salts and chemical inhibitor induced dissociation. The commercial simulator CMG-STARS has also been used to model and simulate gas production from hydrate reservoirs. STARS is a thermal reservoir simulator specifically designed to model and simulate thermal and chemical enhanced oil recovery processes such as in-situ combustion, steam flooding, water flooding, surfactant and polymer injection. However, the chemical reaction module may be used to simulate gas production from hydrate reservoir by making suitable modifications to the phases and components section. Uddin et al. [244–246] using STARS modelled a binary component gas phase composed of methane and CO_2 in a simultaneous methane hydrate dissociation and CO_2 hydrate formation. Their model consists of five components (water, methane, CO_2, methane hydrate and CO_2-hydrate) partitioned into three phases (water, gas, solid (hydrate)).

The described simulators lack the capacity to model hydrate dissociation caused by phase boundary shift in a multi-component gas mixture in the gas in the vapour phase. Moreover, the permeability models in these simulators do not represent the peculiarities in permeability behaviour of hydrate-bearing sediment reported in **CHAPTER 7**.

Modelling hydrate dissociation by phase boundary shift in a multi-component gas mixture in the gas in the vapour phase is potentially a complex system involving multiphase, multicomponent flow, and heat transfer in porous media and a reaction involving methane hydrate dissociation, CO_2-hydrate and other types of $CO_2/N_2/O_2$ mixed hydrate formation. This would require a great amount of effort and time.

However, it is necessary for better understanding and the design of methane recovery from gas hydrate reservoirs by flue gas/air injection, and for long term forecasting. It would also help in carrying out sensitivity analysis studies of certain parameters which may otherwise not be simulatable experimentally.

Enhanced understanding of the gas flow peculiarities in hydrate-bearing sediments, at pore scales, could be aided by powerful imaging equipment such as magnetic resonance imaging (MRI) with cryogenic capacity. This is needed for better understanding of capillary breakthrough, flow path evolution, hydrate heaving effect, and Klinkenberg effect as it relates to hydrate-bearing sediments. This may also help in development of permeability models that can predict a variety of hydrate-associated phenomena such as heaving phenomenon, grain migration, pore structure change, etc. Furthermore, it is worth studying gas permeation in hydrate-bearing sediments under a wide range of confining pressures to understand its possible influence on gas permeabilities and hydrate heaving. The permeability model prediction will be input to the kinetic models to simulate methane recovery process from gas hydrate reservoirs by injection of flue gas or air.

REFERENCES

[1] Z.R. Chong, S.H.B. Yang, P. Babu, P. Linga, X.-S. Li, Review of natural gas hydrates as an energy resource: Prospects and challenges, Applied Energy. (2015).

[2] A. Nago, A. Nieto, Natural Gas Production from Methane Hydrate Deposits Using CO Clathrate Sequestration: State-of-the-Art Review and New Technical Approaches, Journal of Geological Research. 2011 (2011) 1–6.

[3] ExxonMobil. The Outlook for Energy: A View to 2040 by ExxonMobil 2015.

[4] I.E.A. World energy outlook special report: are we entering the golden age of gas? Paris, France: International Energy Agency; 2011.

[5] M. Clarke, P.R. Bishnoi, Determination of the Activation Energy and Intrinsic Rate Constant of Methane Gas Hydrate Decomposition, The Canadian Journal of Chemical Engineering. 79 (2001).

[6] J. Priestly, Experiments and Observations on Different Kinds of Air and Other Branches of Natural Philosophy Connected with the Subject. In Vol. 3, T. Pearson., (1790).

[7] H. Davy, The Bakerian Lecture: On Some of the Combinations of Oxymuriatic Gas and Oxygene, and on the Chemical Relations of These Principles, to Inflammable Bodies, Philosophical Transactions of the Royal Society of London. 101 (1811) 1–35.

[8] E. Hammerschmidt, Formation of gas hydrates in natural gas transmission lines, Industrial and Engineering Chemistry. 26 (1934).

[9] E. Hammerschmidt, Gas hydrate formation, Gas. 15 (1939) 30–34.

[10] W.M. Deaton, E.M. Frost, Gas hydrates and their relation to their operation of natural gas pipelines, U. S. Bureau of Mines Monograph 8, (1946).

[11] D.C. Bond, N.B. Russell, Effect of Antifreeze Agents on the Formation of Hydrogen Sulphide Hydrate, Trans. AIME. 179 (1949) 192–198.

[12] R. Kobayashi, H.J. Withrow, G.B. Williams, D.L. Katz, Gas hydrate formation with brine and ethanol solutions, in: Proceedings of the 13th Annual Convention of Ntaural Gasoline Association of America, San Antonio, Texas, 1951: pp. 27–31.

[13] R.M. Woolfolk, Methanol as a hydrate inhibitor, Oil and Gas Journal. 50 (1952).

[14] Y.F. Makogon, Natural gas hydrates: the state of study in the USSR and perspectives for its use, in: Proceedings of The 3rd Chemical Congress of North America, Toronto, Canada, 1988.

[15] T.S. Collet, Detection and evaluation of natural gas hydrates from well logs, Prudhoe Bay Alaska, M. S. Thesis, University of Alaska, 1983.

[16] C. Billy, J.W.L. Dick, Naturally occurring gas hydrate in the Mackenzie Delta, NWT, Bulletin of Canadian Petroleum Geology. 22 (1974) 340–352.

[17] C.K. Paull, R. Matsumoto, P.J. Wallace et al., Proceedings of the Ocean Drilling Program, Initial Reports, Leg 164, College Station, Texas, Ocean Drilling Program, 1996.

[18] M.E. Torres, A.M. Tréhu, N. Cespedes, M. Kastner, U.G. Wortmann, J. Kim, et al., Methane hydrate formation in turbidite sediments of northern Cascadia , IODP Expedition 311, 271 (2008) 170–180.

[19] M. Riedel, T.S. Collett, M. Malone et al., Expedition 311 synthesis : scientific findings 1, in: Proceedings of the Integrated Ocean Drilling Program, Volume 311, 2010.

[20] M. von Stackelberg, Feste Gashydrate, Naturwissenschaften. 36 (1949) 327–359.

[21] M. von Stackelberg, H.R. Muller, Feste Gashydrate II, Zeitschrift Für Elektrochemie. 58 (1954) 104.

[22] J.A. Ripmeester, J.S. Tse, C.I. Ratcliffe, B.M. Powell, A new clathrate hydrate structure, Nature. 325 (1987) 135–136.

[23] E.D. Sloan, Fundamental principles and applications of natural gas hydrates, Nature. 426 (2003) 353–359.

[24] http://www.pet.hw.ac.uk/research/hydrate/hydrates_what.cfm, (n.d.).

[25] E.D. Sloan, C.A. Koh, Clathrate hydrates of natural gases, 3rd Edition, Taylor and Francis, 2007.

[26] W.L. Mao, H. Mao, A.F. Goncharov, V. V. Struzhkin, Q. Guo, J. Hu, et al., Hydrogen Clusters in Clathrate Hydrate, Science. 297 (2002) 2247–2250.

[27] G.A. Jeffrey, Hydrate inclusion compounds, Journal of Inclusion Phenomena. 1 (1984) 211–222.

[28] K.A. Udachin, C.I. Ratcliffe, J.A. Ripmeester, A Dense and Efficient Clathrate Hydrate Structure with Unusual Cages, Angewandte Chemie. 113 (2001) 1343–1345.

[29] J.S. Loveday, R.J. Nelmes, M. Guthrie, S.A. Belmonte, D.R. Allan, Stable methane hydrate above 2 GPa and the source of Titan's atmospheric methane, Nature. 410 (2001) 661–663.

[30] B. Canyon, Thermogenic Gas Hydrates in the Northern Cascadia Margin, EOS, Transactions, American Geophysical Union. 85 (2004) 361–368.

[31] J.W. Pohlman, E. a. Canuel, N.R. Chapman, G.D. Spence, M.J. Whiticar, R.B. Coffin, The origin of thermogenic gas hydrates on the northern Cascadia Margin as inferred from isotopic (13C/12C and D/H) and molecular composition of hydrate and vent gas, Organic Geochemistry. 36 (2005) 703–716.

[32] C.K. Paull, W. Ussler, W. Borowski, Sources of biogenic methane to from marine gas hydrates-in situ production or upward migration, Annals of the New York Academy of Sciences. 715 (1994).

[33] D.D. Rice, G.E. Claypool, Generation , Accumulation , and Resource Potential of Biogenic Gas, AAPG Bulletin. (1981).

[34] J.M. Brooks, H.B. Cox, W.R. Bryant, M.C.K. Ii, R.G. Mann, T.J. Mcdonald, Association of gas hydrates and oil seepage in the Gulf of Mexico, 10 (1986) 221–234.

[35] T.S. Collet, Natural gas hydrates of Prudhoe Bay and Kuparuk River Area, North Slope, Alaska, The American Association of Petroleum Geologists Bulletin. 77 (1992) 793–812.

[36] N.L. Guinasso, J.M. Brooks, Organic geochemistry of sediments from chemosynthetic communities, Gulf of Mexico slope, Geomarine Letters. 14 (1994) 110–119.

[37] M. Kida, O. Khlystov, T. Zemskaya, N. Takahashi, H. Minami, H. Sakagami, et al., Coexistence of structure I and II gas hydrates in Lake Baikal suggesting gas sources from microbial and thermogenic origin, Geophysical Research Letters. 33 (2006) L24603.

[38] R.D. Malone, Gas Hydrates Topical Reports, DOE/METC/SP-218, U. S. Department of Energy, April (1985), 1985.

[39] J. Korenaga, W.S. Holbrook, S.C. Singh, T.A. Minshull, Natural gas hydrates on the southeast U.S. margin: Constraints from full waveform and travel time inversions of wide-angle seismic data, Journal of Geophysical Research. 102 (1997) 15345–15365.

[40] C.K. Paull, R. Matsumoto, 1. Leg 164 overview, Proceedings of the Ocean Drilling Program, Scientific Results. 164 (2000) 3–10.

[41] D. Grauls, Gas hydrates: importance and applications in petroleum exploration, Marine and Petroleum Geology. 18 (2000) 519–523.

[42] J. Dai, F. Snyder, D. Gillespie, A. Koesoemadinata, N. Dutta, Exploration for gas hydrates in the deepwater, northern Gulf of Mexico: Part I. A seismic approach based on geologic model, inversion, and rock physics principles, Marine and Petroleum Geology. 25 (2008) 830–844.

[43] K.A. Kvenvolden, Gas hydrates-geological perspective and global change, Reviews of Geophysics. 31 (1993) 173–187.

[44] R.D. Mciver, Role of Naturally Occurring Gas Hydrates in Sediment Transport[1], (1982) 789–792.

[45] W. Xu, L.N. Germanovich, Excess pore pressure resulting from methane hydrate dissociation in marine sediments: A theoretical approach, Journal of Geophysical Research. 111 (2006) B01104.

[46] C.P. Summerhayes, B.D. Bornhold, R.W. Embley, Surficial slides and slumps on the continental slope and rise of South West Africa, Marine Geology. 31 (1979) 265–277.

[47] Z. Ben-Avraham, G. Smith, M. Reshef, E. Junglasger, Gas hydrate and mud volcanoes on the southwest African continental margin off South Africa, Geology. 30 (2002) 927–930.

[48] G. Carpenter, Coincident sediment slump-clathrate complexes on the US Atlantic continental slope, Geo-Marine Letters. 1 (1981) 29–32.

[49] C. Berndt, J. Mienert, M. Vanneste, B. Stefan, Gas hydrate dissociation and sea-floor collapse in the wake of the storregga slide Norway, Norwegian Petroleum Society Special Publications. 12 (2005) 285–292.

[50] P. Bryn, K. Berg, C.F. Forsberg, A. Solheim, T.J. Kvalstad, Explaining the Storegga Slide, Marine and Petroleum Geology. 22 (2005) 11–19.

[51] P. Cochonat, J. Cadet, S.J. Lallemant, C. Fouchet, J. Paul, S. Mazzotti, Slope instabilities and gravity processes in fluid migration and tectonically active environment in the eastern Nankai accretionary wedge (KAIKO-Tokai 1996 cruise), Marine Geology. 187 (2002) 193–202.

[52] R. Rodríguez-Ochoa, F. Nadim, J.M. Cepeda, M. a. Hicks, Z. Liu, Hazard analysis of seismic submarine slope instability, Georisk: Assessment and Management of Risk for Engineered Systems and Geohazards. 9 (2015) 128–147.

[53] V.S. Yakushev, T.S. Collett, Gas hydrates in arctic regions: risk to drilling and production, in: Prcceedings of the Second International Offshore and Polar Engineering Conference, San Francisco, USA, 14-19 June, 1992: pp. 669–673.

[54] M. Salehabadi, M. Jin, J. Yang, R. Ahmed, B. Tohidi, The Effect of Casing Eccentricity on the Casing Stability Analysis of a Wellbore Drilled in Gas Hydrate Bearing Sediments, in: SPE EUROPEC/EAGE Annual Conference and Exhibition, Barcelona, Spain, 14-17 June, 2010.

[55] T. Khabibullin, G. Falcone, A. Texas, C. Teodoriu, Drilling Through Gas-Hydrate Sediments : Managing Wellbore-Stability Risks, SPE Drilling & Completion. (2011).

[56] M. Maslin, M. Owen, R. Betts, S. Day, T. Dunkley Jones, A. Ridgwell, Gas hydrates: past and future geohazard?, Philosophical Transactions. Series A, Mathematical, Physical, and Engineering Sciences. 368 (2010) 2369–93.

[57] (IPCC)Intergovernmental Panel on Climate Change. The scientific basis. Contribution of Working Group I to the Fourth Assessment Report of the Intergovernmental Panel on Climate Change (IPCC), Cambridge University Press, Cambridge, MA., 2007.

[58] G. Moridis, T. Collett, Strategies for gas production from hydrate accumulations under various geologic conditions, in: Proceedings of TOUGH Symposium, Lawrence Berkeley National Laboratory, Berkeley, California, May 12–14, 2003.

[59] G. Li, G.J. Moridis, K. Zhang, X. Li, L. Berkeley, C. Road, et al., Evaluation of Gas Production Potential from Marine Gas Hydrate Deposits in Shenhu Area of South China Sea, Energy & Fuels. 21 (2010) 6018–6033..

[60] S. Silpngarmlert, Numerical modeling of gas recovery from methane hydrate reservoirs, Pennsyvania State University, 2007.

[61] G.J. Moridis, T.S. Collett, S.R. Dallimore, T. Satoh, S. Hancock, B. Weatherill, Numerical studies of gas production from several CH4 hydrate zones at the Mallik site, Mackenzie Delta, Canada, Journal of Petroleum Science and Engineering. 43 (2004) 219–238.

[62] G.J. Moridis, E.D. Sloan, Gas production potential of disperse low-saturation hydrate accumulations in oceanic sediments, Energy Conversion and Management. 48 (2007) 1834–1849.

[63] Gas Hydrates Primer, U.S. Geological Survey Gas Hydrates Project, (n.d.).

[64] V.P. Trofimuk, A. A., Cherskiy, N. V., & Tsarev, T, The reserves of biogenic methane in the ocean, Dokl.Akad.Nauk SSSR. 225 (1975).

[65] V.A. Soloviev, Global estimation of gas content in submarine gas hydrate accumulations, Russ Geol Geophys. 43 (2002) 609–24.

[66] J.B. Klauda, S.I. Sandler, Global Distribution of Methane Hydrate in Ocean Sediment, Energy & Fuels. 19 (2005) 459–470.

[67] M.K. Davie, B.A. Buffett, A numerical model for the formation of gas hydrate below the seafloor, Journal of Geophysical Research: Solid Earth. 106 (2001) 497–514.

[68] M.K. Davie, B. A. Buffett, A steady state model for marine hydrate formation: Constraints on methane supply from pore water sulfate profiles, Journal of Geophysical Research: Solid Earth. 108 (2003).

[69] J.A. H., Global resource potential of gas hydrate – a new calculation, Fire in the Ice: NETL. (2011) 1–5.

[70] A. V. Milkov, Global estimates of hydrate-bound gas in marine sediments: how much is really out there?, Earth-Science Reviews. 66 (2004) 183–197.

[71] R. Boswell, T.S. Collett, Current perspectives on gas hydrate resources, Energy Environ. Sci. 4 (2011) 1206–1215.

[72] M.H. Yousif, H.H. Abass, M.S. Sellm, E.D. Sloan, Experimental and Theoretical Investigation of Methane-Gas-Hydrate Dissociation in Porous Media, SPE Reservoir Engineering. February (1991) 69–76.

[73] L. Xiong, X. Li, Y. Wang, C. Xu, Experimental Study on Methane Hydrate Dissociation by Depressurization in Porous Sediments, Energies. 5 (2012) 518–530.

[74] S. Circone, L.A. Stern, S.H. Kirby, J.C. Pinkston, W.B. Durham, Methane hydrate dissociation rates at 0.1 MPa and Temperatures above 272 K, Ann N. Y. Acad Sci. 912 (2000) 544–555.

[75] H.O. Kono, S. Narasimhan, F. Song, D.H. Smith, Synthesis of methane gas hydrate in porous sediments and its dissociation by depressurizing, Powder Technology. 122 (2002) 239–246.

[76] J. Yang, B. Tohidi, Characterization of inhibition mechanisms of kinetic hydrate inhibitors using ultrasonic test technique, Chemical Engineering Science. 66 (2011) 278–283.

[77] S. Kawamura, T., Ohtake, M., Sakamoto, Y., Yamamoto, Y., Haneda, H., Komai, T., Higuchi, Experimental study on steam injection method using methane hydrate core samples, in: 7th International Offshore and Polar Engineering Conference (ISOPE), Ocean Mining Symposium, Lisbon, 2007: pp. 83–86.

[78] J. Zhao, C. Cheng, Y. Song, W. Liu, Y. Liu, K. Xue, et al., Heat Transfer Analysis of Methane Hydrate Sediment Dissociation in a Closed Reactor by a Thermal Method, Energies. 5 (2012) 1292–1308.

[79] G.C. Fitzgerald, M.J. Castaldi, Thermal Stimulation Based Methane Production from Hydrate Bearing Quartz Sediment, Industrial and Engineering Chemistry Research. 52 (2013) 87–92.

[80] B. Li, G. Li, X. Li, Q. Li, B. Yang, Y. Zhang, et al., Gas Production from Methane Hydrate in a Pilot-Scale Hydrate Simulator Using the Huff and Puff Method by Experimental and Numerical Studies, Energy and Fuels. 29 (2012) 7183–7194.

[81] W.X. Pang, W.Y. Xu, C.Y. Sun, C.L. Zhang, G.J. Chen, Methane hydrate dissociation experiment in a middle-sized quiescent reactor using thermal method, Fuel. 88 (2009) 497–503.

[82] M.R. Islam, A new recovery technique for gas production from Alaskan gas hydrates, Journal of Petroleum Science and Engineering. 11 (1994) 267–281.

[83] M.J. Castaldi, Y. Zhou, T.M. Yegulalp, Down-hole combustion method for gas production from methane hydrates, Journal of Petroleum Science and Engineering. 56 (2007) 176–185.

[84] T. Kawamura, Y. Sakamoto, M. Ohtake, Y. Yamamoto, H. Haneda, Dissociation Behavior of Hydrate Core Sample Using Thermodynamic Inhibitor, International Journal of Offshore and Polar Engineering. 16 (2006) 5–9.

[85] S.C. Nam, P. Linga, C. Haligva, J.A. Ripmeester, P. Englezos, B. Engineering, et al., Kinetics of hydrate formation and decomposition of methane in silica sand. in: Proceedings of the 6th International Conference on Gas Hydrates (ICGH 2008), Vancouver, British Columbia, Canada, July 6-10, 2008.

[86] G. Li, X. Li, L. Tang, Y. Zhang, Experimental Investigation of Production Behavior of Methane Hydrate under Ethylene Glycol Injection in Unconsolidated Sediment, Energy & Fuels. 21 (2007) 3388–3393.

[87] F. Dong, X. Zang, D. Li, S. Fan, D. Liang, Experimental Investigation on Propane Hydrate Dissociation by High Concentration Methanol and Ethylene Glycol Solution Injection, Energy & Fuels. 23 (2009) 1563–1567.

[88] W. Sung, H. Lee, H. Lee, C. Lee, Numerical Study for Production Performances of a Methane Hydrate Reservoir Stimulated by Inhibitor Injection, Energy Sources. 24 (2010) 499–512.

[89] J. Lee, Experimental Study on the Dissociation Behavior and Productivity of Gas Hydrate by Brine Injection Scheme in Porous Rock, Energy & Fuels. 24 (2010) 456–463.

[90] Y. Bai, Q. Li, Simulation of gas production from hydrate reservoir by the combination of warm water flooding and depressurization, Science China Technological Sciences. 53 (2010) 2469–2476.

[91] X.-S. Li, B. Yang, G. Li, B. Li, Y. Zhang, Z.-Y. Chen, Experimental study on gas production from methane hydrate in porous media by huff and puff method in Pilot-Scale Hydrate Simulator, Fuel. 94 (2012) 486–494.

[92] X.-S. Li, B. Yang, L.-P. Duan, G. Li, N.-S. Huang, Y. Zhang, Experimental study on gas production from methane hydrate in porous media by SAGD method, Applied Energy. 112 (2013) 1233–1240.

[93] G. Li, X.-S. Li, B. Yang, L.-P. Duan, N.-S. Huang, Y. Zhang, et al., The use of dual horizontal wells in gas production from hydrate accumulations, Applied Energy. 112 (2013) 1303–1310.

[94] H. Lee, Y. Seo, Y.-T. Seo, I.L. Moudrakovski, J. a Ripmeester, Recovering methane from solid methane hydrate with carbon dioxide., Angewandte Chemie (International Ed. in English). 42 (2003) 5048–51.

[95] B. A. Baldwin, J. Stevens, J.J. Howard, A. Graue, B. Kvamme, E. Aspenes, et al., Using magnetic resonance imaging to monitor CH_4 hydrate formation and spontaneous conversion of CH_4 hydrate to CO_2 hydrate in porous media., Magnetic Resonance Imaging. 27 (2009) 720–6.

[96] A. Graue, B. Kvamme, B.A. Baldwin, J. Stevens, et al., MRI Visualization of Spontaneous Methane Production From Hydrates in Sandstone Core Plugs When Exposed to CO_2, SPE Journal, June, (2008) 1–4.

[97] Y.A. Oghaki, K., Inoue, A proposal for gas storage on the bottom of the ocean using gas hydrates, International Chemical Engineering. 34 (1994) 417–419.

[98] Y. Seo, H. Lee, Multiple-Phase Hydrate Equilibria of the Ternary Carbon Dioxide, Methane, and Water Mixtures, Journal of Physical Chemistry. 105 (2001) 10084–10090.

[99] B.R. Lee, C. a Koh, A.K. Sum, Quantitative measurement and mechanisms for CH_4 production from hydrates with the injection of liquid CO_2., Physical Chemistry Chemical Physics : PCCP. 16 (2014) 14922–7.

[100] N. Goel, In situ methane hydrate dissociation with carbon dioxide sequestration: Current knowledge and issues, Journal of Petroleum Science and Engineering. 51 (2006) 169–184.

[101] J.L. Panter, A.L. Ballard, A.K. Sum, E.D. Sloan, C.A. Koh, Hydrate Plug Dissociation via Nitrogen Purge : Experiments and Modeling, Energy & Fuels. 25 (2011) 2572–2578.

[102] M. Masuda, Y., Konno, U., Hasegawa, T., Haneda, H., Ouchi, H., Kurihara, Prediction of methane hydrate dissociation behavior by nitrogen injection, in: Proceedings of 6th International Conference on Gas Hydrates, Vancouver, British Columbia, Canada, 2008.

[103] Y. Lee, Y. Kim, J. Lee, H. Lee, Y. Seo, CH_4 recovery and CO_2 sequestration using flue gas in natural gas hydrates as revealed by a micro-differential scanning calorimeter, Applied Energy. 150 (2015) 120–127.

[104] N. Garapati, P. Mcguire, B.J. Anderson, Modeling the Injection of Carbon Dioxide and Nitrogen into a Methane Hydrate Reservoir and the Subsequent Production of Methane Gas on the North Slope of Alaska, in: Proceedings of Unconventional Resources Technology Conference (URTeC), Denver, Colorado, USA, 12-14 August 2013.

[105] W.S. White, M., Lee, Guest Molecule Exchange Kinetics for the 2012 Ignik Sikumi Gas Hydrate, in: Offshore Technology Conference, Houston, Texas, 5-8 May 2014.

[106] D.-Y. Koh, H. Kang, D.-O. Kim, J. Park, M. Cha, H. Lee, Recovery of methane from gas hydrates intercalated within natural sediments using CO_2 and a CO_2/N_2 gas mixture., ChemSusChem. 5 (2012) 1443–8.

[107] Y. Park, M. Cha, J. Cha, K. Shin, H. Lee, Swapping carbon dioxide for complex gas hydrate structures, in: 6th International Conference on Gas Hydrates (ICGH 2008) Vancouver, British Columbia, Canada 6-10 July, 2008.

[108] T.S. Collett, U.S.G. Survey, G.D. Ginsburg, S. Petersburg, Gas Hydrates in the Messoyakha Gas Field of the West Siberian Basin — A Re-Examination of the Geologic Evidence, International Journal of Offshore and Polar Engineering. 8 (1998).

[109] T.S. Collett, W.F. Agena, M. Lee, M. V. Zyrianova, K.J. Bird, R.R. Charpentier et al., Assessment of Gas Hydrate Resources on the North Slope , Alaska , 2008. U. S. Geological Survey Fact Sheet 2008-3073, 2008.

[110] B.J. Anderson, M. Kurihara, M.D. White, G.J. Moridis, S.J. Wilson, M. Pooladi-Darvish, et al., Regional long-term production modeling from a single well test, Mount Elbert gas hydrate stratigraphic test well, Alaska North Slope, Marine and Petroleum Geology. 28 (2011) 493–501.

[111] S.H. Hancock, T.S. Collett, S.R. Dallimore, T. Satoh, T. Inoue, E. Huenges, et al., Overview of thermal-stimulation production-test results for the JAPEX/ JNOC/GSC et al . Mallik 5L-38 gas hydrate production research well, Bulletin-Geological Survey Of Canada 585 (2005) 1–2.

[112] S.H. Hancock, S.R. Dallimore, T.S. Collett, D. Carle, B. Weatherill, T. Satoh, et al., Overview of pressure-drawdown production-test results for the JAPEX/JNOC/GSC et al. Mallik 5L-38 gas hydrate production research well, Bulletin-Geological Survey Of Canada 585. (2005) 134.

[113] M. Kurihara, A. Sato, K. Funatsu, H. Ouchi, et al, SPE 132155 Analysis of Production Data for 2007 / 2008 Mallik Gas Hydrate Production Tests in Canada, in: CPS/SPE International Oil & Gas Conference and Exhibition, Beijing, China, 8-10 June, 2010.

[114] D. Schoderbek, H. Farrell, K. Hester, J. Howard, K. Raterman, S. Silpngarmlert, et al., ConocoPhillips Gas Hydrate Production Test Final Technical Report, 2013.

[115] K. Yamamoto, Japan Completes First Offshore Methane Hydrate Production Test — Methane Successfully Produced from Deepwater Hydrate Layers, Fire in the Ice: NETL. 13 (2013).

[116] K. Yamamoto, Y. Terao, T. Fujii, M.N. Corporation, Operational overview of the first offshore production test of methane hydrates in the Eastern Nankai Trough, in: Offshore Technology Conference, Houston, Texas, 2014: pp. 2007–2008.

[117] B. Metz, O. Davidson, H. de Connick, Carbon Dioxide Capture and Storage, IPCC Special Report, 2005.

[118] P. Englezos, D. Lee, Gas Hydrates : A Cleaner Source of Energy and Opportunity for Innovative Technologies, Korean Journal of Chemical Engineering. 22 (2005) 671–681.

[119] B. McKee, Zero Emissions Technologies for Fossil Fuels: Energy Security, Environmental Protection and Economic Development, Status Report, OECD/IEA, Paris, 2002.

[120] S.M. Klara, R.D. Srivastava, U. S. DOE Integrated Collaboratove Technology Development Program for CO2 Separation and Capture, Environmental Progress. 21 (2002).

[121] M. Yang, W. Jing, J. Zhao, Z. Ling, Y. Song, Promotion of hydrate-based CO_2 capture from flue gas by additive mixtures (THF (tetrahydrofuran) + TBAB (tetra-n-butyl ammonium bromide)), Energy. 106 (2016) 546–553.

[122] B. Castellani, M. Filipponi, A. Nicolini, F. Cotana, F. Rossi, Carbon Dioxide Capture Using Gas Hydrate Technology, Journal of Energy and Power Engineering. 7 (2013) 883–890.

[123] S. Kang, H. Lee, Recovery of CO_2 from Flue Gas Using Gas Hydrate : Thermodynamic Verification through Phase Equilibrium Measurements, Environmental Progress. 34 (2000) 4397–4400.

[124] Y. Wang, X. Lang, S. Fan, Hydrate capture CO_2 from shifted synthesis gas, flue gas and sour natural gas or biogas, Journal of Energy Chemistry. 22 (2013) 39–47.

[125] M.M. Mooijer-van Den Heuvel, Phase Behaviour and Structural Aspects of Ternary Clathrate Hydrate Systems The Role of Additives. PhD thesis., Delft University of Technology, 2004.

[126] J.M. Smith, H.C. van Ness, M.M. Abbott, Introduction to Chemical Engineering Thermodynamics, 6th ed., McGraw Hill, Singapore, 2001.

[127] K. M. Sabil, Phase Behaviour, Thermodynamics and Kinetics of Clathrate Hydrate Systems of Carbon Dioxide in Presence of Tetrahydrofuran and Electrolytes, PhD thesis., Delft University of Technology, 2009.

[128] T.W. de Loos, Understanding Phase Diagrams, In: Supercritical Fluids, Kiran, E., Levelt-Sengers, J. M. H., Applied Sciences, 273, (1994) 65–88.

[129] J.C. Platteeuw, J.H. van der Waals, Thermodynamic properties of gas hydrates, Molecular Physics. 1 (1958).

[130] E.D. Sloan, K.A. Sparks, J.J. Johnson, Two-phase liquid hydrocarbon-hydrate equilibrium for ethane and propane, Industrial Engineering Chemistry Research. 26 (1987) 1173–1179.

[131] P.R. Bishnoi, A.K. Gupta, P. Englezos, N. Kalogerakis, Multiphase equilibrium flash calculations for systems containing gas hydrates, Fluid Phase Equilobria. 53 (1989).

[132] B. Tohidi, A. Danesh, A. C. Todd, Modeling Single and Mixed Electrolyte-Solutions and Its Applications to Gas Hydrates, Chemical Engineering Research & Design. 73 (1995) 464–472.

[133] A. Martin, A Simplified van der Waals-Platteeuw Model of Clathrate Hydrates with Multiple Occupancy of Cavities, Journal of Physical Chemisry. 114 (2010) 9602–9607.

[134] G. Chen, T. Guo, Thermodynamic modelling of hydrate formation based on new concepts, Fluid Phase Equilibria. 122 (1996) 43–65.

[135] A.L. Ballard, E.D. Sloan, The Next Generation of Hydrate Prediction: An Overview, Journal of Supramolecular Chemistry. 2 (2002) 385–392.

[136] A.L. Ballard, E.D.S. Jr, The next generation of hydrate prediction I . Hydrate standard states and incorporation of spectroscopy, Fluid Phase Equilibria. 197 (2002) 371–383.

[137] A.L. Ballard, E.D. Sloan, The next generation of hydrate prediction Part III. Gibbs energy minimisation formalism, Fluid Phase Equilibria. 218 (2004) 15–31.

[138] L. Ballard, E. Sloan, The next generation of hydrate prediction IV, Fluid Phase Equilibria. 216 (2004) 257–270.

[139] D.A. Avlonitis, Thermodynamics of gas hydrate equilibria, PhD thesis, Heriot-Watt University, 1992.

[140] G. Soave, Equilbrium constants from a modified Redlich_Kwong equation of state, Chemical Engineering Science. 27 (1972) 1197–1203.

[141] D.B. Robinson, D.-Y. Peng, The characterization of the heptanes and heavier fractions for the GPA Peng-Robinson programs, Gas Processors Association, Tulsa, Okla., 1978.

[142] J.H. van der Waals, J.C. Platteeuw, Clathrate solutions, Advances in Chemical Physics. 2 (1959).

[143] P.B. Dharmawardhana, W.R. Parrish, E.D. Sloan, Experimental thermodynamic parameters for the prediction of natural gas hydrate dissociation conditions, Industrial & Engineering Chemistry Fundamentals. 19 (1980) 410–414.

[144] G.D. Holder, G. Corbin, K.D. Papadopoulos, Thermodynamic and molecular properties of gas hydrates from mixtures containing methane, argon, and krypton, Industrial and Engineering Chemistry Fundamentals. 19 (1980) 282–286.

[145] A.P. Mehta, E. Dendy Sloan, A thermodynamic model for structure-H hydrates, AIChE Journal. 40 (1994) 312–320.

[146] W.R. Parrish, J.M. Prausnitz, Dissociation pressures of gas hydrate formed by gas mixture, Industrial and Engineering Chemistry Process Design and Development. 11 (1972).

[147] A.H. Mohammadi, R. Anderson, B. Tohidi, Carbon Monoxide Clathrate Hydrates : Equilibrium Data and Thermodynamic Modeling, AIChE Journal. 51 (2005) 2825–2833.

[148] J. E. Lennard-Jones, A.. F.. Devonshire, Critical Phenomena in Gases I, Proceedings of the Royal Society of London. Series A, Mathematical and Physical Sciences. 163 (1937) 53–70.

[149] J.E. Lennard-Jones, A.F. Denoshire, Critical Phenomena in Gases II. Vapour Pressures and Boiling Points, Proceedings of the Royal Society of London . Series A , Mathematical and Physical Sciences. 165 (1938) 1–11.

[150] V. McKoy, O. Sinanoğlu, Theory of Dissociation Pressures of Some Gas Hydrates, The Journal of Chemical Physics. 38 (1963) 2946.

[151] A. Vysniauskas, P.R. Bishnoi, A kinetic study of methane hydrate formation, Chemical Engineering Science. 38 (1983) 1061–1072.

[152] P. Englezos, N. Kalogerakis, P.D. Dholabhai, P.R. Bishnoi, Kinetics of formation of methane and ethane gas hydrates, Chemical Engineering Science. 42 (1987) 2647–2658.

[153] P. Englezos, N. Kalogerakis, P.D. Dholabhai, P.R. Bishnoi, Kinetics of gas hydrate formation from mixtures of methane and ethane, Chemical Engineering Science. 42 (1987) 2659–2666.

[154] P. Skovborg, H.J. Ng, P. Rasmussen, U. Mohn, Measurement of induction times for the formation of methane and ethane gas hydrates, Chemical Engineering Science. 48 (1993) 445–453.

[155] V. Natarajan, P.R. Bishnoi, N. Kalogerakis, Induction phenomena in gas hydrate nucleation, Chemical Engineering Science. 49 (1994) 2075–2087.

[156] D. Kashchiev, A. Firoozabadi, Driving force for crystallization of gas hydrates, Jopurnal of Crystal Growth. 241 (2002) 220–230.

[157] D. Kashchiev, A. Firoozabadi, Nucleation of gas hydrates, Journal of Crystal Growth. 243 (2002) 476–489.

[158] A.R. Nerheim, T.M. Svartaas, E.K. Samuelsen, Investigation of hydrate kinetics in the nucleation and early growth phase by laser light scattering, in: Second International Offshore and Polar Engineering Conference, San Francisco, USA, 1992.

[159] P. Englezos, Nucleation and growth of gas hydrate crystals in relation to kinetic inhibiton, Revue de l'Institut Francais Du Petrole,. 51 (1996) 789–795.

[160] L. Jensen, K. Thomsen, N. von Solms, Propane hydrate nucleation: Experimental investigation and correlation, Chemical Engineering Science. 63 (2008) 3069–3080.

[161] J.P. Long, E.D. Sloan, Hydrates in the ocean and evidence for the location of hydrate formation, International Journal of Thermophysics. 17 (1996) 1–13.

[162] Z. Huo, E. Freer, M. Lamar, B. Sannigrahi, D.M. Knauss, E.D.S. Jr, Hydrate plug prevention by anti-agglomeration, Chemical Engineering Science. 56 (2001) 4979–4991.

[163] K.K. Østergaard, B. Tohidi, R.W. Burgass, A. Danesh, A.C. Todd, Hydrate equilibrium data of multicomponent systems in the presence of structure-II and structure-H heavy hydrate formers, Journal of Chemical and Engineering Data. 46 (2001) 703–708.

[164] C.J. Taylor, K.T. Miller, C. a. Koh, E.D. Sloan, Macroscopic investigation of hydrate film growth at the hydrocarbon/water interface, in: 6th International Conference on Gas Hydrates (ICGH 2008), Vancouver, British Columbia, Canada., 2008.

[165] Y. Fujioka, K. Takeuchi, Y. Shindo, H. Komiyama, Shrinkage of liquid CO_2 droplets in water, International Journal of Energy Research. 18 (1994) 765–769.

[166] H. Kimuro, F. Yamaguchi, K. Ohtsubo, T. Kusayanagi, M. Morishita, Energy Conversion Management, Energy Conversion and Management. 34 (1993) 1089–1094.

[167] S. Hirai, K. Okazaki, N. Araki, K. Yoshimoto, H. Ito, K. Hijikata, Experiments for the dynamic behavior of carbon dioxide in deep sea, Energy Conversion and Management. 36 (1995) 471–474.

[168] Y.H. Mori, Clathrate hydrate formation at the interface between liquid CO_2 and water phases-a review of rival models characterizing “hydrate films,” Energy Conversion and Management. 39 (1998) 1537–1557.

[169] A. Vysniauskas, P.R. Bishnoi, Kinetics of ethane hydrate formation, Chemical Engineering Science. 40 (1985) 299–303.

[170] H.C. Kim, P.R. Bishnoi, R.A. Heidemann, S.S.H. Rizvi, Kinetics of methane hydrate decomposition, Chemical Engineering Science. 42 (1987) 1645–1653.

[171] G.J. Moridis, Numerical studies of gas production from methane hydrates, in: SPE Gas Technology Symposium, Calgary, Alberta, Canada, 2002.

[172] H. Hong, M. Pooladi-Darvish, P.R. Bishnoi, Analytical modelling of gas production from hydrates in porous media, Journal of Canadian Petroleum Technology. 42 (2003) 45–56.

[173] S.R. Davies, M.S. Seliim, E.D. Sloan, P. Bollavaram, D.J. Peters, Hydrate plug dissociation, AIChE Journal. 52 (2006).

[174] A. Gupta, Methane hydrate dissociation measurements and modeling: the role of heat transfer and reaction kinetics, PhD thesis, Colorado School of Mines, Golden. CO, 2007.

[175] X. Zhou, S. Fan, D. Liang, J. Du, Determination of appropriate condition on replacing methane from hydrate with carbon dioxide, Energy Conversion and Management. 49 (2008) 2124–2129.

[176] J. Zhao, L. Zhang, X. Chen, Z. Fu, Y. Liu, Y. Song, Experimental Study of Conditions for Methane Hydrate Productivity by the CO_2 Swap Method, Energy & Fuels. 29 (2015) 6887–6895.

[177] C. Deusner, N. Bigalke, E. Kossel, M. Haeckel, Methane Production from Gas Hydrate Deposits through Injection of Supercritical CO_2, Energies. 5 (2012) 2112–2140.

[178] J. Yang, A. Chapoy, B. Tohidi, P.S. Jadhawar, J. Lee, Thermodynamic Conditions and Kinetics of Integrated Methane Recovery and Carbon Dioxide Sequestration, in: OTC, 2008.

[179] S.-P. Kang, H. Lee, C.-S. Lee, W.-M. Sung, Hydrate phase equilibria of the guest mixtures containing CO_2, N_2 and tetrahydrofuran, Fluid Phase Equilibria. 185 (2001) 101–109.

[180] I.B.A. Sfaxi, V. Belandria, A.H. Mohammadi, R. Lugo, D. Richon, Phase equilibria of CO_2+N_2 and CO_2+CH_4 clathrate hydrates: Experimental measurements and thermodynamic modelling, Chemical Engineering Science. 84 (2012) 602–611.

[181] N. Garapati, B.J. Anderson, Statistical thermodynamics model and empirical correlations for predicting mixed hydrate phase equilibria, Fluid Phase Equilibria. 373 (2014) 20–28.

[182] S.H.B. Yang, P. Babu, S.F.S. Chua, P. Linga, Carbon dioxide hydrate kinetics in porous media with and without salts, Applied Energy. 162 (2016) 1131–1140.

[183] J.M. Schicks, M. Luzi, The Conversion Process of Hydrocarbon Hydrates into CO_2 Hydrates and Vice Versa : Thermodynamic Considerations, (2011) 13324–13331.

[184] M. Ota, Y. Abe, M. Watanabe, R.L. Smith, H. Inomata, Methane recovery from methane hydrate using pressurized CO2, Fluid Phase Equilibria. 228-229 (2005) 553–559.

[185] J. Yoon, T. Kawamura, Y. Yamamoto, T. Komai, Transformation of Methane Hydrate to Carbon Dioxide Hydrate : In Situ Raman Spectroscopic Observations, (2004) 5057–5059.

[186] S. Lee, Y. Lee, J. Lee, H. Lee, Y. Seo, Experimental Verification of Methane − Carbon Dioxide Replacement in Natural Gas Hydrates Using a Differential Scanning Calorimeter, Environmental Science and Technology. 47 (2013) 13184-13190.

[187] M. Ben Clennell, M. Hovland, J.S. Booth, P. Henry, W.J. Winters, Formation of natural gas hydrates in marine sediments: 1. Conceptual model of gas hydrate growth conditioned by host sediment properties, Journal of Geophysical Research: Solid Earth. 104 (1999) 22985–23003.

[188] X. Zhou, S. Fan, D. Liang, J. Du, Replacement of Methane from Quartz Sand-Bearing Hydrate with Carbon Dioxide-in-Water Emulsion, Energy & Fuels. 22 (2008) 1759–1764.

[189] Y. Park, D. Kim, J. Lee, D. Huh, K. Park, J. Lee, et al., Sequestering carbon dioxide into complex structures of naturally occurring gas hydrates, in: Proceedings of the National Academy of Science, 2006: pp. 1–5.

[190] K. Shin, Y. Park, M. Cha, K. Park, D. Huh, J. Lee, et al., Swapping Phenomena Occurring in Deep-Sea Gas Hydrates, Energy & Fuels. 22 (2008) 3160–3163.

[191] Y. Seo, W. Jang, S.P. Kang, Study on Mechanism of Methane Hydrate Replacement by Carbon Dioxide Injection, in: Proceedings of the Nineteenth International Offshore and Polar Engineering Conference, Osaka, Japan, June 21-26, 2009: p. 880653.

[192] Y. Masuda, H. Maruta, S. Naganawa, K. Amikawa, Methane recovery from hydrate-bearing sediments by N_2-CO_2 gas mixture injection : experimental investigation on CO_2-CH_4 exchange ratio, in: Proceedings of 7th International Conference on Gas Hydrates,, Edinburgh, Scotland, United Kingdom, July 17-21, 2011: p. 7492.

[193] G.J. Moridis, L. Berkeley, T.S. Collett, J. Rutqvist, M.B. Kowalsky, et al., Challenges, Uncertainties, and Issues Facing Gas Production From Gas-Hydrate Deposits, SPE Reservoir Evaluation and Engineering. 14 (2011) 76–112.

[194] M.H. Yousif, D.B. Young, A simple correlation to predict the hydrate point suppression in drilling fluids, in: The 1993 SPE/IADC Drilling Conference, Amsterdam, The Netherlands, 1993: pp. 287–294.

[195] D. Mei, J. Liao, J. Yang, T. Guo, Hydrate formation of a synthetic natural gas mixture in aqueous solutions containing electrolyte , methanol , and (electrolyte + methanol), Journal of Chemical and Engineering Data. 43 (1998) 178–182.

[196] B. Tohidi, A. Danesh, A.C. Todd, On the mechanism of gas hydrate formation in subsea sediments, ACS Division of Fuel Chemistry, Preprints. 42 (1997) 485–487.

[197] I. Valko, Development of physical techniques for hydrate monitoring and early warning systems, PhD thesis, Heriot-Watt University, 2011.

[198] H. Lu, R. Matsumoto, Y. Tsuji, H. Oda, Anion plays a more important role than cation in affecting gas hydrate stability in electrolyte solution? - A recognition from experimental results, Fluid Phase Equilibria. 178 (2001) 225–232.

[199] J.L. De Roo, C.J. Peters, R.N. Lichtenthaler, G.A.M. Diepen, Occurrence of methane hydrate in saturated and unsaturated solutions of sodium chloride and water in dependence of temperature and pressure, AIChE Journal. 29 (1983) 651–657. doi:10.1002/aic.690290420.

[200] P.D. Dholabhai, P. Englezos, N. Kalogerakis, P.R. Bishnoi, Equilibrium conditions for methane hydrate formation in aqueous mixed electrolyte solutions, The Canadian Journal of Chemical Engineering. 69 (1991) 800–805.

[201] T. Maekawa, Equilibrium conditions for gas hydrates of methane and ethane mixtures in pure water and sodium chloride solution, Geochemical Journal. 35 (2001) 59–66. doi:10.2343/geochemj.35.59.

[202] M.D. Jager, E.D. Sloan, The effect of pressure on methane hydration in pure water and sodium chloride solutions, Fluid Phase Equilibria. 185 (2001) 89–99.

[203] M.D. Jager, C.J. Peters, E.D. Sloan, Experimental determination of methane hydrate stability in methanol and electrolyte solutions, Fluid Phase Equilibria. 193 (2002) 17–28.

[204] H. Najibi, A. Chapoy, H. Haghighi, B. Tohidi, Experimental determination and prediction of methane hydrate stability in alcohols and electrolyte solutions, Fluid Phase Equilibria. 275 (2009) 127–131.

[205] Y. Zhang, X.-S. Li, Y. Wang, Z.-Y. Chen, K.-F. Yan, Decomposition conditions of methane hydrate in marine sediments from South China Sea, Fluid Phase Equilibria. 413 (2016) 110–115.

[206] Y.P. Handa, D. Stupin, Thermodynamic Properties and Dlssociation Characteristics of Methane and Propane Hydrates in 70-A-Radius Silica Gel Porest, Journal of Physical Chemisry. 96 (1992) 8599–8603.

[207] J. Husebø, G. Ersland, A. Graue, B. Kvamme, Effects of salinity on hydrate stability and implications for storage of CO_2 in natural gas hydrate reservoirs, Energy Procedia. 1 (2009) 3731–3738.

[208] P. Mekala, P. Babu, J.S. Sangwai, P. Linga, Formation and dissociation kinetics of methane hydrates in seawater and silica sand, Energy & Fuels. 28 (2014) 2708–2716.

[209] P.D. Dholabhai, N.E. Kalogerakis, P.R. Bishnoi, Kinetics of methane hydrate formation in aqueous electrolyte solutions, Canadian Journal of Chemical Engineering. 71 (1993) 68–74.

[210] Z.R. Chong, A.H.M. Chan, P. Babu, M. Yang, P. Linga, Effect of NaCl on methane hydrate formation and dissociation in porous media, Journal of Natural Gas Science and Engineering. 27 (2015) 178–189.

[211] S. Bando, F. Takemura, M. Nishio, E. Hihara, M. Akai, Solubility of CO_2 in Aqueous Solutions of NaCl at (30 to 60) °C and (10 to 20) MPa, Journal of Chemical and Engineering Data. 48 (2003) 576–579.

[212] M. Sadeghi, H. Salami, V. Taghikhani, M.A. Robert, A comprehensive study on CO_2 solubility in brine: Thermodynamic based and neural network modeling, Fluid Phase Equilibria. 403 (2015).

[213] E. Mohammadian, H. Hamidi, M. Asadullah, A. Azdarpour, S. Motamedi, R. Junin, Measurement of CO_2 Solubility in NaCl Brine Solutions at Different Temperatures and Pressures Using the Potentiometric Titration Method, Journal of Chemical and Engineering Data. 60 (2015).

[214] T. Uchida, T. Ebinuma, T. Ishizaki, Dissociation Condition Measurements of Methane Hydrate in Confined Small Pores of Porous Glass, Journal of Phy. 103 (1999) 3659–3662.

[215] V.S. Yakushev, Peculiarities of mass-exchange in dispersed rocks during hydrate formation, Natural and Technogenic Gas Hydrates. (1990) 174–187.

[216] R. Matsumoto, Y. Watanabe, M. Satoh, H. Okada, Y. Hiroki, M. Kawasaki, Distribution and occurrence of marine gas hydrates Preliminary results of ODP Leg164: Blake Ridge Drilling, Journal-Geological Society Of Japan. 102 (1996) 932–944.

[217] C. Ruppel, Anomalously cold temperatures observed at the base of the gas hydrate stability zone on the U . S . Atlantic passive margin, Geology. 25 (1997) 699–702.

[218] T. Uchida, T. Ebinuma, S. Takeya, J. Nagao, H. Narita, Effects of Pore Sizes on Dissociation Temperatures and Pressures of Methane, Carbon Dioxide, and Propane Hydrates in Porous Media, Journal of Physical Chemisry. 106 (2002) 820–826.

[219] R. Anderson, M. Llamedo, B. Tohidi, R.W. Burgass, Experimental measurement of methane and CO_2 clathrate hydrate equilibria in mesoporous silica., J. Physical Chemistry. 107 (2003) 3507–3514.

[220] T. Uchida, S. Takeya, E.M. Chuvilin, R. Ohmura, J. Nagao, V.S. Yakushev, et al., Decomposition of methane hydrates in sand, sandstone, clays and glass beads, Journal of Geophysical Research: Solid Earth. 109 (2004) 1–12.

[221] S.B. Cha, T.R. Wildeman, E.D. Sloan, A Third-Surface Effect on Hydrate Formation, Journal of Physical Chemisry. 92 (1988) 6492–6494.

[222] T.S. Kotkoskle, B.A.I. Ubaldl, T.R. Wildeman, E.D.S. Jr, Inhibition of Gas Hydrates in Water-Based Drilling Muds, SPE Drliing Engineering. (1992).

[223] S. Park, G. Sposito, Do Montmorillonite Surfaces Promote Methane Hydrate Formation? Monte Carlo and Molecular Dynamics Simulations, Journal of Physical Chemisry. 107 (2003) 2281–2290.

[224] K.-F. Yan, X.-S. Li, Z.-Y. Chen, Z.-M. Xia, C.-G. Xu, Z. Zhang, Molecular Dynamics Simulation of the Crystal Nucleation and Growth Behavior of Methane Hydrate in the Presence of the Surface and Nanopores of Porous Sediment., Langmuir : the ACS Journal of Surfaces and Colloids. 32 (2016) 7975–84.

[225] H. Ji, G. Wu, M. Zi, D. Chen, Microsecond Molecular Dynamics Simulation of Methane Hydrate Formation in Humic-Acid-Amended Sodium Montmorillonite, Energy & Fuels. 30 (2016) 7206–7213.

[226] Y. Seo, J. Seol, S. Yeon, D. Koh, M. Cha, S. Kang, et al., Structural, Mineralogical , and Rheological Properties of Methane Hydrates in, Journal of Chemical and Engineering Data. 54 (2009) 1284–1291.

[227] L. Ruffine, Exploring methane-hydrate formation and dissociation in geologic materials through laboratory experiments : Kinetic behavior and morphology, FUEL. 141 (2015) 173–184.

[228] Y. Ahn, H. Kang, D. Koh, H. Lee, Production of Natural Gas Hydrate by Using Air and Carbon Dioxide, International Journal of Chemical, Molecular, Nuclear, Materials and Metallurgical Engineering. 9 (2015) 796–800.

[229] A. Okwananke, J. Yang, B. Tohidi, Experimental studies of methane recovery from methane hydrate in sediments by a combination of flue gas injection and depressurisation, in: Proceedings of the 8th International Conference on Gas Hydrates (ICGH8-2014), Beijing, China, 28 July - 1 August, 2014.

[230] J. Yang, A. Okwananke, B. Tohidi, E. Chuvilin, K. Maerle, V. Istomin, et al., Flue gas injection into gas hydrate reservoirs for methane recovery and carbon dioxide sequestration, Energy Conversion and Management. 136 (2017) 431–438.

[231] H. Kang, D.-Y. Koh, H. Lee, Nondestructive natural gas hydrate recovery driven by air and carbon dioxide., Scientific Reports. 4 (2014) 6616.

[232] H. Haneda, Y. Sakamoto, T. Kawamura, K. Aoki, T. Komai, Experimental study on dissociation behavior of methane hydrate by air, in: Proceedings of the Fifth International Conference on Gas Hydrates, June 12-16, 2005. Trondheim, Norway.

[233] R.L. Kleinberg, C. Flaum, D.D. Griffin, P.G. Brewer, G.E. Malby, E.T. Peltzer, et al., Deep sea NMR: Methane hydrate growth habit in porous media and its

relationship to hydraulic permeability, deposit accumulation, and submarine slope stability, Journal of Geophysical Research: Solid Earth. 108 (2003).

[234] W.F. Waite, J.C. Santamarina, D.D. Cortes, B. Dugan, D.N. Espinoza, J. Germaine, et al., Physical properties of hydrate-bearing sediments, Reviews of Geophysics. 47 (2009) 1–38.

[235] T.J. Kneafsey, L. Berkeley, Permeability of Laboratory-Formed Methane-Hydrate-Bearing Sand : Measurements and Observations Using X-Ray Computed Tomography, SPE Journal. (2011) 78–94.

[236] G.R. Dickens, J.R. O'Neil, D.K. Rea, R.M. Owen, Dissociation of oceanic methane hydrate as a cause of the carbon isotope excursion at the end of the Paleocene, Paleoceanography. 10 (1995) 965–971.

[237] L.A. Stern, S.H. Kirby, W.B. Durham, Peculiarities of methane clathrate hydrate formation and solid-state deformation, including possible superheating of water ice, Science. 273.5283 (1996) 1843–1848.

[238] L.A. Stern, S.H. Kirby, S. Circone, W.B. Durham, Scanning Electron Microscopy investigations of laboratory-grown gas clathrate hydrates formed from melting ice, and comparison to natural hydrates, American Mineralogist. 89 (2004) 1162–1175.

[239] J. A. Priest, E.V.L. Rees, C.R.I. Clayton, Influence of gas hydrate morphology on the seismic velocities of sands, Journal of Geophysical Research. 114 (2009) B11205.

[240] B. Tohidi, R. Anderson, M. Ben Clennell, R.W. Burgass, A.B. Biderkab, Visual observation of gas-hydrate formation and dissociation in synthetic porous media by means of glass micromodels, Geology. 29 (2001) 867–870.

[241] A. Kumar, B. Maini, M. Clarke, O. Zatsepina, S. Srinivasan, Experimental determination of permeability in the presence of hydrates and its effect on the dissociation characteristics of gas hydrates in porous media, Journal of Petroleum Science and Engineering. 70 (2010) 114–122.

[242] M.L. Delli, J.L.H. Grozic, Experimental determination of permeability of porous media in the presence of gas hydrates, Journal of Petroleum Science and Engineering. 120 (2014) 1–9.

[243] G.J. Moridis, M.B. Kowalsky, K. Pruess, TOUGH + HYDRATE v1 . 2 A code for the simulation of system behavior in hydrate-bearing geologic media, Earth Sciences Division, Lwarence |Berkeley National Laboratory, Berkeley, CA., 2012.

[244] M. Uddin, D. Coombe, D. Law, B. Gunter, Numerical Studies of Gas Hydrate Formation and Decomposition in a Geological Reservoir, Journal of Energy Resources Technology. 130 (2008) 032501.

[245] M. Uddin, F. Wright, D. Coombe, Numerical Study of Gas Evolution and Transport Behaviours in Natural Gas-Hydrate Reservoirs, Journal of Canadian Petroleum Technology, (2010) 19–21.

[246] M. Uddin, D. Coombe, F. Wright, Modeling of CO_2-Hydrate Formation in Geological Reservoirs by Injection of CO_2 Gas, Journal of Energy Resources Technology. 130 (2008) 032502.